Springer Proceedings in Physics 300

Luca Argenti
Michael Chini
Li Fang *Editors*

Proceedings of the 8th International Conference on Attosecond Science and Technology

Springer

Springer Proceedings in Physics

Volume 300

Indexed by Scopus

The series Springer Proceedings in Physics, founded in 1984, is devoted to timely reports of state-of-the-art developments in physics and related sciences. Typically based on material presented at conferences, workshops and similar scientific meetings, volumes published in this series will constitute a comprehensive up to date source of reference on a field or subfield of relevance in contemporary physics. Proposals must include the following:

– Name, place and date of the scientific meeting
– A link to the committees (local organization, international advisors etc.)
– Scientific description of the meeting
– List of invited/plenary speakers
– An estimate of the planned proceedings book parameters (number of pages/articles, requested number of bulk copies, submission deadline).

Please contact:

For Americas and Europe: Dr. Zachary Evenson; zachary.evenson@springer.com
For Asia, Australia and New Zealand: Dr. Loyola DSilva; loyola.dsilva@springer.com

Luca Argenti • Michael Chini • Li Fang
Editors

Proceedings of the 8th International Conference on Attosecond Science and Technology

Springer

Editors
Luca Argenti
Department of Physics & CREOL,
The College of Optics and Photonics
University of Central Florida
Orlando, FL, USA

Michael Chini
Department of Physics & CREOL,
The College of Optics and Photonics
University of Central Florida
Orlando, FL, USA

Li Fang
Department of Physics & CREOL,
The College of Optics and Photonics
University of Central Florida
Orlando, FL, USA

ISSN 0930-8989 ISSN 1867-4941 (electronic)
Springer Proceedings in Physics
ISBN 978-3-031-47937-3 ISBN 978-3-031-47938-0 (eBook)
https://doi.org/10.1007/978-3-031-47938-0

This work was supported by University of Central Florida.

This Springer imprint is published by the registered company Springer Nature Switzerland AG
The registered company address is: Gewerbestrasse 11, 6330 Cham, Switzerland

Paper in this product is recyclable.

Preface

ATTO is the largest and most prestigious world conference in the field of attosecond science, covering topics such as attosecond pulse generation and characterization, time-resolved spectroscopies of ultrafast phenomena taking place on the attosecond and femtosecond timescales, and attosecond science with free-electron lasers.

The ATTO conference series started August 1–5, 2007 under the name of "Attosecond Physics", with the scientific coordination of Paul Corkum (National Research Council of Canada, Ottawa, Canada), Ferenc Krausz (MPI für Quantenoptik, Garching, Germany), and Jan-Michael Rost (MPI für Physik komplexer Systeme, Dresden, Germany). The original announcement read

> The interaction between intense ultra-short laser pulses and matter constitutes a new field of research. It challenges the experiment and also theory, since a non-perturbative description with regard to high non-linear multi-photon processes is required. So far, the biggest breakthrough which has emerged from the experimental and theoretical attosecond research in this highly non-linear non-perturbative regime of laser-matter-interaction, was the creation and measurement of attosecond pulses. Having them at our disposal we are at the beginning of a new scientific era, the age of attosecond science. It will give researchers a completely new microscopic insight into electron processes, taking place in atoms, molecules, biosystems, clusters, semiconductor nanostructures or plasmas. They can be observed in real-time and even controlled to an increasing extent on their natural (attosecond) time scale.
>
> The main purpose of the workshop will be to discuss the current status of attosecond research and the obstacles for further development of attosecond measurements towards shorter time intervals and higher intensities, as well as methods to resolve them. A second important aim is to discuss, understand and propose new applications of attosecond technique in biology, chemistry, physics and plasma physics.

The subsequent editions were held: July 29–August 1, 2009, at Kansas State University (Manhattan, Kansas, USA) co-chaired by Chii-Dong Lin and Zenghu Chang; July 6–8, 2011, at Hokkaido University (Sapporo, Japan), co-chaired by Katsumi Midorikawa and Kaoru Yamanouchi; July 8–12, 2013, at the Institut Pasteur (Paris, France), co-chaired by Pascal Salières and Eric Constant; July 5–10, 2015,

at Manoir Saint-Sauveur (Saint-Sauveur, Quebec, Canada), co-chaired by François Légaré and Paul Corkum; July 2–7, 2017, at Shaanxi Zhangbagou Guesthouse (Xi'an, China), co-chaired by Zhiyi Wei and Zenghu Chang; July 1–5, 2019, at the University of Szeged Congress Centre (Szeged, Hungary, EU), co-chaired by Katalin Varjú and Dimitris Charalambidis. The 2022 edition of the conference, therefore, was the first since 2009 to take place in the USA.

We received more than 300 contributed abstracts. The geographic distribution of the contributed abstracts was exceptionally diverse: 26% came from 18 different states within the United States, and the others 74% came from 30 different countries from all over the world.

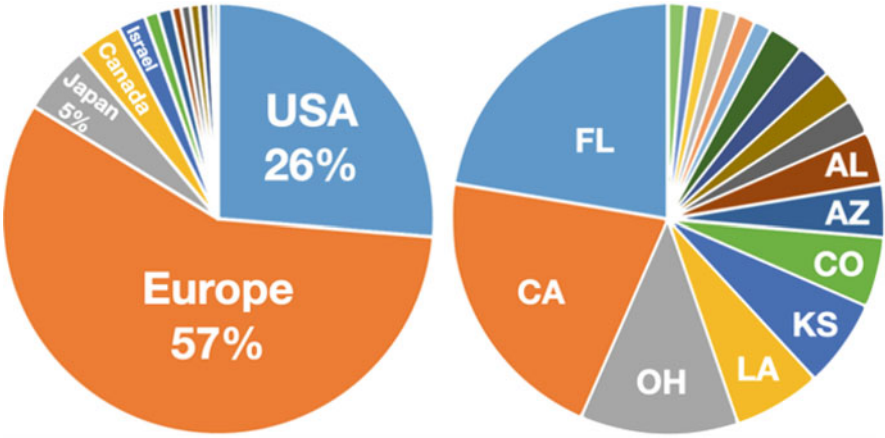

The contributed abstracts covered the whole set of attosecond topics, and were classified according to four criteria: (1) Gas vs. Condensed Phase; (2) In situ vs. Ex situ; (3) Photon vs. Fragment (electrons, ions) detection; (4) Experimental vs. Theoretical vs. Both. Gas-phase ex situ photoelectron spectroscopies were a third of all the abstracts, so they were divided in atomic and molecular targets.

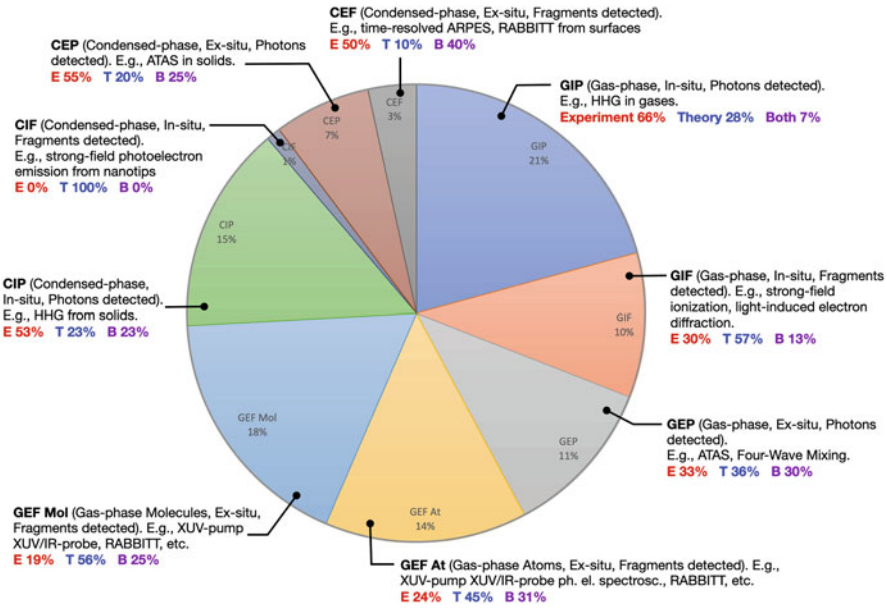

The main objectives of the conference were: (i) to outline the state of the art of attosecond research; (ii) to jump-start national and international collaborations that have been hindered by the pandemic; (iii) to promote recruiting and training of postdocs and tenure-track candidates; (iv) to consolidate the global and diverse identity of the attosecond science community (Fig. 1).

Conference sessions began on the morning of Monday, July 11, 2022, and continued until Friday afternoon, July 15. In addition to the scientific program, four special scientific and business events were held at the conference: (1) The conference was opened by a Wolf-Prize session dedicated to three invited talks by the three 2022 Physics Wolf-Prize laureates, Dr. Anne L'Huillier, Dr. Ferenc Krausz, and Dr. Paul Corkum, who received the award as pioneers of the field of attosecond science. (2) An evening round table on "The Future of Attosecond Science" was held, composed of established and emerging female leaders in the field, with the goals of highlighting the important contributions of women in attosecond science and inspiring the next generation of attosecond scientists. (3) The conference featured an evening session giving an overview of US funding in attosecond science, with the goal of introducing junior scientists to the world of research grants. (4) The conference also hosted an evening session devoted to AttoChem, a network funded by the European Cooperation in Science and Technology (COST) to coordinate experimental and theoretical efforts in attosecond chemistry, with the goal of stimulating a discussion on the need for similar coordination efforts in the United States.

Fig. 1 Top left panel: Audience in the main session at the Celeste Hotel. Other panels: Poster session at the Morgridge International Reading Center, on the main UCF campus

The conference included a social program which was comprised of an excursion to the Kennedy Space Center and a post-conference social gathering at Blue Springs State Park.

Orlando, FL, USA
August 2023

Luca Argenti
Michael Chini
Li Fang

Acknowledgements

This conference would not have been possible without the endorsement and material support of countless colleagues, administrators, federal agencies, and private sponsors, to whom we are deeply grateful. Even counting only the material contribution to the conference, American institutions and sponsors have contributed almost 40% of the overall conference budget, allowing us to offer many prime services to the ATTO community, and financial support to many of its junior members, while keeping the registration fee affordable.

We are grateful to Dr. Eduardo Mucciolo, chair of the Physics department in 2019, who allowed the formation of an *ad hoc* ATTO committee as a part of our departmental service assignment, and for directing the department's administrative staff to aid us in organizing the conference. This decision directed departmental resources to the organization of ATTO and allowed the members of the local organizing committee to dedicate sufficient time for this demanding task.

From the beginning, Dr. Michael Johnson, who in 2019 was Dean of the College of Sciences (COS), has granted the strongest support to the conference. He generously offered to cover the expenses associated with accounts at Continuing Education, the unit responsible for management of all conferences held at UCF. Dr. Johnson's support has continued in his subsequent role as Provost. In this capacity, he agreed to sign the contract with the Conference Hotel, thus relieving us from the liability associated to a possible cancellation of the event. Seresa Cruz, COS HR and Budget director, has assisted us with the stipulation of the contract with Continuing Education and with the Conference Hotel. She has also provided valuable guidance, and has been instrumental in helping us to cut through a large amount of "red tape".

UCF President, Dr. Alexander N. Cartwright, has endorsed the conference and, in collaboration with Provost Johnson, he has initiated a process to prepare a master contract between the University and the Celeste hotel to facilitate the organization of future conferences and events on campus.

We thank Bahaa Saleh, who in 2019 was Dean of CREOL, the College of Optics, and supported the conference by assigning to us the assistance of Denise Whiteside, Assistant to the Dean, and other administrative staff at CREOL to guide us in contracting with the conference hotel. Denise, who has professional experience in

the hotel industry, was instrumental in helping us frame the initial conversations with the hotel, and following up with them in the negotiation for the hotel spaces. Mark Wagenhauser, the Budget Director of CREOL, directed us to the appropriate resources at UCF for Risk Management and for Contract administration.

Since 2019, both the College of Sciences and the College of Optics have new Deans, and the Department of Physics has a new Chair. The two new Deans, Dr. Maggy Tomova, at COS, and Dr. David Hagan, at CREOL, have been tremendously supportive of the conference and have provided assistance with completing the hotel contract, providing contacts with industrial sponsors, and other essential activities. Dr. Joshua Colwell, the current Physics Chair, has continued the support from the department and offered guidance on how to overcome the occasional hiccup.

Dr. Eric Van Stryland, Emeritus Dean of CREOL, and past president of the Optical Society of America (now OPTICA), has helped us establish contact with the right people at OPTICA and has manifested his endorsement to the conference throughout the last three years.

The AMOS program at the Department of Energy, managed by Dr. Thomas Settersten, the Modern Optics Program at the Army Research Office, managed by Dr. James Joseph, and the Ultrashort Pulse Laser-Matter Interactions Program at the Air Force Office for Scientific Research, managed by Dr. Andrew Stickrath, have each committed grant funding to the conference, which has promoted the participation of colleagues and junior scientists who wouldn't otherwise have been able to participate. IUPAP Commission *C15. Atomic, Molecular and Optical Physics* has also provided financial support, which has contributed making the conference proceedings open access.

We thank the Industrial Sponsors of the conference, whose generous support has enabled many of the conference functions, and whose participation will help foster future advances in the field.

We wish to thank the team at Continuing Education, Kevin Parker and Jana Breburdova, for their work in setting up the registration page and for managing the conference account. We are very grateful to the staff at the Department of Physics: Jessica Brooks, Nikitta Campbell, Sierra Cliburn, and Leida Vera Nater, for assisting us in the many administrative transactions of the conference, managing the spending from federal grants, and providing practical guidance in event organization.

We are grateful to the members of the *ad hoc* National and International Advisory Boards, who have helped us and the International Program Committee to put together a large pool of outstanding scientists from which the International Program Committee selected the invited speakers.

The International Program Committee has done a tremendous job in vetting not only the invited speakers but also the 300+ contributed abstracts we received. They have also been supportive of the local organization, consenting to postpone the conference by one year and thus giving us the opportunity to meet in-person.

We are thankful to our colleagues in the Local Organizing Committee, Nicolas Douguet, Madhab Neupane, and Mihai Vaida, who each took on important tasks.

We are grateful for the support of Dr. Samuel Harrison, the Editor of Springer Nature, who has guided us through the stipulation of the contract for the publication

of the Conference Proceedings and the setup of the OCS webpage for abstract submission, and who has generously offered to donate relevant books to be used as awards to poster-prize winners.

ATTO VIII was comprised of 14 technical oral sessions, 9 highlight sessions, and 3 evening sessions, for a total of 26 different functions. We wouldn't have been able to manage this complex program without the expert and generous assistance of many colleagues who agreed to serve as chairs: Cord Arnold, Cosmin Blaga, Nicolas Douguet, Zenghu Chang, Jan Marcus Dahlström, Per Eng-Johnsson, Li Fang, Mette B. Gaarde, Mathieu Gisselbrecht, Wendell T. Hill, Jiro Itatani, Kyung-Taec Kim, François Légaré, C. William McCurdy, Madhab Neupane, Mauro Nisoli, Thomas Pfeifer, Thierry Ruchon, Pascal Salières, Richard Taïeb, Uwe Thumm, Mihai Vaida, Katalin Varjú, Marc Vrakking, and Linda Young.

We thank the many undergraduate students who, even if they did not attend ATTO as presenters, agreed to serve as Conference Staff to welcome its participants and to facilitate their access and contribution to the Conference.

Finally, we thank all the conference participants, who have enthusiastically contributed to the conference with their best science and decided to attend it in person, and the authors of these proceedings.

Orlando, FL, USA
August 2023

Luca Argenti
Michael Chini
Li Fang

ATTO VIII Governance

1 Local Organizing Committee

The Local Organizing Committee was responsible for all the activities necessary for the successful conduction of the conference, as well as for facilitating and coordinating the activities of the International Program Committee.

• Luca Argenti, chair	Univ. Central Florida	Florida	USA
• Michael Chini, chair	Univ. Central Florida	Florida	USA
• Nicolas Douguet	Kennesaw University	Georgia	USA
• Li Fang	Univ. Central Florida	Florida	USA
• Madhab Neupane	Univ. Central Florida	Florida	USA
• Mihai Vaida	Univ. Central Florida	Florida	USA

2 International Program Committee

The International Program Committee is responsible for the governance and the scientific program of the ATTO conference. Its members oversee the conduction of ATTO, decide the conference program sessions and the list of invited speakers, vet the abstracts submitted to the conference, select the contributed speakers, and appoint the organizers of future ATTO conferences.

• Andrius Baltuška	Technical Univ. Vienna	Austria	EU
• Cosmin Blaga	Kansas State University	Kansas,	USA
• Thomas Brabec	University of Ottawa	Canada	
• Dimitris Charalambidis	University of Crete	Greece	EU
• Oren Cohen	Technion	Israel	
• Eleftherios Goulielmakis	University of Rostock	Germany	EU
• Jiro Itatani	University of Tokyo	Japan	
• Kyung Taec Kim	Institute for Basic Science	Korea	
• Matthias Kling	SLAC National Laboratory	California	USA
• François Légaré	INRS	Canada	
• Eva Lindroth	Stockholm University	Sweden	EU
• Johan Mauritsson	Lund University	Sweden	EU
• Daniel M Neumark	UC Berkeley	California	USA
• José A Pérez-Hernández	Pulsed Laser Center (CLPU)	Spain	EU
• Thierry Ruchon	CEA Saclay	France	EU
• Kenneth J Schafer	Louisiana State University	Louisiana	USA
• Olga Smirnova	Max Born Institute	Germany	EU
• Vasily Strelkov	Russian Acad. Sciences	Russia	
• Richard Taieb	Sorbonne Université	France	EU
• John Tisch	Imperial College London	UK	
• Katalin Varjú	ELI ALPS, Szeged	Hungary	EU
• Caterina Vozzi	CNR, Milano	Italy	EU
• Hans Jakob Wörner	ETH Zurich	Switzerland	
• Kun Zhao	Institute of Physics, CAS	China	

3 Advisory Boards

The Local Organizing Committee relied on the expertise and advice of all colleagues working in attosecond science to prepare an event that meets the needs of the international attosecond community at large. To pursue this conversation in a systematic, transparent, and manageable fashion, the Local Organizing Committee identified a selected group of researchers, representative of the various geographic regions and scientific interests of the attosecond community, who agreed to serve in a National and an International Advisory Board on the occasion of ATTO VIII. The members of the advisory board received periodic updates on the progress of the conference organization, and hence they had the chance of offering feedback and suggestions on its practical aspects. Furthermore, the advisory board members were asked to bring to the attention of the Local Organizing Committee, as well as, ultimately, of the International Program Committee, any new and relevant research trend in their region and field of interest.

3.1 International Advisory Board

• Jens Biegert	ICFO - Inst. Photonic Sciences	Spain	EU
• Paul Corkum	National Research Council	Canada	
• Nirit Dudovich	Weizmann Institute of Science	Israel	
• Feng He	Shanghai Jiaotong University	China	
• Ursula Keller	ETH Zurich	Switzerland	
• Ferenc Krausz	Max Planck Inst. Quantum Optics	Germany	EU
• Igor Litvinyuk	Griffith University	Australia	
• Jon Marangos	Imperial College London	UK	
• Fernando Martín	Universidad Autónoma de Madrid	Spain	EU
• Chang Hee Nam	Institute for Basic Science	Korea	
• Thomas Pfeifer	Max Planck Inst. Nuclear Physics	Germany	EU
• Françoise Remacle	University of Liège	Belgium	EU
• Pascal Salières	Paris-Saclay University	France	EU
• Kiyoshi Ueda	Tohoku University	Japan	

3.2 National Advisory Board

• Andreas Becker	UC Boulder	Colorado	USA
• Nora Berrah	University of Connecticut	Connecticut	USA
• Zenghu Chang	University of Central Florida	Florida	USA
• Lou DiMauro	The Ohio State University	Ohio	USA
• Mette B Gaarde	Louisiana State University	Louisiana	USA
• Wendell Hill	University of Maryland	Maryland	USA
• Stephen R Leone	UC Berkeley	California	USA
• C. William McCurdy	UC Davis	California	USA
• David Reis	Stanford University	California	USA
• Uwe Thumm	Kansas State University	Kansas	USA
• Linda Young	Argonne Natl. Lab., U. Chicago	Illinois	USA

Contents

Part I
Light Sources, High-Order Harmonics, and Attosecond Pulse Generation

Single-Cycle Infrared Waveform Generation and Control

Nathalie Nagl, Philipp Steinleitner, Maciej Kowalczyk, Jinwei Zhang, Vladimir Pervak, Christina Hofer, Aleksander Głuszek, Jarosław Sotor, Alexander Weigel, Ka Fai Mak, and Ferenc Krausz

Abstract Tailoring the electric-field waveform of few-cycle light pulses lays the foundation for controlling nonlinear optical phenomena on their genuine, attosecond time scale. So far, waveform control has been demonstrated mostly in the visible-to-near-infrared spectral region. Extending it to the mid-infrared range will open up new prospects in ultrafast optoelectronics as well as broadband field-resolved spectroscopy. We present a novel approach for shaping few-cycle waveforms, and thereby achieved the first multi-octave synthesis of single-cycle transients in the mid-infrared spectral range, with a continuously adjustable and highly-reproducible

N. Nagl (✉)
Max Planck Institute of Quantum Optics, Garching, Germany

Ludwig Maximilian University Munich, Garching, Germany
e-mail: nathalie.nagl@mpq.mpg.de

P. Steinleitner · K. F. Mak
Max Planck Institute of Quantum Optics, Garching, Germany

M. Kowalczyk · C. Hofer · F. Krausz
Max Planck Institute of Quantum Optics, Garching, Germany

Ludwig Maximilian University Munich, Garching, Germany

Center for Molecular Fingerprinting, Budapest, Hungary

J. Zhang
School of Optical and Electronic Information, Huazhong University of Science and Technology, Wuhan, China

V. Pervak
Ludwig Maximilian University Munich, Garching, Germany

A. Głuszek · J. Sotor
Wrocław University of Science and Technology, Wrocław, Poland

A. Weigel (✉)
Max Planck Institute of Quantum Optics, Garching, Germany

Center for Molecular Fingerprinting, Budapest, Hungary
e-mail: alexander.weigel@mpq.mpg.de

L. Argenti et al. (eds.), *Proceedings of the 8th International Conference on Attosecond Science and Technology*, Springer Proceedings in Physics 300,
https://doi.org/10.1007/978-3-031-47938-0_1

electric-field evolution. The concept is generalizable towards the synthesis of a broader variety of infrared waveforms, with a diversity of applications in ultrafast opto-electronics, attosecond metrology and field-resolved mid-infrared sensing.

Keywords Infrared and far-infrared lasers · Ultrafast lasers · Ultrafast nonlinear optics · Nonlinear wave mixing · Supercontinuum generation

1 Motivation

Confining laser light to a few cycles of its oscillating electromagnetic field and controlling the underlying electric-field waveform gave access to a variety of novel applications. They include the generation of isolated attosecond pulses [1] as well as sub-femtosecond optical control of solid-state electronic processes [2, 3]. Due to tremendous progress in the field of precision dispersion management, waveform control and synthesis of few-cycle pulses could be demonstrated in the near-infrared and visible spectral ranges [4, 5]. Extending waveform control to the mid-infrared region will enable a plethora of new applications, ranging from advances in electric-field-resolved vibrational spectroscopy of biological samples [6] to novel optoelectronic devices based on low-bandgap heavily-doped semiconductors [7]. To date, however, common approaches [8–11] for generating and controlling coherent mid-infrared radiation typically suffer from system complexity and limited reproducibility of the output waveforms. In addition, full phase control over bandwidths spanning an octave or more is lacking thus far.

In this work, we demonstrate a novel approach for generating coherent multi-octave mid-infrared radiation with the intrinsic capability of shaping the emerging waveforms. The concept is based on intrapulse difference-frequency generation (IPDFG) [12] in a single nonlinear crystal and demonstrated using the 7-fs single-cycle pulses from a diode-pumped, Kerr-lens-mode-locked, carrier-envelope-phase (CEP)-stabilized Cr:ZnS laser system. Specifically, we created infrared continua spanning 3.7 optical octaves in several spectral bands via cascaded IPDFG and manipulated their spectral phases by exploiting their different dependence on the CEP of the driving laser. This allows to manipulate the electric field of the single-cycle mid-infrared waveforms in the time domain, using the CEP of the driving laser as a control parameter. Our approach yields the first multi-octave control of single-cycle mid-infrared waveforms, with a continuous and highly reproducible adjustment of the electric-field evolution.

2 Overview of the Experimental Setup

Major components of this work have been demonstrated in a recent publication [13] and are illustrated in Fig. 1. While this section serves to provide a general overview

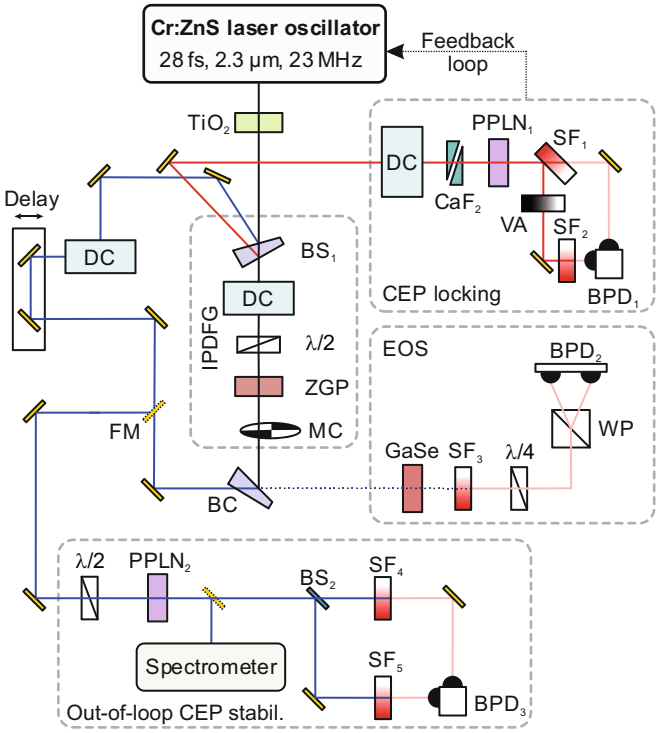

Fig. 1 Schematic of the experimental setup. The output pulses of the Cr:ZnS laser oscillator are spectrally broadened in a 0.5-mm-thick TiO_2 plate and subsequently split into three individual channels by using a wedged beam splitter (BS_1): the transmitted beam is used for intrapulse difference-frequency generation (IPDFG), the primary wedge reflection (blue line) acts as a gate pulse for electro-optic sampling (EOS) and the secondary wedge reflection (red line) is used for carrier-envelope-phase (CEP) locking. *DC* dispersion compensation unit, λ/2 half-wave plate, λ/4 quarter-wave plate, *MC* mechanical chopper, *BC* beam combiner, $SF_{1–5}$ spectral bandpass filters, $BPD_{1–3}$ balanced photodetectors, *WP* Wollaston prism, $BS_{1–2}$ beam splitters, $PPLN_{1–2}$ periodically poled lithium niobate crystals, *VA* variable attenuator, CaF_2 Calcium Fluoride, *FM* flip mirror

of the experimental layout, further details on specific parts of the setup are discussed in subsequent sections, namely the generation of CEP-stable single-cycle pulses (Sect. 3) and their use for single-cycle infrared waveform generation and control (Sect. 4).

Briefly, the core of the system constitutes a carrier-envelope-phase-stabilized, Kerr-lens-mode-locked, diode-pumped Cr:ZnS laser system, generating trains of 28-fs-long pulses with pulse energies of 24 nJ. In a first step, the direct output of the oscillator is sent into a highly nonlinear bulk dielectric medium (rutile TiO_2) to spectrally broaden the laser output and generate an octave-spanning spectrum. The broadened pulses span a spectral range of 1.1 to 3.2 µm (at −20 dB) and are compressed with a combination of custom-made dispersive mirrors and bulk material (dispersion control units DC) to durations of 7 fs, corresponding to a single

cycle of the electric field at the spectral centroid of 2.24 μm. For our experiment, we split the broadened pulses first into three beams with a wedged ZnS beam splitter (BS_1) and compressed each of the beams individually.

A coherent near- to mid-infrared continuum is generated via cascaded IPDFG by focusing the beam traversing BS_1 into a zinc germanium phosphide (ZGP) crystal. The reflection off the beam splitter's front surface (blue line) is used as a gate pulse for characterizing the mid-infrared electric-field waveforms with electro-optic sampling (EOS). For that, a thin ZnS wedge (BC) combines the gate and infrared continuum beams, followed by EOS in GaSe and ellipsometric detection. The influence of water absorption on mid-infrared generation and detection was minimized by purging this part of the experimental setup with nitrogen.

The carrier-envelope offset frequency (f_{CEO}) of the single-cycle pulses is detected by sending the reflection off the back surface of BS_1 (red line) into a common-path f-2f interferometer. From the f_{CEO} beating signal an electronic feedback is generated to control and stabilize the CEP of the laser by active pump-power modulation. We characterized the performance of our CEP stabilization with a separate out-of-loop phase-noise measurement, enabled by redirecting the gate pulses with a flip mirror (FM).

3 Single-Cycle CEP-Stable Laser Pulses

Spectral broadening of the laser output in rutile serves several purposes: (i) It generates sufficient spectral bandwidth for compressing the pulses to the single-cycle regime. (ii) The 1.5-octave-spanning spectrum supports f-2f interferometry for f_{CEO} detection and CEP stabilization. (iii) The single-cycle pulses allow efficient, ultra-broadband mid-infrared generation in ZGP, creating a supercontinuum spanning from 0.9 to 12 μm. (iv) The detection bandwidth of EOS is limited towards the blue by the pulse duration of the gate pulses. With our merely 7-fs-long pulses we could measure EOS waveforms with spectral components down to 3 μm.

3.1 Spectral Broadening and Temporal Compression in TiO_2

Strong nonlinear spectral broadening via self-phase modulation (SPM) was achieved by focusing the 28-fs-long pulses from the Cr:ZnS oscillator tightly (20 μm ($1/e^2$) focal spot size) into a 0.5-mm-thick, bulk rutile plate (TiO_2), anti-reflection-coated for the range between 1.2 and 3.2 μm. In order to suppress any birefringent effects, the TiO_2 medium was cut in the (001) orientation and to be used under normal incidence. The corresponding output spectrum (Fig. 2a) spans from 1.1 to 3.2 μm, at the −20-dB-level, featuring a Fourier-transform-limited pulse duration of 6 fs. The choice of using a thin plate under strong focusing conditions minimizes the degradation of the beam profile; due to strong Kerr-lensing, a high

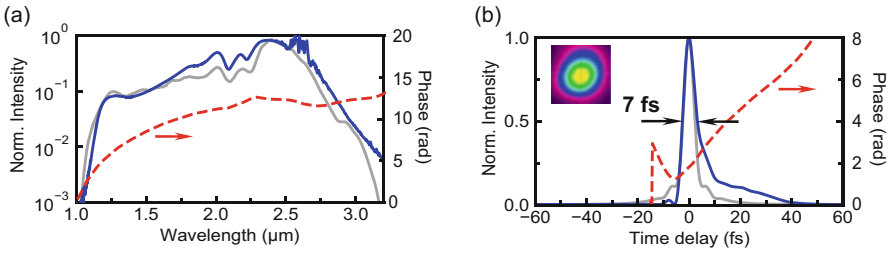

Fig. 2 (**a**) Nonlinearly broadened output spectrum (blue curve) in comparison to the spectrum (grey curve) and spectral phase (red curve) retrieved from an SHG-FROG measurement. (**b**) Retrieved temporal intensity profile (blue curve), temporal phase (red curve), and Fourier-transform limit (grey curve) of the laser pulse

spatial and temporal beam quality is retained. Thus, the far-field beam profile remains clean (inset of Fig. 2b) and we obtain excellent focusing properties, with a beam quality parameter $M^2 < 1.4$—ideal for downstream nonlinear conversion stages.

Compression of the super-octave-spanning spectra was achieved with a set of custom-designed chirped mirrors, combined with the material dispersion provided by a thin BaF_2 plate, and was optimized for each arm after beam splitter BS_1 individually. The duration of the compressed pulses was measured with a home-built, all-reflective second-harmonic-generation frequency-resolved optical gating instrument (SHG-FROG) using a 0.1-mm-thick $LiIO_3$ crystal (type-I phase-matching, $\theta = 20.5°$). The resulting retrieved pulse (blue in Fig. 2b) has a duration of only 7 fs (full width at half maximum). This is equivalent to a mere single optical cycle at the spectral centroid position of 2.24 μm and slightly shorter than what has been demonstrated previously [13].

3.2 CEP-Stabilization

The super-octave-spanning spectrum allows us to directly perform carrier-envelope offset frequency (f_{ceo}) detection of the Cr:ZnS laser in an f-$2f$ interferometer. For this, a fraction (36 mW, red beam) of the broadened pulses after the rutile plate is pre-chirped with dispersive mirrors and focused into a 1-mm-thick periodically poled lithium niobate crystal ($PPLN_1$). The latter is optimized for second harmonic generation (SHG) of the signal at 2460 nm. Subsequently, the beam is spectrally bandpass-filtered (SF_1) at around 1230 nm to isolate the $2f$ and frequency-doubled f components. Their beating is detected with a balanced photodetector (BPD_1). The light reflected from the optical bandpass filter enters the other port of the detector, allowing to control the power of the fundamental repetition rate (f_{rep}) radio-frequency signal. We achieved a remarkably high signal-to-noise ratio reaching 70 dB for the detected f_{ceo} beat note. For CEP-stabilization (i.e. locking f_{ceo} to 0) a

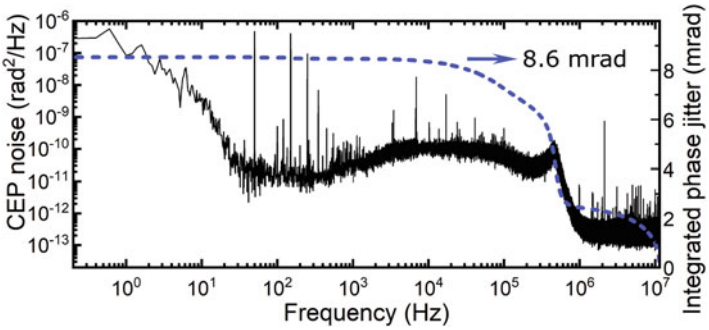

Fig. 3 CEP noise power spectral density, and the corresponding integrated phase jitter for the phase-stabilized laser

self-referencing technique is implemented [14]. CaF_2 wedges in front of the PPLN crystal allow to control the CEP without changing the spectral phase of the main beam used for the experiment.

The CEP-noise of the stabilized laser was measured in a separate out-of-loop *f-2f* interferometer. By using a 0.5-mm-thick PPLN crystal ($PPLN_2$) for SHG, a beating signal was generated and sent into two separate channels for noise characterization. Slow drifts and components below 12 Hz were measured by evaluating the evolution of the spectral interference fringes in the *f-2f* spectral overlap region recorded with a spectrometer (Ocean Optics). Faster CEP noise components up to the Nyquist frequency (11.43 MHz) were measured with a separate balanced detection scheme [15]: the beam was split by a 50:50 nonpolarizing beam splitter (BS_2) and filtered by optical bandpass filters ($SF_{4,5}$). The filters isolated spectral components on opposing slopes of the interference fringes, which were then sent onto the photodiodes of a balanced detector (BPD_3), with the balanced detection signal being directly proportional to the CEP fluctuations. The results of slow and fast CEP noise measurements were combined to give the CEP noise spectral density (Fig. 3, black). We find an integrated CEP noise of only 8.6 mrad for the range between 0.2 Hz and 11.5 MHz (Nyquist limit, Fig. 3, blue), which represents an improvement of around 20% compared with our previous result [13]. Moreover, it is approaching the level of the lowest CEP-noise ever demonstrated for ultrafast oscillators [16–18].

4 CEP-Controlled Mid-Infrared Waveform Synthesis

For frequency down-conversion of the single-cycle laser pulses, the process of cascaded intrapulse difference-frequency generation (IPDFG) [12, 19] is used. In this way, coherent mid-infrared radiation spanning 3.7 optical octaves is generated. By varying the carrier-envelope phase of the driving pulses, the relative phase of different spectral regions of the supercontinuum is changed—thereby shaping

the emerging waveforms. To trace changes in the electric field, the mid-infrared waveforms are recorded with the method of electro-optic sampling (EOS) [20].

4.1 *Cascaded Intrapulse Difference-Frequency Generation (IPDFG) and its CEP-Dependence*

When laser pulses are focused into a nonlinear crystal with suitable phase-matching conditions, difference-frequency mixing between the various spectral components of the input laser generates a 0th-order IPDFG field (Fig. 4). Upon further propagation through the crystal, newly generated frequency components sequentially re-mix with driving laser components creating down-converted radiation of higher cascading orders (first, second, etc.). Each higher-order component arises from mixing of components of the preceding order with that of the driving laser. Depending on the cascading order, the CEP of the newly generated spectral components is either following the CEP of the driver (odd orders) (Fig. 4, blue), or will be invariant to it (even orders) (Fig. 4, green). If the CEP of the incident laser pulses was not stabilized, the combined electric-field waveforms of the multi-octave output would vary from pulse to pulse. For a fixed CEP of the driving laser, the spectral distribution of CEP dependence remains stable. This approach enables waveform adjustment across multiple octaves without the need for spatial separation of specific spectral bands. Moreover, the spectral region in which odd- and even-order components overlap will exhibit pronounced interference effects when tuning the CEP of the driving laser (Fig. 4, light-red-shaded area).

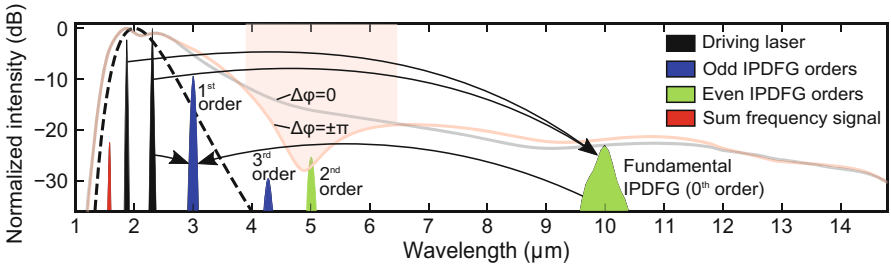

Fig. 4 Mid-IR spectra arising from the difference-frequency mixing in a ZGP crystal, simulated by using commercial nonlinear pulse propagation software. The basic principle of cascaded IPDFG is illustrated through a simplified modelling of the mixing of two isolated spectral components of the driving laser (black), which share the same CEP. For a broadband driving laser (dashed black), the mixing products merge into a continuum. The light-red and light-grey curves depict the intensity distribution for the driving field's CEP set to yield constructive ($\Delta\varphi = 0$) and destructive ($\Delta\varphi = \pm\pi$) interference, respectively

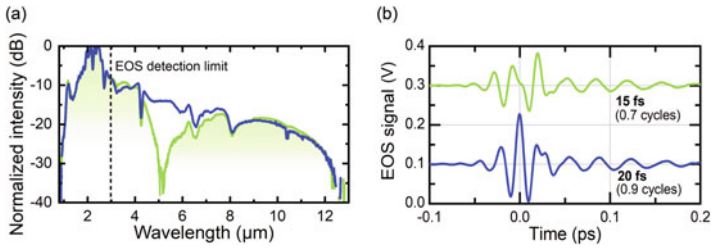

Fig. 5 (**a**) Supercontinuum from cascaded IPDFG for the extreme cases of constructive (blue) and destructive (green) interference between the even and odd cascaded IPDFG orders. The measurements were taken with a monochromator. The dashed line indicates the detection limit of the EOS measurement technique when using a 7-fs gating pulse, which allows to measure spectral components with wavelengths longer than about 3 μm. (**b**) EOS time-domain data for relative phases $\Delta\varphi$ of 0 (blue curve, constructive interference) and π (green curve, destructive interference). For better comparison, the two traces are offset by a constant factor (0.2 V). The pulse durations correspond to the full-width at half-maxima (FWHM) of the intensity envelopes. For calculating the number of optical cycles, the spectral centroids of the waveforms are considered

4.2 CEP-Controlled Multi-Octave Mid-Infrared Generation

Experimentally, we achieve cascaded IPDFG by focusing the super-octave-spanning single-cycle pulses into an anti-reflection-coated (1.5–12 μm) 1-mm-thick $ZnGeP_2$ (ZGP) crystal. The beam diameter inside the crystal was measured to be 30 μm ($1/e^2$), resulting in an estimated peak intensity of ca. 150 GW/cm^2. In order to optimize the IPDFG process and compensate for the ZGP dispersion, we have pre-chirped the input beam with a single dispersive mirror and an achromatic half-waveplate. The latter also serves for rotating the driver polarization to 45° in order to achieve two orthogonal polarization components of equal magnitude for type-I birefringent phase-matching ($\varphi = 0°$; $\theta = 51°$). The down-converted IPDFG output spectrally overlaps with the driver radiation resulting in an ultrabroadband supercontinuum covering 3.7 optical octaves from 0.9 to 12 μm (−30 dB level, Fig. 5a). As described in the previous section, the output spectral intensity and phase can be modified by adjusting the CEP of the driver. In the two extreme cases shown in Fig. 5a, this leads to fully constructive (blue curve in Fig. 5a) or destructive (green curve in Fig. 5a) interference between the even and odd cascaded IPDFG orders, correspondingly modulating the spectral intensity around 5 μm. The average power of the mid-IR part of the supercontinuum ($\lambda > 3.6$ μm) for the case of constructive interference is 31 mW, corresponding to an IPDFG power conversion efficiency of 14%.

4.3 Observing Waveform Control with Electro-Optic Sampling

Electro-optic sampling (EOS) was used to directly observe changes of the mid-infrared waveform induced by varying the CEP of the driving laser. For EOS detection, the gate and mid-infrared beams, combined by BC (Fig. 1), are focused

into a 0.1-mm-thick GaSe crystal, optimized for type-I phase-matching ($\varphi = 30°$) at an external angle of $\theta = 35°$. Under these conditions, our gate pulse duration of 7 fs allows us to capture spectral components up to a maximum frequency of about 100 THz, corresponding to a wavelength of 3 μm with EOS (dashed black line in Fig. 5a). For a relative phase of $\Delta\varphi = 0$, corresponding to constructive interference (see previous section), the EOS trace, indicative of the actual electric waveform, exhibits a clean cosine-pulse-like temporal profile (Fig. 5b, blue curve). The pulse duration of 20 fs corresponds to 0.9 cycles of the waveform at the EOS spectral centroid. For $\Delta\varphi = \pi$ the EOS trace changes to a sine-pulse-like waveform, as a result of the phase changes and destructive interference in the spectral domain (Fig. 5a, b, green curves). Thus, changing the CEP of the driving laser allows us to reproducibly modify both the phase *and* intensity of the mid-infrared waveforms.

5 Conclusion

In conclusion, a new approach for coherent multi-octave mid-infrared generation was presented, which offers an intrinsic capability to change the relative phase and amplitude of different spectral regions. Driven by cascaded intrapulse difference-frequency generation, the emerging single-cycle mid-infrared waveforms are shaped in time, with the CEP of the driving laser as the control parameter. Due to the unprecedented CEP and amplitude stability of the diode-pumped laser, multi-octave-spanning waveforms with high fidelity and reproducibility are generated. This concept is generalizable towards the synthesis of a broader variety of infrared waveforms by combining it with other techniques [4], and gives access to a variety of new applications exploiting long-wavelength electric-field control on the sub-cycle level.

Acknowledgments This work was funded by the Center for Molecular Fingerprinting (CMF), the Center for Advanced Laser Applications (CALA) of the Ludwig-Maximilians-Universität München, Department of Laser Physics, and the Max Planck Institute of Quantum Optics (MPQ), Laboratory for Attosecond Physics, Germany. J.S. thanks the 'NLPQT—National Laboratory for Photonics and Quantum Technologies' (Poland) for providing the vector network analyser to test the low-noise laser diode driver performance. We thank I. Pupeza for valuable discussions, D. Gerz for assistance in the pulse characterization and M. Kling for feedback on the manuscript.

References

1. Baltuška, A., Fuji, T., Kobayashi, T.: Controlling the carrier-envelope phase of ultrashort light pulses with optical parametric amplifiers. Phys. Rev. Lett. **88**, 133901 (2002)
2. Schiffrin, A., et al.: Optical-field-induced current in dielectrics. Nature. **493**, 70–74 (2013)
3. Dombi, P.: Strong-field nano-optics. Rev. Mod. Phys. **92** (2020)
4. Manzoni, C., et al.: Coherent pulse synthesis: Towards sub-cycle optical waveforms. Laser Photonics Rev. **9**, 129–171 (2015)

5. Ridente, E., et al.: Electro-optic characterization of synthesized infrared-visible light fields. Nat. Commun. **13**, 1111 (2022)
6. Pupeza, I., et al.: Field-resolved infrared spectroscopy of biological systems. Nature. **577**, 52–59 (2020)
7. Fischer, M.P., et al.: Field-resolved detection of the temporal response of a single plasmonic antenna in the mid-infrared. Optica. **8**, 898–903 (2021)
8. Gaida, C., et al.: Watt-scale super-octave mid-infrared intrapulse difference frequency generation. Light Sci. Appl. **7**, 94 (2018)
9. Elu, U., et al.: Seven-octave high-brightness and carrier-envelope-phase-stable light source. Nat. Photonics. **15**, 277–280 (2021)
10. Krogen, P., et al.: Generation and multi-octave shaping of mid-infrared intense single-cycle pulses. Nat. Photonics. **11**, 222–226 (2017)
11. Jakob, M.A., et al.: Generation and characterization of tailored MIR waveforms for steering molecular dynamics. Opt. Express. **27**, 26979–26988 (2019)
12. Wang, Q., et al.: Broadband mid-infrared coverage (2-17 μm) with few-cycle pulses via cascaded parametric processes. Opt. Lett. **44**, 2566–2569 (2019)
13. Steinleitner, P., et al.: Single-cycle infrared waveform control. Nat. Photonics. **16**, 512–518 (2022)
14. Okubo, S., et al.: Offset-free optical frequency comb self-referencing with an f-2f interferometer. Optica. **5**, 188–192 (2018)
15. Liehl, A., et al.: Ultrabroadband out-of-loop characterization of the carrier-envelope phase noise of an offset-free Er:fiber frequency comb. Opt. Lett. **42**, 2050–2053 (2017)
16. Endo, M., et al.: Ultralow noise optical frequency combs. IEEE J. Sel. Top. Quantum Electron. **24**, 1–13 (2018)
17. Liao, R., et al.: Active f-to-2f interferometer for record-low jitter carrier-envelope phase locking. Opt. Lett. **44**, 1060–1063 (2019)
18. Lemons, R., et al.: Carrier-envelope phase stabilization of an Er:Yb:glass laser via a feed-forward technique. Opt. Lett. **44**, 5610–5613 (2019)
19. Kessel, A., et al.: Generation of multi-octave spanning high-energy pulses by cascaded nonlinear processes in BBO. Opt. Express. **24**, 5628–5637 (2016)
20. Wu, Q., Zhang, X.-C.: Free-space electro-optics sampling of mid-infrared pulses. Appl. Phys. Lett. **71**, 1285–1286 (1997)

Increase in Photon Flux of Attosecond Pulses

Bing Xue, Kotaro Nishimura, Eiji J. Takahashi, and Katsumi Midorikawa

Abstract High-intensity attosecond pulses capable of inducing a two-photon process are desired to realize an attosecond pump–attosecond probe experiment. In this work, we show the increase of the intensity of attosecond pulses in the water-window region by combining a loose focusing method with high-energy mid-IR drivers. Meanwhile, the effectiveness of an ideal driving field waveform produced by a multi-wavelength synthesizer is demonstrated to improve the conversion efficiency.

Keywords Mid-IR · OPA · Multi-color waveform synthesizer

1 Introduction

Since breaking the barrier of one femtosecond in 2001 [1], attosecond science has progressed rapidly for two decades, supported by advances in ultrafast laser technology and understanding of the interaction of strong optical fields with matter. Research on attosecond pulses has changed significantly around 2010. Before 2010, the Ti:sapphire laser was the de facto standard as the driving light source, so the cutoff energy was limited to about 100 eV and the repetition rate was on the order of 1 kHz. After 2010, the mid-infrared (MIR) optical parametric amplifier (OPA), which is advantageous for the extending the cutoff and increasing the repetition rate, has found increasing use as a driving source. Owing to the quadratic dependence of the cutoff energy on the driving wavelength, the harmonic photon energy, previously limited to around 100 eV, was extended to over 300 eV, reaching the water-window spectral region, by using an OPA [2]. However, the increase in driving wavelength results in a significant decrease in conversion efficiency. This is due to the combined effects of the electron wave packet spreading (quantum diffusion) and the increase in

B. Xue · K. Nishimura · E. J. Takahashi · K. Midorikawa (✉)
RIKEN Center for Advanced Photonics, RIKEN, Wako, Japan
e-mail: kmidori@riken.jp

L. Argenti et al. (eds.), *Proceedings of the 8th International Conference on Attosecond Science and Technology*, Springer Proceedings in Physics 300,
https://doi.org/10.1007/978-3-031-47938-0_2

the harmonic order [3]. As a result, the conversion efficiency decreases rapidly with increasing the driving wavelength. In order to compensate for the low photon flux associated with the low conversion efficiency, attempts to optimize the waveform of the driving laser pulse as well as to increase the driving laser energy and repetition rate have been pursued vigorously [4]. Here, we report our efforts to increase photon flux of attosecond pulses.

2 Generation of High-Flux High Harmonics in the Water-Window Region

A straightforward method for generating high-flux attosecond pulses is to use the loose focusing method [5], which has successfully generated intense attosecond pulse trains. In this method, the interaction volume can be increased by loosely focusing a driving laser pulse of 10 mJ or more into a long gas cell with long-focal-length optics. In this work, we used this method to increasing the photon flux of high harmonics (HHs) in the water-widow region by using a high-energy MIR driving laser [6, 7].

Figure 1 shows the schematic of the experimental setup. It consists of a driving laser system based on dual-chirped optical parametric amplifier (DC-OPA) [8, 9] and the vacuum chambers for high-order harmonic generation (HHG). For the DC-OPA, we used a chirped femtosecond pumping pulse from the Ti:sapphire laser. The

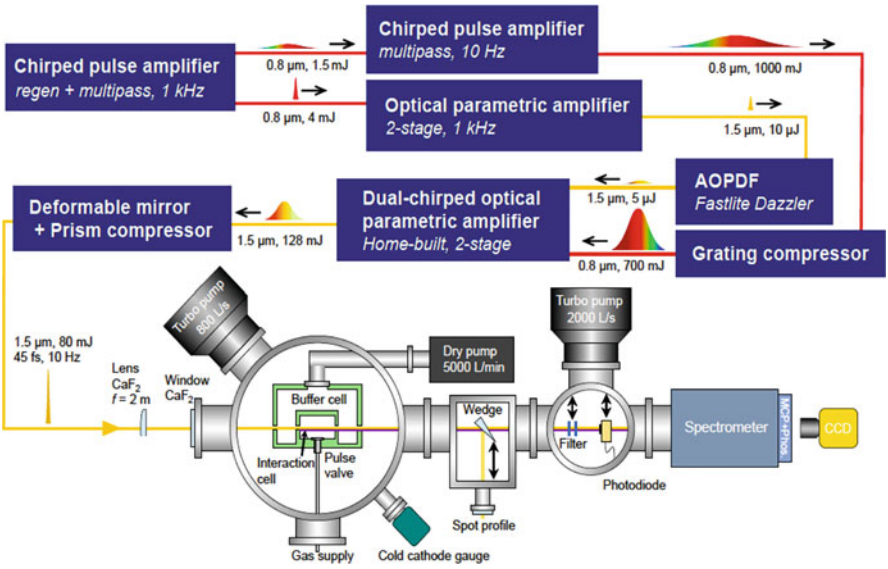

Fig. 1 Schematic of the driving laser system and vacuum chamber for HHG [7]

seed pulse has been stretched to overlap with the pump pulse. Our DC-OPA system can generate MIR pulses in the range of 1.2–4.0 μm with TW-class peak power [9]. For HHG, we set the center wavelength of the driving laser to 1.55 μm that corresponds to a transmission window of the air. The seed pulses were stretched in time by the acoustooptic programmable dispersive filter (AOPDF). The chirped seed pulse was amplified with the type-II BBO crystal pumped by the chirped Ti:sapphire pulses in two stages. After the amplification, the pulse energy reached 128 mJ with the pulse duration of a few picoseconds. The output pulse was coarsely compressed by the prism compressor (SK1300) and finely compressed by tuning the phase of AOPDF. The final pulse energy and duration were up to 80 mJ and 45 fs, respectively. This driving pulse was loosely focused with a 2 m CaF_2 convex lens and delivered to the target chamber through a CaF_2 window. The HH pulse energy can be measured directly using a photodiode (Opto Diode AXUV100G) with proper filters. The HH spectrum was taken by a 2400 grooves/mm flat-field grating and a microchannel plate with a phosphor screen.

A static gas cell is widely adopted for the loose-focusing geometry because it allows easy extension of the cell length and ensures homogeneous gas density distribution along the laser propagation axis. We designed and adopted a pulsed gas cell having a double-cell structure for the differential pumping to decrease the amount of gas leaking at high-pressure operations. Figure 2 shows the He pressure dependence of HH intensity for an interaction length of 30 mm, and it reaches the peak value at around 1.2 bar (12 bar backing pressure). Figure 3 shows the two-dimensional HH spectrogram after a 0.25-μm parylene-C thin film. The HHs are bright enough to obtain the fine absorption structure with spatial information. The measured HH pulse energy in the water window region was 3.53 nJ with a conversion efficiency of 7.20×10^{-8}. The conversion efficiency was improved by more than ten times compared to previously reported values.

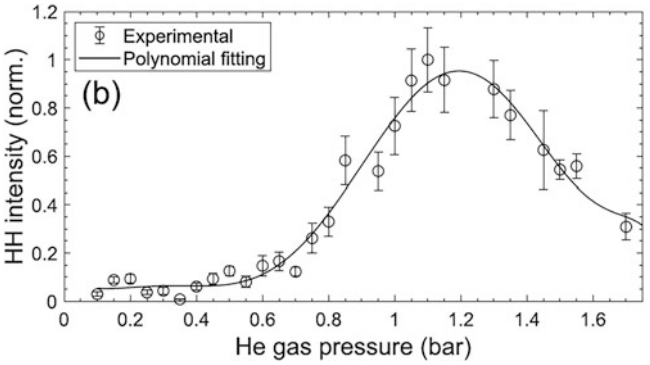

Fig. 2 He pressure dependence of HH intensity for a 30-mm-long pulsed gas cell [7]

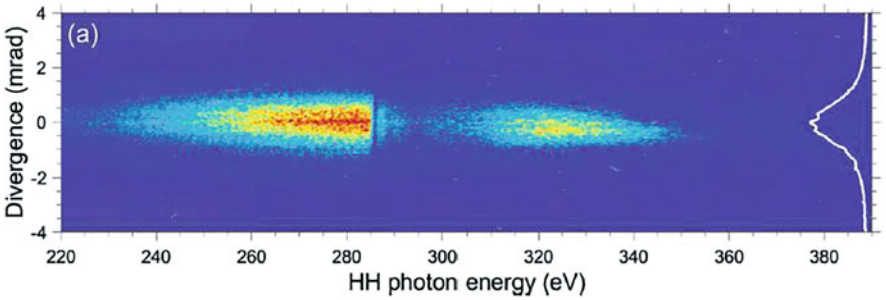

Fig. 3 Two-dimensional HH spectrum from He generated after passing through a 0.25-μm parylene-C thin film [7]

3 Generation of GW-Class Isolated Attosecond Pulses Driven by a Multi-Wavelength Synthesizer

We have successfully increased the output energy of HHs in the water-window region by using high-energy MIR drivers. However, there is still a big issue for the use of long wavelengths, which is a low conversion efficiency. When we further increase the wavelength of the driver pulse to extend the cutoff energy to the sub-keV region, conversion efficiency rapidly deceases due to the combined effects of electron wavepacket spreading and an increase in the number of harmonics. To solve this fundamental problem, we need to use an arbitrarily shaped drive field instead of a sinusoidal field to control the motion of electrons within a single cycle. To create an arbitrarily shaped driving field by multi-wavelength synthesis, two approaches are used. The first is a method of synthesizing a few cycle pulses with different wavelengths to form subcycle pulses with arbitrary shapes. The second is a method of combining multiple multicycle pulses, which are advantageous for increasing the synthesized pulse energy. The generation of isolated attosecond pulses (IAPs) does not necessarily require subcycle pulses. If the intensity ratio of the main peak to adjacent peaks is sufficiently large, the continuum spectrum required for an IAP is obtained in the cutoff region, even with multicycle pulses.

We developed a multi-terawatt three-channel parallel parametric waveform synthesizer with complete stabilization of all synthesis parameters, consisting of pulses with 800-nm (25-fs), 1350-nm (44-fs) and 2050-nm (80-fs) wavelengths [10]. The subpulses of the synthesized waveforms are focused by using two separate long focal-length lenses (4.5 m for pump pulse and 3.5 m for signal and idler pulses) into an 8-cm-long gas cell filled with 2.9-torr Ar gas. The focused intensity in the three-color case is measured to be 1×10^{14} W/cm^2 with input pulse energies of 20.3, 4.3, and 1.6 mJ for the pump, signal, and idler, respectively. To realize the full stabilization of the synthesizer, a CEP-stabilized high-energy Ti:sapphire chirped-pulse amplifier operating at 10 Hz was also developed [11].

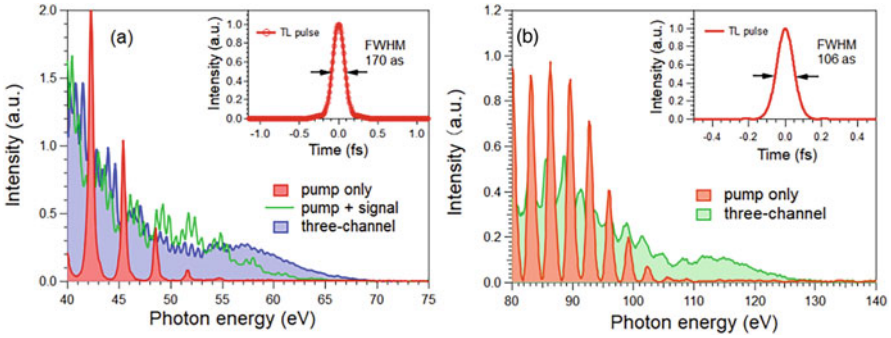

Fig. 4 Single-shot HH spectra measured using one-, two-, and three-channel input; the inset shows the Fourier-transform-limited (TL) pulse from the cutoff continuum spectrum. (**a**) Ar (continuum energy range: 50–70 eV) and (**b**) Ne (continuum energy range: 100–130 eV)

By combining the waveform synthesizer and the loose focusing method for HHG, a shot-to-shot-reproducible high-energy (~0.24 μJ) harmonic continuum in the soft X-ray region was achieved. The peak power of the soft X-ray continuum was evaluated to be beyond 1 GW with a 170-as transform limit duration. Figure 4a shows single-shot HH spectra when one-, two- and three-color driver waveforms are used in Ar. In the one-color case, clear discrete harmonics that ended at the 35th order with a photon energy of ~54 eV were generated. With two-color (pump and signal) driving, a supercontinuum spectrum appeared in the cutoff region (above 50 eV). However, a week modulation pattern was still visible in the spectrum, which indicated the existence of satellite pulses around the main attosecond pulse. When the third idler pulse was also injected, a smooth continuum harmonic spectrum was observed, and the HH cutoff region was further extended to 70 eV. By changing the gas medium from Ar to Ne, further extension of the cutoff to 130 eV was observed as shown in Fig. 4b [12]. Input pulse energies of the pump, signal, and idler are 20.3, 4.3, and 1.6 mJ, respectively, while the gas cell length and pressure are 50 mm and 8.8 torr.

To experimentally characterize the IAP duration from the generated supercontinuum, we achieved a streaking measurement at 10 Hz. The detail of the experimental setup is reported in [13]. In the measurements, the gating pulse (800 nm) delay was varied using the piezo-controlled stage. The measured streaking trace is shown in Fig. 5a. The delay step of the gating pulse is set as 100 as. For each delay time of the gating pulse, 200 shots of photoelectron spectra measured with the electron-TOF are collected and averaged with a oscilloscope. Thanks to the high-energy continuum harmonics generated, owing to a sufficient flux of ionized electrons, the TOF signal can be observed directly with an oscilloscope instead of a digital converter in counting mode. By getting rid of the digital converters, the data acquisition time is greatly reduced, even at the 10 Hz repetition rate. The streaking trace exhibits a clear modulation with a roughly 2.7 fs time period. This period corresponds to one cycle of the gating pulse, which has a center wavelength of 800 nm. This

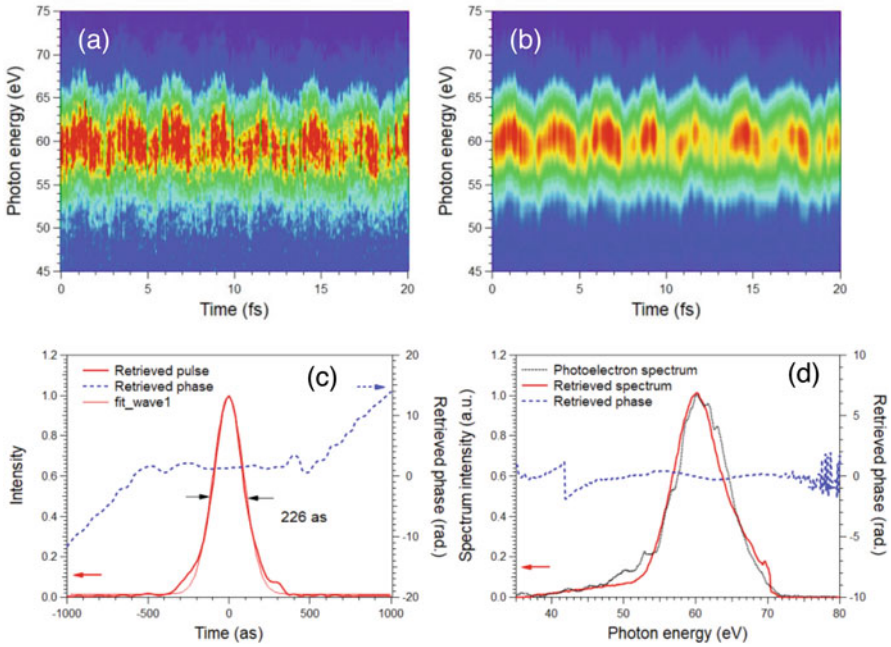

Fig. 5 Characterization of isolated attosecond pulse. (**a**) Experimentally measured streaking trace. (**b**) Trace retrieved using FROG-CRAB with the PCGP algorithm. (**c**) Retrieved results of the pulse duration and phase. (**d**) Measured photoelectron spectrum, and retrieved spectrum and phase

modulation lasts through the entire 20-fs scan range. It is related to the multicycle pulse duration (30 fs) of the gating pulse, and it also can be seen in the retrieved gating vector. We programmed homemade calculation software to retrieve the input pulses using the FROG-CRAB method with the principal component generalized projections (PCGP) algorithm [14]. The retrieved trace shown in Fig. 5b has a mean square error of 3.5%. From the retrieved results for the IAP shown in Fig. 5c, we obtain an IAP duration of 226 as FWHM. By comparing the measured photoelectron spectrum and the Fourier transform spectrum obtained from the retrieved IAP profile, we find that the two spectra overlap quite well, as shown in the inset in Fig. 5d. Thus, we conclude that this retrieved result is reliable. Accordingly, this experimentally confirms the generation of a GW-scale IAP using a fully stabilized, three channel optical waveform synthesizer [13]. As far as we know, this result is the first demonstration of an as streaking experiment at a 10 Hz repetition rate, and it provides conclusive evidence for the realization of a GW-scale, soft X-ray IAP source on a tabletop.

4 Future Prospects

Recently, our DC-OPA system has been upgraded to generate 1.7-μm two-cycle TW-class pulses [15, 16]. The results showed a similar pulse duration and OPA laser spectra with which islated attosecond pulses were generated [17]. The conversion efficiency of the water window IAP can be estimated by scaling the conversion efficiency obtained in our Ne HHG experiment [6] with $\propto \lambda^{-6}$. The measured conversion efficiency was 7.4×10^{-9} at 250 eV in 1% bandwidth, while the scaling factor was 0.57. Therefore, the estimated conversion efficiency is 4.3×10^{-9} at 250 eV in 1% bandwidth. A total HH pulse energy of approximately 2 nJ is expected with tens of attosecond pulse duration. This intense water-window IAP has the potential to open the door for unexplored attosecond science in the water-window region including intra-atomic energy transfer, ultrafast electron transfer, and so on. Meanwhile, synthesis of multicycle pulses exhibits a new ability to tune the phases of each component pulse freely through changing its delay. Multicycle and multichannel synthesis may bring more degrees of freedom on experimentally achieving a "designed" electric field (such as the "perfect waveform" for IAP generation), which may be used for other high-intensity electric-field research, such as laser electron accelerators and strong-field physics.

References

1. Hentschel, M., et al.: Attosecond metrology. Nature. **414**, 509–513 (2001)
2. Takahashi, E.J., Kanai, T., Ishikawa, K.L., Nabekawa, Y., Midorikawa, K.: Coherent water window X ray by phase-matched high-order harmonic generation in neutral media. Phys. Rev. Lett. **101**, 253901 (2008)
3. Tate, J., et al.: Scaling of wave-packet dynamics in an intense midinfrared field. Phys. Rev. Lett. **98**, 013901 (2007)
4. Midorikawa, K.: Progress on table-top isolated attosecond light sources. Nat. Photo. **16**, 267–278 (2022)
5. Takahashi, E., Nabekawa, Y., Otsuka, T., Obara, M., Midorikawa, K.: Generation of highly coherent submicrojoule soft X-rays by high-order harmonics. Phys. Rev. A. **66**, 021802 (2002)
6. Fu, Y., et al.: High efficiency ultrafast water-window harmonic generation for single-shot soft x-ray spectroscopy. Commun. Phys. **3**, 92 (2020)
7. Nishimura, K., Fu, Y., Suda, A., Midorikawa, K., Takahashi, E.J.: Apparatus for generation of nanojoule-class water-window high-order harmonics. Rev. Sci. Instrum. **92**, 063001 (2021)
8. Zhang, Q., Takahashi, E.J., Mücke, O.D., Lu, P., Midorikawa, K.: Dual-chirped optical parametric amplification for generating few hundred mJ infrared pulses. Opt. Exp. **19**, 7190–7212 (2011)
9. Fu, Y., Midorikawa, K., Takahashi, E.J.: Towards a petawatt-class few-cycle infrared laser system via dual-chirped optical parametric amplification. Sci. Rep. **8**, 7692 (2018)
10. Xue, B., et al.: Fully stabilized multi-TW optical waveform synthesizer: Toward gigawatt isolated attosecond pulses. Sci. Adv. **6**, eaay2802 (2020)
11. Takahashi, E.J., Fu, Y., Midorikawa, K.: Carrier-envelope phase stabilization of a 16 TW, 10 Hz Ti:sapphire laser. Opt. Lett. **40**, 4835–4838 (2015)

12. Xue, B., et al.: A custom-tailored multi-TW optical electric field for gigawatt soft-X-ray isolated attosecond pulses. Ultrafast Sci. **2021**, 9828026 (2021)
13. Xue, B., Midorikawa, K., Takahashi, E.J.: Gigawatt-class, tabletop, isolated-attosecond-pulse light source. Optica. **9**, 360–363 (2022)
14. Mairessse, Y., Quéré, F.: Frequency-resolved optical gating for complete reconstruction of attosecond bursts. Phys. Rev. A. **71**, 011401 (2005)
15. Xu, L., Nishimura, K., Suda, A., Midorikawa, K., Takahashi, E.J.: Optimization of a multi-TW few-cycle 1.7-mm source based on type-I BBO dual-chirped optical parametric amplification. Opt. Exp. **28**, 15138–15147 (2020)
16. Xu, L., et al.: 100-mJ class, sub-two-cycle, carrier-envelop phase-stable dual-chirped optical parametric amplification. Opt. Lett. **47**, 3371–3374 (2022)
17. Li, J., et al.: 53-attosecond X-ray pulses reach the carbon K-edge. Nat. Commun. **8**, 186 (2017)

Bright Coherent XUV Generation in Microfluidic Glass Devices for Ultrafast X-ray Spectroscopy

A. G. Ciriolo, R. Martìnez Vàzquez, G. Crippa, M. Devetta, D. Faccialà, P. Barbato, F. Bariselli, E. Cinquanta, F. Frassetto, A. Frezzotti, L. Poletto, V. Tosa, R. Osellame, S. Stagira, and C. Vozzi

Abstract Ultrafast X-ray spectroscopy allows studying light-matter interaction with an unprecedented temporal resolution, with the further advantage of being element-selective and oxidation- and spin-state specific. Here we will discuss the recent developments we implemented toward attosecond X-ray spectroscopy based on tabletop sources, namely a bright XUV source based on high-order harmonic generation in micro-channels and a new beamline for XUV transient absorption spectroscopy experiments up to a few hundred eV.

Keywords Attosecond optics · Nonlinear optical processes · Laser micromachining · Attosecond pulses · Microfluidic devices

1 Introduction

High Harmonic Generation (HHG), arising from the interaction of intense femtosecond laser pulses with noble gases, led to the realization of table-top sources of

A. G. Ciriolo (✉) · R. M. Vàzquez · M. Devetta · D. Faccialà · E. Cinquanta · R. Osellame · C. Vozzi (✉)
Istituto di Fotonica e Nanotecnologie CNR-IFN, Milan, Italy
e-mail: annagabriella.ciriolo@polimi.it; caterina.vozzi@cnr.it

G. Crippa · P. Barbato · S. Stagira
Istituto di Fotonica e Nanotecnologie CNR-IFN, Milan, Italy

Dipartimento di Fisica, Politecnico di Milano, Milan, Italy

F. Bariselli · A. Frezzotti
Dipartimento di Scienze e Tecnologie Aerospaziali, Politecnico di Milano, Milan, Italy

F. Frassetto · L. Poletto
Istituto di Fotonica e Nanotecnologie CN-IFN, Padova, Italy

V. Tosa
National Institute for R&D of Isotopic and Molecular Technologies, Cluj-Napoca, Romania

L. Argenti et al. (eds.), *Proceedings of the 8th International Conference on Attosecond Science and Technology*, Springer Proceedings in Physics 300,
https://doi.org/10.1007/978-3-031-47938-0_3

coherent Extreme UltraViolet (EUV) and Soft-X ray radiation. As a result, ultrafast spectroscopy can nowadays be performed with extreme temporal resolutions, down to the attosecond regime, and site and chemical selectivity. These peculiar features grant access to purely electronic dynamics initiated by ultrafast laser pulses in molecules and solids, and to fundamental processes of light-matter interaction.

One of the most promising all-optical techniques to perform these experiments is *transient absorption* in the EUV. However, the full exploitation of ultrafast spectroscopy in this spectral range is somehow hindered, even today, by the technological complexity of the required setups and the low generation efficiency of the HHG sources, particularly when moving towards higher photon energies.

Here, we report the efficient EUV generation inside a microfluidic device fabricated by *femtosecond laser irradiation followed by chemical etching* (FLICE) [1]. This microfluidic approach allows controlling and manipulating the harmonic generation conditions in gas on the micro-meter scale with unprecedented flexibility, enabling a high photon-flux and phase-matching on broadband harmonics above 100 eV.

We also report on the design and commissioning of a new beamline for transient absorption/reflectivity measurements in molecules and solids, equipped with a flexible EUV spectrometer for high-resolution and high dynamic range measurement, with a polarimeter for the characterization of the HHG polarization.

2 Efficient Generation of EUV in a Microfluidic Device

In our experimental setup, we excite the high-order harmonic generation by focusing ultrashort laser pulses in a gas-filled hollow waveguide realized inside a microfluidic glass device. The device is fabricated by using the advanced laser micromachining FLICE technique [2, 3]. FLICE allows building hollow three-dimensional structures embedded in the bulk of dielectric substrates. It provides a well-established platform to develop and prototype microfluidic systems for fine control of fluid dynamics on the micrometer scale. In our specific application, we realized a microfluidic system to accurately control and manipulate the gas density distribution inside the embedded capillary where the laser-gas interaction takes place. Specifically, we shaped the gas flow along the waveguide to achieve an almost uniform gas density along the laser propagation. The device is fabricated on a fused silica slab and is intended to work in a vacuum environment. Herein, we measured bright EUV generation on a spectral range between 40 and 160 eV.

2.1 Design of the Microfluidic Source

Figure 1a shows the structure of the device applied to HHG. It is realized on a $10 \times 8 \times 1$ mm^3 fused silica plate. It is composed of an embedded microchannel

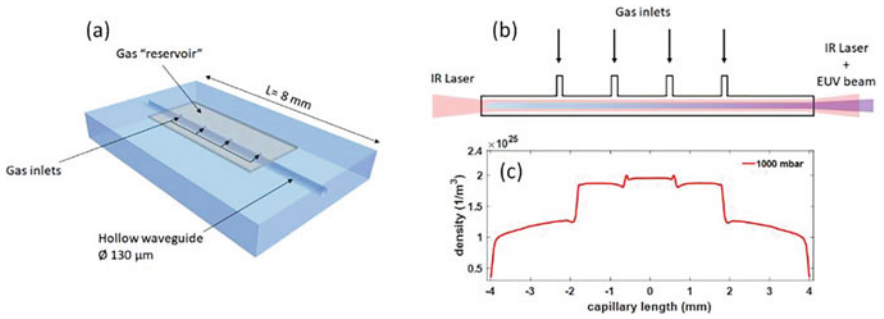

Fig. 1 (**a**) Structure of the chip used for EUV generation. (**b**) Scheme showing the working principle of the microfluidic system. Laser pulses are coupled inside the hollow waveguide that is filled with gas by small upper micro-channels. The interaction between the laser field and the gas lead to the generation of EUV radiation by HHG. (**c**) Numerical gas density along the central axis of the waveguide calculated at a backing pressure of 1 bar in the reservoir. The simulations are performed using COMSOL Multiphysics. (Figure adapted from [2])

that acts as a hollow waveguide for ultrashort laser pulses. The microchannel is 8 mm long and has a diameter of 130 µm [1]. A $2 \times 4.7 \times 0.1$ mm^3 rectangular micro-chamber is dug on the upper surface working as a gas reservoir. The waveguide is connected to the reservoir through an array of four micro-channels, placed at a relative distance of 1.2 mm (see panel 1(b)). The gas, injected by these micro-channels, flows through the 8-mm-long hollow waveguide under the pressure gradient imposed by the high-vacuum environment (10^{-4} mbar) where the generation is performed. The device is operated in a continuous gas flow regime.

The steady-state gas dynamics inside the device were modeled by using the commercial Comsol Multiphysics™ CFD platform [4]. As predicted by numerical simulation, the flow is nearly isothermal, with the density profile smoothly varying from the center to the outputs of the waveguide, thus giving a central region with almost a constant gas density profile shown in Fig. 1c.

2.2 Characterization of the EUV Photon Flux

To generate the high-order harmonics, we used 800-nm pulses of amplified Ti:Sapphire laser source (Amplitude, Aurora laser system: 15 mJ, 25 fs, 1 kHz). The pulse duration for this experiment was 30 fs and the energy was 500 µJ. The beam is focused inside the devices by a lens with a 30-cm focal length and the measured full width at half maximum in the focus is 90 µm. The coupling efficiency is ~80%. The device is mounted in an aluminum holder and the gas is delivered to the hollow waveguide by a pipeline that is directly interfaced with the mechanical mounting. The gas backing pressure can be manually tuned by a needle valve and is monitored by a capacitive pressure gauge. The alignment of the device to the laser beam is

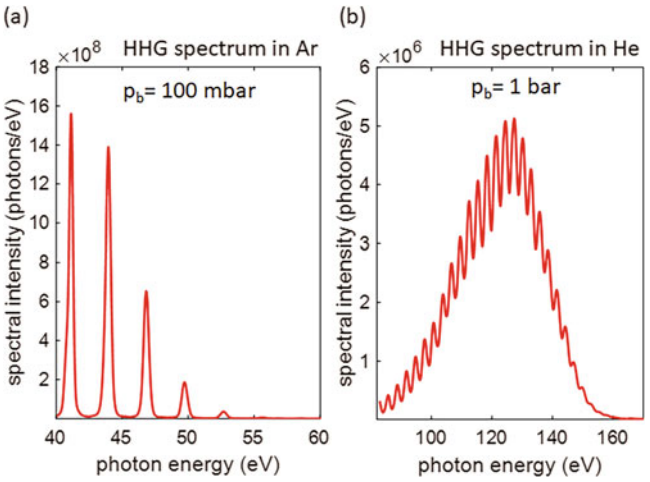

Fig. 2 HHG spectra generated in the microfluidic cell (**a**) by filling the waveguide with Argon gas at a backing pressure of 100 mbar and (**b**) Helium gas at a backing pressure of 1 bar. The spectral intensity per single laser pulse is expressed in photons/eV. (Figure adapted from [5])

performed with a high-precision five-axis motorized translational system. The EUV radiation is collected by a grazing incidence spectrometer (see Sect. 3).

Figure 2a, b show HHG spectra generated inside the microfluidic device filled with Argon and Helium, respectively. The spectral intensity reported in the graphs corresponds to the intensity *per* single pulse. By making a pressure scan up to 1 bar, we found that by using Argon as a target gas, the generation yield was maximized at a backing pressure of 100 mbar. In this condition, harmonics up to 60 eV were generated. The brightest harmonic peak is observed at 42 eV (H 27th), with an intensity of 1.6×10^9 photons/eV. The photon flux of H27 at a 1 kHz repetition rate approaches 10^{12} photons/s in 1% bandwidth, corresponding to a conversion efficiency of 8×10^{-6} in 1% bandwidth [5]. Compared to most advanced EUV sources [6–10], the conversion efficiency achieved inside the microfluidic source provides one of the highest reported in the literature, with the advantage of being obtained with low gas pressures (< 1 bar) and low pulse energies, on the sub-mJ scale.

HHG in Helium required a higher backing pressure (1 bar). The harmonics spectrum ranged from 80 eV up to 160 eV, with a photon flux peak-value of 8×10^8 photons/s in 1% bandwidth at 130 eV, corresponding to a conversion efficiency of 1.8×10^{-8} in 1% bandwidth. For He, we expected an improvement of the photon flux at backing pressures above 1 bar. For this purpose, a differential pumping system is currently under development, allowing continuous gas flow in the device at the multi-bar regime.

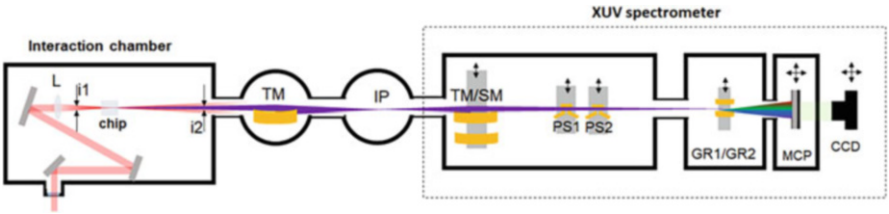

Fig. 3 Schematic view of the vacuum beamline and of the EUV spectrometer

3 A Flexible EUV Spectrometer for Transient Absorption Spectroscopy

To detect EUV radiation we developed a flexible, versatile, and user-friendly spectrometer [11]. Our spectrometer is designed to work in the 1–100 nm spectral range in both stigmatic and astigmatic configurations, it is extremely sensitive to low-power signals and is equipped with a polarimeter to spectrally resolve the polarization state of the EUV radiation down to 12 nm. A schematic view of the spectrometer is reported in Fig. 3.

The EUV radiation after the interaction point (IP) undergoes focusing by a mirror. Here, a toroidal (TM) or a spherical mirror (SM) can be selected to switch from a stigmatic to astigmatic focusing onto the detector. The two mirrors are mounted on a precision motorized translation stage equipped with encoder for high reproducibility (Smaract SLLV42). After the focusing mirror, a polarimeter composed of two stages (PS1 and PS2) can be inserted into the beam path, allowing the full characterization of the polarization state of the radiation.

For a broadband detection, two Spherical Varied-Line-Space gratings can be selected (GR1 and GR2) depending on the spectral region of interest, the first one covering the range 120–5 nm and the second one dispersing the radiation up to 1 nm (1 keV). A high-precision remotely controlled translation stage allow accurate positioning of the two grating.

Finally, the EUV detection is performed with a double stack Micro-Channel Plate (MCP) in chevron configuration with independent voltages followed by a phosphor screen and a CCD, allowing a high dynamic range and sensitivity. Both the MCP and the visible CCD can be remotely moved to follow the whole dispersion curve of the two gratings.

4 Conclusion

We reported the progress on the development of an innovative HHG source based on a microfluidic device, realized on a glass substrate through the FLICE technique. The high-order harmonics generated inside this device exhibited a very high

photon flux up to 160 eV, reaching the performances of the state-of-the-art EUV sources. Moreover, we showed the new design of a EUV spectrometer for full characterization of the spatial and polarization properties of the EUV radiation.

The high photon flux EUV source combined with the high flexibility and sensitivity of the detection system provides an ideal lab-scale beamline for HHG spectroscopy and EUV transient absorption experiments in molecules, solids and diluted samples.

References

1. Vishnubhatla, K.C., Bellini, N., Ramponi, R., Cerullo, G., Osellame, R.: Shape control of microchannels fabricated in fused silica by femtosecond laser irradiation and chemical etching. Opt. Express. **17**, 8685–8695 (2009)
2. Ciriolo, A.G., Vázquez, R.M., Tosa, V., Frezzotti, A., Crippa, G., Devetta, M., Faccialá, D., Frassetto, F., Poletto, L., Pusala, A., Vozzi, C., Osellame, R., Stagira, S.: High-order harmonic generation in a microfluidic glass device. J. Phy. Photo. **2**(2), 024005 (2020)
3. He, F., Lin, J., Cheng, Y.: Fabrication of hollow optical waveguides in fused silica by three-dimensional femtosecond laser micromachining. Appl. Phys. B. **105**, 379–384 (2011)
4. COMSOL Multiphysics, v. 5.4. www.comsol.com. COMSOL AB, Stockholm: Sweden
5. A. G. Ciriolo et al., Submitted https://doi.org/10.48550/arXiv.2206.11075
6. Ding, C., Xiong, W., Fan, T., Hickstein, D.D., Popmintchev, T., Zhang, X., Walls, M., Murnane, M., Kapteyn, H.C.: High flux coherent super-continuum soft X-ray source driven by a single-stage, 10mJ, Ti: sapphire amplifier-pumped OPA. Opt. Express. **22**, 6194–6202 (2014)
7. Takahashi, E.J., Nabekawa, Y., Midorikawa, K.: Low-divergence coherent soft x-ray source at 13 nm by high-order harmonics. Appl. Phys. Lett. **84**, 4–6 (2004)
8. Takahashi, E.J., Nabekawa, Y., Mashiko, H., Hasegawa, H., Suda, A., Midorikawa, K.: Generation of strong optical field in soft X-ray region by using high-order harmonics. IEEE J. Sel. Top. Quantum Electron. **10**, 1315–1328 (2004)
9. Hädrich, S., Klenke, A., Rothhardt, J., Krebs, M., Hoffmann, A., Pronin, O., Pervak, V., Limpert, J., Tünnermann, A.: High photon flux table-top coherent extreme-ultraviolet source. Nat. Photonics. **8**, 779–783 (2014)
10. Rudawski, P., Heyl, C.M., Brizuela, F., Schwenke, J., Persson, A., Mansten, E., Rakowski, R., Rading, L., Campi, F., Kim, B., Johnsson, P., L'Huillier, A.: A high-flux high-order harmonic source. Rev. Sci. Instrum. **84**, 073103 (2013)
11. G. Crippa et al., In preparation

Attosecond Physics and Quantum Information Science

M. Lewenstein, N. Baldelli, U. Bhattacharya, J. Biegert, M. F. Ciappina, T. Grass, P. T. Grochowski, A. S. Johnson, Th. Lamprou, A. S. Maxwell, A. Ordóñez, E. Pisanty, J. Rivera-Dean, P. Stammer, and P. Tzallas

Abstract In this article, we will discuss a possibility of a symbiosis for attophysics (AP) and quantum information (QI) and quantum technologies (QT). We will argue that within few years AP will reach Technology Readiness Level (RTL) 4–5 in QT, and will thus become a legitimate platform for QI and QT.

Keywords Quantum optics · Laser-matter interaction · Attosecond physics

---

The original version of the chapter has been revised. A correction to this chapter can be found at https://doi.org/10.1007/978-3-031-47938-0_21

M. Lewenstein (✉) · J. Biegert
ICFO—Institut de Ciéncies Fotóniques, The Barcelona Institute of Science and Technology, Barcelona, Spain

ICREA, Pg. Lluís Companys 23, Barcelona, Spain
e-mail: maciej.lewenstein@icfo.eu

N. Baldelli · U. Bhattacharya · A. S. Johnson · A. Ordóñez · J. Rivera-Dean · P. Stammer
ICFO—Institut de Ciéncies Fotóniques, The Barcelona Institute of Science and Technology, Barcelona, Spain

T. Grass
DIPC—Donostia International Physics Center, Paseo Manuel de Lardizábal, San Sebastián, Spain

IKERBASQUE, Basque Foundation for Science, Bilbao, Spain

ICFO—Institut de Ciéncies Fotóniques, The Barcelona Institute of Science and Technology, Barcelona, Spain

M. F. Ciappina
Physics Program, Guangdong Technion - Israel Institute of Technology, Shantou, Guangdong, China

Technion - Israel Institute of Technology, Haifa, Israel

L. Argenti et al. (eds.), *Proceedings of the 8th International Conference on Attosecond Science and Technology*, Springer Proceedings in Physics 300,
https://doi.org/10.1007/978-3-031-47938-0_4

1 Introduction

Contemporary Quantum Technologies face major difficulties in fault tolerant quantum computing with error correction, and focus instead on various shades of quantum simulation (Noisy Intermediate Scale Quantum, NISQ) devices [1], analogue and digital Quantum Simulators [2], and quantum annealers [3]. There is a clear need and quest for systems that, without necessarily simulating quantum dynamics of some physical systems, can generate massive, controllable, robust entangled and superposition states. This will, in particular, allow for the use of decoherence in a controlled manner, enabling the use of these states for quantum communications [4] (e.g. to achieve efficient transfer of information in a safer and quicker way), quantum metrology [5], sensing and diagnostics [6] (e.g. to precisely measure phase shifts of light fields, or to diagnose quantum materials).

In this lecture, we propose an answer to these needs, by opening new avenues for Quantum Information (QI) science via the symbiosis with Attophysics (AP) and Quantum Optics (QO). To date, there are no existing platforms that can bring processes at such short time-scales to Quantum Information systems. We will illustrate how recent developments in AP aim at realizing a universal and firmly established tool to offer completely unknown solutions and avenues for QI. In particular, we will discuss how AP offers a set of stable and reproducible methods to generate massively entangled states and massive quantum superpositions [7, 8]. These methods apply, in the first place, to fundamental Quantum Information

P. T. Grochowski
ICFO—Institut de Ciéncies Fotóniques, The Barcelona Institute of Science and Technology, Barcelona, Spain

Institute for Quantum Optics and Quantum Information of the Austrian Academy of Sciences, Innsbruck, Austria

Institute for Theoretical Physics, University of Innsbruck, Innsbruck, Austria

Center for Theoretical Physics, Polish Academy of Sciences, Warsaw, Poland

Th. Lamprou
Department of Physics, University of Crete, Heraklion, Crete, Greece

Foundation for Research and Technology-Hellas, Institute of Electronic Structure & Laser, Heraklion, Crete, Greece

A. S. Maxwell
Department of Physics and Astronomy, Aarhus University, Aarhus C, Denmark

E. Pisanty
Max Born Institute for Nonlinear Optics and Short Pulse Spectroscopy, Berlin, Germany

Department of Physics, King's College London, Strand, London, UK

P. Tzallas
Foundation for Research and Technology-Hellas, Institute of Electronic Structure & Laser, Heraklion, Crete, Greece

ELI-ALPS, ELI-Hu Non-Profit Ltd., Szeged, Hungary

science, but with the final goal of bringing them to Quantum Technologies (QT). This will be accomplished by studying:

(i) The detection of topology, strongly correlated systems, chirality, etc. in AP;
(ii) The generation of entangled/quantum correlated states using conditioning methods;
(iii) Strong-field physics and atto-second science driven by non-classical light;
(iv) The generation of entangled/quantum correlated states in *Zerfall* processes;
(v) Quantitative and measurable effects of decoherence in AP.

The lecture is organized around three projects that are being realized at ICFO:

– European Research Council Advanced Grant "NOvel Quantum SImulAtors (NOQIA)", run by M. Lewenstein.
– Future and Emerging Technologies project Optical Topological Logic (OPTOLOGIC), coordinated by J. Biegert (ICFO).
– Not-yet-financed project Attophysics and Quantum information Science (ATTOQUIS), coordinated by M. Lewenstein. This project summons experts in the fields of QO, QI, and AP who will join forces to invent new mechanisms for generating massive, controllable, robust, entangled light states, and understand the process of decoherence in them, thus identifying new laws and limits of QI. In a nutshell: Our results will set up the basis for a road map toward a novel platform of AS for QT.

In this lecture we will focus on ATTOQUIS (to be read as ATTOKISS), the new joint project of ICFO, FORTH, Technion, CEA, and IOTA toward a symbiosis of attophysics and quantum information science. This is in particular aimed at studying the generation of entangled/quantum correlated states using conditioning methods. We will describe our joint efforts to generate Schrödinger cat states (SCS) of photons conditioned on high harmonic generation (HHG) [9] (see Fig. 1) and/or above threshold ionization [7, 10]. We will also talk about generation of topological

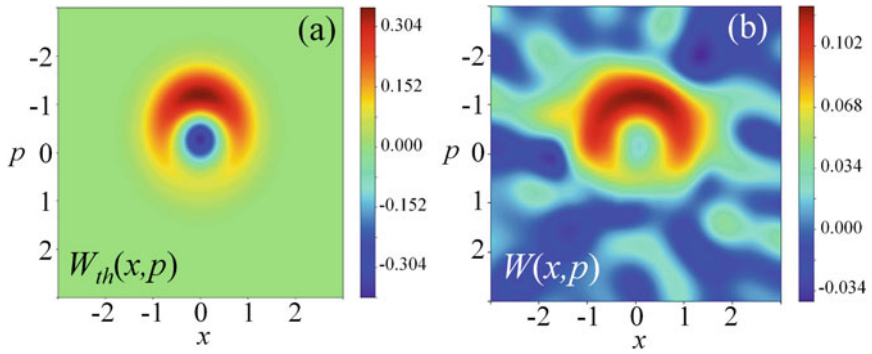

Fig. 1 High-photon number optical cat state created by conditioning on HHG. (**a**) Theoretical prediction for the Wigner function according to [7, 9]. (**b**) Experimental reconstruction of the Wigner function with mean photon number $\langle n \rangle \approx 9.4 \pm 0.1$, which represents an optical Schrödinger cat state. For visualization reasons, the plots have been centered to zero. The figure has been extracted from [7]

order using laser pulses with orbital angular momentum (OAM) [11]. We will also discuss HHG as a tool to detect phase transitions and topological order in strongly correlated systems [12, 13]. Finally, we will speculate about measurement of entanglement of OAM of electrons in double ionization [14], and violation of Bell inequalities by SCS. This paper is by no means a review—it is rather a review of progress, based on a selection of relevant references, actually mostly from external and collaborating groups. It follows the structure of the invited lecture of M. Lewenstein at ATTOVIII Conference in Orlando [15].

2 Detection of Topology, Strongly Correlated Systems, Chirality, etc.

Recently, there is an explosion of interest in applying AP methods to diagnose and detect topological order, strongly correlated systems, and chirality. The primary role is played here by the process of high harmonic generation (HHG).

2.1 Detection of Topological Order with HHG

The pioneering work of R. Huber *et consortes* [16] studied lightwave-driven Dirac currents in a topological surface band. It was noted that "Harnessing the carrier wave of light as an alternating-current bias may enable electronics at optical clock rates" [16, 17]. "Lightwave-driven currents have been assumed to be essential for high-harmonic generation in solids" (cf. [18, 19]). They report angle-resolved photoemission spectroscopy with subcycle time resolution that enables them to observe directly how the carrier wave of a terahertz light pulse accelerates Dirac fermions in the band structure of the topological surface state of Bi_2Te_3. This work opened a path toward all-coherent lightwave-driven electronic devices.

Perhaps the first papers where HHG was considered for detection of topology were the series of papers by D. Bauer with his collaborators on detection of topological edge states in dimerized chains [20, 21]. In the first work, HHG in the two topological phases of a finite, one-dimensional, periodic structure is investigated using a self-consistent time-dependent density functional theory approach. For harmonic photon energies smaller than the band gap, the harmonic yield is found to differ by up to 14 orders of magnitude for the two topological phases. Similar conclusions were obtained in the study of the Su-Schrieffer-Heeger (SSH) chains that display topological edge states. The authors calculated high-harmonic spectra of SSH chains that are coupled to an external laser field of a frequency much smaller than the band gap. In recent works, this method has been extended to the detection of Majorana fermions in the Kitaev chain [22] and in quantum wires with proximity-induce p-wave superconductivity [13] (see Fig. 2). Specifically, their harmonic emission spectrum in strong fields is shown to exhibit spectral features due to radiating edge modes, which characterize the spectrum and the density of states in the topological phase, and which are absent in the trivial phase. These features

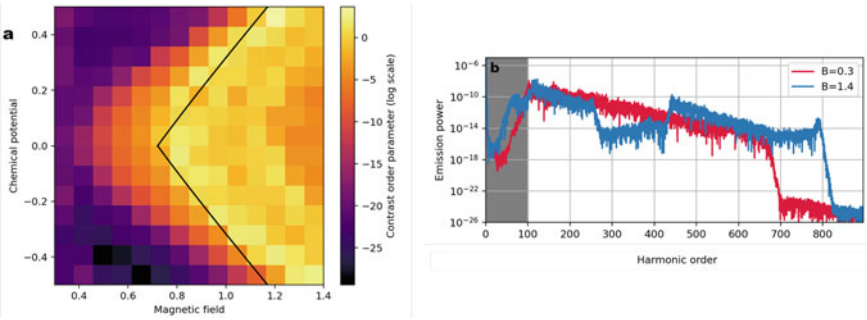

Fig. 2 (**a**) The phase diagram of the proximity-induced p-wave superconductor is obtained from an order parameter based on the harmonic emission spectrum, exemplarily shown in (**b**) for two parameter choices, in the topological and in the trivial phase. At frequencies below the bandgap, emission is suppressed in the trivial phase (red), whereas in the topological phase emission is possible already at frequencies above half the bandgap due to the edge state in the middle of the bandgap. The figures have been reprinted from Ref. [13]

allow us to define an order parameter, obtained from emission measurements, that unambiguously differentiates between the two phases. Local probing provides insight into the localized and topologically protected nature of the modes. The presented results establish that high harmonic spectroscopy can be used as a novel all-optical tool for the detection of Majorana zero modes.

In the seminal Nature Photonics paper, M. Ivanov *et consortes* discuss topological strong-field physics on sub-laser-cycle timescale [23]. These authors study response of the paradigmatic Haldane model [24] to ultrashort, ultrastrong laser pulses. Here, they show that electrons tunnel differently in trivial and topological insulators, for the same band structure, and identify the key role of the Berry curvature in this process. These effects map onto topologically dependent attosecond delays and helicities of emitted harmonics that record the phase diagram of the system. As they say: "These findings create new roadmaps in studies of topological systems, building on the ubiquitous properties of the sub-laser-cycle strong-field response—a unique mark of attosecond science". Moreover, they show that strong fields can also be used for the manipulation of topological properties of 2D materials, relevant for valleytronic devices [25]. In a complementary approach, A. Chacón et al. [26] studied circular dichroism in higher-order harmonic generation from the Haldane model. These effect clearly heralds topological phases and transitions in Chern insulators (see also A. Chacón's contribution to [15]).

2.2 Detection of Strongly Correlated Systems with HHG

This is another rapidly developing area. As pointed out in the recent review [27]: "A hallmark effect of extreme nonlinear optics is the emission of high-order harmonics of the laser from the bulk of materials. The discovery and detailed study of this phenomenon over the course of the past decade has offered a broad range of

possibilities and seen the dawn of a new field of extreme solid-state photonics. In particular, it opens the way to previously inaccessible spectral ranges, as well as the development of novel solid-state spectroscopy and microscopy techniques that enable detailed probing of the electronic structure of solids."

An example of pioneering studies of HHG in strongly correlated materials is described in the paper by Silva et al. [28], where the authors show that HHG can be used to time-resolve ultrafast many-body dynamics associated with an optically driven phase transition to Mott insulator state, with accuracy far exceeding one cycle of the driving light field. In Ref. [29], the authors establish time-resolved high harmonic generation (tr-HHG) as a powerful spectroscopy method for tracking photoinduced dynamics in strongly correlated materials through a detailed investigation of the insulator-to-metal phase transitions in vanadium dioxide. Further examples include the mentioned studies of detection of Majorana fermions [13, 22].

Very recently, MBI group of Smirnova and Ivanov, using advanced techniques of dynamical mean field theory to study the strong field response of the two-band Hubbard model (see M. Ivanov's contribution to [15, 30] proposed sub-cycle multidimensional spectroscopy of strongly correlated materials). In this work they introduce a new type of non-linear approach that allows to unravel the sub-cycle dynamics of strongly correlated systems interacting with few-cycle infrared pulses For the two-dimensional Hubbard model under the influence of ultra-short, intense electric field transients, they demonstrate that our approach can resolve pathways of charge and energy flow between localized and delocalized many-body states on the sub-cycle timescale, including the creation of a highly correlated state surviving after the end of the laser pulse.

HHG may be also used for extraction of higher-order nonlinear electronic response in solids [31]. Moreover, high harmonics may undergo spectacular enhancement in solid state nano-structures, such as graphene heterostructures [32]. Very recently, HHG was used to characterize quantum criticality in strongly correlated systems [33]. By employing the exact diagonalization method, we investigate the high-harmonic generation (HHG) of the correlated systems under the strong laser irradiation. For the extended Hubbard model on a periodic chain, HHG close to the quantum critical point (QCP) is more significant compared to two neighboring gapped phases (i.e., charge-density-wave and spin-density wave states), especially in low frequencies.

In Ref. [12], HHG has also been applied to cuprates in a broad temperature range from 80K to 300K, probing different phases of the high-Tc material. This work demonstrates that strong-field emission is able to distinguish between various strongly correlated phases: The superconducting phase is marked by a strong increase of emission at all odd harmonic frequencies (3rd, 5th, and 7th), whereas the transition from the pseudogap phase to the strange metallic phase is reflected by a intensity drop only in the highest harmonics (7th). These experimental findings are reproduced by simulating the strong-field dynamics of a two-band model in the BCS mean-field regime and in the presence of phenomenological scattering terms.

All of there findings, discussed in this subsection, open a way to a regime of imaging and manipulating strongly correlated materials at optical rates, far beyond the multi-cycle approach employed in Floquet engineering of quantum systems.

2.3 Detection of Chirality with HHG

Detection of chirality is somewhat similar to the detection of topological order with HHG, but mostly refers to molecular targets. Chirality is the norm among biological molecules and the technological importance of distinguishing molecules which differ only by their chirality cannot be overstated. Absolutely seminal results along this direction in the context of ultrafast imaging have been achieved by the group of O. Smirnova and collaborators [34] (see [35] for a recent review). In particular, in Refs. [36, 37] they introduce the concept of *locally chiral light*—light which is chiral within the electric-dipole approximation by means of its 3D chiral Lissajous figure—and show how this type of chiral light can be synthesized and exploited to dramatically enhance the contrast between HHG spectra in molecules with opposite chiralities. They show that such contrast can be enhanced either at the level of angle-integrated harmonic emission or at the level of direction of harmonic emission, depending on the pattern of the light's local chirality over the interaction region. In Ref. [38], they address the role of the transverse spin of the light (which emerges whenever light is confined to a small region of space) in ultra-fast chiral imaging. They show that the interaction of chiral molecules with a strong, tightly focused, few-cycle pulse results in harmonics with a polarization that depends on the molecular chirality.

In turn, we have recently studied the role of the orbital angular momentum (OAM) of photoelectrons in ultrafast chiral imaging [39]. We found that chiral molecules subject to strong-field ionization with a few-cycle, IR, linearly polarized pulse serve as natural sources of *twisted* photoelectrons, with the twist depending on the molecular chirality. Besides exposing an alternative road towards ultrafast chiral imaging, this effects suggests intriguing perspectives regarding the role of the electron OAM in recollision-based phenomena in chiral molecules.

3 Generation of Topology, Strongly Correlated Systems, Chirality, etc.

While AP and HHG have proven to be great detection tools, ultrafast laser pulse and attophysics methods may also be used for generation of topological order, strongly correlated states, chirality, etc. These ideas are, of course, very close to the attempts to generate room temperature high T_c superconductivity [40], or Chern insulators [41], which belong more to the domain of ultrafast, but Terahertz physics.

In fact, we have already some experience with laser induced phase transitions; we have worked with the experimental group of S. Wall on Terahertz field control of in-plane orbital order in $La_{0.5}Sr_{1.5}MnO_4$ [42]. We have also started to work on laser induce fluctuating bonds superconductivity [43] in the hole-doped cuprates. But, for this section perhaps the most relevant is our recent Phys. Rev. B Lett. [11],

where we demonstrate the theoretical possibility of generation of fermionic Chern insulator from twisted light with linear polarization in graphene-like material.

Particularly interesting line of research connects generation of topology, strongly correlated systems, chirality, etc. with the use of more complex *structured laser light*, combining polarization and OAM effects. A perfect example is the light, which knots fractional-order knots in the dynamics of the electric field vector employing the polarization state of light and superposition of the fundamental and doubled frequency [44]. Application of strong laser pulsed of this form to atomic targets lead to "exotic" conservation of torus-knot angular momentum in high-order harmonic generation [45]. Combining two delayed circularly polarized pulses of frequency ω and 2ω, one can generate a light with a self-torque: extreme-ultraviolet beams of HHG with time-varying orbital angular momentum [46].

As shown in Ref. [47], *locally chiral light* [36, 37], another type of structured light, can be used to efficiently (i.e. at the level of the electric-dipole approximation) imprint 3D chirality on achiral matter, such as atoms. Locally chiral light sculpts a chiral orbital out of the initially achiral ground state. That is, it excites the electron into a superposition of excited states such that the resulting orbital acquires a chiral shape.

4 Generation of Massively Quantum Correlated States

The generation of massively quantum correlated states is another spectacular line of research of the ATTOQUIS platform. This direction it is driven by the first and the very encouraging experimental and theoretical results published/submitted on this subject within the last year [7–10, 48–50]. In the following sub-sections we emphasize on the two main ideas underlying this research direction. The "QED and conditioning in strongly laser driven interactions" (Sect. 4.1) and the "QED of strong field processes driven by non-classical light fields" (Sect. 4.2).

4.1 QED and Conditioning in Strongly Laser Driven Interactions

The basic idea of this approach, which is schematically illustrated in Fig. 3a, is the following (here we focus in conditioning on HHG):

- We describe the intense laser–matter interaction fully quantum-electrodynamically using coherent light states. In Fig. 3a the coherent state of the driving laser field is given by $|\alpha_L\rangle$.
- During the interaction with the target, the driving pulse remains a coherent state, but is modified due to the interactions with the matter. The resulted driving field after the interaction is an amplitude shifted coherent state $|\alpha_L + \chi_L\rangle$ and the

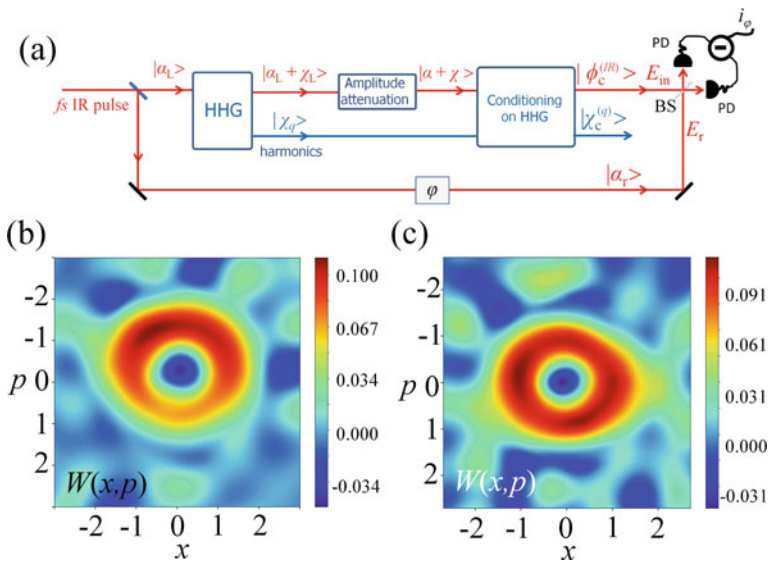

Fig. 3 (**a**) Schematic illustration of the operation principle of the conditioning approach. HHG is the area where the intense laser–matter interaction takes place and the high harmonics are generated. $|\alpha_L\rangle$ is the initial coherent state of the driving field. $|\alpha_L + \chi_L\rangle$, $|\alpha + \chi\rangle$ are the states of the IR field after the interaction and attenuation, respectively. $|\chi_q\rangle$ are the coherent states of the harmonic modes. $|\phi_c^{(IR)}\rangle$ and $|\chi_c^{(q)}\rangle$ are the field states after conditioning on the HHG. A scheme of the QT method used for the quantum state characterization. $|\alpha_r\rangle$ is the state of the local oscillator reference field. φ is a controllable phase shift. BS is a beam splitter. PD are identical IR photodiodes used from the balanced detector. i_φ is the φ dependent output photocurrent difference used for the measurement of the electric field operator and the reconstruction of the Wigner function. (**b**) and (**c**) Reconstructed Wigner functions of an optical "cat" and "kitten" state, respectively. Panels (**b**) and (**c**) have been reproduced from Ref. [7]

generated harmonics are in coherent state $|\chi_q\rangle$. These can be calculated using various methods. For atomic and molecular targets one can use TDSE or SFA [51], for solids sometimes the semiconductor Bloch equations [52], and for strongly correlated systems more sophisticated methods.

– After passing the target, the fundamental laser field in attenuated in a coherent manner (resulting in $|\alpha + \chi\rangle$) in the range of few–photons and conditioned to HHG by means of quantum spectrometer (QS) method [9, 10, 53, 54]. The QS is a shot–to–shot IR vs HH photon correlation–based method, which selects only the IR shots that are relevant to the harmonic emission. It relies on photon statistics measurements and the energy conservation, i.e., q IR photons need to be absorbed from the IR field for the generation of a photon of the q_{th} harmonic. The output of the QS contains only the IR shots conditioned on the HHG process, resulting in the creation of non-classical light states. In case of intense laser–atom interaction, this state is a coherent state superposition i.e. an optical Schrödinger

"cat" state of the form $|\phi_c^{(IR)}\rangle = |\alpha + \chi\rangle - \xi\,|\alpha\rangle$, where ξ is the overlap between $|\alpha + \chi\rangle$ and $|\alpha\rangle$.

- The quantum character of the light field after the conditioning (E_{in}) can be obtained by the measurement of its Wigner function. This can be archived by means of a homodyne detection system and the quantum tomography method [55, 56]. The E_{in} is spatiotemporally overlapped on a beam splitter (BS) with the field of a local oscillator E_r (with $E_r >> E_{in}$). The E_r is coming from the 2nd branch of the interferometer which introduces a controllable phase shift φ between the E_{in} and E_r. The fields after the BS are detected by a balanced differential photodetection system consisting of two identical photodiodes (PD). This provides at each value of φ the photocurrent difference i_φ. The characterization of the quantum state of light can be achieved by recording for each shot the value of i_φ as a function of φ. These values are directly proportional to the measurement of the electric field operator $\hat{E}_{in}(\varphi) \propto \cos(\varphi)\hat{x} + \sin(\varphi)\,\hat{p}$ and are used for the reconstruction of the Wigner function via Radon transformation [57]. $\hat{x} = (\hat{a} + \hat{a}^\dagger)/\sqrt{2}$ and $\hat{p} = (\hat{a} - \hat{a}^\dagger)/i\sqrt{2}$ are the non-commuting quadrature field operators, and $\hat{a}$, $\hat{a}^\dagger$ are the photon annihilation and creation operators, respectively.
- The scheme has been used for the generation of high–photon number shifted optical "cat" states (Fig. 1) and coherent state superposition with controllable quantum features using intense–laser atom interaction [7, 9]. The control of the quantum features is shown in Fig. 3b, c where an optical "cat" state switches to a "kitten" for lower values of χ. The same scheme can be applied for conditioning on ATI [7, 10, 50], two-electron ionization, etc. In our recent study [7], it has been theoretically shown that conditioning on ATI process can also lead to the generation of optical cat states. This, besides its fundamental interest associated with electron-photon correlation during the ATI/HHG process, provides an additional "knob" of controlling the quantum character of the optical cat states, a feature extremely valuable for applications in quantum technology. Also, according to our recent theoretical investigation performed for laser-atom interactions [8], single and two-color driven laser-atom interactions can result in the generation of "massively" entangled optical coherent states in the spectral range from extreme ultraviolet (XUV) (shown in Fig. 3a as $|\chi_c^{(q)}\rangle$) to the far infrared. Such states in combination with passive linear optical elements (such as phase shifters, beam splitters, and optical fibers) [49, 58] can be considered as unique resources for novel applications in quantum technology.

4.2 *QED of Strong Field Processes Driven by Non-classical Light Fields*

All the quantum optical studies of strong field driven processes have thus far been approached by assuming a coherent state description for the driving field. The

corresponding field is classical, even if Hilbert space methods are used for its description. However, in a recent work, presented at ATTO VIII by Even Tzur et al. [59], this assumption was abandoned, and the process of HHG driven by non-classical light fields has been presented for the first time. They show, that the photon statistics of the driving field leaves its signatures in the observed high harmonic spectrum. This will open the path for investigating the interplay between non-classical properties of the driving source, and how they are imprinted in the observables of the harmonic field modes.

5 Studies of Quantum Correlated States/Decoherence in *Zerfall* Processes

5.1 Generation of Entanglement in Zerfall Processes

Finally, AP is a perfect playground to study generation of quantum correlations and entanglement in *Zerfall* processes, i.e. processes of decay of a "whole" in products. A prime example of this is non-sequential double ionization (NSDI), where strong-field ionization followed by laser induced recollision leads to double ionization of the target, see Fig. 4a. Strong correlation between the ionization products, in particular the two photoelectrons, has long been known [60]. Previously, coherence and interference between the two photoelectrons has been studied in great detail [61–64]. More recently, A. Maxwell et al. [14] studied generation of entanglement in non-sequential double ionization, by using correlation in the OAM of the outgoing electrons, for a mini-review on OAM in strong-field ionization see [65, 66]. A key step, is to exploit the intermediate excited state, and its inherent superposition over OAM, which is present for the 'second' electron for the low-intensity regime.[1] Thus, simple conservation laws dictate that the final OAM of the two electrons must be anti-correlated, which at certain final momentum leads to a maximally entangled qutrit, see Fig. 4b, while remaining robust to incoherent effects, such as focal averaging or decoherence with the ion.

Continuum products in a *typical* strong-field Zerfall processes will be quantified through continuous variables, which can complicate analysis of entanglement measures. However, the use of OAM makes the task of quantifying and measuring entanglement much easier, the computations of the reduced density matrix of ionized product in the OAM space becomes simple, and in the case of NSDI, clearly exhibits entanglement. This also enables quantification by the, so called, logarithmic negativity, which may be used for mixed states to model incoherent effects.

[1] This is known as the recollision with subsequent ionization (RESI) mechanism.

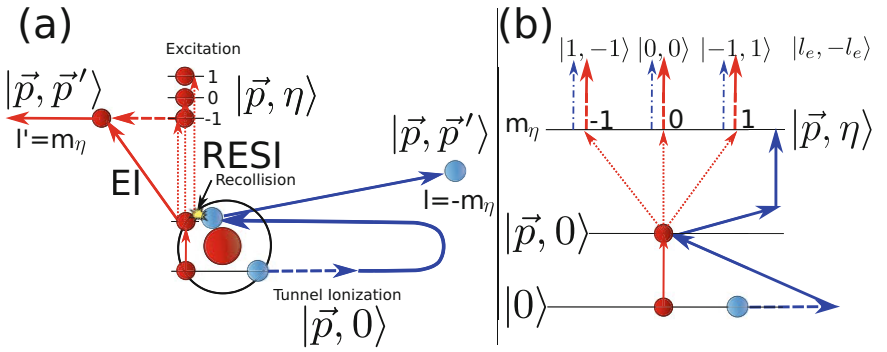

Fig. 4 Non-sequential double ionization (NSDI), a 'Zerfall' processes, leading to entanglement between the orbital angular momentum (OAM) of the two photoelectrons. In panel (**a**), an electron is ionized via a strong laser field and recollides with the parent atom/molecule. This leads to either: direct ionization of a second electron in electron impact (EI) ionization, or excitation with subsequent ionization (RESI) of a second electron. Panel (**b**) focuses on RESI, the OAM superposition in the excited state is transferred to the final state along with anti-correlation between the electrons

5.2 *Characterizing Decoherence in Zerfall Processes*

Finally, studies of *Zerfall* processes offer a unique opportunity to understand and characterize quantum and classical decoherence. This goes back to seminal and pioneering theoretical works by R. Santra et al. [67–69], F. Martín et al. [70], or M. Vacher et al. [71]. All of these works dealt essentially with the single electron ionization process that might lead to entanglement of the electron with the parent ion. Measuring reduced density matrix of the electron provides thus information about decoherence and thus entanglement Mark Vrakking et al. has developed both theoretical and the first experimental ideas in this context [72, 73] (see also M. Vrakking's contribution to [15]). One of the main problems in this line of research is to make sure that the source of decoherence is truly quantum. Indeed, by analyzing with great care various classical and quantum models of decoherence in the process of single electron ionization, Ch. Bourassin-Bouchet et al. demonstrated dominantly classical sources of decoherence.

In contrast, in the recent work [74], A. L'Huillier et al. investigated decoherence due to entanglement of the radial and angular degrees of freedom of the photoelectron. They study two-photon ionization via the $2s2p$ autoionizing state in He using high spectral resolution photoelectron interferometry. Combining experiment and theory, we show that the strong dipole coupling of the $2s2p$ and $2p^2$ states results in the entanglement of the angular and radial degrees of freedom. This translates, in angle integrated measurements, into a dynamic loss of coherence during autoionization.

6 Conclusions

This paper provides a progress review on a new emerging interdisciplinary area of science, namely ATTOQUIS, in which ultrafast laser physics and attoscience merge with quantum optics and quantum information science. We provide examples of the ATTOQUIS research directions that are already at a step where theoretical and proof-of-principle experimental investigations have been developed. Based on these examples, we briefly discuss how the fully quantized description of intense laser-matter interaction and high-harmonic generation, in combination with conditioning methods, can be used for: (i) the generation of controllable massively entangled quantum state superpositions in all states of matter, (ii) the generation and detection of chirality and topological order in strongly correlated systems, (iii) the generation of high–harmonics using intense quantum light, and (iv) investigations quantum correlated states and decoherence effects in atoms. In few words, the results demonstrated in the aforementioned directions constitute the beginning of a very long "story". They show the power of intense laser–matter interaction as a new resource for novel investigations in attosecond science and quantum technology, a goal that the ATTOQUIS platform strives for.

Acknowledgments ICFO group acknowledges support from: ERC AdG NOQIA; Ministerio de Ciencia y Innovation Agencia Estatal de Investigaciones (PGC2018-097027-B-I00/ 10.13039/501100011033, CEX2019-000910-S/10.13039/501100011033, Plan National FIDEUA PID2019-106901GB-I00, FPI, QUANTERA MAQS PCI2019-111828-2, QUANTERA DYNAMITE PCI2022-132919, Proyectos de I+D+I "Retos Colaboración" QUSPIN RTC2019-007196-7); European Union NextGenerationEU (PRTR C17.I1); Fundació Cellex; Fundació Mir-Puig; Generalitat de Catalunya (European Social Fund FEDER and CERCA program (AGAUR Grant No. 2017 SGR 134, QuantumCAT U16-011424, co-funded by ERDF Operational Program of Catalonia 2014-2020); Barcelona Supercomputing Center MareNostrum (FI-2022-1-0042); EU Horizon 2020 FET-OPEN OPTOlogic (Grant No 899794); National Science Centre, Poland (Symfonia Grant No. 2016 /20/W/ST4/00314); European Union's Horizon 2020 research and innovation programme under the Marie-Skłodowska-Curie grant agreement No 101029393 (STREDCH) and No 847648 ("La Caixa" Junior Leaders fellowships ID100010434: LCF/BQ/PI19/11690013, LCF/BQ/PI20/11760031, LCF/BQ/PR20/11770012, LCF/BQ/PR21/11840013); the Government of Spain (FIS2020-TRANQI and Severo Ochoa CEX2019-000910-S). M. F. C. acknowledges financial support from the Guangdong Province Science and Technology Major Project (Future functional materials under extreme conditions - 2021B0301030005). J. B. acknowledges financial support from the European Research Council for ERC Advanced Grant "TRANSFORMER" (788218) and ERC Proof of Concept Grant "miniX" (840010), FET-OPEN "PETACom" (829153), FET-OPEN "OPTOlogic" (899794), EIC-2021-PATHFINDEROPEN "TwistedNano" (101046424), Laserlab-Europe (654148), Marie Sklodowska-Curie ITN "smart-X" (860553), Plan Nacional PID-PID2020-112664GB-I00-210901; AGAUR for 2017 SGR 1639, "Severo Ochoa" (SEV- 2015-0522), Fundació Cellex Barcelona, the CERCA Programme/Generalitat de Catalunya, and the Alexander von Humboldt Foundation for the Friedrich Wilhelm Bessel Prize. P. Tzallas group at FORTH acknowledges LASERLABEUROPE V (H2020-EU.1.4.1.2 grant no. 871124), FORTH Synergy Grant AgiIDA (grand no. 00133), the H2020 framework program for research and innovation under the NEP-Europe-Pilot project (no. 101007417). ELI-ALPS is supported by the European Union and co-financed by the European Regional Development Fund (GINOP Grant No. 2.3.6-15-2015-00001). E.P. acknowledges Royal Society University Research Fellowship funding under

URF\R1\211390. J.R-D. acknowledges support from the Secretaria d'Universitats i Recerca del Departament d'Empresa i Coneixement de la Generalitat de Catalunya, as well as the European Social Fund (L'FSE inverteix en el teu futur)–FEDER. P. S. acknowledges funding from the European Union's Horizon 2020 research and innovation programme under the Marie Sklodowska-Curie grant agreement No 847517. A. S. M. acknowledges funding support from the European Union's Horizon 2020 research and innovation programme under the Marie Skłodowska-Curie grant agreement SSFI No.\887153.

References

1. Preskill, J.: Quantum computing in the NISQ era and beyond. Quantum **2**, 79 (2018)
2. Georgescu, I.M., Ashhab, S., Nori, F.: Quantum simulation. Rev. Mod. Phys. **86**, 153 (2014)
3. Farhi, E., Goldstone, J., Guttmann, S., Lapan, J., Lundgren, A., Preda, D.: A quantum adiabatic evolution algorithm applied to random instances of an NP-complete problem. Science **292**, 5516 (2001)
4. Gisin, N., Thew, R.: Quantum communication. Nat. Phot. **1**, 165–171 (2007)
5. Giovannetti, V., Lloyd, S., Maccone, L.: Advances in quantum metrology. Nat. Phot. **5**, 222–229 (2011)
6. Degen, C.L., Reinhard, F., Cappellaro, P.: Quantum sensing. Rev. Mod. Phys. **89**, 035002 (2017)
7. Rivera-Dean, J., Lamprou, Th., Pisanty, E., Stammer, P., Ordóñez, A.F., Ciappina, M.F., Lewenstein, M., Tzallas, P.: Strong-laser fields and their power to generate controllable high-photon-number coherent-state superpositions. Phys. Rev. A **105**, 033714 (2022)
8. Stammer, P., Rivera-Dean, J., Lamprou, Th., Pisanty, E., Ciappina, M.F., Tzallas, P., Lewenstein, M.: High photon number entangled states and coherent state superposition from the extreme-ultraviolet to the far infrared. Phys. Rev. Lett. **128**, 123603 (2022). arXiv:2107.12887
9. Lewenstein, M., Ciappina, M.F., Pisanty, E., Rivera-Dean, J., Stammer, P., Lamprou, Th., Tzallas, P.: Generation of optical Schrödinger cat states in intense laser–matter interactions. Nat. Phys. **17**, 1104–1108 (2021). arXiv:2008.10221
10. Stammer, P., Rivera-Dean, J., Maxwell, A.S., Lamprou, Th., Ordóñez, A.F., Ciappina, M.F., Tzallas, P., Lewenstein, M.: Quantum electrodynamics of ultra-intense laser-matter interactions. Invited tutorial for PRX Quantum 4, 010201 (2023). arXiv:2206.04308
11. Bhattacharya, U., Chaudhary, S., Graß, T., Johnson, A., Wall, S., Lewenstein, M.: Fermionic Chern insulator from twisted light with linear polarization. Phys. Rev. B **105**, L081406 (2022). arXiv:2006.10688
12. Alcalà, J., Bhattacharya, U., Biegert, J., Ciappina, M.F., Elu, U., Graß, T., Grochowski, P.T., Lewenstein, M., Palau, A., Sidiropoulos, T.P.H., Steinle, T., Tyulnev, I.: High harmonic spectroscopy of quantum phase transitions in a high-Tc superconductor. Proc. Natl. Acad. Sci. U.S.A. **119**, e2207766119 (2022). https://doi.org/10.1073/pnas.220776611
13. Baldelli, N., Bhattacharya, U., González-Cuadra, D., Lewenstein, M., Graß, T.: Detecting Majorana Zero Modes via Strong Field Dynamics. ACS Omega **7**, 47424 (2022). arXiv:2202.03547
14. Maxwell, A.S., Madsen, L.B., Lewenstein, M.: Entanglement of orbital angular momentum in non-sequential double ionization. Nat. Commun. **13**, 4706 (2022). arXiv:2111.10148
15. Argenti, L., et al.: ATTO 8th International Conference on Attosecond Science and Technology, UCF (2022)
16. Reimann, J., Schlauderer, S., Schmid, C., Langer, F., Baierl, S., Kokh, K., Tereshchenko, O., Kimura, A., Lange, C., Güdde, J., Höfer, U., Huber, R.: Subcycle observation of lightwave-driven Dirac currents in a topological surface band. Nature **562**, 396–400 (2018)
17. Krausz, F., Stockman, M.I.: Attosecond metrology: from electron capture to future signal processing. Nat. Phot. **8**, 205–213 (2014)

18. Hohenleutner, M., Langer, F., Schubert, O., Knorr, M., Huttner, U., Koch, S.W., Kira, M., Huber, R.: Real-time observation of interfering crystal electrons in high-harmonic generation. Nature **523**, 572–575 (2015)
19. Ghimire, S., Reis, D.A.: High-harmonic generation from solids. Nat. Phys. **15**, 10–16 (2019)
20. Bauer, D., Hansen, K.K.: High-harmonic generation in solids with and without topological edge states. Phys. Rev. Lett. **120**, 177401 (2018)
21. Jürß, C., Bauer, D.: High-harmonic generation in Su-Schrieffer-Heeger chains. Phys. Rev. B **99**, 195428 (2019)
22. Pattanayak, A., Pujari, S., Dixit, G.: Role of Majorana fermions in high-harmonic generation from Kitaev chain. Sci. Rep. **12**, 6722 (2022)
23. Silva, R.E.F., Jiménez-Galán, Á., Amorim, B., Smirnova, O., Ivanov, M.: Topological strong-field physics on sub-laser-cycle timescale. Nat. Phot. **13**, 849–854 (2019)
24. Haldane, F.D.M.: Model for a quantum Hall effect without Landau levels: condensed-matter realization of the 'parity anomaly'. Phys. Rev. Lett. **61**, 2015–2018 (1988)
25. Jiménez-Galán, Á., Silva, R.E.F., Smirnova, O., Ivanov, M.: Lightwave control of topological properties in 2D materials for sub-cycle and non-resonant valley manipulation. Nat. Phot. **14**, 728–732 (2020)
26. Chacón, A., Zhu, W., Kelly, S.P., Dauphin, A., Pisanty, E., Picón, A., Ticknor, C., Ciappina, M.F., Saxena, A., Lewenstein, M.: Circular dichroism in higher-order harmonic generation: Heralding topological phases and transitions in Chern insulators. Phys. Rev. B **102**, 134115 (2020). arXiv:1807.01616
27. Goulielmakis, E., Brabec, T.: High harmonic generation in condensed matter. Nat. Phot. **16**, 411–421 (2022)
28. Silva, R.E.F., Blinov, I.V., Rubtsov, A.N., Smirnova, O., Ivanov, M.: High-harmonic spectroscopy of ultrafast many-body dynamics in strongly correlated systems. Nat. Phot. **12**, 266–270 (2018)
29. Bionta, M.R., Haddad, E., Leblanc, A., Gruson, V., Lassonde, P., Ibrahim, H., Chaillou, J., Émond, N., Otto, M.R., Jiménez-Galán, Á., Silva, R.E.F., Ivanov, M., Siwick, B.J., Chaker, M., Légaré, F.: Tracking ultrafast solid-state dynamics using high harmonic spectroscopy. Phys. Rev. Res. **3**, 023250 (2021)
30. Valmispild, V., Gorelov, E., Eckstein, M., Lichtenstein, A., Aoki, H., Katsnelson, M., Ivanov, M., Smirnova, O.: Sub-cycle multidimensional spectroscopy of strongly correlated materials. arXiv:2208.04647 (2022)
31. Han, S., Ortmann, L., Kim, H., Kim, Y.W., Oka, T., Chacón, A., Doran, B., Ciappina, M.F., Lewenstein, M., Kim, S.-W., Kim, S., Landsman, A.S.: Extraction of higher-order nonlinear electronic response in solids using high harmonic generation. Nat. Commun. **10**, 3272 (2019). arXiv:1904.11103
32. Calafell, I.A., Rozema, L.A., Trenti, A., Bohn, J., Dias, E.J.C., Jenke, P.K., Menghrajani, K.S., Iranzo, D.A., García de Abajo, F.J., Koppens, F.H.L., Hendry, E., Walther, P.: High-harmonic generation enhancement with graphene heterostructures. Adv. Opt. Mater. (2022, in press)
33. Shao, C., Lu, H., Zhang, X., Yu, C., Tohyama, T., Lu, R.: High-harmonic generation approaching the quantum critical point of strongly correlated systems. Phys. Rev. Lett. **128**, 047401 (2022)
34. Cireasa, R., Boguslavskiy, A.E., Pons, B., Wong, M.C.H., Descamps, D., Petit, S., Ruf, H., Thiré, N., Ferré, A., Suarez, J., Higuet, J., Schmidt, B.E., Alharbi, A.F., Légaré, F., Blanchet, V., Fabre, B., Patchkovskii, S., Smirnova, O., Mairesse, Y., Bhardwaj, V.R.: Probing molecular chirality on a sub-femtosecond timescale. Nat. Phys. **11**, 654–658 (2015)
35. Ayuso, D., Ordonez, A.F., Smirnova, O.: Ultrafast chirality: the road to efficient chiral measurements. Phys. Chem. Chem. Phys. (2022, in press). arXiv:2203.00580
36. Ayuso, D., Neufeld, O., Ordonez, A.F., Decleva, P., Lerner, G., Cohen, O., Ivanov, M., Smirnova, O.: Synthetic chiral light for efficient control of chiral light–matter interaction. Nat. Phot. **13**, 866–871 (2019)
37. Ayuso, D., Ordonez, A.F., Decleva, P., Ivanov, M., Smirnova, O.: Enantio-sensitive unidirectional light bending. Nat. Commun. **12**, 3951 (2021)

38. Ayuso, D., Ordonez, A.F., Ivanov, M., Smirnova, O.: Ultrafast optical rotation in chiral molecules with ultrashort and tightly focused beams. Optica **8**, 1243 (2021)
39. Planas, X.B., Ordóñez, A., Lewenstein, M., Maxwell, A.S.: Strong-field chiral imaging with twisted photo-electrons. Phys. Rev. Lett. (2022, submitted). arXiv:2202.07289
40. Cavalieri, A.: Photo-induced superconductivity. Cont. Phys. **59**, 31/46 (2018)
41. McIver, J.W., Schulte, B., Stein, F.-U., Matsuyama, T., Jotzu, G., Meier, G., Cavalleri, A.: Light-induced anomalous Hall effect in graphene. Nat. Phys. **16**, 38–41 (2020)
42. Miller, T.A., Chhajlany, R.W., Tagliacozzo, L., Green, B., Kovalev, S., Prabhakaran, D., Lewenstein, M., Gensch, M., Wall, S.: Terahertz field control of in-plane orbital order in La0.5Sr1.5MnO4. Nat. Commun. **6**, 8175 (2015). arXiv:1506.01546
43. Julià-Farré, S., Dauphin, A., Chhajlany, R.W., Grochowski, P.T., Wall, S., Lewenstein, M., Grzybowski, P.R.: Nanoscale phase separation and pseudogap in the hole-doped cuprates from fluctuating Cu-O-Cu bonds. Phys. Rev. B **101**, 125107 (2020). arXiv:1909.02482
44. Pisanty, E., Jiménez, G., Vicuña-Hernández, V., Picón, A., Celi, A., Torres, J.P., Lewenstein, M.: Knotting fractional-order knots with the polarization state of light. Nat. Phot. **13**, 569–574 (2019). arXiv:1808.05193
45. Pisanty, E., Rego, L., San Román, J., Picón, A., Dorney, K.M., Kapteyn, H.C., Murnane, M.M., Plaja, L., Lewenstein, M., Hernández-García, C.: Conservation of torus-knot angular momentum in high-order harmonic generation. Phys. Rev. Lett. **122**, 203201 (2019). arXiv:1810.06503
46. Rego, L., Dorney, K.M., Brooks, N.J., Nguyen, Q., Liao, C.-T., San Román, J., Couch, D.E., Liu, A., Pisanty, E., Lewenstein, M., Plaja, L., Kapteyn, H.C., Murnane, M.M., Hernández-García, C.: Light with a self-torque: extreme-ultraviolet beams with time-varying orbital angular momentum (in arXiv: Light with a self-torque: extreme-ultraviolet beams with time-varying orbital angular momentum). Science **364**, 6447 (2019). arXiv:1901.10942
47. Mayer, N., Patchkovskii, S., Morales, F., Ivanov, M., Smirnova, O.: Imprinting chirality on atoms using synthetic chiral light. arXiv:2112.02658 (2021)
48. Lamprou, Th., Lopez-Martens, R., Haessler, S., Liontos, I., Kahaly, S., Rivera-Dean, J., Stammer, P., Pisanty, E., Ciappina, M.F., Lewenstein, M., Tzallas, P.: Quantum-optical spectrometry in relativistic laser-plasma interactions using the high-harmonic generation process: a proposal. Photonics **8**(6), 192 (2021). arXiv:2106.00372
49. Stammer, P.: Theory of entanglement and measurement in high harmonic generation. Phys. Rev. A **106**, L050402 (2022). arXiv:2203.04354
50. Rivera-Dean, J., Stammer, P., Maxwell, A.S., Lamprou, Th., Tzallas, P., Lewenstein, M., Ciappina, M.F.: Light-matter entanglement after above-threshold ionization processes in atoms. Phys. Rev. A **106**, 063705 (2022). arXiv:2208.05245
51. Amini, K., Biegert, J., Calegari, F., Chacón, A., Ciappina, M.F., Dauphin, A., Efimov, D.K., Figueira de Morisson Faria, C., Giergiel, K., Gniewek, P., Landsman, A.S., Lesiuk, M., Mandrysz, M., Maxwell, A.S., Moszyński, R., Ortmann, L., Pérez-Hernández, J.A., Picón, A., Pisanty, E., Prauzner-Bechcicki, J., Sacha, K., Suárez, N., Zaïr, A., Zakrzewski, J., Lewenstein, M.: Symphony on strong field approximation. Rep. Prog. Phys. **82**, 116001 (2019)
52. Vampa, G., McDonald, C.R., Orlando, G., Klug, D.D., Corkum, P.B., Brabec, T.: Theoretical analysis of high-harmonic generation in solids. Phys. Rev. Lett. **113**, 073901 (2014)
53. Tsatrafyllis, N., Kominis, I.K., Gonoskov, I.A., Tzallas, P.: High-order harmonics measured by the photon statistics of the infrared driving-field exiting the atomic medium. Nat. Commun. **8**, 15170 (2017)
54. Tsatrafyllis, N., Kühn, S., Dumergue, M., Foldi, P., Kahaly, S., Cormier, E., Gonoskov, I.A., Kiss, B., Varju, K., Varro, S., Tzallas, P.: Quantum optical signatures in a strong laser pulse after interaction with semiconductors. Phys. Rev. Lett. **122**, 193602 (2019)
55. Lvovsky, A.I., Raymer, M.G.: Continuous-variable optical quantum-state tomography. Rev. Mod. Phys. **81**, 299 (2009)
56. Breitenbach, G., Schiller, S., Mlynek, J.: Measurement of the quantum states of squeezed light. Nature **387**, 471 (1997)

57. Herman, G.T.: Image Reconstruction from Projections: The Fundamentals of Computerized Tomography. Academic Press, New York (1980)
58. Rivera-Dean, J., Stammer, P., Pisanty, E., Lamprou, Th., Tzallas, P., Lewenstein, M., Ciappina, M.F.: New schemes for creating large optical Schrodinger cat states using strong laser fields. J. Comput. Elecron. **20**, 2111 (2021). arXiv:2107.12811
59. Even Tzur, M., Gorlach, A., Birk, M., Rivera, N., Krüger, M., Kaminer, I., Cohen, O.: High harmonic generation driven by quantum light. In: ATTO 8th International Conference on Attosecond Science and Technology (Book of Abstracts), p. 88 (2022)
60. Weber, T., Giessen, H., Weckenbrock, M., Urbasch, G., Staudte, A., Spielberger, L., Jagutzki, O., Mergel, V., Vollmer, M., Dörner, R.: Correlated electron emis- sion in multiphoton double ionization. Nature **405**, 658–661 (2000)
61. Maxwell, A.S., Figueira de Morisson Faria, C.: Quantum interference in time-delayed nonsequential double ionization. Phys. Rev. A **92**, 023421 (2015)
62. Maxwell, A.S., Figueira de Morisson Faria, C.: Controlling below-threshold nonsequential double ionization via quantum interference. Phys. Rev. Lett. **116**, 143001 (2016)
63. Hao, X., Chen, J., Li, W., Wang, B., Wang, X., Becker, W.: Quantum effects in double ionization of argon below the threshold intensity. Phys. Rev. Lett. **112**, 073002 (2014)
64. Quan, W., Hao, X., Wang, Y., Chen, Y., Yu, S., Xu, S., Xiao, Z., Sun, R., Lai, X., Hu, S., Liu, M., Shu, Z., Wang, X., Li, W., Becker, W., Liu, X., Chen, J.: Quantum interference in laser-induced nonsequential double ionization. Phys. Rev. A **96**, 032511 (2017)
65. Maxwell, A.S., Armstrong, G.S.J., Ciappina, M.F., Pisanty, E., Kang, Y., Brown, A.C., Lewenstein, M., Figueira de Morisson Faria, C.: Manipulating twisted electrons in strong-field ionization. Faraday Discuss. **228**, 394–412 (2021). arXiv:2010.08355
66. Kang, Y., Pisanty, E., Ciappina, M., Lewenstein, M., Figueira de Morisson Faria, C., Maxwell, A.S.: Conservation laws for electron vortices in strong-field ionisation. Eur. Phys. J. D **75**, 199 (2021)
67. Pabst, S., Greenman, L., Ho, P.J., Mazziotti, D.A., Santra, R.: Decoherence in attosecond photoionization. Phys. Rev. Lett. **106**, 053003 (2011)
68. Arnold, C., Vendrell, O., Santra, R.: Electronic decoherence following photoionization: full quantum dynamical treatment of the influence of nuclear motion. Phys. Rev. A **95**, 033425 (2017)
69. Arnold, C., Lariviére-Loiselle, C., Khalili, K., Inhester, L., Welsch, R., Santra, R.: Molecular electronic decoherence following attosecond photoionisation. J. Phys. B **53**, 164006 (2020)
70. Lara-Astiaso, M., Ayuso, D., Tavernelli, I., Decleva, P., Palacios, A., Martín, F.: Decoherence, control and attosecond probing of XUV-induced charge migration in biomolecules. a theoretical outlook. Faraday Discuss. **194**, 41–59 (2016)
71. Vacher, M., Bearpark, M.J., Robb, M.A., Malhado, J.P.: Electron dynamics upon ionization of polyatomic molecules: coupling to quantum nuclear motion and decoherence. Phys. Rev. Lett. **118**, 083001 (2017)
72. Vrakking, M.J.J.: Control of attosecond entanglement and coherence. Phys. Rev. Lett. **126**, 113203 (2021)
73. Koll, L.-M., Maikowski, L., Drescher, L., Witting, T., Vrakking, M.J.J.: Experimental control of quantum-mechanical entanglement in an attosecond pump-probe experiment. Phys. Rev. Lett. **128**, 043201 (2022)
74. Busto, D., Laurell, H., Finkelstein-Shapiro, D., Alexandridi, C., Isinger, M., Nandi, S., Squibb, R.J., Turconi, M., Zhong, S., Arnold, C.L., Feifel, R., Gisselbrecht, M., Salières, P., Pullerits, T., Martín, F., Argenti, L., L'Huillier, A.: Probing electronic decoherence with high-resolution attosecond photoelectron interferometry. Eur. J. Phys. D **76**, 112 (2022)

Part II
Attosecond Spectroscopy of Atoms and Molecules

Dynamics via Attosecond Four-Wave Mixing

James D. Gaynor, Ashley P. Fidler, Yen-Cheng Lin, Nicolette G. Puskar, Daniel M. Neumark, and Stephen R. Leone

Abstract Attosecond four-wave mixing spectroscopy is a relatively new technique for studying ultrafast dynamics of highly excited states with exquisite temporal precision and spectral resolution. The attosecond four-wave mixing technique, as described in this paper, uses non-collinear beam geometries of one attosecond pulse together with two optical pulses to obtain background-free, spatially isolated emission signals in the extreme ultraviolet range that directly resolve coherent dynamics in the time domain. This method is advantageous by avoiding the strong spectral modulations that often complicate the interpretation of collinear attosecond transient absorption studies while also enabling greater control over the spatial and temporal characteristics of each light-matter interaction used to probe the ultrafast processes. This paper describes a broad range of attosecond four-wave mixing experiments performed in gas phase atoms and molecules, and a recent extension into solids.

Keywords Attosecond · Four wave mixing · Atomic and molecular dynamics

J. D. Gaynor
Department of Chemistry, Northwestern University, Evanston, IL, USA

A. P. Fidler
Department of Chemistry, University of California, Berkeley, CA, USA

Chemical Sciences Division, Lawrence Berkeley National Laboratory, Berkeley, CA, USA

Currently: Department of Chemistry, Princeton University, Princeton, NJ, USA

Y.-C. Lin · N. G. Puskar · D. M. Neumark
Department of Chemistry, University of California, Berkeley, CA, USA

S. R. Leone (✉)
Department of Chemistry, University of California, Berkeley, CA, USA

Chemical Sciences Division, Lawrence Berkeley National Laboratory, Berkeley, CA, USA

Department of Physics, University of California, Berkeley, CA, USA
e-mail: srl@berkeley.edu

L. Argenti et al. (eds.), *Proceedings of the 8th International Conference on Attosecond Science and Technology*, Springer Proceedings in Physics 300,
https://doi.org/10.1007/978-3-031-47938-0_5

1 Introduction

As the methods for generating light pulses of sub-femtosecond durations with broadband extreme ultraviolet (XUV) photon energies are becoming routinely achievable, exciting new uses of these pulses to investigate photophysical and photochemical processes have accelerated. Attosecond transient absorption (ATA) spectroscopy is widely used to study attosecond and femtosecond (fs) photochemical dynamics in atoms, molecules, and solids [1, 2]. While ATA spectroscopy has proven extremely valuable for monitoring ultrafast dynamics with simultaneous high temporal and spectral resolution, strong spectral modulations on-axis can obfuscate and overwhelm underlying temporal dynamics of interest [3–5]. Although the origin of the spectral modulations, such as AC Stark effects and Autler-Townes splittings, are interesting topics in their own right, it is also important to disentangle direct time-domain measurements of ultra-short lived coherent dephasing dynamics and highly excited state lifetimes. Attosecond Four-Wave Mixing (FWM) spectroscopy using a non-collinear geometry is realized as a method that circumvents the strongly modulated ATA spectral features measured on-axis, providing direct access to the lifetimes and coherent dynamics of highly excited states [6]. The development of attosecond FWM spectroscopy in the Leone and Neumark groups is detailed in this paper with emphasis on how technique developments have revealed new ways to measure chemical dynamics with increasing precision.

1.1 Attosecond Four-Wave Mixing (FWM) Spectroscopy

Attosecond FWM spectroscopy falls within a family of third order nonlinear spectroscopies used to probe the macroscopic polarization that is created in a sample following a series of three incident light-matter interactions. Many popular techniques within this class of experiments use pulses with photon energies in the ultraviolet, visible, infrared and terahertz regimes. The attosecond FWM technique combines one attosecond pulse with XUV photon energies (11–35 eV in the experiments discussed here) with two few-cycle near-infrared (NIR) pulses that have broadband spectra spanning the visible/NIR (1.25–2.25 eV) region. The third-order polarization of interest is the third term in the expansion:

$$P = \epsilon_0 \left(\chi^{(1)} E_1 + \chi^{(2)} E_1 E_2 + \chi^{(3)} E_1 E_2 E_3 + \cdots \right) \tag{1}$$

where the vacuum permittivity is given by ϵ_0, the nth order susceptibility is $\chi^{(n)}$, and each sequentially incident electric field is given by E_i (i = 1, 2, or 3 for third order processes). The attosecond FWM experiment uses various pulse sequences; here E_1 is taken to be an XUV attosecond pulse train or isolated attosecond pulse produced on a tabletop apparatus by high harmonic generation (HHG) – this pulse can come first, simultaneously, or last – and $E_{2,3}$ are sub-6 fs NIR pulses (see Fig. 1). The

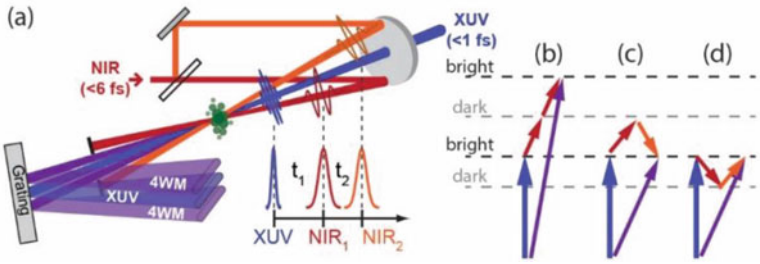

Fig. 1 Principle of Attosecond Four-Wave Mixing Spectroscopy. (**a**) Simplified experimental schematic of the beams overlapping at the sample; translation stages not shown in NIR beam path. Several wave-mixing pathways are shown in (**b**)–(**d**). The "ladder up" coupling scheme is shown in (**b**), the "Λ" coupling scheme is shown in (**c**), and the "V" coupling scheme is shown in (**d**)

FWM pulse sequence can be completed or initiated by two light-matter interactions from a single NIR pulse or two independently controlled and timed NIR pulses; several scenarios have been realized and are discussed below.

Similar to other nonlinear spectroscopies, a phase-matching condition due to momentum conservation of all three input wavevectors distinguishes the attosecond FWM signals of interest as a fourth XUV wave that is emitted. The attosecond FWM phase matching condition is

$$\mathbf{k}_{signal} = \mathbf{k}_{XUV} \pm \mathbf{k}_{NIR1} \pm \mathbf{k}_{NIR2} \tag{2}$$

where $\mathbf{k}_{\mathrm{XUV}}$ is the XUV wavevector and $\mathbf{k}_{\mathrm{NIR1}}$ ($\mathbf{k}_{\mathrm{NIR2}}$) specifies the first (second) NIR wavevector of the incident light-matter interactions. The phase matching condition may be satisfied by one NIR photon from each NIR laser beam, or by two NIR photons from one NIR laser beam. Three of the possible wavevector combinations shown in Fig. 1 produce different wave-mixing signals (e.g., $\mathbf{k}_{\mathrm{XUV}} + \mathbf{k}_{\mathrm{NIR1}} - \mathbf{k}_{\mathrm{NIR2}}$ known as "Λ-type" coupling, $\mathbf{k}_{\mathrm{XUV}} - \mathbf{k}_{\mathrm{NIR1}} + \mathbf{k}_{\mathrm{NIR2}}$ known as "V-type" coupling, and $\mathbf{k}_{\mathrm{XUV}} + \mathbf{k}_{\mathrm{NIR1}} + \mathbf{k}_{\mathrm{NIR2}}$ known as "ladder up" coupling, which can also be ladder down, not shown). In the fully non-collinear geometry, all three light matter interactions have distinct spatial components of the wavevector in the laboratory frame, giving rise to a background free, spatially-isolated signal. The XUV-NIR1 and XUV-NIR2 overlap angles (θ_1 and θ_2, respectively) can be separately controlled during the FWM signal emission, which is emitted at an angle $\theta_{\mathrm{emission}}$ expressed as

$$\theta_{emission} \approx \frac{\omega_{NIR1}\theta_1 + \omega_{NIR2}\theta_2}{\omega_{XUV}} \tag{3}$$

for the V-type and Λ-type pathways, with the photon frequencies of the incident photons specified as ω_{XUV}, ω_{NIR1}, and ω_{NIR2}. By controlling the relative timings of the three incident pulses, different types of FWM experiments can be performed to probe the evolution of different states. In what is referred to as a "bright state"

scan, the $\mathbf{k}_{XUV}$ pulse arrives first and $\mathbf{k}_{NIR1}$ and $\mathbf{k}_{NIR2}$ pulses occur simultaneous to each other while the delay between $\mathbf{k}_{XUV}$ and the two NIR interactions is scanned to measure the evolution of the XUV-bright states. In what is known as the "dark state" scan, the $\mathbf{k}_{XUV}$ and $\mathbf{k}_{NIR1}$ pulses are temporally coincident first, exciting XUV-dark states, which are scanned by the delay between the $\mathbf{k}_{NIR1}$ and $\mathbf{k}_{NIR2}$ pulses. In a transient grating mode, a spatial grating can be generated by two NIR pulses arriving first, for example, to create a grating composed of altered carrier densities in a solid.

The FWM apparatus for many of the experiments discussed here utilized a Femtopower Ti:sapphire laser (1 kHz repetition rate, 1.7 mJ, 22 fs, 780 nm center wavelength) with a hollow core fiber compressor and chirped mirrors to spectrally broaden and temporally compress the amplifier output down to pulses with <6 fs durations and a spectrum spanning 500–1000 nm. Typically ~70% of the beam is split off for the HHG process while the remaining portion is used to drive the NIR light matter interactions. The XUV pulses formed by HHG are optionally filtered using a thin metallic foil filter to remove the collinear NIR driving field before the XUV beam is focused to the sample area by a toroidal mirror. The other ~30% of the NIR beam not used for HHG is routed through piezo driven computer-controlled translation stages to adjust the relative time delay with respect to the XUV pulse. In the fully non-collinear geometry, this NIR beam is split again by a 50:50 beamsplitter to produce the $\mathbf{k}_{NIR1}$ and $\mathbf{k}_{NIR2}$ pulses. The NIR beams are spatially and temporally overlapped on the sample with $\mathbf{k}_{XUV}$ using an annular mirror to produce the FWM signals. A thin metallic foil filter is used after the sample to remove residual NIR scatter from the detector, the signals are spectrally dispersed by a grazing incidence concave XUV-grating onto a two-dimensional CCD camera to collect a spectrum. The vertical dimension is the angular divergence of the signal due to the wave vector matching, while the horizontal direction is the XUV spectrally resolved dimension. See references for specific experimental configurations used in each experiment.

2 Discovering Phase-Matched Wave-Mixing Signals with Attosecond XUV Pulses and Few-Cycle NIR Pulses

The initial observations of phase-matched attosecond FWM signals arose from an experimental configuration used for ATA spectroscopy on Ne atoms consisting of one NIR beam and one XUV beam in a collinear geometry [6]. Clear phase-matched wave-mixing signals from ladder-type upconversion pathways were revealed in this collinear experiment using selective XUV wavelength-filtering to suppress the 13th harmonic in the XUV beam. In a follow-up experiment, the first non-collinear geometry with one non-collinear NIR pulse was implemented in Ne, generating the first "off-axis" signal shown in Fig. 2a. Necessarily, the only signals detectable off-axis from $\mathbf{k}_{XUV}$ in this configuration were the ladder-type. Another non-collinear experiment was promptly done to begin exploring the new wave-mixing based

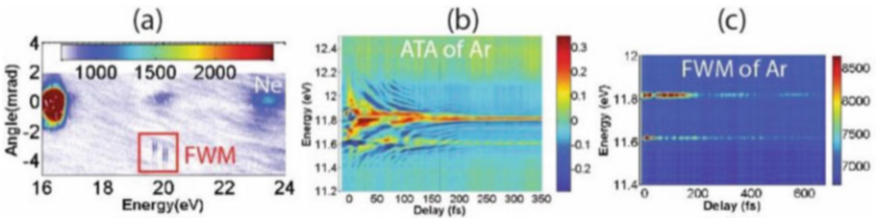

Fig. 2 Initial FWM demonstrations: Ne and Ar. (**a**) The off-axis FWM signal of Ne $2p^{-1}ns/nd$ coupled through ladder-type pathways is observed at −3 mrad. For comparison, the ATA signals of Ar $3p^{-1}ns/nd$ are shown in (**b**) and the off-axis FWM signals are shown in (**c**). (Reprinted with permission from [4], copyright 2016 by the American Physical Society)

spectroscopy [4]. Realizing the phase-matched wave-mixing signals enabled the disentanglement of complex transition pathways in highly excited states, generating deeper insight into coherent dynamics of gas phase atoms and molecules.

2.1 *Electronic and Vibronic Coherences in Atoms and Molecules*

Utilizing an attosecond pulse train in the 15–25 eV range, Cao et al. [6] found that once the $2s^22p^5$ $[^2P_{3/2,1/2}]3s/3s'$ states in Ne were excited near 16.8 eV, a two-NIR-photon transition could resonantly couple the XUV-excited states to the *ns/nd* states located around 20 eV. A coherent emission of XUV light was observed at −3 mrad divergence from the $\mathbf{k}_{XUV}$ beam, simultaneously imaged on the CCD and shown to be a phase-matched nonlinear signal over a range of Ne gas pressures, see Fig. 2a. Ladder coupling pathways ($\mathbf{k}_{XUV} + \mathbf{k}_{NIR1} + \mathbf{k}_{NIR1}$) drove the transition resonantly through XUV-dark 3p states. Notably, very strong oscillations were observed as the time delay between the XUV and NIR interactions was scanned. Two principal electronic coherences were identified for the bound electronic wavepacket, corresponding to a strong 3s/3s′ state spin-orbit splitting (~0.17 eV) and the weaker "which-way" interference of the one- and three-photon transition pathways (~3 eV) [6].

A rich and direct view of coherent dynamics was then measured by performing a similar experiment on the Ar $3s^23p^5[^2P_{3/2,1/2}]ns/nd$ states using 11–16 eV excitation, only now with a non-collinear NIR beam [4]. The comparison to on-axis ATA signals demonstrated the enhanced clarity of time-dependent signals in FWM (see Fig. 2b, c), avoiding the strong AC-Stark effect spectral modulations seen in ATA. The FWM signal complexity increased with two different ladder-coupled pathways observed above ($+\theta_{emission}$) and below ($-\theta_{emission}$) $\mathbf{k}_{XUV}$, corresponding to emission from the $3p^{-1}$ 4s/4s′ states and the $3p^{-1}$ 4d/4d′ and 5d/5d′ states, respectively, which resonantly coupled through dark 4p states. The 4s/4s′ emission in Fig. 2c comprises multiple coherent oscillation frequencies in the 0–0.5 eV range

representing the interference of many wave-mixing pathways initiated by launching the XUV wavepacket. Further control over the NIR-couplings was achieved by allowing the NIR pulse that is collinear with the XUV and drives the HHG process to provide one of the NIR interactions. This experimental adjustment enabled higher orders of diffraction (i.e., six-wave mixing) to be viewed and showed off-axis V- and Λ-couplings for the first time. Dynamics of very long-lived (>600 fs) 4p dark states were then accessible, capturing electronic coherences among the spin-orbit split 4p states.

To extend FWM to molecular dynamics investigations, the vibronic wavepacket dynamics of XUV-excited H_2 were measured [7]. A vibronic wavepacket was created by exciting the B′ and D states in addition to vibrational progressions supported in these states. The complex evolution of the wavepacket propagation was directly resolved by Fourier transform analysis of the ladder-type, Λ-type, and V-type coupling pathways. Many types of coherences are disentangled in this experiment, providing an in-depth tomographic perspective of complex wavepacket evolution involving multiple vibrations, electronic states, and truly vibronic coherences.

3 Increasing Resolution: Fully Non-Collinear Wave-Mixing

Implementing the collinear NIR field used for the HHG process to also serve as the $\mathbf{k}_{\mathrm{NIR1}}$ wavevector increased the versatility of attosecond FWM spectroscopy by enabling Λ- and V-type pathways to be measured off-axis. However, this geometry inherently restricts the timing control between $\mathbf{k}_{\mathrm{XUV}}$ and $\mathbf{k}_{\mathrm{NIR1}}$. Consequently, additional developments led to two independent NIR beamlines, each with temporal control, to maximally interrogate the generated nonlinear signals in space and time using a fully non-collinear beam geometry. These two NIR beams are experimentally recombined above and below the XUV beam in a vertically stacked fashion.

3.1 Exploring the Fully Non-Collinear Geometry

Similar to transient-grating spectroscopy, an attosecond FWM experiment having both NIR beams non-collinearly aligned with respect to the XUV pulse can be thought of as forming a grating during the phase-matching process. The parameter space of the temporal delays is a distinguishing factor for FWM from other transient-grating spectroscopies. The FWM signals of interest in many of the experiments considered here are those that use the grating as a ‘probe’ of the XUV-excited dynamics and deliberately scan each of the pulse delays to target dynamics of interest. The grating can also be written first, for future measurements, for example, of transient carrier dynamics in solids.

During temporal overlap of all three pulses and in the first few femtoseconds of the XUV-NIR time delay, Fidler et al. [8] showed that the grating formation in atomic He results in a time-dependence of the diffraction orders measured off-axis. Up to the third diffraction order – labeled m = −3, indicating eight-wave-mixing – was experimentally characterized and theoretically simulated for He 1s*np* resonances around 21.2 eV and nearby 3s-, 3d-, 4s-, and 2s + light-induced states. In this experiment, the two non-collinear NIR pulses were held at relative temporal overlap while the delay between the XUV pulse and the two NIR pulses was scanned. A delay-dependent emergence of FWM signals for increasing diffraction orders was observed while lower diffraction orders showed enhanced spectral shifting. Theoretical investigation of these phenomena using an AC Stark phase grating model attributed the effects to the diffraction orders accumulating AC Stark phase and lower orders formed more rapidly. Broadly, this showed that AC Stark effects can still influence spectral features in FWM spectra, especially for light-induced states.

The fully non-collinear geometry has proven fruitful for investigating complex molecular potential energy landscapes where relative timing of the light-matter interactions is key. As an example, Warrick et al. [9] were successful in mapping out the potential energy surface of the $a'' \, ^1\Sigma_g^+$ double-well dark state in N_2 using judicious timing of the NIR pulses in the FWM pulse sequence (see Fig. 3). An attosecond XUV pulse first excited the $b' \, ^1\Sigma_u^+$ valence state around 14 eV with an excess of vibrational quanta, launching a vibronic wave packet that propagated toward greater internuclear distances. The relative orientation of the b' and a'' potential energy surfaces are such that the b' Franck-Condon region overlaps with the inner well of the a'' dark state and the b' outer turning point overlaps with the second outer well of the a'' dark state; both wells are accessible with one NIR photon. To characterize the inner well of the a'' dark state, $\mathbf{k}_{XUV}$ and $\mathbf{k}_{NIR1}$ were held at temporal overlap while the delay between $\mathbf{k}_{NIR1}$ and $\mathbf{k}_{NIR2}$ was scanned. The observed coherences in the FWM signals identified a primary 0.267 eV oscillation

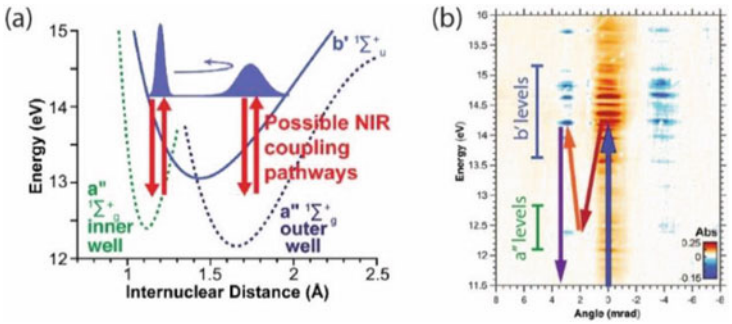

Fig. 3 Non-Collinear FWM in N_2. (**a**) A schematic potential of the bright b' state and the dark a' state probed selectively using the fully non-collinear FWM pulse sequence. (**b**) The CCD image of the FWM signal at time zero relating the bright and dark states

frequency, matching very well with known vibrational levels of the a′′ inner well dark state. By adjusting the $\mathbf{k}_{\mathrm{NIR1}}$ pulse to be delayed 25 fs from the b′ state excitation, corresponding to a half vibrational period of the b′ state, a substantially lower coherence frequency of 0.1 eV is observed while the 0.267 eV oscillations of the a′′ inner well are diminished. The a′′ outer well vibrational frequency agrees well with calculated values and is expected to be lower than the inner well due to extended internuclear separations. This is a salient example of where the background free FWM signal and fully controllable non-collinear beam geometry enabled a high resolution and temporally precise spectroscopic investigation of a complex excited state molecular dynamics.

3.2 *Direct Time-Domain Characterization of Highly Excited States*

Attosecond FWM spectroscopy can enable accurate time-domain lifetime measurements of highly excited states with very short lifetimes. The autoionizing $4s^2 4p^5 [^2P_{1/2}]$ *ns/nd* Rydberg states of Kr were studied with FWM spectroscopy by Fidler et al. [10] where the background-free signals were essential to accurately characterize the lifetimes. The autoionizing $4p^{-1}$*ns/nd* lifetime dynamics in the ATA measurement are dramatically overwhelmed with AC Stark induced spectral modulation, rendering the time-domain characterization nearly impossible. However, the off-axis FWM signals directly resolve the autoionization lifetimes unobscured by strong spectral modulations. Strong coherent oscillations are present in the FWM signals, reflecting the evolution of a Rydberg wavepacket excited with the attosecond XUV pulse. Despite these complex oscillations, the underlying decay dynamics were fitted for the $4s^{-1}[^2P_{1/2}]$6d, 7d, and 8d states as 22 ± 8 fs, 33 ± 6 fs, and 49 ± 6 fs, respectively, which agrees with frequency-domain linewidth data (see Fig. 4a). These *nd* states are also embedded in near degenerate *ns* states but are clearly separable in the time domain due to the *ns* states having picosecond lifetimes. These are the first short-lived lifetime measurements of atoms in the time-domain using attosecond FWM spectroscopy.

In systems with complex manifolds of near-degenerate excited states, direct time-domain measurements can be desirable to separate different excited state dynamics when spectral congestion renders linewidth measurements difficult. Additionally, when states undergo competing decay mechanisms, high temporal resolution measurements may be useful to investigate specific relaxation channels. An excellent example of this is in the Rydberg series converging to the O_2^+ $c\ ^4\Sigma_u^+$ state, which can decay both through predissociation of vibrational levels *via* tunneling and through autoionization. Lin et al. [11] used attosecond FWM spectroscopy to measure the 3s Rydberg state dynamics in this series for the $v = 0$ and $v = 1$ vibrational levels to be 5.8 ± 0.5 fs and 4.5 ± 0.7 fs, respectively (see Fig. 4b). The fully non-collinear beam geometry was crucial to the success of this experiment, as

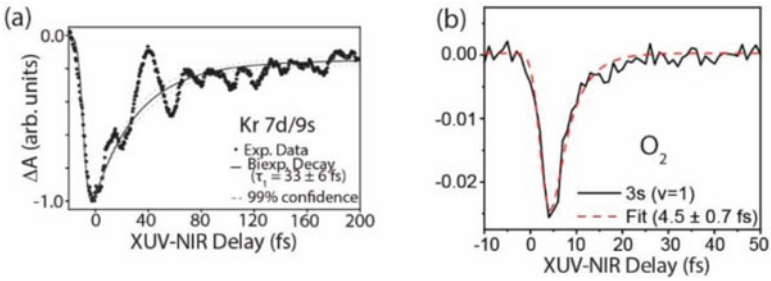

Fig. 4 Time-domain Lifetime Measurements with FWM. (**a**) The 33 ± 6 fs autoionization decay time of the Kr $4p^{-1}7d/9s$ resonance is accurately measured in the time-domain. (Reprinted from [10] with permission of AIP Publishing). (**b**) The v = 1 decay time of the O_2 3s Rydberg state measured as 4.5 ± 0.7 fs. (reproduced from [11] with permission from the Royal Society of Chemistry)

each of the two NIR beams required different overlap angles with the XUV beam to further separate FWM signals from Λ-type and ladder-type coupling pathways. With accompanying theoretical work, electron-nuclear couplings were identified as playing a major role in the relaxation of the O_2 3s Rydberg state. The more rapid decay of the v = 1 state was shown to be largely due to electronic autoionization, rather than due to different predissociation rates for v = 0 and v = 1. Interestingly, the autoionization rate was found to be very sensitive to the O-O internuclear distance, depending upon the vibrational level of the excited O_2 3s Rydberg state.

4 New Advancements: Techniques and Applications

The advantages of driving the FWM process resonantly with full temporal and spatial control over each light-matter interaction in the fully non-collinear geometry are clearly illustrated by the above examples. Namely, greater precision in the measurement is obtained to investigate the atomic or molecular response of interest. The advancements discussed below lay the foundations for FWM with phase-sensitivity using heterodyned detection and, in NIR-resonant cases, for gaining NIR-frequency specific FWM pathway information using pulse shaping methods. In addition to technical advancements, the application of attosecond FWM to exciton dynamics in solid state materials is opening new fields of inquiry.

4.1 Technique Developments

The background-free signals generated in the attosecond FWM experiment are homodyne-detected signals, meaning that the signals are detected without a ref-

erence field to provide phase-sensitive detection through interference. The intensity of the FWM signal is given by $|E_{signal}|^2$ where E_{signal} is the electric field of the background-free FWM emission. In the presence of a reference field, referred to as a "local oscillator", the interference of the signal field and the reference field produces cross terms that enable the relative phase of the signal field to be measured and provide signal enhancement. This detection scheme is often referred to as heterodyned detection. In attosecond FWM spectroscopy, an XUV-replica local oscillator is needed to perform a self-heterodyned detection scheme, which is widely used in other nonlinear spectroscopies in the optical and infrared regions. Such a scheme was demonstrated by Fidler et al. [12] on the FWM signals in 1s*nl* Rydberg states of He by deliberately optimizing the HHG process to favor an angularly diffuse $\mathbf{k}_{XUV}$ beam with a divergence of ~ ±2 mrad in the CCD imaging plane. The implementation of the self-heterodyned detection scheme allowed eight light-induced states to be observed in total, while the homodyned case could only detect one, showing the enhanced sensitivity of features with comparably small cross sections. Further improvement and implementations of heterodyned detection schemes in attosecond FWM spectroscopy will enable detailed electronic dynamics investigations in increasingly complex systems.

Multidimensional spectroscopies are widely implemented in the optical and infrared regions to give greater insight into photoexcited dynamics and photochemical pathways. These methods increase the spectral dimensionality of the measured signals by resolving the frequency dependence of multiple transitions in an experimental pulse sequence. In a key development, Marroux et al. [13] translated this methodology into the realm of attosecond XUV science by implementing a spatial light modulator into one of the NIR beamlines of the non-collinear FWM geometry. The NIR-frequency dependence of FWM pathways in the Ar $3s^2 3p^5$ [$^2P_{3/2,1/2}$] *ns/nd* excited states were mapped by using pulse sequences with narrowband (1.4–2.2 meV) amplitude and phase slices altered in the broadband NIR pulse bandwidth (Fig. 5a). The resulting two-dimensional XUV-NIR spectrum directly relates the relative energetic locations of the XUV-forbidden dark states with respect to the XUV emission from the FWM pathways. Coherent superpositions detected as quantum beats in the FWM emission from interfering pathways are also decomposable through this multidimensional method by selecting specific transition pathways to follow in a time-dependent manner. Moving forward, two-dimensional XUV-NIR spectroscopy holds promise for disentangling resonant wave-mixing phenomena in highly congested excited state manifolds to accurately characterize state-specific energies and lifetimes.

4.2 New Applications in Materials

With the success of the attosecond FWM technique in characterizing short-lived dynamics of highly excited states in gaseous atoms and molecules, this approach was recently extended to study highly localized "atomic-like" core-level excitons in solids. Gaynor et al. [14] used attosecond FWM spectroscopy to characterize the

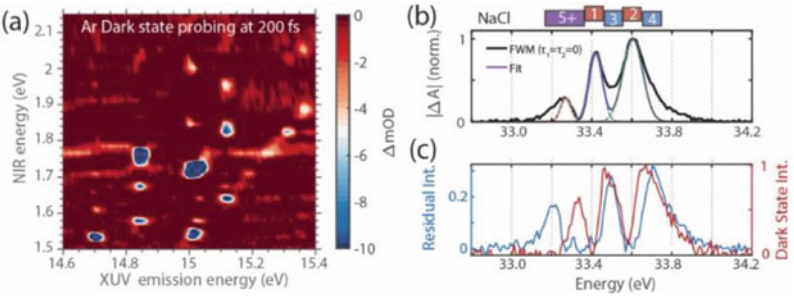

Fig. 5 Advancements in attosecond FWM spectroscopy. (**a**) The fully non-collinear FWM geometry enabled NIR-pulse-shaping based two-dimensional spectra, demonstrated by mapping out Ar $3p^{-1}np$ dark states. (Reproduced from [13] with permission from AAAS). (**b**, **c**) The deconvolution of the Na^+ $L_{2,3}$-edge spectrum for crystalline NaCl showing at least five core-excitons. (Reprinted with permission from [14], copyright 2021 by American Physical Society). (**b**) The time-zero FWM spectrum is fit to the three prominent bright core-excitons measured in the FWM bright state scan. (**c**) The residual of the fit identifies more core-excitons measured separately by the dark state scan

spectral and temporal dynamics of these core-level excitons localized on Na^+ in polycrystalline NaCl thin films. Here, an atomic-like Na^+ $2p^{-1}3s$ state is formed by XUV excitation around 33.5 eV where the 3s electron remains Coulombically bound with the core-level hole in the 2p level, forming the core-exciton. In this study, the inhomogeneous broadening of the Na^+ core-exciton spectrum was deconvolved, identifying at least five distinct core-exciton features that underlie the linear absorption, all of which were observed to decay on sub-10 fs timescales (Fig. 5b).

The physical relaxation mechanisms of the core-excitons were ascribed to electron-electron interactions due to the presence of many energetically overlapping core-excitons and ultrafast decay times that outpace the reported timescales of longitudinal-optical phonons and Auger decay in the literature. This study demonstrated that attosecond FWM spectroscopy can be a viable technique for studying ultrafast phenomena in materials, and it suggests that the atomic spectroscopic intuition applied to the gas phase FWM studies may also be productively applied to more complex materials systems.

5 On the Horizon

The simultaneous high-temporal precision and high spectral resolution afforded by the background-free signal generation of attosecond FWM spectroscopy makes it advantageous for studying ultrashort dynamics of highly excited states in atoms, molecules, and materials. Nearly all of the atomic and molecular attosecond FWM studies to-date have benefitted from NIR-resonant dark states for a resonantly enhanced wave-mixing pathway. The possibility for non-resonantly driven FWM

experiments is known at free electron laser experiments [15] and should be explored further. To understand the non-resonant effects of the FWM experiment better will help broaden the understanding and applications of the technique [16].

Future studies of core-excited state dynamics in small molecules will allow for unambiguous exploration of few-fs electronic and vibrational decay channels with more localized reporting from the element-specific core-level transitions accessed by higher photon energy attosecond light sources. Incorporating UV photon energies into the non-collinear wave-mixing pulses will enhance the background-free isolation of FWM signals and enable UV-resonant FWM pathways that can involve valence-level transitions in small organic molecules. In some cases, using an actinic pump pulse to photo-initiate a dynamical process of interest, which is then probed by the attosecond FWM pulse sequence, may prove particularly exciting. An example is where bond-length dependent electronic dynamics are approachable by triggering photodissociation or photoisomerization.

As the solid-state materials studies\enlargethispage*{12pt} using attosecond FWM are still very new, many directions in this research area are wide open and unexplored. Combining time-dependent theoretical simulations with attosecond FWM experiments is a difficult challenge but will be very helpful for the field. A systematic understanding of how localized excitations in solids form, evolve in time, and play a role in specific material properties – especially in correlated electronic behaviors and topological states – is an exciting potential research direction. On a fundamental level, attosecond FWM spectroscopy seems to be sensitive to atomically localized excitations. However, a comparison of dynamics measured by FWM to those dynamics measured by other means and interpreted in the typical delocalized band structure picture will be particularly instructive.

Acknowledgements The authors gratefully acknowledge group alumni for their contributions to the four-wave mixing laboratory: Wei Cao, Erika Warrick, Hugo Marroux, Etienne Bloch, Clare Keenan, Ruoyi Yin, and Max Schuchter. This work was performed by personnel and equipment supported by the Office of Science, Office of Basic Energy Sciences through the Atomic, Molecular and Optical Sciences Program of the Division of Chemical Sciences, Geosciences, and Biosciences of the U.S. Department of Energy under Contract No. DE-AC02-05CH11231. J.D.G. is grateful to the Arnold and Mabel Beckman Foundation for support as an Arnold O. Beckman Postdoctoral Fellow. A.P.F. acknowledges support from the N.S.F. Graduate Research Fellowship Program. Y-C.L. acknowledges financial support from the Taiwan Ministry of Education.

References

1. Geneaux, R., Marroux, H.J.B., Guggenmos, A., Neumark, D.M., Leone, S.R.: Transient absorption spectroscopy using high harmonic generation: A review of ultrafast X-ray dynamics in molecules and solids. Phil. Trans. R. Soc. A. **377**, 20170463 (2019)
2. Ramasesha, K., Leone, S.R., Neumark, D.M.: Real-time probing of electron dynamics using Attosecond time-resolved spectroscopy. Ann. Rev. Phys. Chem. **67**, 41–63 (2016)
3. Wu, M.X., Chen, S.H., Camp, S., Schafer, K.J., Gaarde, M.B.: Theory of strong-field attosecond transient absorption. J. Phys. B-At. Mol. Opt. **49**, 062003 (2016)

4. Cao, W., Warrick, E.R., Fidler, A., Neumark, D.M., Leone, S.R.: Noncollinear wave mixing of Attosecond XUV and few-cycle optical laser pulses in gas-phase atoms: Toward multidimensional spectroscopy involving XUV excitations. Phys. Rev. A. **94**, 053846 (2016)
5. Beck, A.R., Neumark, D.M., Leone, S.R.: Probing ultrafast dynamics with attosecond transient absorption. Chem. Phys. Lett. **624**, 119–130 (2015)
6. Cao, W., Warrick, E.R., Fidler, A., Leone, S.R., Neumark, D.M.: Near-resonant four-wave mixing of attosecond extreme-ultraviolet pulses with near-infrared pulses in neon: Detection of electronic coherences. Phys. Rev. A. **94**, 021802 (2016)
7. Cao, W., Warrick, E.R., Fidler, A., Leone, S.R., Neumark, D.M.: Excited-state Vibronic wavepacket dynamics in H_2 probed by XUV transient four-wave mixing. Phys. Rev. A. **97**, 023401 (2018)
8. Fidler, A.P., Camp, S.J., Warrick, E.R., Bloch, E., Marroux, H.J.B., Neumark, D.M., Schafer, K.J., et al.: Nonlinear XUV signal generation probed by transient grating spectroscopy with attosecond pulses. Nat. Commun. **10**, 1384 (2019)
9. Warrick, E.R., Fidler, A.P., Cao, W., Bloch, E., Neumark, D.M., Leone, S.R.: Multiple pulse coherent dynamics and wave packet control of the N_2 $a''\,{}^1\Sigma_g{}^+$ dark state by Attosecond four-wave mixing. Faraday Discuss. **212**, 157–174 (2018)
10. Fidler, A.P., Marroux, H.J.B., Warrick, E.R., Bloch, E., Cao, W., Leone, S.R., Neumark, D.M.: Autoionization dynamics of $(^2P^{1/2})ns/d$ states in krypton probed by noncollinear wave mixing with Attosecond extreme ultraviolet and few-cycle near infrared pulses. J. Chem. Phys. **151**, 114305 (2019)
11. Lin, Y-C., Fidler, A.P., Sandhu, A., Lucchese, R.R., McCurdy, C.W., Leone, S.R., Neumark, D.M.: Coupled nuclear–electronic decay dynamics of O2 inner valence excited states revealed by attosecond XUV wave-mixing spectroscopy. Faraday Discuss. **228**, 537–554 (2021)
12. Fidler, A.P., Warrick, E.R., Marroux, H.J.B., Bloch, E., Neumark, D.M., Leone, S.R.: Self-heterodyned detection of dressed state coherences in helium by noncollinear extreme ultraviolet wave mixing with attosecond pulses. J. Phys. Photo. **2**, 034003 (2020)
13. Marroux, H.J.B., Fidler, A.P., Neumark, D.M., Leone, S.R.: Multidimensional spectroscopy with attosecond extreme ultraviolet and shaped near-infrared pulses. Sci. Adv. **4**, eaau3783 (2018)
14. Gaynor, J.D., Fidler, A.P., Lin, Y-C., Chang, H.-T., Zuerch, M., Neumark, D.M., Leone, S.R.: Solid state core-exciton dynamics in NaCl observed by tabletop attosecond four-wave mixing spectroscopy. Phys. Rev. B. **103**, 245140 (2021)
15. Bohinc, R., Pamfilidis, G., Rehault, J., Radi, P., Milne, C., Szlachetko, J., Bencivenga, F., et al.: Nonlinear XUV-optical transient grating spectroscopy at the Si $L_{2,3}$ edge. Appl. Phys. Lett. **114**, 181101 (2019)
16. Gaynor, J.D., Fidler, A.P., Kobayashi, Y., Lin, Y-C., Keenan, C.L., Neumark, D.M., Leone, S.R.: Non-resonant coherent amplitude transfer in attosecond four-wave mixing spectroscopy. Phys. Rev. A. **107**(2), 023526 (2022)

Optical Control of Autoionizing States in Argon

S. Yanez-Pagans, C. Cariker, N. Harkema, M. Shaikh, L. Argenti, and A. Sandhu

Abstract We use tunable attosecond transient absorption to study the autoionizing polaritonic states in argon. Our approach provides new avenues for optical control of autoionization dynamics in polyelectronic systems. We highlight the stabilization of autoionizing states as a function of the detuning and time-delay of the dressing laser pulse. Furthermore, we use the relative polarization between the pump and probe pulses to control the branching of the polaritons, where the selection rules allow us to include or exclude specific states from the radiative coupling.

Keywords Autoionization · Optical control · Polaritons · Attosecond

1 Introduction

The study and control of autoionization is essential for understanding multi-electron interactions and the formation of ion-electron pairs in atomic and molecular systems. Extreme-ultraviolet (XUV) attosecond pulses are ideal to excite bright localized states above the ionization threshold, which decay to various ionization continua, and which are known as autoionizing states (AISs). In the photoionization

S. Yanez-Pagans · N. Harkema · M. Shaikh
Department of Physics, University of Arizona, Tucson, AZ, USA

C. Cariker
Department of Physics, University of Central Florida, Orlando, FL, USA

L. Argenti
Department of Physics, University of Central Florida, Orlando, FL, USA

CREOL, University of Central Florida, Orlando, FL, USA

A. Sandhu (✉)
Department of Physics, University of Arizona, Tucson, AZ, USA

College of Optical Sciences, University of Arizona, Tucson, AZ, USA
e-mail: asandhu@arizona.edu

L. Argenti et al. (eds.), *Proceedings of the 8th International Conference on Attosecond Science and Technology*, Springer Proceedings in Physics 300,
https://doi.org/10.1007/978-3-031-47938-0_6

spectrum, these states appear as resonances with asymmetric line shapes known as Fano profiles [1]. Polyelectronic atoms feature also dark AISs, which cannot be reached by means of one-photon transitions from the ground state due to dipole selection rules. In the presence of an infrared (IR) dressing-field, the dark states can also be populated thanks to the absorption of one XUV and multiple IR photons, giving rise to features in the XUV spectrum known as autoionizing light-induced states (ALISs). The same dressing field, furthermore, makes available to the bright AISs additional radiative decay channels to continua with different symmetry. The transiently bound electronic component of a bright AIS and of an ALIS are associated with a different number of dressing-field photons. If the laser parameters are chosen so that a bright AIS and an ALIS are nearly degenerate, these two states mix, giving rise to entangled light-matter states referred to as autoionizing polaritons (AIPs).

In this paper, we demonstrate XUV attosecond transient absorption with tunable infrared (IR) pulses as an ideal tool for resolving and modifying light-induced couplings between autoionizing continuum resonances in the argon atom. The frequency tunability of the dressing IR field (ω_{IR}) provides control over the formation and subsequent dynamics of AIPs. We show how the pump-probe time delay, the intensity, and the frequency of the dressing field play a role in the control and stabilization of the AIPs. The polarization of the laser field is investigated as another control knob that modifies the couplings between AIS, thanks to dipole selection rules, thus affecting the polaritonic branching. The experimental results are in excellent agreement with *ab initio* theoretical calculations carried out with the NewStock code [2] and open new avenues for applications of optical control of AISs, ALISs, and AIPs in polyelectronic systems.

The manuscript is organized as follows. Section 2 describes the experimental techniques used for our photoabsorption studies in argon. Section 3 provides information on our theoretical methods. In Sect. 4, we present our experimental and theoretical results for optical control of AIP dynamics. Finally, in Sect. 5, we summarize our findings and discuss future research avenues for characterizing and manipulating autoionization dynamics.

2 Experimental Setup

Our attosecond transient absorption setup employs XUV-IR pump-probe schemes and has been described in detail in [3].

Briefly, the experimental setup combines extreme-ultraviolet (XUV) attosecond pulse trains (APT) with strong-field infrared (IR) femtosecond pulses, as shown in Fig. 1. Initially, a Ti:sapphire laser amplifier is used to generate 790 nm, 2 mJ, 1 kHz near-infrared (NIR) pulses. The beam is subsequently divided into two arms of equal pulse energy (50%) with the aid of a beam splitter. The first beam path is used for high harmonic generation in xenon, to produce XUV attosecond pulse trains (APT). The second arm is redirected to an optical parametric amplifier (OPA), which allows us to tune the frequency of the NIR pulse from 1.57 eV to 0.73–1.03 eV.

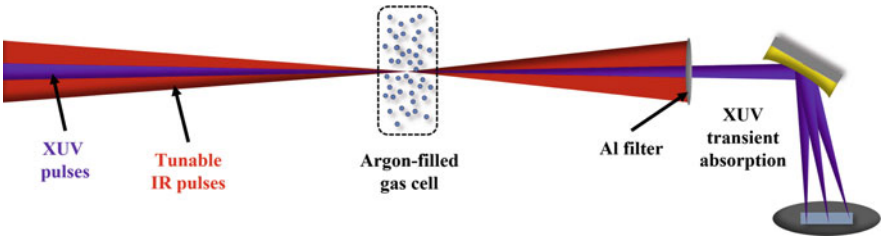

Fig. 1 Experimental setup for time-resolved photoabsorption studies. A tunable dressing-field provides control over different XUV-induced autoionizing dynamics of polaritons and electronic wave packets

The intensity of these tunable IR pulses is controlled by a half-wave plate and polarizer. In addition, a delay stage controls the relative time delay between the XUV APT and the IR pulses and a shutter allows us to isolate the IR contribution to the XUV spectrum. Finally, an annular mirror combines both the XUV and the IR beams into a gas cell for photoabsorption spectrometry. In the experiments reported here, the XUV APT excites the $3s^{-1}4p$ autoionizing state in argon, which can be subsequently coupled to other states by the tunable IR field.

3 Theoretical Simulations

To confirm and interpret the experiment, we conduct time-dependent *ab initio* simulations for an isolated argon atom, subject to the influence of external light pulses. For full details, see [2, 3]. To reproduce the single-ionization dynamics triggered in the argon atom by the experimental pulses, we build a close-coupling space that comprises the configurations obtained by coupling either the ground ($3p^{-1}$) or the first-excited ($3s^{-1}$) states of the Ar^+ ion to a set of single-particle states for the photoelectron. The states of the ion are computed at the multi-reference Hartree-Fock level (MRHF), using the ATSP2K package [4], whereas the states of the photoelectron are expanded in a spherical basis, with angular part given by spherical harmonics with orbital angular momentum up to $\ell_{\max} = 4$, and radial part given by a set of B-spline functions in a quantization box with radius $R_{\text{box}} = 500$ a.u. Furthermore, the configuration space comprises also all those states obtained by augmenting any of the configurations represented in the MRHF parent ion with any of the orbitals active in the parent-ion. The total field-free Hamiltonian H_0 is diagonalized in this basis, in the presence of a complex absorbtion potential (CAP), V_{CAP}, with support confined in a small radial layer next to the wall of the quantization box. This procedure ensures that any wavepacket built from the eigenstates of such complex Hamiltonian, $\tilde{H}_0 = H_0 + V_{\text{CAP}}$, is vanquished by the CAP before it has the opportunity of reaching the box boundary and give rise to unphysical reflections back to the origin. In particular, autoionizing states appear as eigenstates of the complex Hamiltonian, satisfying outgoing boundary conditions. This circumstance allows us to selectively

include in or exclude from the simulation any autoionizing state of the system, to ascertain their individual contribution to spectral features of interest. The use of a spectral basis for a complex Hamiltonian allows us also to eliminate from the basis a large number of states (as many as 99%) that do not appreciably affect the result of the observables of interest in our simulation, thus drastically accelerating the calculations. Starting from the ground state of the atom, the system is evolved under the influence of a sequence of external pulses, by integrating the time-dependent Schrödinger equation, $\Psi(t+dt) = U(t+dt,t)\Psi(t)$, where $U(t+dt,t) = \exp(-i\tilde{H}_0 dt/2)\exp\Big[-i\alpha A(t+dt/2)P_z\Big]\exp(-i\tilde{H}_0 dt/2)$ is a second-order split exponential propagator, α is the fine-structure constant, $A(t)$ is the vector potential of the radiation field, and P_z is the z component of the total canonical electronic momentum. From the expectation value of the dipole operator as a function of time, $p_z(t) = \langle\Psi(t)|P_z|\Psi(t)\rangle$, we extract the spectral response and the transient absorption spectrum of the atom, $\sigma = -\frac{4\pi}{\omega}\,\mathrm{Im}\left(\tilde{p}(\omega)/\tilde{A}(\omega)\right)$, where $\tilde{f}(\omega) = \int_{-\infty}^{\infty} dt\, e^{i\omega t} f(t)$ is a Fourier Transform. Figure 2 shows the single-atom XUV absorption spectrum of argon, in the vicinity of the $3s^{-1}4p$ bright resonance, in the presence of an IR dressing pulse with duration ~ 45 fs, as a function of the XUV-pump IR-probe delay, for several choices of the laser central frequency and peak intensity.

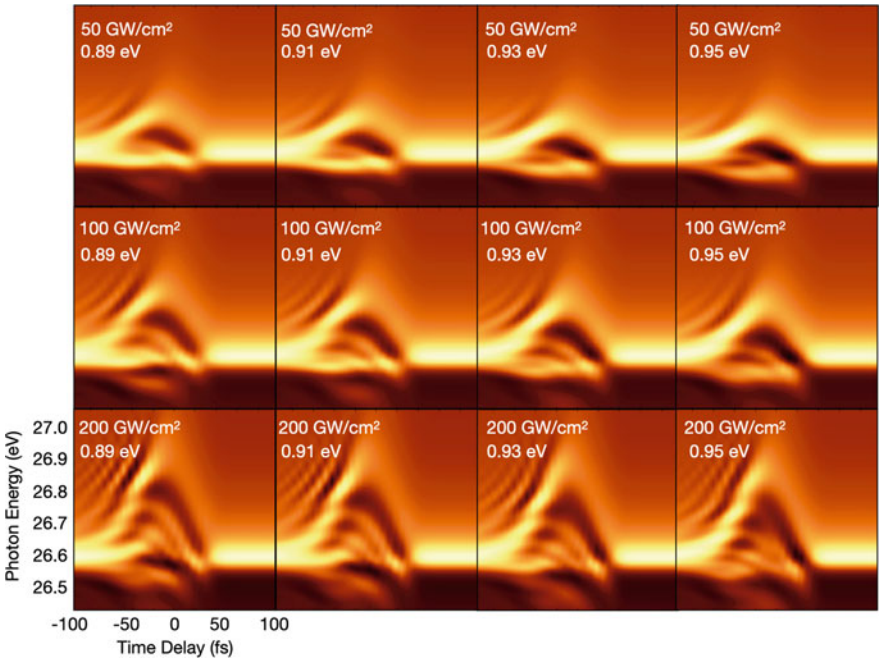

Fig. 2 ATAS simulated spectrum in the proximity of the $3s^{-1}4p$ resonance, illustrating the profile of the polaritons as a function of the pump-probe delay, for several values of the intensity and frequency of the dressing lasers

As the intensity increases, the resonance features split into two or more components, whose position, width, and relative contrast is altered by the IR frequency. As discussed below, these features illustrate the radiative coupling between multiple autoionizing states of several different symmetries ($^1S^e$, $^1P^o$, $^1D^e$, and $^1F^o$).

4 Optical Control of Autoionizing Polaritons

Figure 3 shows the formation of AIPs in the continuum. These structures arise from the near-resonant interaction between bright ($|\alpha\rangle$) and dark ($|\beta\rangle$) AISs in the presence of a strong IR dressing field. The degeneracy between the bright AIS and the ALISs of the nearby dark states leads to a change of the electronic structure, which can be described in terms of entangled light-matter states, termed polaritons [2].

In the case of one AIS interacting with one ALIS, as highlighted in Fig. 3, two polaritonic branches result. Each polariton is a superposition of two components, and can decay either through autoionization (AI) or radiative-ionization (RI). In AI, the number of photons does not change, whereas RI is accompanied by the stimulated emission or absorption of one photon. The interference between these different decay pathways to a same continuum can modulate the linewidth and hence the lifetime of the state. In particular, a destructive interference can lead to stabilization against autoionization, as demonstrated in [2].

Our photoabsorption experiment uses the 17th harmonic of the XUV APT to excite the ground state population of argon to the $3s^{-1}4p$ bright AIS. The IR dressing field can be tuned to couple the aforementioned state to the $3s^{-1}3d$ (27.51 eV), $3s^{-1}5s$ (27.55 eV), or $3s^{-1}4f$ (~28.31 eV) dark states through one- and two-photon transitions. Stated otherwise, the ALISs of these dark states can be tuned to be degenerate with the $3s^{-1}4p$ bright state using the tunability of IR photons in our setup. Near resonance, different AIP multiplets emerge in the photoabsorption spectra. To clearly observe these AIPs, we compare the photoabsorption spectrum

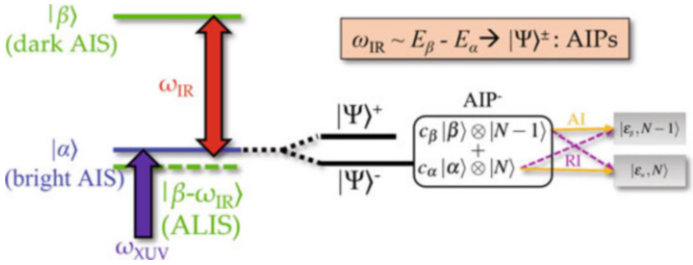

Fig. 3 Schematic representation of AIP formation and subsequent decay pathways. Near resonance, the degeneracy of between a bright ($|\alpha\rangle$) AIS and an ALIS ($|\beta - \omega_{IR}\rangle$) leads to AIP multiplets, which then decay through autoionization and radiative ionization. Destructive interference between these pathways can lead to stabilization of the atom against ionization

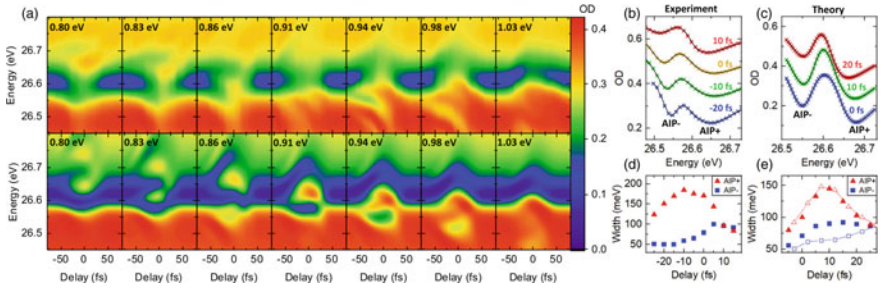

Fig. 4 (**a**) Experimental (top) and theoretical (bottom) XUV photoabsorption in the vicinity of argon $3s^{-1}4p$ AIS, as a function of the IR pulse delay, for several values of IR photon energy. Color map represents the OD. Positive delay implies IR pulse arrives before XUV. Interaction of AISs with ALISs gives rise to the polariton splitting prominently visible between 0.86 and 0.98 eV IR photon energy. Experimental (**b**) and theoretical (**c**) polaritonic line shapes for the near resonant case of 0.94 eV IR energy, for several time delays. In the absence of interference between radiative and Auger channels, the two polaritons are expected to have comparable widths. Stabilization is evidenced by the delay-dependent reduction of AIP− width and marked difference between the AIP± widths in both experiment (**d**) and theory (**e**). Open symbols are for 0.93 eV case [Reused with permission, Fig. 2 in doi.org/10.1103/PhysRevLett.127.023202]

of the IR-dressed medium, $I_{\mathrm{XUV+IR}}(\omega;\tau)$, with the spectrum of the incident XUV radiation, $I_{\mathrm{ref}}(\omega)$, expressing our results in terms of the absolute optical density (OD), $\mathrm{OD}(\omega;\tau) = -\log_{10}[I_{\mathrm{XUV+IR}}(\omega;\tau)/I_{\mathrm{ref}}(\omega)]$, where $\tau = t_{\mathrm{XUV}} - t_{\mathrm{IR}}$ is the delay between the XUV and the IR pulses ($\tau < 0$ if the IR pulse follows the XUV pulse). Negative values of the OD indicate transparency windows associated to different states in the continuum.

In our earlier work [2], we employed this tunable attosecond transient to explore the impact of different dressing-field parameters (frequency, intensity, and time delay) on the AIP dynamics. Our investigations demonstrated the AIP stabilization through the coherent interference of the AI and RI pathways [2], thus experimentally confirming an effect that was predicted several decades ago [5].

In Fig. 4a, each column corresponds to different ω_{IR} values, showing how the AIP structure changes as different ALISs come into resonance with the $3s^{-1}4p$ AIS. For each ω_{IR} value, the top panels show the experimental results and bottom panels show the ab-initio theoretical results. At large detuning, we only observe an energy shift in the $3s^{-1}4p$ absorption line, which is upward (downward) when the ALIS lies below (above) the $3s^{-1}4p$ AIS. In the near resonance condition (∼0.94 eV), we observe the splitting of the $3s^{-1}4p$ AIS in two AIPs around zero time delay. The lower branch has noticeably smaller width than the upper branch indicating stabilization against autoionization.

Next, we explored the intensity dependence of the polaritonic widths by using time-delay as a proxy for the instantaneous field strength. The experimental and theoretical results of delay-dependence of Fano profiles of AIP window resonances are shown in the energy line outs plotted in Fig. 4b and c, respectively. We extracted the width of these resonances and plotted them in Fig. 4d and e for experiment

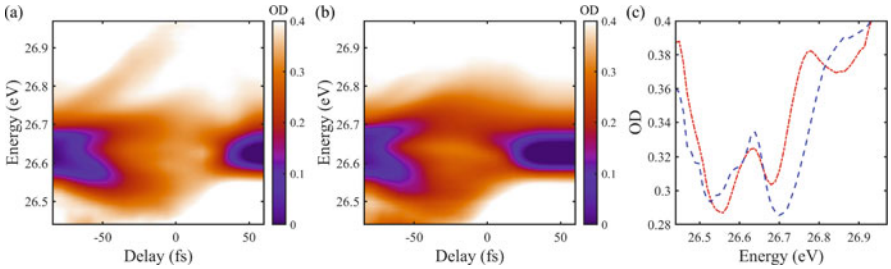

Fig. 5 AIP spectrograms corresponding to (**a**) parallel and (**b**) perpendicular dressing-field polarizations. Here the IR frequency is held fixed at 0.85 eV and with a beam intensity of $\sim$150 GW/cm^2. (**c**) OD line-outs at $\tau = -30$ fs corresponding to panels (**a**) and (**b**). When the XUV and IR polarizations are perpendicular to each other (blue line), fewer AIP branches are observed in comparison to the parallel case (red line)

and theory. As we move from positive time delays towards zero, we see a clear divergence in polaritonic widths with upper branch getting broader and lower branch getting narrower.

The analysis in terms of two polaritonic branches resulting from the interaction of two AISs is somewhat simplistic, and the presence of other couplings limits the degree of control we can exert. In particular, the region above $\omega_{\mathrm{IR}} > 0.90$ eV is governed by one-photon couplings (3d and 5s) whereas $\omega_{\mathrm{IR}} < 0.90$ eV exhibits a significant contribution of two-photon couplings, corresponding to the $3s^{-1}4f$ AIS. The radiative coupling between multiple AIS leads to the formation of polariton multiplets near time-delay zero. In a recent work, we discussed the important role of intermediate resonances in such two-photon AIP formation [3].

All these investigations only considered the case in which both the XUV APT and the IR dressing field have relative parallel polarizations. Here we explore the role of the dressing field polarization as an additional knob to control AIP structure and dynamics. Figure 5a and b shows spectrograms in the vicinity of the $3s^{-1}4p$ AIS for IR field polarization parallel and perpendicular to the XUV polarization, respectively. The IR frequency is held fixed at 0.85 eV and with a beam intensity of $\sim$150 GW/cm^2. Our results show a remarkable difference in AIP structure, especially in terms of the number of branches. We observe that, when the IR polarization is parallel, three AIP branches are clearly visible in the photoabsorption spectrum. Conversely, when the dressing field polarization is perpendicular, the AIP feature around 26.85 eV disappears, and we see only two observable branches. We emphasize this point by taking lineouts near $\tau \sim 0$. in Fig. 5c.

We attribute this difference in polaritonic structure to the ${}^1P^o - {}^1S^e$ coupling vanishing in the case of perpendicular polarization. Indeed, if we take the polarization of the XUV pulse to define the quantization axis, $\hat{z}$, then the exchange of an IR photon can only take place between states whose magnetic quantum number m_ℓ differ by ± 1. The absorption of an XUV photon from the ground state, populates ${}^1P^o$ states with $m_\ell = 0$, which are coupled, by means of one-photon transitions, only to the ${}^1D^e$ states with $m = \pm 1$ (there are no metastable ${}^1P^e$ states in the energy region under consideration). Figure 5a shows a renormalized basis consisting of the $4p$,

$3d$, and $5s$ states, and Fig. 5b pertains to only $4p$ and $3d$ states. This comparison demonstrates yet another form of optical control, one which allows the selection of polaritonic branches.

5 Concluding Remarks

Tunable ATA provides unique insight into the effects the frequency, intensity, and time-delay of a dressing field have on the creation and evolution of AIPs multiplets. Our observations suggest a dynamic control over the AIPs by the laser field, and demonstrate stabilization of the autoionizing states. We used the polarization of IR field as another parameter to control the electron couplings, which in turn determines the number of polaritonic branches observed in our data. In conclusion, the light-induced stabilization and branching of metastable states offers new opportunities for coherent control in the continuum.

Acknowledgments This work was supported by the U.S. Department of Energy, Office of Science, Basic Energy Sciences Award #DE-SC0018251. LA and SM acknowledge support from the NSF Theoretical AMO grants N 1607588 and N 1912507, as well as computer time at UCF Advanced Research Computing Center.

References

1. Fano, U.: Effects of configuration interaction on intensities and phase shifts. Phys. Rev. **124**(6), 1866–1878 (1961)
2. Harkema, N., Cariker, C., Lindroth, E., Argenti, L., Sandhu, A.: Autoionizing polaritons in attosecond atomic ionization. Phys. Rev. Lett. **127**, 023202 (2021)
3. Yanez-Pagans, S., Cariker, C., Shaikh, M., Argenti, L., Sandhu, A.: Multipolariton control in attosecond transient absorption of autoionizing states. Phys. Rev. A **105**, 063107 (2022)
4. Jonsson, T., Froese-Fischer, C., Brage, C.: Computational Atomic Structure. IOP Publishing, Philadelphia (1997)
5. Lambropoulos, P., Zoller, P.: Autoionizing states in strong laser fields. Phys. Rev. A **24**, 379–397 (1981)

Retrieving a Complex Molecular Structure from Laser-Induced Electron Diffraction Using Machine Learning

Xinyao Liu, Kasra Amini, Aurelien Sanchez, Blanca Belsa, Tobias Steinle, Katharina Chirvi, and Jens Biegert

Abstract We image the structure of the complex chiral molecule Fenchone ($C_{10}H_{16}O$) from laser-induced electron diffraction data by applying a machine learning algorithm with a convolutional neural network (CNN).

Keywords Laser-induced electron diffraction · Machine learning · Complex molecule · Structural retrieval

1 Introduction

Imaging ultrafast molecular dynamics addresses fundamental science, which helps us understand chemical reactions' basics. Laser-induced electron diffraction (LIED) [1] is a powerful laser-based imaging method that has the ability to image the three-dimensional structure of a single gas-phase molecule with combined sub-atomic picometre and femtosecond spatiotemporal resolution [2]. Taking snapshots of molecular dynamics via the LIED technique gives an inside into the intertwining of molecules, how they react, change, break or bend.

However, retrieving complex molecular structures from diffraction patterns is challenging. As the structural complexity increases, it becomes more challenging to identify the extremum with current retrieval algorithms, and therefore they are still limited to few-atom molecular systems [3].

X. Liu · K. Amini · A. Sanchez · B. Belsa · T. Steinle · K. Chirvi
ICFO – Institut de Ciencies Fotoniques, The Barcelona Institute of Science and Technology, Barcelona, Spain
e-mail: Katharina.Chirvi@icfo.eu

J. Biegert (✉)
ICFO – Institut de Ciencies Fotoniques, The Barcelona Institute of Science and Technology, Barcelona, Spain

ICREA, Barcelona, Spain
e-mail: jens.biegert@icfo.eu

L. Argenti et al. (eds.), *Proceedings of the 8th International Conference on Attosecond Science and Technology*, Springer Proceedings in Physics 300,
https://doi.org/10.1007/978-3-031-47938-0_7

A machine learning (ML) algorithm is fully capable of solving these difficulties based on its ability to consider multiple degrees of freedom simultaneously. Based on an ML-LIED framework, we demonstrate the accurate retrieval of a large and complex molecule's three-dimensional (3D) structure.

2 ML Algorithm

Our ML algorithm utilizes a convolutional neural network (CNN). It will be trained to find the relationship between a molecular structure and its molecular interference signal from the two-dimensional differential cross-section maps 2D-DCS. The DCS contains the fingerprints of the internuclear distance of atoms of the molecule and is used as the algorithm's input data. Using a convolutional neural network, we take advantage of its ability for image recognition. Here, the convolution of the 2D-DCS maps with different filters enhances at first subtle features of the maps providing a collection of feature maps (Fig. 1a). Subsequently, the feature maps pass through the fully connected neural network by multiplying the weights between each neuron to predict the atomic position in the molecule (Fig. 2b).

For training the ML algorithm, we first generated a database containing thousands of molecular structures spanning possible geometries. We calculated the

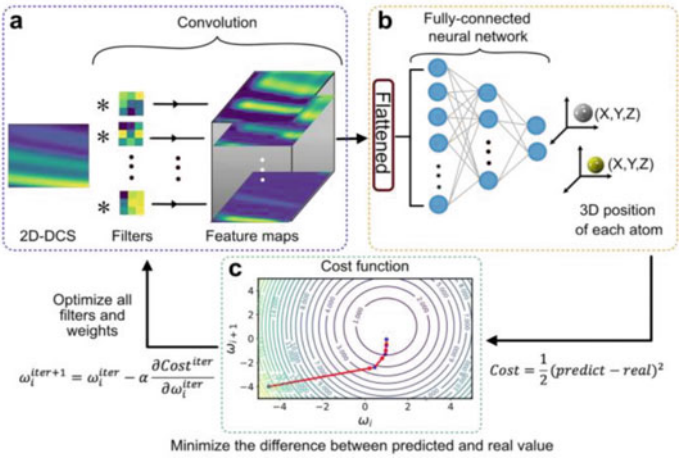

Fig. 1 (**a**) Subtle features of the 2D-DCS are enhanced by different filters. (**b**) The generated feature maps are flattened to a 1D array and passed through the fully-connected neural network to predict the atomic position in the molecule. (**c**) A schematic contour plot of the used cost function for two neuron weights (ωi and ωi + 1). The blue dots symbolize the cost function value, and the red arrows indicate the direction of the gradient of the cost function. The cost function is minimized during the five iterations

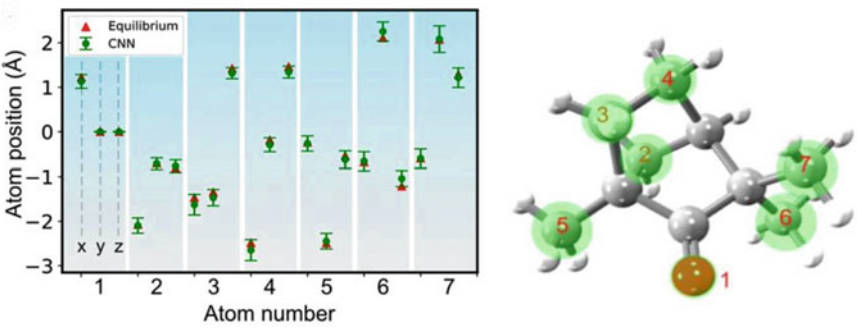

Fig. 2 3D Cartesian coordinates (*x, y, z*) for seven atoms in (+)-fenchone are predicted by the CNN (green circles). ML-LIED-measured (+)-fenchone structure shows only slighty deviates from the equilibrium ground-state neutral molecular structure (red triangle). The schematic of the predicted 3D molecular structure is presented on the right. Here, the green circles indicate the area of uncertainty

corresponding 2D-DCS map for each structure by simulating the elastic scattering of electrons on the molecule using the independent atom model (IAM).

The database is split into training, validation, and test sets to validate the ML model. To evaluate the model's accuracy during training, we define the absolute difference between the predicted and actual atom position (mean absolute error MAE) as our prediction error.

Once the ML model is satisfactorily trained, the experimental 2D-DCS map is used as an input to generate the predicted molecular structure that most likely contributes to the measured interference signal [4].

3 Extracting Molecular Structure

Before we use our ML framework to retrieve the molecular structure of a complex molecule, we firstly exam the ML model accuracy by revisiting published experimental LIED data of a small linear 1D molecule acetylene (C_2H_2) [5] and a planar 2D molecule carbon disulfide (CS_2) [6]. Table 1 summarizes the ML predicted structural parameters of the C_2H_2 and CS_2 molecules. The predicted structures agree

Table 1 Summary of C2H2 and CS2 structures predicted by machine learning (ML)

Molecule	Parameter	Equilibrium	QRS	ML
C2H2	R_{CC}(Å)	1.20 [7]	1.24 ± 0.04 [5]	1.23 ± 0.11
CS2	R_{CH}(Å)	1.06 [7]	1.10 ± 0.03 [5]	1.08 ± 0.03
	R_{CS} (Å)	1.55 [8]	1.86 ± 0.23 [6]	1.87 ± 0.14
	θ_{SCS}(°)	180 [8]	104.0 ± 20.2 [6]	104.7 ± 6.4

nicely with previous publications where the structure was extracted from the LIED data by a standard fitting routine.

Then, we use our ML framework to study the configuration of a (+)-fenchone ($C_{10}H_{16}O$; 27 atoms) molecule which experimental 2D-DCS map is also determined with LIED. Retrieving the structure of such a complex molecule by using a standard fitting routine would require an unrealistic calculation time. For example, a calculation time of 1.4e+9 h would be needed to calculate only five variations of its possible structures. ML has the decisive advantage of interpolating and learning between the course grids of precalculated molecular geometries. Thus, we can sufficiently create an interpolated database that only considers the variation of four groups of atoms and a molecule-wide global change in structure. Let the machine itself interpolate the relationship between the molecular structures and corresponding 2D-DCSs with a reduced database, drastically minimizing computational time. Observing the MAE converges to a constant value of ~0.02 involved with the training and validation data sets, we verify that the model is not over/underfitting and is satisfactorily trained. Furthermore, the Pearson correlation coefficient is found to be 0.94, confirming the strong correlation between the experimental and predicted theoretical 2D-DCS.

Figure 2 shows the predicted 3D Cartesian coordinates (*x, y, z*) for seven atoms in (+)-fenchone that are retrieved from the experimental data by the ML model (green circles). The error bars included the predicted model error as well as the experimental statistical error. The equilibrium ground-state 3D positions of neutral (+)-fenchone are presented by red triangles. The slight deviation of the ML-LIED measured, and the equilibrium ground-state molecular structure is caused involuntarily by the LIED laser field. In addition, the schematic of the predicted 3D (+)-fenchone molecule is also shown. Here, the green circles indicate the degree of uncertainty.

4 Summary

We implement ML-LIED to retrieve atomic positions of 1D, 2D, and complex 3D molecules with picometer and attosecond resolution. The ML-based framework achieves high-accuracy pattern matching in complex solution spaces while overcoming scaling limitations in a standard fitting routine. Not just LIED, the problem of unfavorable scaling also arises with other diffraction methods. Combining ML with LIED offers a new general solution to overcome long-standing problems and opens up new opportunities to image the structure of large, complex molecules.

References

1. Zuo, T., Bandrauk, A.D., P.B.: Corkum "laser-induced electron diffraction: a new tool for probing ultrafast molecular dynamics". Chem. Phys. Lett. **259**, 313 (1996)
2. Sanchez, A., et al.: Molecular structure retrieval directly from laboratory-frame photoelectron spectra in laser-induced electron diffraction. Nat. Commun. **12**, 1520 (2021)
3. Sanchez-Gonzalez, A., et al.: Accurate prediction of X-ray pulse properties from a free-electron laser using machine learning. Nat. Commun. **8**, 15461 (2017)
4. Liu, X., et al.: Machine learning for laser-induced electron diffraction imaging of molecular structures. Comm. Chem. **4**, 154 (2021)
5. Pullen, M.G., et al.: Imaging an aligned polyatomic molecule with laserinduced electron diffraction. Nat. Commun. **6**, 7262 (2015)
6. Amini, K., et al.: Imaging the Renner–Teller effect using laser-induced electron diffraction. Proc. Natl. Acad. Sci. U. S. A. **116**, 8173–8177 (2019)
7. Dalton, D.R.: Foundations of Organic Chemistry: Unity and Diversity of Structures, Pathways, and Reactions. Wiley (2020)
8. Herzberg, G.: Molecular Spectra and Molecular Structure III: Electronic Spectra and Electronic Structure of Polyatomic Molecules. D. Van Nostrand, New York (1966)

Imaging Ultrafast Dissociation Dynamics: OCS & Roaming in Formaldehyde

Tomoyuki Endo, Simon P. Neville, Karl Michael Ziems, Philippe Lassonde, Chen Qu, Bruno E. Schmidt, Hikaru Fujise, Mizuho Fushitani, Akiyoshi Hishikawa, Stefanie Gräfe, Paul L. Houston, Joel M. Bowman, Michael S. Schuurman, François Légaré, and Heide Ibrahim

Abstract Upon photoexcitation, molecules break apart, following different dissociation reactions. We can image these dissociation pathways using Coulomb explosion imaging (CEI) and sometimes we can control them using asymmetric laser fields. In the formaldehyde molecule, we can see fragments following the direct, conventional dissociation path, as well as fragments deviating from this minimum energy path. So-called roaming fragments or "roamers" explore the potential energy landscape in a statistical manner and could be directly captured in real-time, despite the signal's statistical character. This is possible due to the single-molecule sensitivity of CEI and we could show that the onset of roaming occurs actually several orders of

T. Endo
Advanced Laser Light Source (ALLS) at Institut national de la recherche scientifique, Varennes, QC, Canada

Kansai Photon Science Institute, National Institutes for Quantum Science & Technology, Kyoto, Japan

S. P. Neville
National Research Council Canada, Ottawa, ON, Canada

K. M. Ziems · S. Gräfe
Institute of Physical Chemistry and Abbe Center of Photonics, Friedrich Schiller University and Max Planck School of Photonics, Jena, Germany

P. Lassonde · F. Légaré · H. Ibrahim (✉)
Advanced Laser Light Source (ALLS) at Institut national de la recherche scientifique, Varennes, QC, Canada
e-mail: heide.ibrahim@inrs.ca

C. Qu
Department of Chemistry & Biochemistry, University of Maryland, College Park, MD, USA

B. E. Schmidt
Few-Cycle Inc, Varennes, QC, Canada

H. Fujise
Chemistry Department, Graduate School of Science, Nagoya University, Aichi, Japan

L. Argenti et al. (eds.), *Proceedings of the 8th International Conference on Attosecond Science and Technology*, Springer Proceedings in Physics 300,
https://doi.org/10.1007/978-3-031-47938-0_8

magnitude earlier than previously expected. In the polar molecule OCS we go one step further by controlling the fragmentation process using two-color asymmetric laser fields. In addition to expected direct ionization effects, we also see post-ionization contributions, which are usually not visible in heavy polar molecules. We thus show in two different examples that CEI provides the means to extract new, unexpected pathways, which would otherwise remain hidden underneath a strong background.

Keywords Realtime roaming dynamics · Ultrafast imaging · Coulomb explosion imaging · Femtosecond dynamics · Coherent quantum control · Molecular movie

1 Introduction

How to image statistical dynamics of individual reaction pathways hidden in an overwhelming background? How to image and differentiate the dynamics of various ionization pathways, which are otherwise only visual in high-resolution spectroscopy? We are addressing these questions by making use of the capability of Coulomb explosion imaging (CEI) to detect the ion-breakup of single-molecules in real time. The beauty of CEI is, that it provides full 3D reconstruction of the molecular fragment momenta for each molecule, individually. This allows us to separate channels, which would be smeared out in other time resolved spectroscopy approaches.

M. Fushitani
Research Center for Materials Science, Nagoya University, Nagoya, Japan

A. Hishikawa
Chemistry Department, Graduate School of Science, Nagoya University, Aichi, Japan

Research Center for Materials Science, Nagoya University, Nagoya, Japan

P. L. Houston
Cornell University, Ithaca, NY, USA

Ggeorgia Institute of Technology, Atlanta, GA, USA

J. M. Bowman
Chemistry Department and Cherry L. Emerson Center for Scientific Computation, Emory University, Atlanta, GA, USA

M. S. Schuurman
National Research Council Canada, Ottawa, ON, Canada

Department of Chemistry and Biomolecular Sciences, University of Ottawa, Ottawa, ON, Canada

Conventional time-resolved spectroscopy would often struggle to separate features that are occurring on a few-percent level from the background, since in general one would average over an ensemble of molecules. If these features relate to a coherent motion (like e.g. wavepacket dynamics showing up as a clear oscillation) one might still be able to identify this on top of a background. However, statistically occurring events like uni-molecular dissociation signatures (including roaming) would not be separable from the background [1]. The fact that CEI allows to identify specific signatures of specific pathways to separate dissociation channels in a time resolved way is what makes it unique, since it allows to directly probe the evolution of the distance between fragments during a statistical decay.

2 Roaming in Formaldehyde

We investigated the unimolecular dissociation reactions in the deuterated formaldehyde molecule (D_2CO). In addition to the conventional dissociation channels – molecular and radical dissociation – a third channel termed roaming has been discovered in 2004 [2], which bypasses the transition state. Identified through spectroscopic footprints in this prototypical molecule using high-resolution spectroscopy and found later in a variety of other molecules, roaming fragments had however never been observed directly and in a time-resolved way. We succeeded in doing so by using the highly sensitive CEI method in combination with high-level (i.e. rigorous) first-principles simulations of all critical experimental steps [3, 4]. For animated trajectories of the direct dissociation path and the roaming path, see Ref. [5]. The schematic of the experimental excitation step leading to the roaming reaction is shown in Fig. 1, together with the probing step, which induces the Coulomb explosion.

Distinctive roaming signatures were identified in the experimental data, based on simulations (see Fig. 2 for three different time delays between the pump and the probe pulse). These roaming signatures were rendered observable by extracting rare stochastic events out of an overwhelming background. To identify the individual pathways, gates have been defined based on the individual analysis of 1500 semi-classical trajectories. These gates allow to extract an experimental observable for transient roaming features. Additionally, the identification of transient roaming features allowed to generalize the definition of roaming. While it was previously assumed that roaming results in molecular dissociation only, we observed that roaming might also be followed by radical dissociation. We further studied how

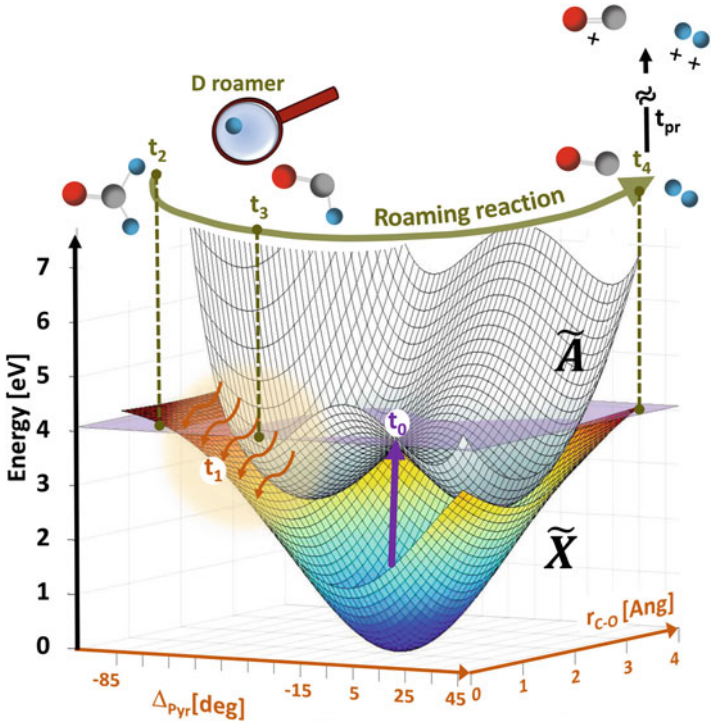

Fig. 1 Schematic of roaming dynamics in D_2CO visualized for two coordinate systems; the orange axis correspond to relevant vibrational modes, the green curved line shows the roaming reaction coordinate. A pump pulse (purple arrow, 304 nm) excites the $\tilde{A}$ state at time t_0 to the purple energy level. Because of vibronic coupling of the out-of-plane bending (pyramidization) and the C–O stretching mode with hot vibrational states of the ground state, a nonradiative population transfer is initiated at t_1. Once on the hot ground state, three reaction types can occur: D_2 + CO molecular dissociation, D + DCO radical dissociation, and roaming, each following its own reaction potential that is not explicitly shown here. Corresponding exemplary molecular structures for three subsequent times are given along the roaming reaction coordinate (green curved line). Excited molecules experience D_2 vibrations (t_2), which lead to one deuteron roaming around the remaining DCO fragment at large interatomic distances (t_3). Eventually, the roamer D abstracts the bound deuteron and together they leave the CO fragment, which leads to D_2 formation and abstraction (t_4). Note that t_1 to t_4 do not correspond to specific absolute times but rather indicate the order of these steps within a statistical process. A strong NIR pulse (800 nm, ~8 fs duration, black arrow) probes the molecular structure at variable time delays (t_{pr}). (Figure reprint with permission from Ref. [3])

the pump step and the overall dissociation depends on the employed UV pump wavelength [6]. Out of the four different wavelengths investigated (304, 314, 329, and 337 nm, corresponding to different selective populations of vibrational modes), 304 nm exhibits the fastest population transfer and dissociation times.

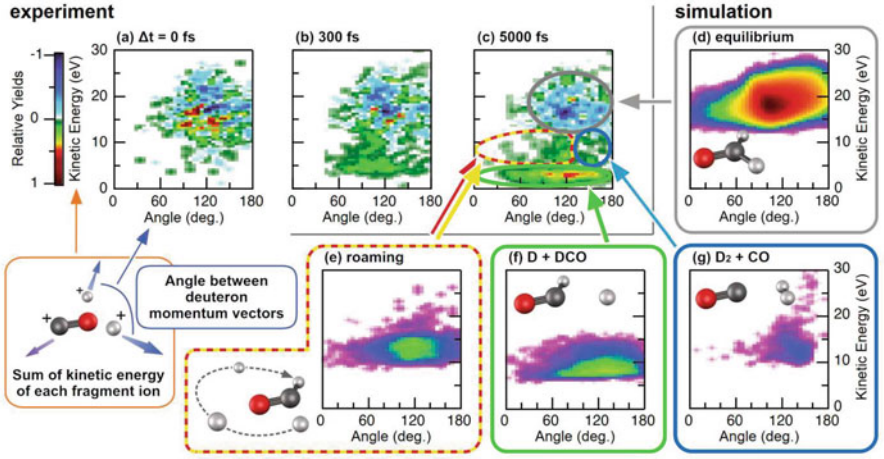

Fig. 2 Snapshots of dissociating D_2CO molecules for different time delays in experiment, pumped by 304 nm (**a**–**c**), with the total kinetic energy released in the Coulomb explosion plotted against the angle between the two deuteron momentum vectors (see inset on the bottom left). Geometries that correspond to different molecular roads, as obtained from the simulations, are marked by the colored curves: gray, equilibrium (**d**); red–yellow dash, roaming (**e**); green, radical dissociation (**f**); blue, molecular dissociation (**g**)

3 Post-Ionization Dynamics in OCS

In another experiment, we have tailored the laser fields used for excitation to investigate and control the dissociation mechanisms of the prototypical heavy polar molecule OCS into the two break-up channels of the dication, $OCS^{2+} \rightarrow O^+ + CS^+$ and $OC^+ + S^+$, in phase-locked two-color intense laser fields.

Two obtain these asymmetric laser fields, a fundamental beam is superimposed with its second harmonic while controlling the relative time delay between both of them. The electric field of the resulting two-color laser field, composed of the fundamental (carrier frequency of ω) and parallel polarized second harmonic (2ω) pulses, can be expressed as:

$$F(t) = F_\omega \cos(\omega t) + F_{2\omega} \cos(2\omega t + \phi) \quad (1)$$

where F_ω and $F_{2\omega}$ are the electric field amplitudes of the fundamental and second harmonic fields, respectively, and ϕ is the relative phase between both fields.

In these control experiments, the $O^+ + CS^+$ channel accounts for about 10% of the cases and the $OC^+ + S^+$ channel for about 90% (averaged over all phases). The branching ratio of the breaking of the C–O and C–S bonds followed a pronounced 2π-oscillation with a modulation depth of 11%, depending on the relative phase of the two-color laser fields. The fragment ejection direction of both break-up channels reflects the anisotropy of the tunneling ionization rate, following a 2π-periodicity,

as well. The two dissociation pathways in the C–S bond breaking channel show different phase dependencies of the fragment ejection direction, which are assigned to post-ionization dynamics. These observations, resulting from the excitation with asymmetric two-color intense laser fields, supported by state-of-the-art theoretical simulations, reveal the importance of post-ionization population dynamics in addition to tunneling ionization in the molecular fragmentation processes, even for heavy polar molecules [7].

To evaluate the fragment ejection direction quantitatively, the asymmetry parameter A is defined as a function of E_{kin} and ϕ,

$$A\left(E_{kin},\phi\right)=\frac{Y_{+}\left(E_{kin},\phi\right)-Y_{-}\left(E_{kin},\phi\right)}{Y_{+}\left(E_{kin},\phi\right)+Y_{-}\left(E_{kin},\phi\right)}$$

where Y_+ and Y_- are the fragment yields with positive and negative momenta along the laser polarization direction (x-axis), respectively.

The results of this evaluation for both breakup channels are shown in Fig. 3. Both channels peak at around 5.7 eV, as shown in green and purple. This main contribution is assigned to the phase dependence of the direct tunnel ionization step. However, in addition, we observe a shoulder peak at around 4 eV in the $O^+ + CS^+$ channel, which we prove to be related to post-ionization dynamics. For this, we combine experimental analysis and state of the art theory simulations based on real-time time dependent density functional theory (rt-TDDFT) for the ionization step, as

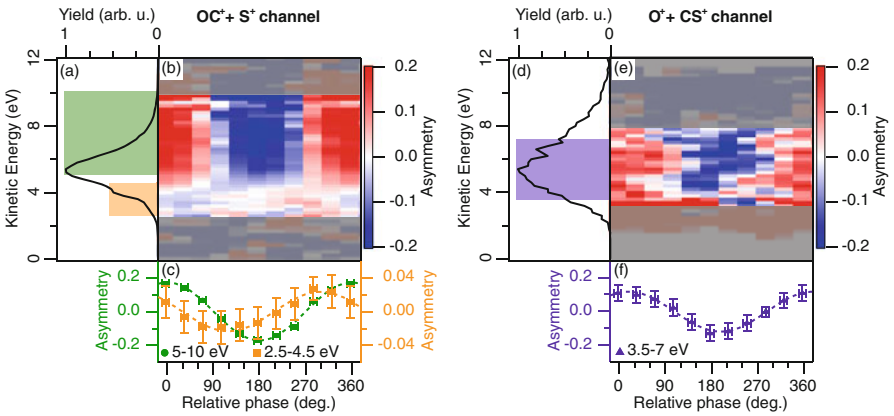

Fig. 3 Phase dependent total kinetic energy release E_{kin} spectrum of the $OC^+ + S^+$ channel (left) and the $O^+ + CS^+$ channel (right). (**a** + **d**) averaged spectrum over the relative phase ϕ between the ω and 2ω laser fields. (**b** + **e**) Two-dimensional plot of the asymmetry parameter as a function of E_{kin} and ϕ. (**c**) Asymmetry parameter of the OC^+ fragments integrated over 5–10 eV (green circles) and 2.5–4.5 eV (orange squares) vs. ϕ. The dotted lines are sine fits. (**f**) Same as (**c**), but the O^+ fragments are integrated over 3.5–7 eV (purple triangles). (Figure reprint with permission from Ref. [7])

Table 1 Summary of two indications for the observation of post-ionization dynamics in the OCS experiment

Observation	Expectation for direct tunnel ionization	Explanation through post-ionization interaction
A shoulder peak is observed in the KER of $OC^+ + S^+$ channel, but not in $O^+ + CS^+$ channel. The relative phase dependence of the asymmetry parameter of this shoulder peak is different to the main peaks in both of the channels and shifted by 270 degrees.	If the shoulder peak originated from direct tunnel ionization, one would expect a max. phase difference of 180 degrees (in the extreme case of diametrical effects of orbital shapes and dipole moments, e.g. ionization from lower lying orbitals).	The observed phase shift of 270 degrees can only be explained by other mechanisms occurring after the actual ionization, such as electron recollisional excitation, potential deformation, or population transfer between electronic states.
In the theoretical analysis, employing real-time real-space time-dependent density functional theory (rtTDDFT) and semi-classical surface-hopping dynamics, a mixing of electronic states of the dication is observed for contributions to the shoulder peak – at a time where the excitation pulse is no longer present.	If the shoulder peak would be populated only via direct ionization, such mixing after the pump pulse should not be present.	Supported by the computational results, we are able to indicate that this shoulder peak arises from a population transfer between electronic excited states in the doubly charged states.

well as semi-classical surface hopping simulations to consider the involved nuclear dynamics.

While post-ionization dynamics has been previously identified in light polar molecules, as well as in non-polar molecules [8, 9], it is in general not visible in heavy polar molecules, due to the dominant nature of the direct tunnel ionization contributions. Here, we have been able to separate these two contributions.

We do observe the influence of post-ionization dynamics in various aspects of our joint experiment – theory work. Not all of the effects are discussed in the here presented text, for a detailed discussion we refer to Ref. [7]. Above table summarizes two observations, pointing out that the main effect occurring after the ionization (and controlled by the two-color laser field) is a population transfer between electronic states of the dication (Table 1):

In summary, the two example cases of roaming in formaldehyde and fragmentation control in the OCS molecule show that the CEI method, sensitive to single molecules, is a powerful tool to identify contributions conventionally hidden under a huge background, even if these contributions relate to a statistically occurring signal.

Acknowledgments We thank A. Larameé for technical support and B. Wales and J. Sanderson from the university of Waterloo for providing the analysis software for the CEI measurement files; Funding: This work was supported by the Canada Foundation for Innovation, NSERC, FRQNT, the JSPS Program for Advancing Strategic International Networks to Accelerate the Circulation of Talented Researchers (grant no. S2602 to T. E. and A. H.), and the World Research Unit (B-1) of

Reaction Infography (R-ing) at Nagoya University, Japan (A. H. and F. L.). J. M. B. acknowledges financial support from NASA (grant no. 80NSSC20K0360).

References

1. Ding, X., Forbes, R., Kübel, M., Lee, K.F., Spanner, M., Naumov, A.Y., Villeneuve, D.M., Stolow, A., Corkum, P.B., Staudte, A.: Threshold photodissociation dynamics of NO2 studied by time-resolved cold target recoil ion momentum spectroscopy. J. Chem. Phys. **151**, 174301 (2019)
2. Townsend, D., Lahankar, S.A., Lee, S.K., Chambreau, S.D., Suits, A.G., Zhang, X., Rheinecker, J., Harding, L.B., Bowman, J.M.: The roaming atom: straying from the reaction path in formaldehyde decomposition. Science. **306**, 1158 (2004)
3. Endo, T., Simon, V., Neville, P., Wanie, S., Beaulieu, C., Qu, J., Dechamps, P., Lassonde, B.E., Schmidt, H., Fujise, M., Fushitani, A., Hishikawa, P.L., Houston, J.M., Bowman, M.S., Schuurman, F.L., Ibrahim, H.: Capturing roaming molecular fragments in real-time. Science. **370**(80), 1072 (2020)
4. Endo, T., Qu, C., Ibrahim, H.: A molecular road movie. Phys. Today. **74**, 62 (2021)
5. H. Ibrahim, The Molecular Road Movie, 2020
6. Endo, T., Neville, S.P., Lassonde, P., Qu, C., Fujise, H., Fushitani, M., Hishikawa, A., Houston, P.L., Bowman, J.M., Légaré, F., Schuurman, M.S., Ibrahim, H.: Electronic relaxation and dissociation dynamics in formaldehyde: pump wavelength dependence. Phys. Chem. Chem. Phys. **24**, 1779 (2022)
7. Endo, T., Ziems, K.M., Richter, M., Fröbel, F.G., Hishikawa, A., Gräfe, S., Légaré, F., Ibrahim, H.: Post-ionization dynamics of the polar molecule OCS in asymmetric laser fields. Front. Chem. **10**, 859750 (2022)
8. Wanie, V., Ibrahim, H., Beaulieu, S., Thiré, N., Schmidt, B.E., Deng, Y., Alnaser, A.S., Litvinyuk, I.V., Tong, X.-M., Légaré, F.: Coherent control of D_2/H_2 dissociative ionization by a mid-infrared two-color laser field. J. Phys. B Atomic Mol. Phys. **49**, 025601 (2016)
9. Ibrahim, H., Lefebvre, C., Bandrauk, A.D., Staudte, A., Légaré, F.: H2: the benchmark molecule for ultrafast science and technologies. J. Phys. B Atomic Mol. Phys. **51**, 42002 (2018)

Controlling the Time Evolution of Electron-Nuclei Entanglement for Steering Vibronic Coherences Dynamics Induced by Short 1–2 fs Optical Pulses

Martin Blavier, Natalia Gelfand, R. D. Levine, and F. Remacle

Abstract Atto pulses allow controlling the charge migration and the spatio-temporal beating of the electronic density on a purely electronic time scale by tailoring the parameters of the pump pulse to excite specific electronic coherences. As the nuclei begin to move, the electronic and nuclear motions are entangled and the engineered electronic coherences can be usefully exploited for steering the vibronic density to specific products through the network of non adiabatic interactions. Three recent examples for which we demonstrate such a control by fully quantum dynamical computations are discussed. Two diatomic molecules, LiH and N_2 excited by a 2 fs deep UV pulse and the ultrafast structural Jahn-Teller rearrangement in CH_4^+. The entanglement between electronic and nuclear degrees of freedom arises from the optical excitation and from non adiabatic coupling induced by the nuclear motion. We provide insight of the coherence control mechanism by analyzing the time evolution of the entanglement using a singular valued decomposition (SVD) of the matricized wave function.

Authors Martin Blavier and Natalia Gelfand have equally contributed to this chapter.

M. Blavier · F. Remacle (✉)
Theoretical Physical Chemistry, RU MolSys, University of Liege, Liège, Belgium

Fritz Haber Research Center, Institute of Chemistry, The Hebrew University of Jerusalem, Jerusalem, Israel
e-mail: fremacle@uliege.be

N. Gelfand
Fritz Haber Research Center, Institute of Chemistry, The Hebrew University of Jerusalem, Jerusalem, Israel

R. D. Levine
Fritz Haber Research Center, Institute of Chemistry, The Hebrew University of Jerusalem, Jerusalem, Israel

Department of Chemistry and Biochemistry, Department of Molecular and Medical Pharmacology, David Geffen School of Medicine, University of California, Los Angeles, CA, USA

L. Argenti et al. (eds.), *Proceedings of the 8th International Conference on Attosecond Science and Technology*, Springer Proceedings in Physics 300,
https://doi.org/10.1007/978-3-031-47938-0_9

Keywords Attosecond molecular quantum dynamics · Time-resolved electron-nuclei entanglement in molecules · Schmidt rank · Singular value decomposition · Matricization of the wave function

1 Introduction

Recently, short optical atto (as) and few femtosecond (fs) pulses have provided new insights into ultrafast dynamics and charge migration in molecular systems and in solids [1–10].

The novel feature brought by such short pulses is that they lead to an initial state that is a superposition of the different electronic states that fall within the broad pulse energy bandwidth. By tuning the pulse parameters, one can engineer electronic coherences between selected electronic states and control the charge migration and the spatio-temporal beating of the electronic density on a purely electronic time scale [11–13]. As the nuclei begin to move, the electronic and nuclear motions become entangled and the engineered electronic coherences can be usefully exploited for steering the vibronic density through the network of non adiabatic interactions to specific products [14–16].

Entanglement arises when the wave function of two subsystems cannot be written as a single product of separable terms depending each of the coordinates of one of them [17, 18]. It is an important property of multipartite systems that plays an essential role in quantum information and quantum communication [19]. Entanglement also plays an important role in quantum dynamics. Non adiabatic interactions between electronic states driven by nuclear motion and the breakdown of the Born and Oppenheimer approximation have been long recognized as a source of electron-nuclei correlation leading to the entanglement of the vibronic wave function [20–25]. One can entangle vibrational modes in a polyatomic molecule, [26] or scattering channels in chemical reactions [27, 28]. Attopulse pump probe schemes were used recently to probe the entanglement between the cation and the leaving photoelectron, in the molecular ion H_2^+ [29, 30] and in atoms [31].

Here, we focus on the entanglement of electrons and nuclei brought by exciting molecules to a superposition of several electronic states with short optical pulses and on the special role of the entanglement for the control of the ensuing non adiabatic quantum dynamics leading to the products [32, 33]. We analyze the time evolution of the entanglement between nuclear and electronic degrees of freedom using singular value decomposition (SVD) of the wave function rewritten as a matrix and known as matricizing [34]. Three cases are investigated: the quantum dynamics on coupled electronic states of two diatomic molecules, LiH and N_2, photoexcited by short UV 2 fs pulses and the multi-dimensional quantum dynamics of the Jahn Teller ultrafast structural rearrangement of the molecular cation CH_4^+ upon strong field ionization of the neutral [35].

2 Quantification of the Time Evolution of Electron-Nuclei Entanglement in Molecules

The entanglement of the wave function of a multipartite system can be quantified using its Schmidt rank [17, 18]. The Schmidt rank is the minimum number of separable product terms necessary to describe the wave function. When the wave function can be described as a single product of separable terms, the system is not entangled and its Schmidt rank is equal to 1. When more than one term is necessary, the wave function is entangled and its Schmidt rank is larger than 1.

2.1 Quantum Vibronic Dynamics in Coupled Electronic States

In the quantum dynamical simulations reported below, we expand the wave function in a double sum of products of a nuclear wave function and an electronic state. The basis of nuclear wave functions is taken to be a set of N_g door functions localized at equally spaced grid points, $|g_n\rangle$, along the nuclear coordinate. The electronic wave function is described in the basis of a band of N_e adiabatic states, $|e_i\rangle$. At the end of the broad in energy exciting pulse, the wave function is a superposition separable products, $|g_n\rangle|e_i\rangle$, the Born Huang expansion

$$|\Psi(t)\rangle = \sum_{n=1}^{Ng} \sum_{i=1}^{Ne} c_{ni}(t)\, |g_n\rangle\, |e_i\rangle \tag{1}$$

The complex coefficients, $c_{ni}(t)$, are obtained by solving the time-dependent Schrödinger equation:

$$i\hbar \frac{d}{dt}\mathbf{c} = \mathbf{H}(t)\mathbf{c} \tag{2}$$

where $\mathbf{c}$ is the vector of the $N_g.N_e$ coefficients $c_{ni}(t)$. $\mathbf{H}(t)$ is the matrix of the molecular Hamiltonian in the separable basis $\{|g_n\rangle|e_i\rangle\}$:

$$\mathbf{H}_{ni,mj}(t) = -\frac{1}{2}\mathbf{T}_{ni,mj}\delta_{ij} + \mathbf{V}_{ni,nj}\delta_{nm}\delta_{ij} - \mathbf{E}(t)\mu_{ni,mj}\delta_{nm} - \left(\frac{1}{i}\tau_{ni,mj}\delta_{mn}.\mathbf{p}_{mi,nj}\right) \tag{3}$$

where *n,m* are the index of the grid points and *i,j* the index of the electronic states. The first two terms on the rhs are the kinetic and potential energies of the nuclei. The interaction with the time-dependent electric field of the short pulse is described in the dipole approximation (third term). $\mathbf{E}(t)$ is the time profile of the electric field defined from the derivative of the vector potential confined in a short Gaussian envelope:

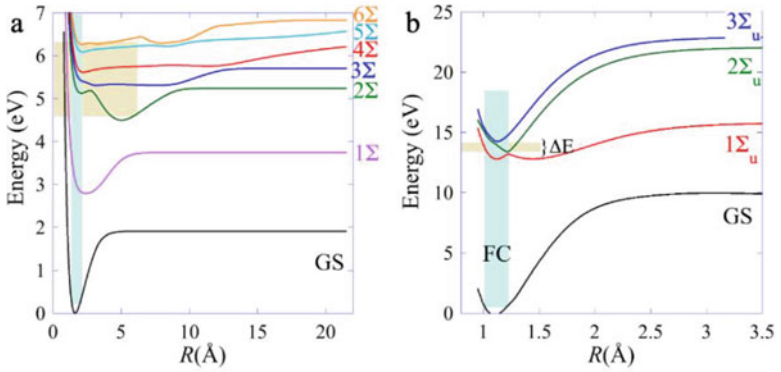

Fig. 1 (**a**) Potential energy curves of the 7 lowest Σ adiabatic states of the LiH molecule included in the computations [36]. (**b**) Potential energy curves of the 4 lowest electronic adiabatic states of N_2 included in the computation [37]. The Franck-Condon (FC) region is indicated in shaded blue and the energy band width, ΔE, of the short pulse in shaded yellow

$$\mathbf{E}(t) = -\frac{d\mathbf{A}(t)}{dt} = \left(\hat{\mathbf{e}} f_0\right) \exp\left(\frac{-(t-t_0)^2}{2\sigma^2}\right)\left(\cos\left(\omega\,(t-t_0)+\phi\right) + \frac{\sin(\omega(t-t_0)+\phi)(t-t_0)}{\omega\sigma^2}\right) \tag{4}$$

The last term in Eq. (3) describes the non adiabatic interactions driven by the nuclear motion. The last two term terms in Eq. (3) are the source of entanglement between electrons and nuclei as the dynamics unfolds. The excitation by the short pulse inherently entangles electron and nuclei because it promotes the ground vibrational state of the ground electronic state (GS) to a superposition of several excited electronic states (Fig.1).

As we show below, as long as all the wave packets on each excited electronic state remain localized in the Franck-Condon (FC) region, the wave function (Eq. (1)) is separable and the Schmidt rank is equal to 1. When the nuclei begin to move, the wave packets on each electronic state experience a different gradient which leads to the entanglement of the wave function, even in the absence of non adiabatic coupling.

2.2 *S Schmidt Rank and Compaction by Singular Value Decomposition of the Matricized Wave Function*

To analyze the time evolution of the entanglement, at each time step, we matricize the $N_g.N_e$ amplitude vector, $\mathbf{c}(t)$, into N_g x N_e rectangular matrix $\mathbf{C}(t)$, followed by a Singular Value Decomposition (SVD) [32, 33]. Since typically$N_g > N_e$, the matrix

$\mathbf{C}(t)$ has at most N_e singular values [38] and the matrix $\mathbf{C}(t)$ can be written as a sum of at most N_e separable terms:

$$\mathbf{C}(t) = \sum_{m}^{Ne} \sigma_m(t) \, |u_m\rangle \, (t). \left|v_m^{\dagger}\right\rangle (t) \tag{5}$$

The wave function will therefore have a maximum Schmidt rank equal to N_e.

In Eq. (5), $|u_m(t)\rangle$are the N_e left eigenvectors of the matrix $\mathbf{C}(t)$**,** $|v_m(t)\rangle$ are its right eigenvectors and $\sigma_m(t)$ are the singular values. The singular values are real and the singular vectors are complex. The vectors $|u_m(t)\rangle$ are the nuclear singular vectors, they have components on the grid basis function only. The vectors $|v_m(t)\rangle$ are the electronic singular vectors. They have components on the electronic states only.

$$|u_m(t)\rangle = \sum_{n=1}^{Ng} u_{nm}(t) \, |g_n\rangle \tag{6}$$

$$|v_m(t)\rangle = \sum_{i=1}^{Ne} v_{im}(t) \, |e_i\rangle \tag{7}$$

Using Eqs. (6) and (7), the Born-Huang amplitudes of Eq. (1) are a sum of N_e separable terms:

$$c_{ni}(t) = \sum_{m=1}^{Ne} \sigma_m(t) u_{nm}(t) v_{im}^{*}(t) \tag{8}$$

From Eq. (8), one sees that the normalization of the wave function is given by:

$$\mathrm{Tr}\left[\rho(t)\right] = \sum_{m=1}^{Ne} \sigma_m^2(t) = 1 \tag{9}$$

The exact expression given by Eq.(5) already provides a significant compaction of the wave function in at most N_e terms compared to the N_e . $N_g$terms of the Born-Hunag expansion Eq. (1):

$$|\Psi(t)\rangle = \sum_{m}^{N_e} \sigma_m(t) \, |u_m\rangle \, (t). \left|v_m^{\dagger}\right\rangle (t) \tag{10}$$

A further compaction can be obtained by ordering the singular values $\sigma_m(t)$ by decreasing values and retaining the $N_{\min}$ terms that provide an approximation of the wave function up to a certain threshold (for example of the normalization):

$$|\Psi(t)\rangle = \sum_{m}^{N_{\min}} \sigma_m(t)\,|u_m\rangle\,(t).\,\left|v_m^{\dagger}\right\rangle(t),\ N_{\min} < N_e \tag{11}$$

When$N_{\min}$ is smaller thanN_e, $\mathrm{Tr}[\rho(t)] < 1$. How well the value of $\mathrm{Tr}[\rho(t)]$ approaches unity can be used for estimating $N_{\min}$.

3 Dynamical Evolution of the Entanglement and of the Singular Components

We begin by comparing the time evolution of the Schmidt rank and of the entanglement in two diatomics: LiH and N_2, excited by short ≈ 2 fs UV pulses.

We show in Fig.2 the dynamics of the populations in the electronic states of the LiH molecule computed by solving the time-dependent Schrödinger equation for the Hamiltonian given by Eq. (3) for 7 coupled Σ electronic states, see Ref. [36] for curves of the transition dipoles and NAC couplings. The vibrational ground state (GS) is excited with a short UV pulse polarized towards the H atom along the molecular axis, so as to selectively access the Σ_2, Σ_4 states. The pulse has a carrier frequency of 5.5 eV and a Gaussian envelope with a Full Width at Half Maximum (FWHM) of 2 fs which corresponds to an energy bandwidth of

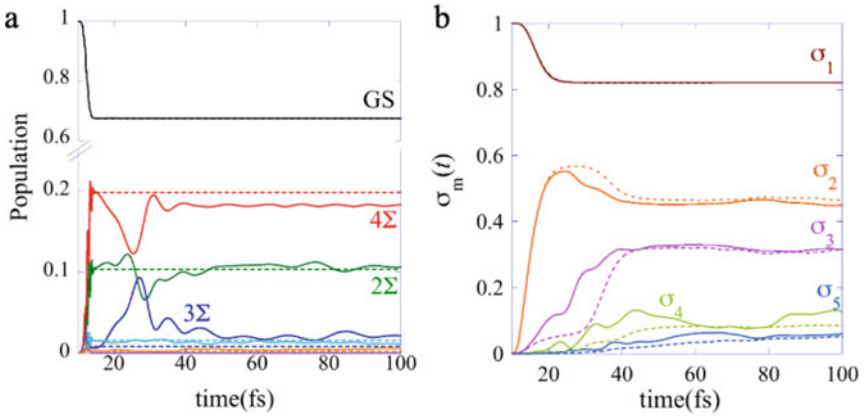

Fig. 2 (**a**) Dynamics of the populations of the adiabatic states in the LiH molecule, full lines NACon and dashed lines NACoff. The dynamics of the two computations is nearly identfical during the pulse. (**b**) singular values,$\sigma_m(t)$, computed by SVD after matricization of the wave function at each time step. Full lines NACon, dashed lines NACoff

1.84 eV. Two computations are carried out, one that includes the NAC term in the Hamiltonian (NACon, full lines) and one that does not (NACoff, dashed lines). The two computations differ significantly by the amount of population in the Σ_3 state, which is not significantly populated in the NACoff computation and is populated transiently in the NACon ones. In the NACoff computations, the populations in the electronic states are stationary after the pulse. By comparing the two curves, one see that towards the end of the pulse, non adiabatic interactions bring population to Σ_3 which is much less optically active than Σ_2 and Σ_4 for a polarization of the pulse towards the H atom. Already during and right after the pulse, there is extensive population exchange between these three states induced by NAC. After 50 fs, the populations are almost stationary as the wave packets proceed to dissociation on these three electronic states.

The time evolution of the singular values, $\sigma_m(t)$, obtained by SVD after the matricization of the wave function at each time step, are plotted in Fig. 2b for the two computations. During the first half of the pulse, the wave function remains separable and is described by a single term for both computations. The onset of nuclear motion is accompanied by the rise of a second component, that describes the exit of the wave packets of the FC region. In the NACoff computations, the time evolution of the entanglement is solely controlled by the superposition of electronic states built by the short pulse and the gradient differences between the electronic states accessed at the excitation step. As long the gradients on each potential curve remain similar, a second principal component suffices for describing the dynamics. In the NACon one, the second and third components rise earlier, as amplitude is transferred to the Σ_3 state by the NAC at the exit of the FC region. In LiH, we therefore observe an increase of the Schmidt rank (and of entanglement) as the nuclear motion sets in, at the exit of the FC region, in the first 50 fs of the dynamics. The increase is driven by the differences in the gradients of the potential curves of the states excited by the pulse and by the non adiabatic interactions, and primarily affects the $\sigma_2(t)$, $\sigma_3(t)$ and $\sigma_4(t)$ singular values plotted in Fig. 2b. On the other hand, in the NACoff computation, the increase is only driven by the difference of the gradient of the poettnial energy cures of these three states, with the result that in the first 50 fs of the dynamics, the increase of the entanglement is slower in the NACoff computation. Asymptotically, there is essentially no difference in the degree of entanglement between the NACon and the NACoff computation since the NAC is very small asymptotically.

Further insights are given by analyzing the components of the nuclear and electronic singular vectors on the grid and on the adiabatic electronic states respectively. Heatmaps of the components of the first four nuclear singular vectors are plotted in Fig. 3 for the NACon and the NACoff computations. The components of the electronic singular vectors are plotted in Fig. 4. The first nuclear singular vector is localized in the FC region (Fig. 3a). It corresponds to the largest singular value since 67% of the population remains in the GS after the pulse. Accordingly, the electronic singular vector is localized on the GS except during the first half of the pulse, when all the wave packets on the excited electronic states are still localized

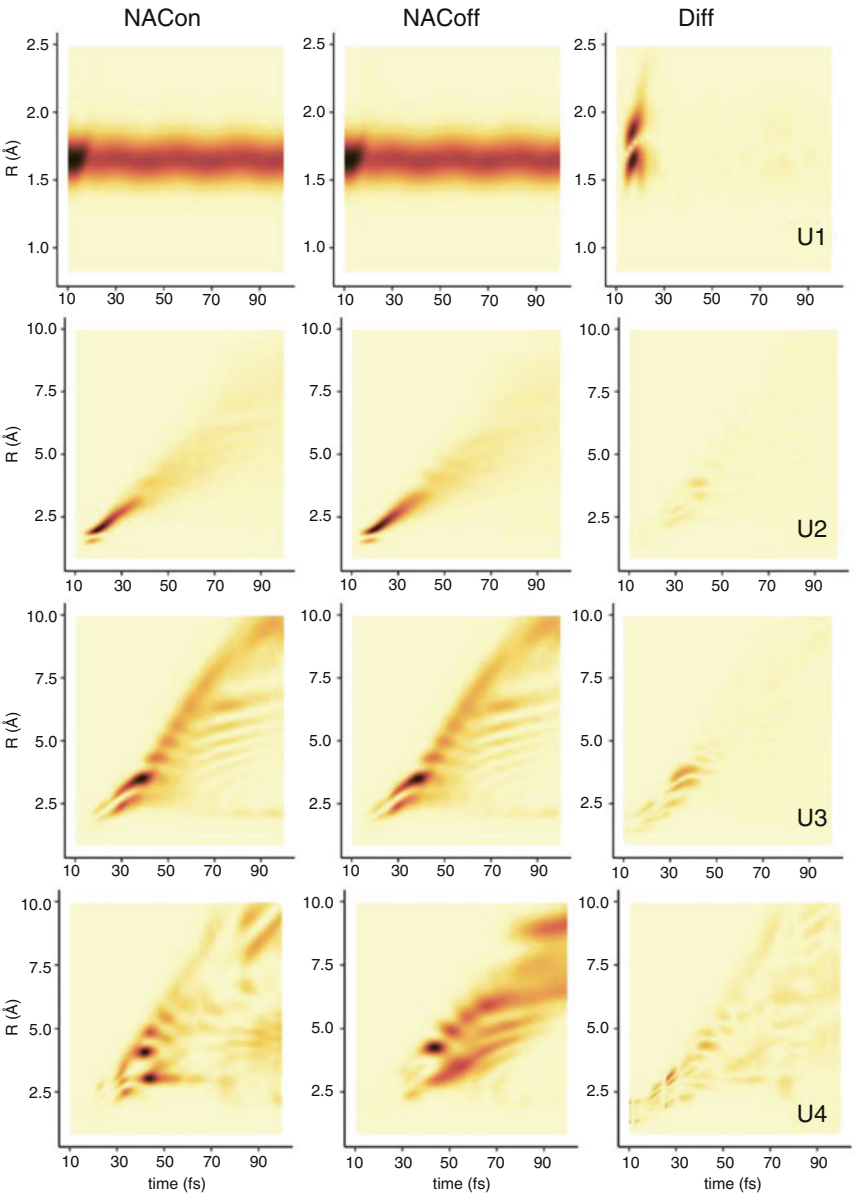

Fig. 3 Heatmaps of the localization of the first four nuclear singular vectors for the NACon computation (left) and the NACoff computation (middle). The weights at each grid point are multiplied by the principal values $\sigma_m^2(t)$. The difference between the unweighted nuclear singular vectors is shown in the right column to illustrate the role of the non adiabatic interactions

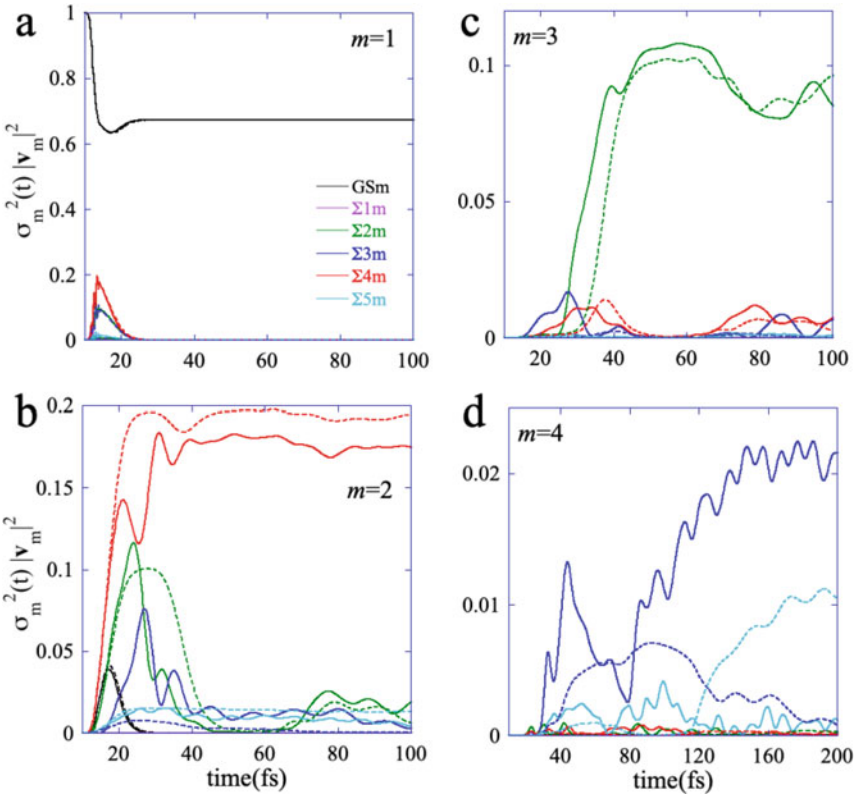

Fig. 4 Weights of the electronic singular vectors of the four largest principal components on the adiabatic electronic states. Full lines: NACon, dashes: NACoff. The weights $|v_{im}|^2$ are multiplied by the principal values $\sigma_m^2(t)$. Note the decrease by a more than an order of magnitude for $m = 4$, that localises on Σ_3 at long times in the NACon computation

in the FC region (Fig. 4a). Then, the electronic singular vector is also localized on the two most active electronic states, Σ_4 and Σ_2. The second principal value, $\sigma_2(t)$, begins to rise in the second half of the pulse (Fig. 2b). Right after the pulse, the second electronic singular vector, $\mathbf{v}_2$**,** has weights on several adiabatic states both in the NACon and in the NACoff computations. The effect of the $\Sigma_4 - \Sigma_3$ and $\Sigma_2 - \Sigma_3$ non adiabatic interactions is clearly seen in the weights of the three electronic singular vectors, $\mathbf{v}_2$, $\mathbf{v}_3$, $\mathbf{v}_4$ on the adiabatic electronic states, Fig. 4b, c, d respectively. In the NACon computation, $\mathbf{v}_2$, $\mathbf{v}_3$, $\mathbf{v}_4$ have a significant component on Σ_3 which is much smaller in the NACoff one. After the NAC region, beyond 50 fs, the second electronic singular vector, $\mathbf{v}_2$, localizes on Σ_4 and the third one, $\mathbf{v}_3$, on Σ_2. In the NACon computation, at long times the fourth electronic singular vector, $\mathbf{v}_4$, localizes on Σ_3 (not shown) while its localizes on Σ_5 in the NACoff

one. As discussed above, below 50 fs, the nuclear vectors are localized on several electronic states coupled by the NAC interactions while at longer times, they reflect the gradient of the potential energy curve on which the singular component is localized. This is clearly seen in the last column of Fig. 3 where we show the difference between the nuclear singular vectors computed for the NACon (first column) and the NACoff (second column).

In the case of the N_2 molecule, the short UV pulse has an excitation wavelength of 13.6 eV and a duration σ of 1.32 fs (FWHM of 1.18 eV) so as to selectively excite the two lowest Σ_u states (the lowest Rydberg state and the valence state, see Fig. 1b) below their dissociation asymptote. Unlike in LiH, the motion of the excited wave packet is bound and the lowest Rydberg state and the valence state are strongly coupled by NAC at the exit of the FC region. The population dynamics is plotted in Fig. 5a. The pulse builds a superposition of the lowest Rydberg state and the valence state. Right at the exit of the FC region, almost all the population of the Rydberg state is transferred to the shallow valence state. The Rydberg state is periodically repopulated each time the valence wave packet revisits the NAC region and comes back to the FC region, every 40 fs. Compared to the LiH case discussed above, this periodic evolution of the population in the two states leads to a rather different time evolution of the entanglement and of the Schmidt rank. The time evolution of the singular values $\sigma_m^2(t)$ is plotted in Fig.5b. Because of the strong non adiabatic interactions and of the very different gradients of the potential of the Rydberg and the shallow valence state, three singular values are needed to describe the wave function at all times. Their time evolution is non monotonic and reflects the periodic motion of the wave packet on the valence state. Each time the wave

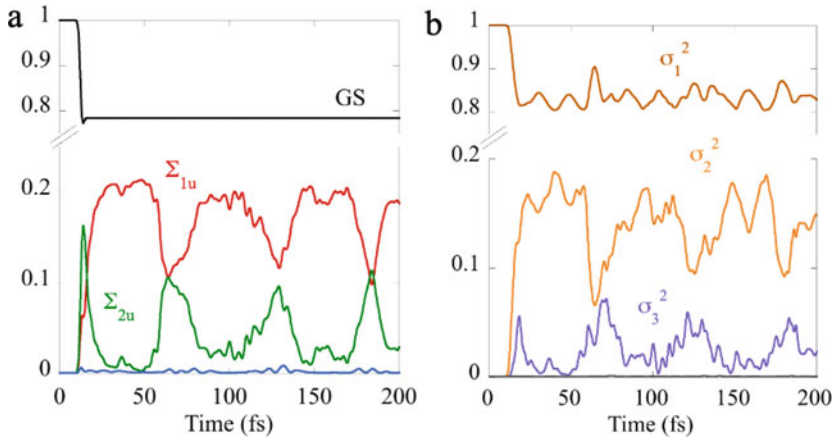

Fig. 5 (**a**) Dynamics of the populations in N_2 excited to the lowest Rydberg and valence states by a 2 fs UV pulse. (**b**) singular values, $\sigma_m(t)$, computed by SVD after matricization of the wave function at each time step

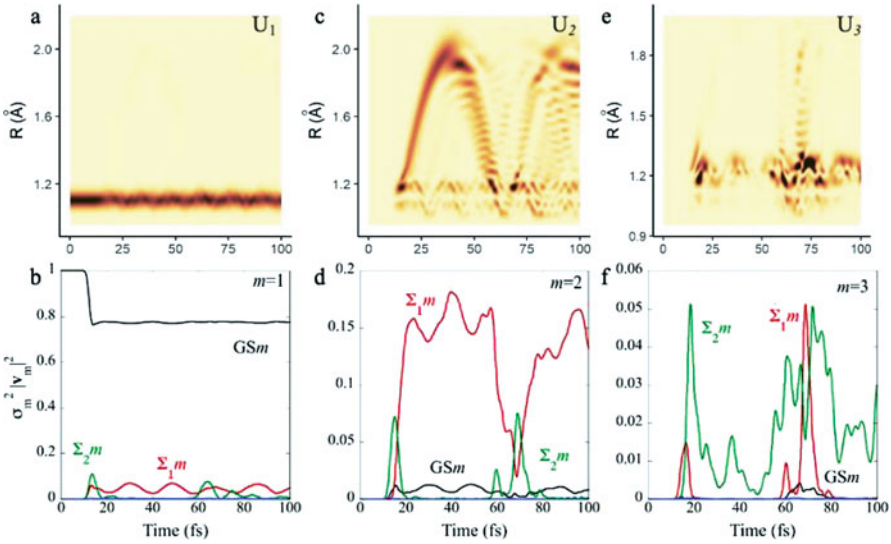

Fig. 6 Heatmaps of the nuclear singular vectors of the three largest principal components in N_2 (panels a, c, d). Corresponding composition of the electronic singular vectors on the adiabatic electronic states (panels b, d, f). The weights of the singular vectors are multiplied by $\sigma_m^2(t)$

packet on the valence state revisits the FC region there is a non monotonic variation of the $\sigma_1(t)$, $\sigma_2(t)$ and $\sigma_3(t)$ singular values: $\sigma_1(t)$ and $\sigma_3(t)$ increase and $\sigma_2(t)$ decreases. This non monotonic change is due to the fact that a larger fraction of the wave packet is localized in the FC region and therefore can be described by the first and third singular component. Indeed, the nuclear singular vector, U1, of the largest principal component is localized in the FC region as in LiH, Fig. 6a. But unlike in LiH, the first electronic singular vector, $\mathbf{v}_1$, has components on the valence and Rydberg states each time the wave packet revisits the NAC region (Fig. 6b). This periodic motion is reflected in the value of the largest singular value which rises when the wave packet passes through the NAC region (Fig. 5b). The second electronic singular vector, $\mathbf{v}_2$, is mainly localized on the valence state except in the NAC region where it has components on the Rydberg state (Fig. 6d). Accordingly, the localization on the second nuclear singular vector, U2, extends in at large R values which correspond to the shallow potential of the valence state (Fig. 6c). The third principal component is localized on the Rydberg state and has a very low weight except in the NAC region where its nuclear and electronic singular vectors acquire a weight on the valence state (Fig. 6e, f).

In both LiH and N_2 (Fig.2b and Fig.4b respectively), one can see that in the regions of non adiabatic interaction, the singular values go through an avoided crossing as a function of time.

4 Extending to More than One Nuclear Degree of Freedom: Ultrafats Dynamics of the Jahn-Teller Effect in the Methane Cation

Upon sudden ionization of the neutral, the methane cation undergoes an ultrafast structural rearrangement triggered by the Jahn-Teller effect. This ultrafast vibronic dynamics has been probed by attosecond High Harmonic Spectroscopy (HHS) by Marangos et al. [39, 40] who reported a strong isotope effect, larger than what is expected classically from the ratio of the reduced masses. Dynamical computations provided insights on the role of the non-adiabatic interactions between the three electronic states of the cation, D_0, D_1 and D_3 involved [35, 41–44]. We have shown [35, 44] using fully quantum dynamics on three coupled electronic states (D_0, D_1, D_2) and two nuclear coordinates (q_1, q_2) that electronic coherences involving the D_2 state are instrumental to yield the unusually strong isotope, whether the sudden ionization results from photoionization by a XUV pulse [44] or from strong field ionization as in HHS [35].

We report here on preliminary results analyzing the time evolution of the entanglement between electron and nuclear in the ultrafast dynamics of the methane cation driven by strong field ionization (SFI) of the neutral. Details of the computations can be found in Ref. [35]. A sketch of the 2-dimensional potential of the three states is plotted in Fig. 7a. For two nuclear coordinates and three electronic states, there are $N_e . N_{q1} . N_{q2} \approx 80{,}000$ separable product terms $(|g_{q1}\rangle|g_{q2}\rangle|e_i\rangle$ in the Born Huang expansion of the wave function (Eq. (1)). Since we have three subsystems, we recast the vector of the amplitudes into a 3-dimensional tensor $\mathbf{C}$ which we decomposed by High Order SVD [45].

$$C_{jki} = \sum_{s=1}^{Nq1} \sum_{t=1}^{Nq2} \sum_{r=1}^{Ne} \sigma_{rst} \mathbf{U}_{js} \mathbf{W}_{kt} \mathbf{V}_{ir} \tag{12}$$

where the indices j and k correspond to the grid points along $q1$ and $q2$ respectively and i is the index of the three electronic states. σ_{rst} are the (complex) values of the core tensor of the HOSV Decomposition [45]. $\mathbf{U}_{js}$ and $\mathbf{W}_{kt}$ are the nuclear singular vectors along the $q1$ and $q2$ coordinate respectively and $\mathbf{V}_{ir}$ the electronic singular vector. We show in Fig7b the dynamics of the populations in the three states of the cation D_0, D_1 and D_2, induced by sudden ionization with a strong IR field (2 10^{14} W/cm^2), as described in Ref. [35]. Compared to LiH and N_2, we obtain a massive compaction of the wave function when applying SVD to the wave function written as a tensor. The number of terms in Eq. (12) needed to recover 99% of the trace of the density matrix, Tr$[\rho(t)]$, is plotted in Fig. 7c. From 10 fs on, ≈2000 terms suffice, compared to 80,000 separable terms in the Born-Huang expansion.

The degree of compaction is even larger at short times, in the first few fs. The localization of the wave function at each grid point ($q1$, $q2$) on the three electronic

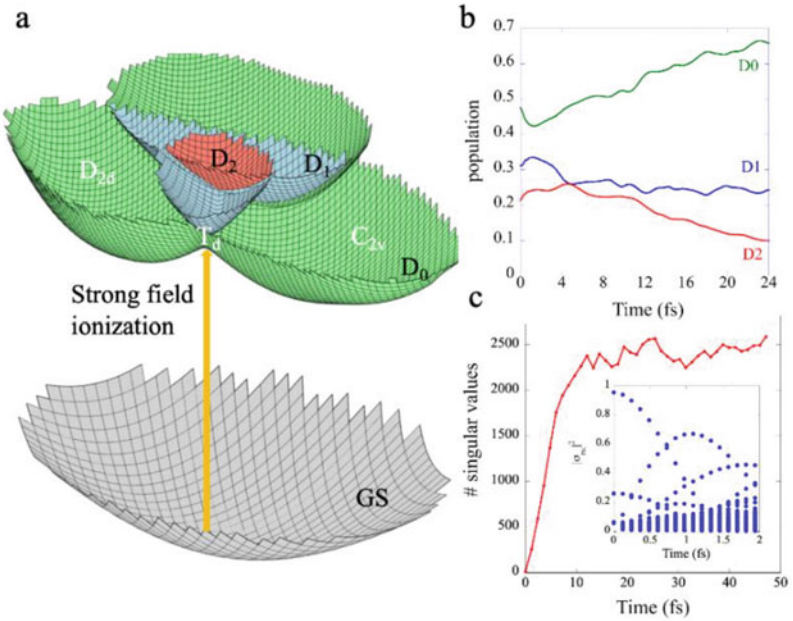

Fig. 7 (**a**) A schematic view of the 2 dimensional potentials of the three electronic states of the cation that are reached by string field ionization [35] (**b**) the time evolution of the populations on the three electronic states of the cation resulting from a sudden ionization process with a strong field of 2 10 ^{14} W/cm^2. (**c**) The number of singular terms in the HOSVD expansion needed to recover 99% of the trace of the density matrix for the first 50 fs of the dynamics. The inset shows the values of the elements of the core tensor for the first two fs

states is plotted in the top row of Fig. 8 at 0.85 fs. In the bottom row, we show the recovered localization on the grid obtained from the 193 separable terms necessary for accounting for 99% of the trace. One can see that the main patterns of the localization of the wave function on the three electronic states are well captured. The same is true at 1.7 fs (Fig. 9) for which 366 terms are needed. Work is in progress on the physical interpretation of the most important separable terms and on the analysis of the entanglement.

5 Conclusion

The matricization of the wave function vector followed by SVD provides an efficient way to follow the time evolution of the Schmidt rank of the wave function and of the entanglement between electronic and nuclei as a function of time. The SVD decomposition leads to a significant compaction of the matricized wave function in terms of a minimum number of separable products of an electronic and nuclear singular vector weighted by singular values arranged in decreasing order. This

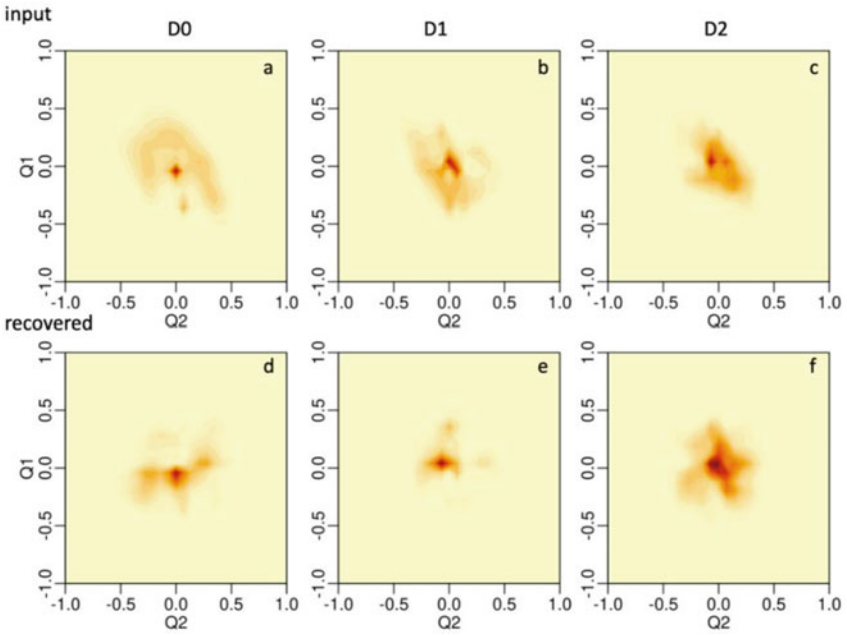

Fig. 8 Top row: Localization of the wave function on the (*q1*, *q2*) grid for the three electronic states D_0(a), D_1(b) and D_2(c) at 0.85 fs, computed by solving the time-dependent Schrödinger equation. Bottom. Recovered localization using 193 separable terms in the HOSVD expansion for D_0(d), D_1(e) and D_2(f)

minimum number of terms corresponds to the Schmidt rank and is significantly smaller than the number of terms of the Born-Huang expansion. The weights of the nuclear and electronic singular vectors on the nuclear and electronic basis sets provide further insights on the physical meaning of the singular components. This analysis can be extended to several nuclear degrees of freedom by HOSVD.

We show that exciting molecules by ultrashort atto and few fs pulses inherently entangles the vibronic wave function because the initial state is a superposition of the several electronic states that fall within the broad energy bandwidth of the pulse. This is unlike excitation with longer pulses where a single electronic state is populated. The entanglement is driven by the nuclear motion. The main contribution to entanglement is the difference in the gradient of the potentials of the different electronic states accessed by the optical pulse. It is therefore possible to control the initial degree of entanglement by exciting specific electronic states using the parameters of the pulse: Its bandwidth, its polarization, its carrier frequency and the carrier-envelope phase for few cycle pulses. The initial entanglement that is controlled by the pulse parameters is further modulated by the non adiabatic interactions which are also driven by nuclear motion. As shown in the case of LiH, these can bring electronic states that were not optically excited in the vibronic wave packet, leading to an increase of the initial entanglement.

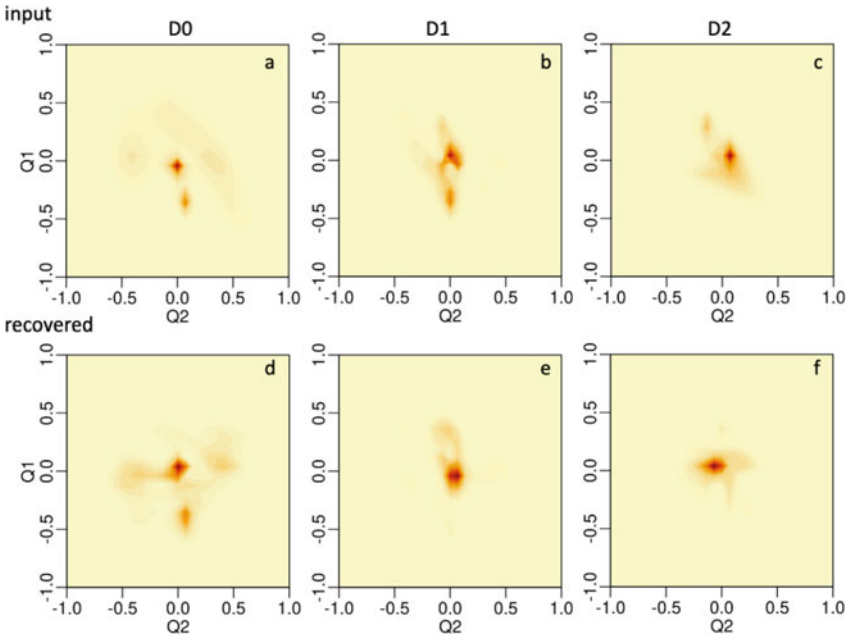

Fig. 9 Top row: Localization of the wave function on the ($q1$, $q2$) grid for the three electronic states D_0(a), D_1(b) and D_2(c) at 1.7 fs, computed by solving the time-dependent Schrödinger equation as described in Ref. [35] Bottom. Recovered localization using 366 separable terms in the HOSVD expansion for D_0(d), D_1(e) and D_2(f)

The compaction of the wave function as a sum of a small number of separable terms opens the way for efficient propagation schemes for the singular states, in connection with recent work based on product matrix states [46–48].

Acknowledgments MB is supported by an Erasmus+ grant between ULiège and HUJI. NG is supported by a joint NSF-BSF project with a BSF award number 2019722. Support from the COST action Attochem(CA18222) is acknowledged. The work of FR and MB is supported by by the Fonds National de la Recherche Scientifique (Belgium), F.R.S.-FNRS, research grant # T.0205.20. Computational resources have been provided by the Consortium des Equipements de Calcul Intensif (CECI), funded by the F.R.S.- FNRS under Grant # 2.5020.11.

References

1. Nisoli, M., Decleva, P., Calegari, F., Palacios, A., Martín, F.: Attosecond electron dynamics in molecules. Chem. Rev. **117**(16), 10760–10825 (2017)
2. Calegari, F., Ayuso, D., Trabattoni, A., Belshaw, L., De Camillis, S., Anumula, S., Frassetto, F., Poletto, L., Palacios, A., Decleva, P., Greenwood, J.B., Martín, F., Nisoli, M.: Ultrafast electron dynamics in phenylalanine initiated by attosecond pulses. Science. **346**(6207), 336–339 (2014)

3. Perfetto, E., Trabattoni, A., Calegari, F., Nisoli, M., Marini, A., Stefanucci, G.: Ultrafast quantum interference in the charge migration of tryptophan. J. Phys. Chem. Lett. **11**, 891–899 (2020)
4. Despré, V., Marciniak, A., Loriot, V., Galbraith, M.C.E., Rouzée, A., Vrakking, M.J.J., Lépine, F., Kuleff, A.I.: Attosecond hole migration in benzene molecules surviving nuclear motion. J. Phys. Chem. Lett. **6**(3), 426–431 (2015)
5. Kling, M.F., Siedschlag, C., Verhoef, A.J., Khan, J.I., Schultze, M., Uphues, T., Ni, Y., Uiberacker, M., Drescher, M., Krausz, F., Vrakking, M.J.J.: Control of electron localization in molecular dissociation. Science. **312**(5771), 246–248 (2006)
6. Kraus, P.M., Mignolet, B., Baykusheva, D., Rupenyan, A., Horný, L., Penka, E.F., Grassi, G., Tolstikhin, O.I., Schneider, J., Jensen, F., Madsen, L.B., Bandrauk, A.D., Remacle, F., Wörner, H.J.: Measurement and laser control of attosecond charge migration in ionized iodoacetylene. Science. **350**(6262), 790–795 (2015)
7. Matselyukh, D.T., Despré, V., Golubev, N.V., Kuleff, A.I., Wörner, H.J.: Decoherence and revival in attosecond charge migration driven by non-adiabatic dynamics. Nat. Phys. **18**, 1206–1213 (2022)
8. Baldini, E., Palmieri, T., Pomarico, E., Auböck, G., Chergui, M.: Clocking the ultrafast electron cooling in Anatase titanium dioxide nanoparticles. ACS Photo. **5**(4), 1241–1249 (2018)
9. Borrego-Varillas, R., Lucchini, M., Nisoli, M.: Attosecond spectroscopy for the investigation of ultrafast dynamics in atomic, molecular and solid-state physics. Rep. Prog. Phys. **85**(6), 066401 (2022)
10. Lucchini, M., Sato, S.A., Lucarelli, G.D., Moio, B., Inzani, G., Borrego-Varillas, R., Frassetto, F., Poletto, L., Hübener, H., De Giovannini, U., Rubio, A., Nisoli, M.: Unravelling the intertwined atomic and bulk nature of localised excitons by attosecond spectroscopy. Nat. Commun. **12**(1), 1021 (2021)
11. Mignolet, B., Levine, R.D., Remacle, F.: Charge migration in the bifunctional PENNA cation induced and probed by ultrafast ionization: a dynamical study. J. Phys. B Atomic Mol. Phys. **47**(12), 124011 (2014)
12. Remacle, F., Nest, M., Levine, R.D.: Laser steered ultrafast quantum dynamics of electrons in LiH. Phys. Rev. Lett. **99**(18), 183902 (2007)
13. Remacle, F., Levine, R.D.: An electronic time scale in chemistry. Proc. Natl. Acad. Sci. U. S. A. **103**(18), 6793–6798 (2006)
14. Valentini, A., van den Wildenberg, S., Remacle, F.: Selective bond formation triggered by short optical pulses: quantum dynamics of a four-center ring closure. Phys. Chem. Chem. Phys. **22**(39), 22302–22313 (2020)
15. Nikodem, A., Levine, R.D., Remacle, F.: Spatial and temporal control of populations, branching ratios, and electronic coherences in LiH by a single one-cycle infrared pulse. Phys. Rev. A. **95**(5), 053404 (2017)
16. Muskatel, B.H., Remacle, F., Levine, R.D.: AttoPhotoChemistry: probing ultrafast electron dynamics by the induced nuclear motion: the prompt and delayed predissociation of N2. Chem. Phys. Lett. **601**(0), 45–48 (2014)
17. Ekert, A., Knight, P.L.: Entangled quantum systems and the Schmidt decomposition. Am. J. Phys. **63**(5), 415–423 (1995)
18. Horodecki, R., Horodecki, P., Horodecki, M., Horodecki, K.: Quantum entanglement. Rev. Mod. Phys. **81**(2), 865–942 (2009)
19. Nielsen, M.A., Chuang, I.L.: Quantum Computation and Quantum Information. Cambridge University Press, Cambridge (2010)
20. Sanz-Vicario, J.L., Pérez-Torres, J.F., Moreno-Polo, G.: Electronic-nuclear entanglement in ${{\mathrm{H}}_{2}}^{+}$: schmidt decomposition of non-born-oppenheimer wave functions expanded in nonorthogonal basis sets. Phys. Rev. A. **96**(2), 022503 (2017)
21. McKemmish, L.K., McKenzie, R.H., Hush, N.S., Reimers, J.R.: Quantum entanglement between electronic and vibrational degrees of freedom in molecules. J. Chem. Phys. **135**(24), 244110 (2011)

22. Haxton, D.J., Lawler, K.V., McCurdy, C.W.: Multiconfiguration time-dependent Hartree-Fock treatment of electronic and nuclear dynamics in diatomic molecules. Phys. Rev. A. **83**(6), 063416 (2011)
23. Haxton, D.J., Lawler, K.V., McCurdy, C.W.: Qualitative failure of a multiconfiguration method in prolate spheroidal coordinates in calculating dissociative photoionization of ${\mathrm{H}}_{2}{}^{+}$. Phys. Rev. A. **91**(6), 062502 (2015)
24. Vatasescu, M.: Entanglement between electronic and vibrational degrees of freedom in a laser-driven molecular system. Phys. Rev. A. **88**(6), 063415 (2013)
25. Izmaylov, A.F., Franco, I.: Entanglement in the born–oppenheimer approximation. J. Chem. Theory Comput. **13**(1), 20–28 (2017)
26. Hou, X.-W., Chen, J.-H., Ma, Z.-Q.: Dynamical entanglement of vibrations in an algebraic model. Phys. Rev. A. **74**(6), 062513 (2006)
27. Li, J., Kais, S.: Entanglement classifier in chemical reactions. Sci. Adv. **5**(8), eaax5283 (2019)
28. Li, J., Sajjan, M., Kale, S.S., Kais, S.: Statistical correlation between quantum entanglement and spin–orbit coupling in crossed beam molecular dynamics. Adv. Quant. Technol. **4**, 2100098 (2021)
29. Vrakking, M.J.J.: Control of attosecond entanglement and coherence. Phys. Rev. Lett. **126**(11), 113203 (2021)
30. Koll, L.-M., Maikowski, L., Drescher, L., Witting, T., Vrakking, M.J.J.: Experimental control of quantum-mechanical entanglement in an attosecond pump-probe experiment. Phys. Rev. Lett. **128**(4), 043201 (2022)
31. Busto, D., Laurell, H., Finkelstein-Shapiro, D., Alexandridi, C., Isinger, M., Nandi, S., Squibb, R.J., Turconi, M., Zhong, S., Arnold, C.L., Feifel, R., Gisselbrecht, M., Salières, P., Pullerits, T., Martín, F., Argenti, L., L'Huillier, A.: Probing electronic decoherence with high-resolution attosecond photoelectron interferometry. Eur. Phys. J. D. **76**(7), 112 (2022)
32. Blavier, M., Levine, R.D., Remacle, F.: Time evolution of entanglement of electrons and nuclei and partial traces in ultrafast photochemistry. Phys. Chem. Chem. Phys. **24**(29), 17516–17525 (2022)
33. Blavier, M., Gelfand, N., Levine, R.D., Remacle, F.: Entanglement of electrons and nuclei: amost compact representation of the molecular wave function. Chem. Phys. Lett. **804**, 139885 (2022)
34. Bradley, T.-D., Stoudenmire, E.M., Terilla, J.: Modeling sequences with quantum states: a look under the hood. Mach. Learn.: Sci. Technol. **1**(3), 035008 (2020)
35. Blavier, M., Komarova, K., Gonçalves, C.E.M., Levine, R.D., Remacle, F.: Electronic coherences steer the strong isotope effect in the ultrafast Jahn–teller structural rearrangement of methane cation upon tunnel ionization. J. Phys. Chem. A. **125**(43), 9495–9507 (2021)
36. van den Wildenberg, S., Mignolet, B., Levine, R.D., Remacle, F.: Temporal and spatially resolved imaging of the correlated nuclear-electronic dynamics and of the ionized photoelectron in a coherently electronically highly excited vibrating LiH molecule. J. Chem. Phys. **151**(13), 134310 (2019)
37. Ajay, J.S., Komarova, K.G., Remacle, F., Levine, R.D.: Time-dependent view of an isotope effect in electron-nuclear nonequilibrium dynamics with applications to N2. Proc. Natl. Acad. Sci. U. S. A. **115**, 5890–5895 (2018)
38. Golub, G.H., Reinsch, C.: Singular value decomposition and least squares solutions. In: Wilkinson, J.H., Reinsch, C., Bauer, F.L. (eds.) Linear Algebra, pp. 134–151. Springer, Berlin/Heidelberg (1971)
39. Baker, S., Robinson, J.S., Haworth, C.A., Teng, H., Smith, R.A., Chirilă, C.C., Lein, M., Tisch, J.W.G., Marangos, J.P.: Probing proton dynamics in molecules on an attosecond time scale. Science. **312**(5772), 424–427 (2006)
40. Marangos, J.P., Baker, S., Kajumba, N., Robinson, J.S., Tisch, J.W.G., Torres, R.: Dynamic imaging of molecules using high order harmonic generation. Phys. Chem. Chem. Phys. **10**(1), 35–48 (2008)
41. Mondal, T., Varandas, A.J.C.: The Jahn-teller effect in the triply degenerate electronic state of methane radical cation. J. Chem. Phys. **135**(17), 174304 (2011)

42. Mondal, T., Varandas, A.J.C.: On extracting subfemtosecond data from femtosecond quantum dynamics calculations: the methane cation. J. Chem. Theory Comput. **10**(9), 3606–3616 (2014)
43. Mondal, T., Varandas, A.J.C.: Structural evolution of the methane cation in subfemtosecond photodynamics. J. Chem. Phys. **143**(1), 014304 (2015)
44. Gonçalves, C.E.M., Levine, R.D., Remacle, F.: Ultrafast geometrical reorganization of a methane cation upon sudden ionization: an isotope effect on electronic non-equilibrium quantum dynamics. Phys. Chem. Chem. Phys. **23**(21), 12051–12059 (2021)
45. Zhang, T., Golub, G.H.: Rank-one approximation to high order tensors. Siam J. Matrix Anal. Appl. **23**(2), 534–550 (2001)
46. Baiardi, A., Reiher, M.: Large-scale quantum dynamics with matrix product states. J. Chem. Theory Comput. **15**(6), 3481–3498 (2019)
47. Larsson, H.R., Zhai, H., Gunst, K., Chan, G.K.-L.: Matrix product states with large sites. J. Chem. Theory Comput. **18**(2), 749–762 (2022)
48. Schollwöck, U.: The density-matrix renormalization group in the age of matrix product states. Ann. Phys. **326**(1), 96–192 (2011)

An MQDT Model for the Description of Time Resolved Pump Probe Experiments

Miguel Alarcón and Chris H. Greene

Abstract A method based on multichannel quantum defect theory (MQDT) for the treatment of perturbative and time resolved photoionization in pump probe experiments is presented. Following an introduction to the theory, examples in two regimes of argon are presented. The theory successfully describes the energy distribution and the dependence on probe delay of the photoionization spectrum. We finalize with a discussion about angular distributions and possible further applications of the method.

Keywords MQDT · Time resolved spectroscopy · Pump-probe spectroscopy

1 Introduction

In a recent study [1] a new methodology to resolve energy levels in pump probe spectroscopy experiments was proposed and used in argon as a proof of concept. The method increases the possible energy resolution by exploiting the photoelectron signal coming from autoionizing states in combination with the oscillation as a function of probe time delay. This study provides details on the theoretical method utilized to describe the experiment. In view of existing theoretical descriptions based on single active electron methods interacting with the atom with effective potentials [2, 3], we propose a method based on the MQDT wave functions [4] which has a more comprehensive description of the atom that describes inter-channel interactions. Section 2 provides a brief introduction to the main ideas of MQDT and points to references where more complete descriptions of the theory are presented. Section 3 describes the method utilized for the description of argon in different energy regions. This section will explain the theory for both autoionizing

M. Alarcón (✉) · C. H. Greene
Department of Physics and Astronomy, Purdue University, West Lafayette, IN, USA
e-mail: malarco@purdue.edu

L. Argenti et al. (eds.), *Proceedings of the 8th International Conference on Attosecond Science and Technology*, Springer Proceedings in Physics 300,
https://doi.org/10.1007/978-3-031-47938-0_10

state wave packets and purely bound state packets. We conclude with an overview of the future directions of research and other possible systems to be treated with this method.

2 Introduction to MQDT

Multichannel quantum defect theory was developed in its current form by Michael Seaton in the mid 1960s with the intention of leveraging the power of analytic methods for the treatment of complex atomic systems in which the outermost electron interacts with the residual ionic core with a known central potential and there are many interacting channels [5]. Initially used to treat Rydberg atoms, it was then extended by the extensive work of Fano [6], C.H. Greene [7, 8] and their collaborators to treat more general systems.

A complete description of the different uses and details about general multichannel calculations and their application for the description of a plethora of experiments can be found in the work of Aymar et al. [4]. Here we will focus on describing multichannel functions for a Rydberg atom using the *eigenchannel* description introduced by Fano [6].

The degenerate solutions to the time independent Schrödinger equation at a fixed energy, at electron distances outside the core where the equation can be separated into a *fragmentation coordinate* (which for our use case will be the distance between the ionic core and the outermost electron) and *core coordinates* (which are the spin and angular degrees of freedom of the atom, as well as the coordinates of all the core electrons) is a linear combination of the form:

$$\psi_\beta = \sum_i \Phi_i(\omega) F_{i\beta}(r)/r \tag{1}$$

where the sum is over all the channels. The functions of the fragmentation coordinate will, in general, follow a set of coupled differential equations. Nonetheless, for a large enough value of r, say $r > R_o$, the equations decouple and the solutions are given in terms of a linear combination of functions known analytically. For a Rydberg atom these functions are the well known Coulomb functions.

The two functions, when energy normalized, are commonly referred to as f and g, the former being regular at the origin and the latter diverging as $r \to 0$. For $r > R_o$ the solution has the form:

$$\psi_\beta = \sum_i \Phi_i(\omega)(f_i(r) I_{i\beta} - g_i(r) J_{i\beta})/r \quad r > R_o, \tag{2}$$

for some coefficient matrices I and J. The functions f and g depend on the channel i and on the independent solution index β since each residual ion state might be different, leading to different kinetic energies for the outer electron and different

angular momentum. In order to completely determine the solution, we must solve the equation for the region $r < R_o$. Here we would impose continuity of the logarithmic derivative and thus find the value of the matrix of coefficients I and J. To find physically relevant solutions, boundary conditions are imposed at infinity. Therefore it is expected that the coefficient matrices vary smoothly with energy, and that the strong variation of the wave functions on energy will derive from the imposition of $r \to \infty$ boundary conditions.

One particularly useful set of solutions are the so called *eigenchannels*. This concept, introduced by Fano [6], assumes that there is a set of channels that are approximate eigenstates of the hamiltonian near the core region. The solutions are then characterized by a set of eigen quantum defects $\{\mu_\alpha\}$, representing the elastic quantum scattering phase of each one of the eigenchannels, and a change of basis matrix $U_{i\alpha}$ that transforms from one set of channels into the other. The physical wave functions are then given by:

$$\psi_\beta = \sum_\alpha \sum_i \Phi_i(\omega)/r \left[f_i(r) U_{i\alpha} \cos(\pi \mu_\alpha) - g_i(r) U_{i\alpha} \sin(\pi \mu_\alpha) \right] A_\alpha^\beta. \tag{3}$$

In general the parameters μ_α and $U_{i\alpha}$ depend on the energy E and, in many cases, a linear E-dependence is enough to describe most of the spectra. The fact that near the core the spin orbit effects are diminished and that the total orbital angular momentum and total spin are approximately conserved, implies that for many atoms the eigenchannels are but small deviations from the LS coupled channels. Therefore it is assumed that the eigenchannel transformation factorizes as $U_{i\alpha} = \sum_{\overline{\alpha}} U_{i\overline{\alpha}} V_{\overline{\alpha}\alpha}$, where channels $\overline{\alpha}$ are the LS coupled channels, $U_{i\overline{\alpha}}$ is the analytically known basis that transforms angular momentum from the scheme in the fragmentation channels into LS coupling, and $V_{\overline{\alpha}\alpha}$ is a matrix close to the identity. The matrix V is generally parameterized as the product of rotation matrices, so that the total number of parameters for n channels is $n(n+1)/2$ or $n(n+1)$ if a linear energy dependence is included.

In order to obtain physically valid wave functions, the coefficients A_α have to be chosen to fulfill the appropriate boundary conditions at infinity. These are: for the closed channels, to vanish at infinity; and for the open channels, to be energy normalized. If angular distribution and/or spin-dependent observables are desired, then it is also necessary to impose the incoming wave boundary condition. In the ionization continuum, there are as many linearly independent physical solutions as there are open channels (channels where the outer electron has a positive energy); those are distinguished by the index β and a phase τ_β. From the asymptotic forms of the coulomb functions it is possible to summarize the boundary conditions in a set of equations:

$$\left.\begin{array}{ll} \sum_\alpha U_{i\alpha} \sin(\pi \mu_\alpha) A_\alpha^\beta = \tan\left(\pi \tau_\beta\right) \sum_\alpha U_{i\alpha} \cos(\pi \mu_\alpha) A_\alpha^\beta & \text{if } i \text{ is open} \\ \sum_\alpha \sin(\pi(\nu_i + \mu_\alpha)) U_{i\alpha} A_\alpha^\beta = 0 & \text{if } i \text{ is closed} \end{array}\right\} \tag{4}$$

When all channels are closed, the system has solutions only for certain energies that correspond to the bound state energies. When there are some open channels the solutions come from a generalized eigenvalue problem which has solutions for all energies, but the coefficients depend strongly on energy owing to the resonance structure of the autoionizing states. Finally, when all channels are open the solution of the eigenvalue problem is $A_\alpha^\beta = \delta_{\alpha\beta}$ and $\tau_\beta = \mu_\beta$.

What we have presented is but one of all the possible, and equivalent, ways of expressing the different solutions. Among them are the reaction (K) and scattering (S) matrix approaches [4], perhaps clearer for scattering problems. Nonetheless this form of the theory is particularly popular since the parameters μ_α and $U_{i\alpha}$ can be optimized to fit experimental data.

3 MQDT of the Argon Atom

Treatments of the noble gas atoms were among the first [9–12] and most successful applications of the MQDT formalism. Motivated by the experimental data we recognized that in order to describe the multi-photon processes we had to determine wave functions for symmetries $J^\Pi = 0^+, 1^-, 2^+, 3^-, 4^+$ and 5^-. We used the eigenchannel formalism described in the previous section, choosing the LS coupled channels as the eigenchannels and J_{cs} coupled channels as the fragmentation channels.

It is not the objective of this study to propose a calculation for the wave function inside the core region. Thus we will assume that the Coulomb solution is valid in all the dissociation coordinate. This is a decent approximation since the excited states are Rydberg states and the outermost electron is mostly outside the core. We regularize the divergence near the origin coming from the irregular Coulomb function by using the Seaton-Burgess cutoff procedure [13].

We must stress that our treatment goes significantly beyond a single active electron model since electron-core collisions and recollisions, that can change the core states and are consistent with angular momentum conservation, are included in the multichannel wavefunction.

3.1 Autoionizing Wave-Packets

In the experiment, a linearly polarized short-pulse laser uses the 9th harmonic to excite the ground state to a linear combination of low-lying bound states. From there the fundamental harmonic excites the autoionizing states of the 2^+ and 0^+ symmetry. These encompass five different outgoing waves. Looking at the density of states in the autoionizing continuum shows that the f states are very narrow, whereby the resonances have predominantly bound character and are long lived. In

comparison, the p states are much shorter lived. Therefore the final autoionizing wave packet will be effectively described by a bound wave-packet of only f states, except for very short times.

The wave function used here is then of the form:

$$\psi_o = \sum_n A_n \psi_n, \tag{5}$$

where the ψ_n function represents the bound part of the nth autoionizing f resonances. These have the explicit form

$$\psi_n = \frac{u_{n,3}(r)}{r} \xi_{1/2} \, |[(1/2, 1/2)1, 3]2, 0\rangle \,, \tag{6}$$

where the kets represent the channel functions in J_{cs} coupling as $|[(j_c, s_e)J_{cs}, \ell]J, M\rangle$ and $\xi_{1/2}$ is the wave function of the core electrons in the $3p_{1/2}$ ion state. In this case only $j_c = 1/2$ are present since this is the excited core state that supports bound states (or strictly speaking, Fano-Feshbach resonances) at this energy.

Following the delayed probe, the wave function acquires a component in the continuum so that the final wave-packet has the form:

$$\psi = \sum_n A_n(t)\psi_n + \sum_{J\in\{1,2,3\}} \sum_{M=-1}^{1} \int dE \, B_E^{J,M}(t)\psi_{J,M}(E) \tag{7}$$

This calculation only includes continuum states as there are no true bound states that lie within the bandwidth of the probe laser. We are interested in the yield of electrons after the laser has passed, so we want to determine the coefficients for $t \to \infty$. Here the continuum states referred to are those that leave the core in the excited $j_c = 1/2$ energy level.

Calculations of the dipole matrix element to the continuum shows that these high lying states are only weakly coupled to the 1^- and 3^- continuum states, allowing for the use of time dependent perturbation theory. Accordingly, the electron potential energy of interaction with the electromagnetic laser field can be treated classically in the length gauge with the operator

$$V(t) = \mathcal{E}_o \exp\left\{-\left(\frac{t - t_o}{\gamma}\right)^2\right\} \cos(\omega t)\epsilon \cdot r. \tag{8}$$

In atomic units, the intensity of the laser is given by $I = \mathcal{E}_o^2$ and the duration of the pulse, defined here as the full width at half maximum (FWHM) of the intensity, is given by $\gamma\sqrt{2\ln(2)}$.

We use perturbation theory to second order in the electric field strength. To this order the unitary time evolution operator is given by:

$$U(t_1, t_2) = 1 - i \int_{t_1}^{t_2} d\tau_1 e^{iH_o\tau_1} V(\tau_1) e^{-iH_o\tau_1} \tag{9}$$

$$- \int_{t_1}^{t_2} \int_{t_1}^{\tau_1} d\tau_1 d\tau_2 e^{iH_o\tau_1} V(\tau_1) e^{-iH_o(\tau_1-\tau_2)} V(\tau_2) e^{-iH_o\tau_2}. \tag{10}$$

Then the transition matrix is $T = U(-\infty, \infty)$, and the photoionization probability can be obtained as the transition matrix element connecting to the initially-excited wave-packet:

$$\begin{aligned} B_E^{J,M}(\infty) = & -i\delta_{j_c,1/2}\delta_{J_{cs},1} \sum_n A_n \mathcal{E}_o \sqrt{\pi}\gamma/2 \exp\left\{-\gamma^2 \frac{(\epsilon_{1/2} - \epsilon_n - \omega)^2}{4}\right\} \\ & e^{i(\epsilon_{1/2}-\epsilon_n-\omega)t_o} \left\langle \epsilon_{1/2}; \ell \left|\left| r^{(1)} \right|\right| \epsilon_n; 3 \right\rangle \times \\ & (-1)^{1+3+J+1}[J][2] \begin{Bmatrix} \ell & J & 1 \\ 2 & 3 & 1 \end{Bmatrix} \sum_q (-1)^q \epsilon_{-q} \begin{pmatrix} 2 & 1 & J \\ 0 & q & -M \end{pmatrix}. \end{aligned} \tag{11}$$

Here $\epsilon_{1/2} = E - E_{1/2}$ is the kinetic energy of the photoelectron relative to the $3p_{1/2}$ argon ionization threshold, ℓ is the orbital angular momentum of the photoelectron, ϵ_n is the energy of the autoionizing state with respect to the same threshold, $\langle \cdot \left|\left| r^{(1)} \right|\right| \cdot \rangle$ is the reduced matrix element of the electric dipole operator and $[x] \equiv \sqrt{2x+1}$. The possible values for ℓ are 2 and 4.

This transition matrix element shows the origin of quantum beats in the photoionization signal as a function of the time delay. Notice also the role of the duration of the laser in limiting the region where these beats take place. The Gaussian factor limits the beats to only those states which can be taken to the same continuum energy with frequencies that are within the bandwidth of the laser.

Conservation of parity implies that the first nonvanishing correction to the initial autoionizing states must be second order in the field strength. For states that are initially populated, this gives a second order correction to the probability deriving from the cross terms involving the initial amplitude:

$$|\langle \psi_f | T | \psi_o \rangle|^2 = |A_f|^2 + \mathrm{Re}\left\{ A_f^* \langle \psi_f | T^{(2)} | \psi_o \rangle \right\} + O(\mathcal{E}_o^4). \tag{12}$$

This insight is key. It explains why the observed modification of the autoionization signal due to the probe laser is observed at the energies of the f $J = 2$ states only. This second order term can be interpreted as a two-photon Raman transition, with the continuum states above the $j_c = 1/2$ threshold as the relevant intermediate states.

The expression involves a time ordered integral over the field profile. In addition, to evaluate the exponential of the unperturbed hamiltonian, it is necessary to represent the identity operator in terms of eigenstates. Nonetheless, we can make some approximations that make the significance of this term clearer and have little diminution of the calculation accuracy.

Indeed, the second order term of transition matrix element looks like:

$$\begin{aligned}\left\langle \psi_f \right| T^{(2)} \left| \psi_o \right\rangle = -\sum_n A_n \mathcal{E}_o^2 \exp\left\{ -\gamma^2 \frac{(E_f - E_n)^2}{8} + i(E_f - E_n)t_o \right\} \times \\ \frac{\gamma^2 \pi}{8} \iint\limits_{\xi} dE_\xi \left\langle \psi_f \right| \epsilon \cdot r \left| E_\xi \right\rangle \left\langle E_\xi \right| \epsilon \cdot r \left| \psi_n \right\rangle \times \\ \exp\left\{ -\gamma^2 \left(E_\xi - (E_f + E_n)/2 - \omega \right)^2 /2 \right\} \times \\ \left[\operatorname{erf}\left(i \frac{\gamma}{\sqrt{2}} \left(E_\xi - (E_f + E_n)/2 - \omega \right) \right) + 1 \right].\end{aligned} \tag{13}$$

The sum $\iint\limits_{\xi} dE_\xi$ represents the sum/integral over all energies and values of the total and orbital angular momenta of the atom. A key element is the interplay of the bandwidth of the laser, the third line in Eq. 13, which indicates that the intermediate energy of greatest importance corresponds to the average energy between the two autoionizing states plus one photon at the central frequency of the laser. This approximation yields:

$$\begin{aligned}\left\langle \psi_f \right| T^{(2)} \left| \psi_o \right\rangle = -\sum_n A_n \mathcal{E}_o^2 \frac{\gamma \pi^{3/2}}{4\sqrt{2}} \exp\left\{ -\gamma^2 \frac{(E_f - E_n)^2}{8} + i(E_f - E_n)t_o \right\} \times \\ \left\{ \left\langle f; 3 \left\| r^{(1)} \right\| \bar{\epsilon}_{1/2}; 2 \right\rangle \left\langle \bar{\epsilon}_{1/2}; 2 \left\| r^{(1)} \right\| n; 3 \right\rangle F_2(J_f, M_f) \right. \\ \left. + \left\langle f; 3 \left\| r^{(1)} \right\| \bar{\epsilon}_{1/2}; 4 \right\rangle \left\langle \bar{\epsilon}_{1/2}; 4 \left\| r^{(1)} \right\| n; 3 \right\rangle F_4(J_f, M_f) \right\},\end{aligned} \tag{14}$$

where the functions F_2 and F_4 are defined as

$$F_2(J_f, M_f) = \sum_{J=1,2,3} (-1)^{1+J_f+2J+M_f}[J]^2[J_f][2] \begin{Bmatrix} \ell_f & J_f & 1 \\ J & 2 & 1 \end{Bmatrix} \begin{Bmatrix} 2 & J & 1 \\ 2 & 3 & 1 \end{Bmatrix} \times \sum_{q,q'} (-1)^q \epsilon_{-q} \epsilon_{-q'} \begin{pmatrix} J & 1 & J_f \\ q' & q & -M_f \end{pmatrix} \begin{pmatrix} 2 & 1 & J \\ 0 & q' & -q' \end{pmatrix} \tag{15}$$

$$F_4(J_f, M_f) = (-1)^{J_f+1+M_f}\sqrt{5}[J_f] \begin{Bmatrix} \ell_f & J_f & 1 \\ 3 & 4 & 1 \end{Bmatrix} \sum_{q,q'} (-1)^q \epsilon_{-q} \epsilon_{-q'} \begin{pmatrix} 3 & 1 & J_f \\ q' & q & -M_f \end{pmatrix} \begin{pmatrix} 2 & 1 & 3 \\ 0 & q' & -q' \end{pmatrix} \tag{16}$$

with the values $J_f = 2$ and $M_f = 0$.

This expression shows that the second order corrections contain the quantum beats deriving from interfering pathways. Figure 1 compares this theory with the experiment. The spectrograms shown can be viewed as a *differential electron spectrogram* [1], because they show the difference between the total yield with and without the probe. In the theory this amounts to isolating only the second order correction term.

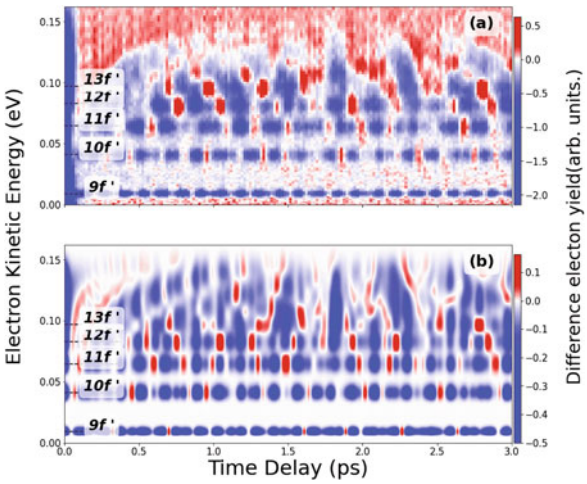

Fig. 1 Differential electron spectrogram for the autoionizing spectrum of argon. Panel (**a**) is the experimental data and panel (**b**) is the theoretical data. Horizontal lines and labels indicate the energy position of the different autoionizing resonances. It is possible to see the how this population transfer sometimes enhances the yield of electrons

3.2 Bound Wave-Packets

After the excitation of the ground state by the 9th harmonic, a wave packet of bound $J^{\Pi} = 1^-$ remains excited. This packet can be photoionized by the probe laser following a two photon absorption. Unlike the previous case, there is a strong coupling between bound states which requires the time propagation of the state to get accurate values for the photoionization probability. Another difference with the previous case is that the multichannel structure of the bound and continuum states is crucial for understanding the experimentally observed spectrogram.

To incorporate all the dynamics, our calculations included states in all the symmetries referenced at the beginning of this section. But we truncated to a limited Hilbert space that includes only the states that are most relevant for the propagation. The calculation includes 4 bound states in the 1^- symmetry and 3 bound states in the 3^- symmetry. At one photon energy above and below these states in the opposite parity there are 17 states in the 0^+, 54 states in the 2^+ symmetry divided into 24 f states and 30 p states and 26 states in the 4^+ symmetry. The first 36 autoionizing states are included for the 0^+ and 2^+ symmetries. Finally, the calculation included 200 states for each open channel, which are uniformly spaced with a resolution of 3.76 meV in the continuum, starting from 50 meV above the $3p_{1/2}$ threshold for the 1^-, 3^- and 5^- symmetries.

For maximum efficiency, the calculation propagates separately the time evolution associated with the probe and the pump pulses. That enables an efficient computation of the cases without overlap, since we can propagate the probe for each one of the bound states and then make a linear combination using the amplitudes found with the pump propagation. The method utilized for time propagating was the split operator method, using the same shape for the time dependent perturbation as in Eq. 8 for both pump and probe. As suggested by Tarana et al. [14], since the time dependence of the perturbation comes only from the electric field profile it is possible to handle the propagation for a single time step as:

$$\psi(t+\delta t) = \exp\{-i\,H_o\delta t/2\}\,O^{\dagger}\exp\left\{-i\hat{\lambda}\int_t^{t+\delta t}\mathcal{E}(\tau)d\tau\right\}O\exp\{-i\,H_o\delta t/2\}\,\psi(t). \tag{17}$$

Here the diagonal operator $\hat{\lambda}$ is the diagonalized form of the dipole operator and the matrix O is its eigenvector-matrix.

As discussed in the introduction, any multichannel wave function is composed of an expansion as in Eq. 3. Therefore, under the current approximation, for any two

multichannel states ψ_1 and ψ_2 the dipole element is expanded as

$$\langle \psi_1 | \hat{\epsilon} \cdot \vec{r} \, | \psi_2 \rangle = \sum_{\alpha_1,\alpha_2} \sum_{i_1,i_2} A^*_{\alpha_1} A_{\alpha_2} U_{i_1\alpha_1} U_{i_2\alpha_2} \mathcal{R}^{i_1\alpha_1 i_2\alpha_2}$$
$$\delta_{j_{c,i_1}, j_{c,i_2}} \delta_{J_{cs,i_1}, J_{cs,i_2}} (-1)^{j_{c,i_1}+l_{i_2}+J_1+1} [J_1][J_2] \begin{Bmatrix} l_{i_1} & J_1 & J_{cs,i_2} \\ J_2 & l_{i_2} & 1 \end{Bmatrix}$$
$$\left\langle \ell_{i_2} \left| \left| r^{(1)} \right| \right| \ell_{i_1} \right\rangle \tag{18}$$

where the symbol $\mathcal{R}$ stands for the Seaton-Burgess cutoff regularized radial integral

$$\mathcal{R}^{i_1\alpha_1 i_2\alpha_2} = \int_0^\infty \left(f_{i_1} \cos(\pi \mu_{\alpha_1}) - g_{i_1} \sin(\pi \mu_{\alpha_1}) \right) r \left(f_{i_2} \cos(\pi \mu_{\alpha_2}) \right.$$
$$\left. - g_{i_2} \sin(\pi \mu_{\alpha_2}) \right) \tag{19}$$

The resulting generated spectrograms, like the ones shown in Fig. 2, capture many of the features observed experimentally. For instance, two features are evidence that indicate ionization with respect to the two different thresholds, even though the pump excites states that are predominantly attached to the $3p_{1/2}$ threshold. This can be observed in this treatment since it utilizes multichannel functions throughout; the small but nonzero mixing of components attached to the $3p_{3/2}$ threshold can accumulate to generate photoelectrons at this energy with

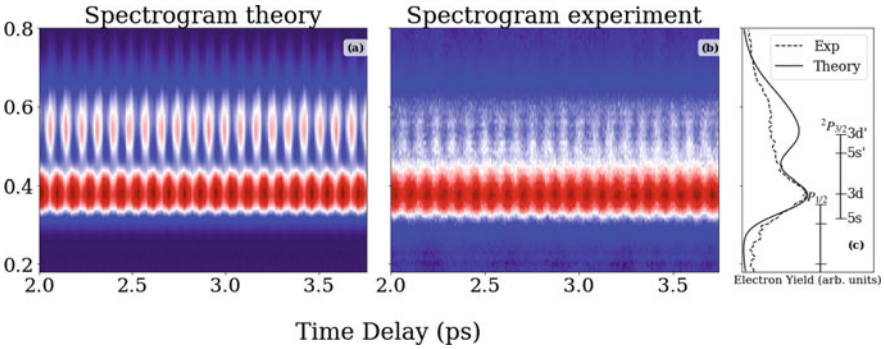

Fig. 2 Panel (**a**) is the theory and panel (**b**) the experiment corresponding to the photoionization of a bound wave-packet of argon following two photon absorption. The two main features correspond to ionization with respect to each distinguishable ion states. The beating demonstrates interference of the interfering two photon absorption pathways from the states excited by the pump. Panel (**c**) shows the position where a monochromatic laser would ionize the aforementioned states and a scaled profile of the mean of the signal. The theory predicts an unobserved excess of electrons leaving the core in the $3p_{3/2}$ state.

considerable probability. Another interesting detail is the fact that the photoelectrons associated with different ionization thresholds have different phases. In this particular atom, the signals are almost $\pi/2$ out of phase. This is also captured by our model as is evident in the figure.

4 Conclusions and Discussion

This study develops a model based on multichannel quantum defect theory to treat photoionization in pump-probe experiments in both time resolved and perturbative methods. We have presented a brief introduction of the MQDT developed by M. Seaton [5] and its recasting by Fano and collaborators [6] based on the concept of eigenchannels.

Two regimes of a pump-probe experiment in argon served as two studied applications of this method. The first was an interpretation of the observed quantum beats in the autoionization region of long-lived nf-states. Even though the model included only the bound part of the wave functions, motivated by the narrowness of the autoionizing resonances, it successfully described the observed quantum beats as well as the energy distribution of the electrons.

The second case explored the photoionization, by two photon absorption, of a bound state wave packet. In this case the strong coupling between bound states via the dipole interactions required the use of a nonperturbative time propagation. Through the use of the split operator formula and a limited Hilbert space composed of the most relevant states, the method was able to describe many of the observed features in the experimental spectrograms. Among them, a considerable phase difference in the electron signal from photoelectrons that leave the ionic core in the different spin orbit thresholds.

One of the key elements this method has not yet explained is the structure of the angular distributions in both cases. As is well known [15], in experiments where all the lasers are linearly polarized and aligned the emitted electrons follow a cylindrically symmetric angular distribution. This distribution is a linear combination of Legendre polynomials. The degree of the maximum Legendre polynomial is determined by the number of photons involved.

In the case of the bound wave packet photoionization, the experiment observes beating angular distributions with a strongly dominant term of order 8. That is the reason behind the inclusion of the 3^-, 4^+ and 5^- symmetries in the Hilbert space, the latter two seemingly unnecessary for a two photon process starting from a 1^- bound state. We discovered that the laser might be strong enough to additionally excite a Raman type transition from the intermediate 2^+ bound states into the 3^- states, which are then photoionized to the 5^- final state symmetry. This is the only discernible pathway so far identified that could account for this process, but in preliminary explorations the theory predicts it to be much weaker than what has been observed experimentally. We leave this study for a future publication.

Another interesting case suitable for a description as presented here is the neon atom. Recently a study of the properties of neon atom photoionization [2, 3] discovered that there is an interesting dependence of the partial wave composition of the photoelectrons with the intensity and the frequency of an array of two co-propagating lasers with commensurate frequencies. Direct application of the model as presented in this article is not possible, since the energy range of the study reaches states that are close to and even in between the ionization thresholds, which would require a number of states that appears to be intractable owing to the small spin orbit splitting in Ne^+. Alternative methods that could extend this method to such a situation are currently being explored. One of them is restricting the valid wave functions to those that fit inside a finite box. We leave the report of those findings for a future publication.

Acknowledgments The research presented here is funded by the U. S. Department of Energy, Office of Science, Office of Basic Energy Sciences, under Award No. DESC0010545. We thank Francis Robicheaux for insightful suggestions. We also thank Arvinder Sandhu, Alexander Plunkett and James K. Wood for their collaboration and invaluable experimental data.

References

1. Plunkett, A., Alarcón, M.A., Wood, J.K., Greene, C.H., Sandhu, A.: Raman interferometry between autoionizing states to probe ultrafast wave-packet dynamics with high spectral resolution. Phys. Rev. Lett. **128**(8), 083001 (2022)
2. Patchkovskii, S., Vrakking, M.J.J., Villeneuve, D.M., Niikura, H.: Selection of the magnetic quantum number in resonant ionization of neon using an XUV-IR two-color laser field. J. Phys. B: At. Mol. Opt. Phys. **53**(13), 134002 (2020)
3. Villeneuve, D.M., Hockett, P., Vrakking, M.J.J., Niikura, H.: Coherent imaging of an attosecond electron wave packet. Science **356**(6343), 1150–1154 (2017)
4. Aymar, M., Greene, C.H., Luc-Koenig, E.: Multichannel Rydberg spectroscopy of complex atoms. Rev. Mod. Phys. **68**(4), 1015–1123 (1996)
5. Seaton, M.J.: Quantum defect theory. Rep. Prog. Phys. **46**(2), 167–257 (1983)
6. Fano, U.: Quantum defect theory of l uncoupling in H2 as an example of channel-interaction treatment. Phys. Rev. A **2**(2), 353–365 (1970)
7. Greene, C.H., Jungene, Ch.: Molecular applications of quantum defect theory. Adv. At. Mol. Phys. **21**(C), 51–121 (1985)
8. Greene, C., Fano, U., Strinati, G.: General form of the quantum-defect theory. Phys. Rev. A **19**(4), 1485–1509 (1979)
9. Lee, C. M., Lu, K.T.: Spectroscopy and collision theory. II. The Ar absorption spectrum. Phys. Rev. A **8**(3), 1241–1257 (1973)
10. Starace, A.: Absolute line strengths by analysis of Lu-Fano plots with application to excited state transitions in neon. J. Phys. B: At. Mol. Phys. **6**(1), 76–92 (1973)
11. Lu, K.T.: Spectroscopy and collision theory. The Xe absorption spectrum. Phys. Rev. A **4**(2), 579–596 (1971)
12. Pellarin, M., Vialle, J.L., Carré, M., Lermé, J., Aymar, M.: Even parity series of argon Rydberg states studied by fast-beam collinear laser spectroscopy. J. Phys. B: At. Mol. Opt. Phys. **21**(23), 3833–3849 (1988)

13. Burgess, A., Seaton, M.J.: A general formula for the calculation of atomic photo-ionization cross sections. Mon. Not. R. Astron. Soc. **120**(2), 121–151 (1960)
14. Tarana, M., Greene, C.H.: Femtosecond transparency in the extreme-ultraviolet region. Phys. Rev. A **85**(1), 013411 (2012)
15. Lindsay, M.D., Cai, L.T., Schinn, G.W., Dai, C. J., Gallagher, T. F.: Angular distribution of ejected electrons from autoionizing 3pns states of magnesium. Phys. Rev. A **45**(1), 231–241 (1992)

ASTRA, A Transition Density Matrix Approach to the Interaction of Attosecond Radiation with Atoms and Molecules

Juan M. Randazzo, Carlos Marante, Siddhartha Chattopadhyay, Heman Gharibnejad, Barry I. Schneider, Jeppe Olsen, and Luca Argenti

Abstract A new formalism and computer code, ASTRA (AttoSecond TRAnsitions), has been developed to treat the interactions of short, intense radiation with molecules. The formalism makes extensive use of transition density matrices, computed using a state-of-the-art quantum chemistry code (LUCIA), to efficiently calculate the many-body inter-channel-coupling interactions required to simulate the highly correlated electron dynamics due to atoms and molecules exposed to attosecond laser radiation.

Keywords Close coupling · Molecular ionization

J. M. Randazzo
Department of Physics and CREOL, University of Central Florida, Orlando, FL, USA

CONICET, San Carlos de Bariloche, Río Negro, Argentina

C. Marante · S. Chattopadhyay · L. Argenti (✉)
Department of Physics and CREOL, University of Central Florida, Orlando, FL, USA
e-mail: luca.argenti@ucf.edu

H. Gharibnejad
National Institute of Standards and Technology, Applied and Computational Mathematics Division, Gaithersburg, MD, USA

Computational Physics Inc., Springfield, VA, USA

B. I. Schneider
National Institute of Standards and Technology, Applied and Computational Mathematics Division, Gaithersburg, MD, USA

J. Olsen
Department of Chemistry, Aarhus University, Aarhus, Denmark

L. Argenti et al. (eds.), *Proceedings of the 8th International Conference on Attosecond Science and Technology*, Springer Proceedings in Physics 300,
https://doi.org/10.1007/978-3-031-47938-0_11

1 Introduction

Advances in laser technology have enabled the production of extreme-ultraviolet and X-ray attosecond pulses with ever increasing intensity and repetition rates [1, 2]. As a result, statistically significant attosecond-pump attosecond-probe experiments for molecular systems of chemical relevance are now possible. This technology has opened the way to the detailed time-resolved study of photoelectron emission from valence and core orbitals, of vibronic coupling in photoemission, and of Auger cascades. Since these experiments entail the formation of highly correlated and entangled photofragments, close-coupling (CC) is an ideal approach to simulate and interpret them. CC single-ionization codes suited for small molecules in interaction with XUV pulses, such as XCHEM [3, 4] and UKRmol+ [5], already exist. However, a common theoretical and software framework that is extensible to multiple ionization, that can represent both slow (∼1 eV) and fast (∼1 keV) photoelectrons and that scales favorably with molecular size is still unavailable.

Based on these requirements, we have developed an innovative approach to the CC scheme, based on the use of high-order Transition Density Matrices (TDMs) between large-scale-CI ionic states with arbitrary symmetry and multiplicity, which we have implemented in a suite of codes named ASTRA (AttoSecond TRAnsitions). These TDMs, are not typically available in standard quantum-chemistry codes. Here, they are computed using the general string formalism [6] of the LUCIA code [7], which enables us to evaluate inter-channel matrix elements of arbitrary many-body operators with high efficiency. Currently, ASTRA is restricted to single-ionization states but work is currently underway to extend it to double-escape channels. ASTRA employs a hybrid Gaussian-B-spline basis and hence most of the one- and two-electron integrals must be computed numerically [5, 8]. In this paper, we illustrate the current capabilities of ASTRA to calculate eigen-energies and total photoionization cross sections (PICS) for several systems. First, we present results on the N_2 molecule and on the boron atom for which accurate benchmark theoretical and experimental results exist. Second, we present some calculations on the PICS in formaldehyde (H_2CO) as an example of an intermediate-size polyatomic molecule for which some experimental results are also available. Finally, we present the results of preliminary calculations for the PICS of magnesium porphyrin ($MgH_{12}C_{20}N_4$), a large polyatomic molecule with 37 atoms.

The paper is organized as follows: in Sect. 2 we summarize the theoretical approach to the many-electron close-coupling (CC) method. First, we present the formulas needed to calculate one- and two-electron matrix elements within the CC space, expressed in terms of transition density matrices. Second, we show how these quantities are used to evaluate some relevant observables such as the parameters of autoionizing states and the total photoionization cross section. Finally we give some remarks about how the hybrid orbital basis is built. Section 3 offers a brief discussion of the workflow in ASTRA and its auxiliary codes. In Sect. 4 we show results for the nitrogen molecule, atomic boron, formaldehyde, and the magnesium-porphyrin complex. Finally, in Sect. 5, we offer our conclusions.

2 Theoretical Methodology

2.1 Single-Ionization Close-Coupling Space

In ASTRA, each CC channel corresponds to an antisymmetrized product of a molecular ionic state $|A\rangle$, with $N-1$ electrons, and a spin-orbital $|P\rangle$ for an additional N-th electron, which may either be bound to the ion or lie in the continuum. The ion and the N-th electron are also coupled so to give rise to a well defined spin multiplicity. In ASTRA, we consistently use the largest spatial-invariance group of the molecule that is also a subgroup of D_{2h} to label all the electronic orbitals. In terms of the second quantization formalism [7], we can write:

$$|A,\, p;\, S\Sigma\rangle = \sum_{\Sigma_A \pi} C^{S\Sigma}_{S_A \Sigma_A, \frac{1}{2}\pi} a^{\dagger}_{p_\pi} |A_{\Sigma_A}\rangle, \tag{1}$$

where $a^{\dagger}_{p\pi}$ is the creator operator for an electron in the spatial orbital p with spin projection $\pi \in \{\frac{1}{2}, -\frac{1}{2}\}$ (spin up or spin down) [9], and $C^{c\gamma}_{a\alpha,b\beta}$ are Clebsch-Gordan coefficients [10]. The correlated ionic states $|A_{\Sigma_A}\rangle$ are obtained with the LUCIA code by means of a Complete Active Space (CAS) configuration-interaction (CI) calculation. The orbitals for this CASCI can be obtained from a single-state multi-configuration self-consistent field (MCSCF) calculation using the DALTON program, or from a state-averaged MCSCF calculation using LUCIA. The state-averaged MCSCF calculations of LUCIA allow the optimization of an ensemble energy of a set of states with identical or different spatial symmetries, multiplicities and number of electrons.

2.2 Operator Matrix Elements with TDM Formalism

Consider next the evaluation of the matrix-elements of general singlet one- and two-body operators [7],

$$\hat{O} = o_{rs} a^{\dagger}_{r\sigma} a_{s\sigma} \qquad \text{and} \qquad \hat{G} = \frac{1}{2} g_{pqrs} a^{\dagger}_{p_\theta} a^{\dagger}_{r_\sigma} a_{s_\sigma} a_{q_\theta}, \tag{2}$$

where summation over repeated indexes is assumed. Using the commutation relations of the creation and annihilation operators, the overlap, one- and two-body CC matrix elements can be written as [11]:

$$\langle A | a_{p_\pi} a^{\dagger}_{q_\theta} | B \rangle = s_{pq} \delta_{\pi\theta} \delta_{AB} - \rho^{BA}_{p_\pi q_\theta}, \tag{3}$$

$$\begin{aligned}\langle A,\, P|\hat{O}|B,\, Q\rangle = s_{pq}\delta_{\pi\theta}\langle A|\hat{O}|B\rangle + \delta_{AB}\delta_{\pi,\theta}o_{pq} \\ -\rho^{BA}_{p_\pi,r_\theta}o_{rq} - o_{ps}\rho^{BA}_{s_\pi,q_\theta} + o_{rs}\pi^{BA}_{s_\sigma p_\pi,q_\theta r_\sigma}\end{aligned} \tag{4}$$

and

$$\begin{aligned}\langle A,\, P|\hat{G}|B,\, Q\rangle = \langle A|\hat{G}|B\rangle s_{pq}\delta_{\pi\theta} + \delta_{\pi\theta}[pq|rs]\rho^{BA}_{s_\rho,r_\rho} - [ps|rq]\rho^{BA}_{s_\pi,r_\theta} \\ + [pt|rs]\pi^{BA}_{t_\pi s_\rho,r_\rho q_\theta} + [qt|rs]\pi^{BA}_{p_\pi s_\rho,r_\rho t_\theta} - \frac{1}{2}[tu|rs]\gamma^{BA}_{u_\tau s_\rho p_\pi,t_\tau r_\rho q_\theta},\end{aligned} \tag{5}$$

respectively. In Eqs. (3)–(5) we have introduced the one-, two- and three-body TDMs between ionic states:

$$\begin{aligned}\rho^{BA}_{q_\theta,p_\pi} &\equiv \langle A|a^\dagger_{p_\pi}a_{q_\theta}|B\rangle, \\ \pi^{BA}_{r_\rho s_\sigma,p_\pi q_\theta} &\equiv \langle A|a^\dagger_{p_\pi}a^\dagger_{q_\theta}a_{s_\sigma}a_{r_\rho}|B\rangle \\ \gamma^{BA}_{s_\sigma t_\tau u_\mu,p_\pi,q_\theta r_\rho} &\equiv \langle A|a^\dagger_{p_\pi}a^\dagger_{q_\theta}a^\dagger_{r_\rho}a_{u_\mu}a_{t_\tau}a_{s_\sigma}|B\rangle.\end{aligned} \tag{6}$$

The evaluation of CC matrix elements only require first-, second- and third-order TDMs between correlated ions, the one- and two-electron integrals between the orbitals and the matrix elements of the operators involving the ionic states. The TDMs between ions of different spatial symmetry and spin multiplicity are the most challenging quantities to evaluate. In ASTRA, this calculation is accomplished with high efficiency using LUCIA. The density matrices are initially calculated over spin-orbitals and can then be transformed to a spin-coupled form. For single ionization, the third-order TDMs are only needed to compute the matrix elements between ionic states augmented by electrons in active orbitals in the ionic states themselves. In this case, however, there is no involvement of hybrid functions and hence all the necessary matrix elements can be directly computed within the LUCIA code. As a result, in the implementation of this method, the third-order TDMs can be and are bypassed.

The equations for general operators in a close coupling space are used to evaluate the Hamiltonian, H, overlap, dipole matrix elements, and complex-absorption potential between states in all the multiplicities and symmetries relevant for an atomic or molecular system of interest. These matrices are the building blocks from which it is possible to compute bound and scattering states of the system, how the system evolves under the action of external pulses, the resulting distribution of the photofragments, as well as the optical response of the system, reflected in the spectrum of the transmitted or emitted radiation.

2.3 Observables

In this work, we focus on the structural parameters of bound and autoionizing states for selected systems, as well as on the total single photoionization cross section of the system from its ground state. All these quantities are obtained by diagonalizing the total fixed-nuclei electronic Hamiltonian, $\tilde{H}$, in a quantization box, with the addition of a complex absorption potential, V_{CAP}, which prevents artificial reflections of the photoelectron from the box boundary,

$$\begin{aligned} \tilde{H} &= H + V_{\mathrm{CAP}} \\ H &= \sum_{A>B} \frac{Z_A Z_B}{|\vec{R}_A - \vec{R}_B|} + \sum_i \left[\frac{p_i^2}{2} - \sum_A \frac{Z_A}{|\vec{r}_i - \vec{R}_A|} \right] + \sum_{i>j} \frac{1}{|\vec{r}_i - \vec{r}_j|} \\ V_{\mathrm{CAP}} &= -ib \sum_i \theta(r_i - R_{\mathrm{CAP}})\,(r_i - R_{\mathrm{CAP}})^2, \qquad b \in \mathbb{R}_0^+ \end{aligned} \tag{7}$$

where Z_A and $\vec{R}_A$ are the charge and position of nucleus A, $\vec{r}_i$ and $\vec{p}_i$ are the position and momentum operator of the i-th electron, $\theta(x)$ is the Heaviside step function, b is a real positive constant, and R_{CAP} is a distance from the from the origin chosen a few tens of atomic units smaller than the size of the quantization box, but larger than the radius within which the ionic states have appreciable electronic density.

Let $|\boldsymbol{\phi}\rangle = (|\phi_1\rangle, |\phi_2\rangle, \ldots)$ be the CC basis and $\tilde{\mathbf{H}} = \langle \boldsymbol{\phi}|\tilde{H}|\boldsymbol{\phi}\rangle$ be the representation of the Hamiltonian with CAPs in this basis. The diagonalization of $\tilde{\mathbf{H}}$ can be written as

$$\tilde{\mathbf{H}} = \mathbf{U}_R \tilde{\mathbf{E}} \mathbf{U}_L^{\dagger}, \tag{8}$$

where $\tilde{\mathbf{E}}_{ij} = \delta_{ij}\tilde{E}_i$ is the diagonal matrix of the complex eigenvalues of the projected $\tilde{H}$, whereas $\mathbf{U}_{L/R}$ are the left/right eigenvectors, normalized so that $\mathbf{U}_L^{\dagger}\mathbf{U}_R = \mathbf{1}$. The complex energies thus obtained can be grouped in three types. (i) Those below the first ionization threshold, which have negligible imaginary part, since they represent bound state that do not reach into the CAP region. (ii) Sequences of eigenvalues that depart from each threshold and acquire rapidly large negative imaginary components, representing non-resonant continuum states. (iii) Isolated complex eigenvalues $\tilde{E}_i = \bar{E}_i - i\,\Gamma_i/2$, where $\bar{E}_i = \Re e(\tilde{E}_i)$ and $\Gamma_i = -2\Im m(\tilde{E}_i)$, which are largely independent on the choice of the extinction parameter c, and which represent the complex energies of autoionizing states. Indeed, such states can be regarded as Siegert states [12], i.e., states that comply with outgoing boundary conditions in all ionization channels. This complex representation of

the Hamiltonian allows us to write down an explicit expression for the retarded resolvent $G_0^+(E) = [E - H + i0^+]^{-1}$ in the CC basis,

$$\mathbf{G}_0^+(E) = \mathbf{U}_R \frac{1}{E - \tilde{\mathbf{E}}} \mathbf{U}_L^\dagger, \tag{9}$$

which we can use to compute the total photoionization cross section as a function of the photon angular frequency ω, for a fixed molecular orientation, $\sigma_{\text{tot}}(\omega)$

$$\begin{aligned}
\sigma_{\text{tot}}(\omega) &= \frac{4\pi^2\omega}{c} \sum_\alpha |\langle \Psi_{\alpha E_g+\omega} | \hat{\epsilon} \cdot \vec{\mu} | g \rangle|^2 = \\
&= \frac{4\pi^2\omega}{c} \langle g | \hat{\epsilon} \cdot \vec{\mu} \left[\int d\varepsilon \sum_\alpha |\Psi_{\alpha\varepsilon}\rangle\langle\Psi_{\alpha\varepsilon}| \delta(\varepsilon - E_g - \omega) \right] \hat{\epsilon} \cdot \vec{\mu} | g \rangle = \\
&= -\frac{4\pi\omega}{c} \Im m \left\{ \langle g | \hat{\epsilon} \cdot \vec{\mu} \left[\int d\varepsilon \sum_\alpha \frac{|\Psi_{\alpha\varepsilon}\rangle\langle\Psi_{\alpha\varepsilon}|}{E_g + \omega - \varepsilon + i0^+} \right] \hat{\epsilon} \cdot \vec{\mu} | g \rangle \right\} = \\
&= -\frac{4\pi\omega}{c} \Im m \Big[\langle g | \, \hat{\epsilon} \cdot \vec{\mu} \; G_0^+(E_g + \omega) \; \hat{\epsilon} \cdot \vec{\mu} \, | g \rangle \Big],
\end{aligned} \tag{10}$$

where $|g\rangle$ is the ground state of the target, $c \simeq 137.035$ is the speed of light, in atomic units, $\hat{\epsilon}$ is the light polarization, $\vec{\mu} = -\sum_{i=1}^{N_e} \vec{r}_i$ is the electronic dipole moment, and $|\Psi_{\alpha E}\rangle$ are a complete set of orthonormal open single-ionization scattering states, $\langle \Psi_{\alpha E} | \Psi_{\beta E'} \rangle = \delta_{\alpha\beta}\delta(E - E')$, labelled by the channel index α. Equation (10), which is nothing other than the optical theorem applied to photoionization processes, is useful because it does not require the actual calculation of a complete set of scattering states satisfying well-defined boundary conditions. Scattering states, which are needed to compute partial differential photoelectron distributions, will be the subject of future studies.

2.4 Orbitals and Integrals

The selection and partitioning of orbitals play an essential role in ASTRA. We represent the ions in a basis of inactive and active self-consistent molecular orbitals, obtained as described in the previous section. An additional set of virtual molecular orbitals are used to represent the polycentric character of the photo-electron functions. A large set of hybrid functions, which are an admixture of polycentric Gaussian and spherical B-spline functions, complete the residual set of accessible single-particle configurations from the origin to a flexible boundary R_0, which is typically as large as 50 Bohr radii, but it can be larger without compromising the convergence of the calculations. Finally, a set of spherical B-splines is used to span the outer region.

It is convenient to divide the whole orbital space into an internal set, whose orbitals are polycentric in character and spatially cover the molecular region, and an external set, spherical in character, which does not overlap with the ion and can extend to distances as large as several hundred atomic units. This distinction enables us to design efficient algorithms, and to reduce the size of the one- and two-electron integrals in the calculations, which are currently calculated using the public GBTO library, developed as part of the UKRmol+ suite [5]. Alternative algorithms to compute these integrals, based on generalizations of the Becke partitioning approach to continuum functions, are being tested [8].

3 Software Structure

In this section, we provide a brief description on how various observables are computed using the ASTRA software and the codes it employs. The molecular geometry, charge, and Gaussian orbital basis set are detailed in the MOLECULE.INP file. ASTRA uses this file, together with the DALTON.INP configuration file, to run the DALTON program [13], which computes the one-body and two-body electronic integrals over atomic orbitals, needed for the subsequent steps of the calculation. Next, ASTRA calls the LUCIA program three times. In the first call, LUCIA uses the atomic integrals generated by DALTON to perform an SCF or MCSCF calculation and determine optimized ionic wave functions. In a second call, LUCIA determines the one-body TDMs between the ionic wave functions. A final call to LUCIA computes higher-order TDMs between ions as well as the Hamiltonian and dipole matrix elements between ionic states augmented by any of the molecular orbitals that are active in the ions. The GBTO library is called to orthonormalize the hybrid basis set and evaluate the one- and two-electron integrals [5]. Subsequently, ASTRA evaluates the matrix elements of any operator required (typically, the Hamiltonian, the overlap, and the electric dipole) in the close-coupling basis generated by augmenting the ions with an electron in either an active molecular orbital, a hybrid orbital, or an external B-spline spherical function, using the formulas listed in Eqs. (3)–(5). From the close-coupling matrix elements of these fundamental operators, ASTRA computes the field-free bound states and the Siegert states [12], as well as the total photoionization cross section of the system, to the lowest order of perturbation theory, or its transient absorption spectrum, by solving the time-dependent Schrödinger equation in the presence of arbitrary external fields. The implementation of a scattering-states solver is under way.

4 Results

In this section we illustrate some of the capabilities of ASTRA by applying it to a few relevant systems: the nitrogen molecule, the boron atom, and the formaldehyde

molecule, for which several data from the literature are available, as well as Mg-porphyrin, a large biologically relevant organo-metallic complex.

4.1 Nitrogen

The N_2 molecule is an attractive benchmark for the fixed-nuclei calculation of the total photoionization cross section since, due to the relatively large mass of its nuclei, the energy separation between different vibrational states is smaller than the Auger width of some autoionizing states that dominate the spectrum. Here, we focus on the energy region within 20 eV from the ground state, where the states are well approximated by single excitations. For this work, we use a cc-pVTZ basis for the ionic orbitals, a quantization box with maximum radius $R_{\text{box}} = 400$ a.u., and a maximum orbital angular momentum for both the internal and the external B-spline basis $\ell_{\max} = 3$. The internuclear distance is chosen to coincide with the equilibrium distance determined experimentally, $R_{\text{N-N}} = 1.098$ Å [14].

In the left panel of Fig. 1, we compare the quantum defect of the $^1\Sigma_g^+$ bound states, $\delta_n = n - [2(E_{\text{th}} - E_n)]^{-1/2}$, where E_{th} is the first ionization threshold, computed with ASTRA and with XCHEM [4], finding an excellent agreement. In the right panel, we compare the XCHEM and ASTRA prediction for the total photoionization cross section between the second and third single-ionization thresholds with four different sets of experimental measurements. Overall, ASTRA is in good agreement with XCHEM and its predictions are marginally closer to the experimental results. ASTRA CC approach captures well not only the position and width of the main resonances and the absolute value of the background signal,

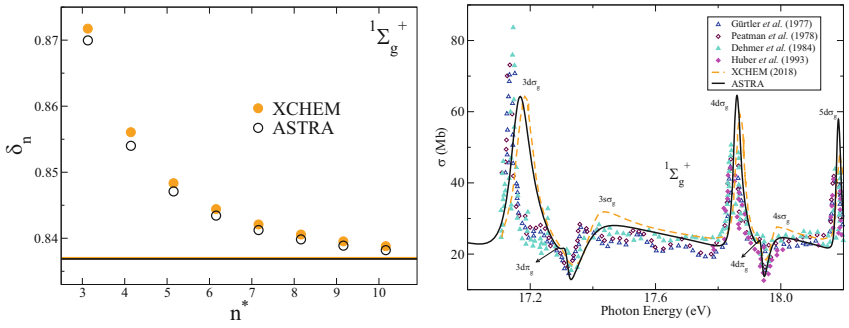

Fig. 1 Left: Comparison of the quantum defect computed with ASTRA (hollow black circle), which corresponds to one of the $^1\Sigma_g^+$ Rydberg series converging to the first ionization threshold of N_2, with the XCHEM benchmark (solid orange circle). The horizontal lines indicate the asymptotic value the series converge to. Right: Total photoionization cross section of N_2, in the energy region comprising the first few resonances converging to the third ionization threshold. The ASTRA cross section (solid black line) is compared with XCHEM (orange dashed line) [4] and four measured spectra [15–18]

but also the interference profiles for overlapping resonances. These results suggest that, for such a simple molecular system dominated by single excitations, the implementation and performance of ASTRA measure up with those of state-of-the-art codes.

4.2 Boron

Boron is an interesting atomic benchmark for ASTRA because it has three active electrons in an open valence shell, thus requiring ions in the CC space with both singlet and triplet multiplicities. This circumstance allows us to test parts of the code that are not active in the case of systems in a global singlet state, such as those examined in the previous subsection. We use two different close-coupling codes as benchmarks, which were developed independently from each other and from ASTRA: (1) the NewStock atomic photoionization code [19], and (2) a special-purpose high-precision three-active-electron code (TAEC) [20]. Accurate experimental values for bound states energies are also available. In this case, we use an aug-cc-pVTQZ Gaussian basis, $\ell_{\max} = 3$, and $R_{\text{box}} = 300$ a.u.

Table 1 compares the excitation energies of the first few bound states of boron, computed with ASTRA, NewStock, and TAEC, and the corresponding NIST experimental values. The CC space used in ASTRA and NewStock comprises twelve parent ions, whereas the TAEC calculations are conducted using a significantly larger CC expansion (twenty parent ions) and are limited to doublet states. The excitation energies are in the right order for the three calculations and they do not deviate from each other by more than 2%.

The calculation with the dedicated TAEC code are clearly in much closer agreement with the experiment, with discrepancies of the order of only 5 meV across the board. NewStock, which is not optimized for three-active-electron systems and is used in a smaller CC basis, gives results which differ from the experiment by few tens meV. Finally, the results generated by ASTRA are of comparable quality to those computed by NewStock, which is in line with the two codes using the same number of parent ions in the CC expansion. This agreement indicates that the formulas concerning ions with different multiplicity are correctly implemented.

Table 1 Bound state energies of B I, $E - E_{2s^2 2p}$ (eV). The data from the `TAEC` calculations are taken from [20], whereas the experimental value are rounded from the NIST CODATA database [21]

Conf.	`ASTRA`	`NewStock`	`TAEC`	Exp.
$2s2p^2\ (^4P^e)$	3.584	3.564	–	3.552
$2s^2 3s\ (^2S^e)$	4.869	4.881	4.958	4.964
$2s2p^2\ (^2D^e)$	5.916	5.927	5.939	5.933
$2s^2 3p\ (^2P^o)$	5.993	5.990	6.021	6.027
$2s^2 3d\ (^2D^e)$	6.707	6.682	6.785	6.790

4.3 Polyatomic Molecules

In this section we present preliminary results for the total photoionization cross section of formaldehyde (H_2CO), a small polyatomic molecule, and of Mg-porphyrin ($MgH_{12}C_{20}N_4$), a comparatively large molecule.

In the case of formaldehyde, our aim is to show that we can reproduce, with limited effort, the results of dedicated low-resolution Random-Phase-Approximation calculations [22] and experimental measurements [23], in the photon-energy interval between 11 and 22 eV, as shown in the left panel of Fig. 2.

In this case, we use a cc-pVTZ Gaussian basis, $\ell_{\max} = 3$, and $R_{\text{box}} = 400$ a.u. The CC space used for this calculation in ASTRA includes up to the first two ions with energies above the spectral region of interest, to improve the convergence of the CC expansion. As the left panel of Fig. 2 shows, the agreement between ASTRA calculations and the experiment is good and comparable to the one found by Cacelli et al. [22]. These results confirm that ASTRA is capable of giving reliable predictions even for non-linear molecules.

Finally, our aim for Mg-porphyrin is not to demonstrate a good comparison with theoretical photoionization benchmarks (which, to the best of our knowledge, are not available) but to show that ASTRA completes all the steps needed to produce an ionization spectrum in a minimal CC basis. For the present calculation, we restrict the ions to single-determinant doublet states obtained from the Hartree-Fock state of the neutral molecule, computed in a 6-31G Gaussian basis, by removing an electron from any of the eight highest occupied molecular orbitals (i.e., from HOMO-7 to HOMO). The CC space generated from these ions, therefore, is a restricted close-coupling single-excitation (CIS) basis. In this case, $\ell_{\max} = 1$, and $R_{\text{box}} = 200$ a.u. The right panel in Fig. 2 shows the contributions to the total photoionization cross section for a randomly oriented Mg-porphyrin molecule due to the light polarized either parallel or perpendicular to the C_4 molecular symmetry axis, across five

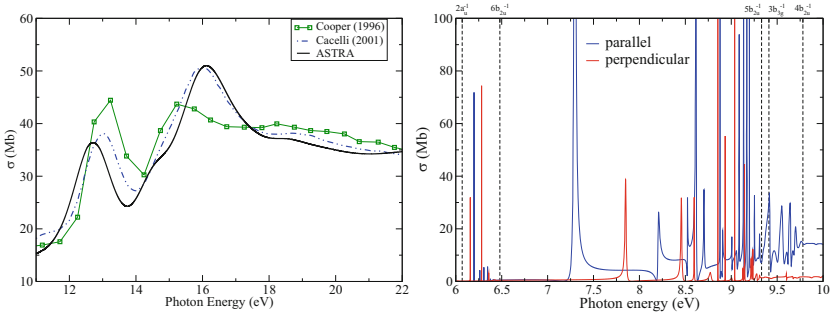

Fig. 2 Left: Comparison of the total PICS of formaldehyde. Both theoretical spectra, ASTRA and Cacelli et al. [22], have been convoluted to simulate the ∼1 eV spectral resolution of the detector used in the experiment [23]. Right: PICS of Mg-porphyrin, computed with ASTRA, for two different directions of the linearly polarized light, across the first six ionization thresholds

consecutive thresholds. The plot shows several complex resonance profiles. While a converged calculation will require further work to properly account for correlation in this complex molecule, it is already clear that this system will exhibit a rich electronic dynamics that ASTRA is well positioned to analyze.

5 Conclusions and Perspectives

We have presented, and implemented in the ASTRA suite of codes, a new close-coupling approach for the ionization of polyatomic molecules that makes extensive use of the efficient transition density matrix formalism (TDMs), and of hybrid Gaussian/numerical basis to accurately reproduce the electronic continuum. The TDMs are obtained from LUCIA, a state-of-the-art quantum-chemistry code for large-scale CI calculations, with excellent scaling properties with respect to the size of the ionic CI expansions. ASTRA implements exact expressions for the matrix elements between arbitrary CC states, including both direct and exchange terms. We have shown that ASTRA can reproduce the results of other established theoretical methods for a few selected atomic and molecular systems for which reliable theoretical ionization cross sections exist. We have also shown that ASTRA is capable of dealing with molecules containing as many as ∼40 atoms. Work to extend ASTRA to the calculation of molecular-frame photoelectron distributions, of ionic states at the Restricted-Active-Space level, and of multiple ionization are currently under way. These extensions hinge on the development of new numerical libraries for the calculation of electronic integrals in hybrid polycentric-Gaussian/numerical bases that converge rapidly regardless of the relative position of the atoms in the system of interest [8].

Acknowledgments This work is supported by the DOE CAREER grant No. DE-SC0020311.

References

1. Duris, J., Li, S., Driver, T., Champenois, E.G., MacArthur, J.P., Lutman, A.A., Zhang, Z., Rosenberger, P., Aldrich, J.W., Coffee, R., Coslovich, G., Decker, F.J., Glownia, J.M., Hartmann, G., Helml, W., Kamalov, A., Knurr, J., Krzywinski, J., Lin, M.F., Marangos, J.P., Nantel, M., Natan, A., O'Neal, J.T., Shivaram, N., Walter, P., Wang, A.L., Welch, J.J., Wolf, T.J.A., Xu, J.Z., Kling, M.F., Bucksbaum, P.H., Zholents, A., Huang, Z., Cryan, J.P., Marinelli, A.: Nat. Photonics **14**(1), 30 (2020). https://doi.org/10.1038/s41566-019-0549-5
2. Saito, N., Sannohe, H., Ishii, N., Kanai, T., Kosugi, N., Wu, Y., Chew, A., Han, S., Chang, Z., Itatani, J.: Optica **6**(12), 1542 (2019). https://doi.org/10.1364/OPTICA.6.001542. http://opg.optica.org/optica/abstract.cfm?URI=optica-6-12-1542
3. Marante, C., Klinker, M., Corral, I.I., González-Vázquez, J., Argenti, L., Martín, F.: J. Chem. Theory Comput. **13**(2), 499 (2017). https://doi.org/10.1021/acs.jctc.6b00907. http://pubs.acs.org/doi/10.1021/acs.jctc.6b00907

4. Klinker, M., Marante, C., Argenti, L., González-Vázquez, J., Martín, F.: J. Phys. Chem. Lett. **9**(4), 756 (2018). https://doi.org/10.1021/acs.jpclett.7b03220. PMID: 29364687
5. Mašín, Z., Benda, J., Gorfinkiel, J.D., Harvey, A.G., Tennyson, J.: Comput. Phys. Commun. **249**, 107092 (2020). https://doi.org/10.1016/j.cpc.2019.107092. https://www.sciencedirect.com/science/article/pii/S0010465519303972
6. Olsen, J.: J. Chem. Phys. **113**(17), 7140 (2000). https://doi.org/10.1063/1.1290005
7. Helgaker, T., Jørgensen, P., Olsen, J.: Molecular Electronic-Structure Theory. Wiley (2000). https://onlinelibrary.wiley.com/doi/book/10.1002/9781119019572
8. Gharibnejad, H., Douguet, N., Schneider, B., Olsen, J., Argenti, L.: Comput. Phys. Commun. **263**, 107889 (2021). https://doi.org/10.1016/j.cpc.2021.107889. https://www.sciencedirect.com/science/article/pii/S0010465521000382
9. Helgaker, T., Coriani, S., Jørgensen, P., Kristensen, K., Olsen, J., Ruud, K.: Chem. Rev. **112**(1), 543 (2012). https://doi.org/10.1021/cr2002239. PMID: 22236047
10. Varshalovich, D.A., Moskalev, A.N., Khersonskii, V.K.: Quantum Theory of Angular Momentum. World Scientific (1988). https://doi.org/10.1142/0270
11. Randazzo, J.M., Marante, C., Chattopadhyay, S., Schneider, B.I., Olsen, J., Argenti, L.: Phys. Rev. Res. **5**, 043115 (2023). https://doi.org/10.1103/PhysRevResearch.5.043115
12. Siegert, A.J.F.: Phys. Rev. **56**, 750 (1939). https://link.aps.org/doi/10.1103/PhysRev.56.750
13. Aidas, K., Angeli, C., Bak, K.L., Bakken, V., Bast, R., Boman, L., Christiansen, O., Cimiraglia, R., Coriani, S., Dahle, P., Dalskov, E.K., Ekström, U., Enevoldsen, T., Eriksen, J.J., Ettenhuber, P., Fernández, B., Ferrighi, L., Fliegl, H., Frediani, L., Hald, K., Halkier, A., Hättig, C., Heiberg, H., Helgaker, T., Hennum, A.C., Hettema, H., Hjertenæs, E., Høst, S., Høyvik, I.M., Iozzi, M.F., Jansík, B., Jensen, H.J.A., Jonsson, D., Jørgensen, P., Kauczor, J., Kirpekar, S., Kjærgaard, T., Klopper, W., Knecht, S., Kobayashi, R., Koch, H., Kongsted, J., Krapp, A., Kristensen, K., Ligabue, A., Lutnæs, O.B., Melo, J.I., Mikkelsen, K.V., Myhre, R.H., Neiss, C., Nielsen, C.B., Norman, P., Olsen, J., Olsen, J.M.H., Osted, A., Packer, M.J., Pawlowski, F., Pedersen, T.B., Provasi, P.F., Reine, S., Rinkevicius, Z., Ruden, T.A., Ruud, K., Rybkin, V.V., Sałek, P., Samson, C.C.M., de Merás, A.S., Saue, T., Sauer, S.P.A., Schimmelpfennig, B., Sneskov, K., Steindal, A.H., Sylvester-Hvid, K.O., Taylor, P.R., Teale, A.M., Tellgren, E.I., Tew, D.P., Thorvaldsen, A.J., Thøgersen, L., Vahtras, O., Watson, M.A., Wilson, D.J.D., Ziolkowski, M., Ågren, H.: WIREs Comput. Mol. Sci. **4**(3), 269 (2014). https://doi.org/https://doi.org/10.1002/wcms.1172. https://wires.onlinelibrary.wiley.com/doi/abs/10.1002/wcms.1172
14. Huber, K.P., Herzberg, G.: Springer New York, NY (1979). https://doi.org/10.1007/978-1-4757-0961-2. https://link.springer.com/book/10.1007/978-1-4757-0961-2
15. Gürtler, P., Saile, V., Koch, E.: Chem. Phys. Lett. **48**(2), 245 (1977). https://doi.org/10.1016/0009-2614(77)80308-4. https://www.sciencedirect.com/science/article/pii/0009261477803084
16. Peatman, W.B., Gotchev, B., Gürtler, P., Koch, E.E., Saile, V.: J. Chem. Phys. **69**(5), 2089 (1978). https://doi.org/10.1063/1.436808
17. Dehmer, P.M., Miller, P.J., Chupka, W.A.: J. Chem. Phys. **80**(3), 1030 (1984). https://doi.org/10.1063/1.446829
18. Huber, K.P., Stark, G., Ito, K.: J. Chem. Phys. **98**(6), 4471 (1993). https://doi.org/10.1063/1.465006
19. Carette, T., Dahlström, J.M., Argenti, L., Lindroth, E.: Phys. Rev. A **87**, 023420 (2013). https://doi.org/10.1103/PhysRevA.87.023420. https://link.aps.org/doi/10.1103/PhysRevA.87.023420
20. Argenti, L., Moccia, R.: Phys. Rev. A **93**, 042503 (2016). https://doi.org/10.1103/PhysRevA.93.042503. https://link.aps.org/doi/10.1103/PhysRevA.93.042503
21. Kramida, A., Ralchenko, Yu., Reader, J., NIST ASD Team: NIST Atomic Spectra Database (ver. 5.9), [Online]. Available: https://physics.nist.gov/asd [2017, April 9]. National Institute of Standards and Technology, Gaithersburg, MD (2021)

22. Cacelli, I., Moccia, R., Montuoro, R.: Chem. Phys. Lett. **347**(1), 261 (2001). https://doi.org/10.1016/S0009-2614(01)01006-5. https://www.sciencedirect.com/science/article/pii/S0009261401010065
23. Cooper, G., Anderson, J.E., Brion, C.: Chem. Phys. **209**(1), 61 (1996). https://doi.org/10.1016/0301-0104(96)00079-1. https://www.sciencedirect.com/science/article/pii/0301010496000791

Symmetry-Protected Chiral Sensitivity in Photoionization with Bichromatic Fields

Andrés Ordóñez, Piero Decleva, and David Ayuso

Abstract We consider photo-ionization of randomly oriented chiral molecules with bichromatic fields of frequencies ω and 2ω linearly polarized perpendicular to each other. Our symmetry analysis reveals a new type of enantio-sensitive signal in the photoelectron angular distribution which does not change its sign upon reversal of the two-color relative phase, i.e. upon reversal of the instantaneous ellipticity of the field. We provide a numerical estimate of the effect in methyloxirane, and propose an experimental setup for its measurement.

Keywords Chirality · Photoionization · Symmetry · Bichromatic · Lissajous · Ellipticity

1 Introduction

The fact that molecular chirality can be very efficiently recorded using table-top femtosecond lasers [1–3] has spurred a flurry of activity in the ultrafast science community (see e.g. [4–14]), partly driven by the immense potential of ultrafast chiral techniques for industrial applications [15–17]. A property common to all

A. Ordóñez (✉)
ICFO-Institut de Ciencies Fotoniques, The Barcelona Institute of Science and Technology, Castelldefels, Barcelona, Spain

Max-Born-Institut, Berlin, Germany

Current Affiliation: Imperial College London, London, UK
e-mail: andres.ordonez@imperial.ac.uk

P. Decleva
Università degli Studi di Trieste, Trieste, Italy

D. Ayuso
Max-Born-Institut, Berlin, Germany

Imperial College London, London, UK

L. Argenti et al. (eds.), *Proceedings of the 8th International Conference on Attosecond Science and Technology*, Springer Proceedings in Physics 300,
https://doi.org/10.1007/978-3-031-47938-0_12

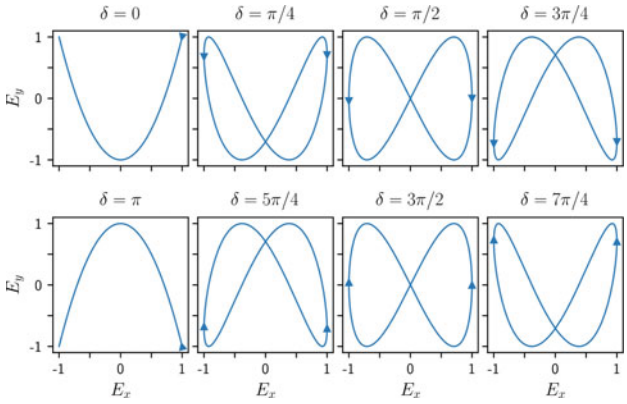

Fig. 1 Lissajous figures traced by a field [Eq. (1)] with frequencies ω and 2ω linearly polarized along x and y, respectively, for different values of the relative phase δ between the x and y components

ultrafast chiral techniques is that reversing the ellipticity of the driving field results in a reversal of the enantio-sensitive signal. Indeed, recent simulations and experiments [6, 18] have shown that even in bichromatic fields of the form

$$\boldsymbol{E} = E_x \cos(\omega t)\hat{\boldsymbol{x}} + E_y \cos(2\omega t + \delta)\hat{\boldsymbol{y}}, \tag{1}$$

tracing ∞-like Lissajous figures (see Fig. 1) with zero average ellipticity, the enantio-sensitive part of the photoelectron angular distribution (PAD) is reversed upon reversal of their instantaneous ellipticity, i.e. upon a change of π in the relative phase δ between the x and y components.

We have recently found that, contrary to intuition, the bichromatic field in Eq. (1) can also lead to an enantio-sensitive contribution to the PAD which does not change sign upon reversal of the instantaneous ellipticity [19]. Moreover, this Enantio-sensitive and Non-Elliptically-Dichroic (ENED) signal can be entirely independent of the relative phase δ and thus provides an enantio-sensitive signal robust with respect to variations of δ, a very desirable feature for industrial applications.

This robustness stems from the symmetry properties of the Hamiltonian of the interacting system. Our analysis [19] reveals that these symmetries, constraining which tensors (spherical harmonics) contribute to the PAD, allow for the emergence of a subset of ENED tensors, in particular for direct ionization pathways. Thus, the enantio-sensitivity of the ENED signal (a subset of the tensors contributing to the PAD) is symmetry-protected with respect to variations of δ. This phenomenon is reminiscent of the robustness of the Haldane phase with respect to perturbations with certain symmetries [20].

The simplest scenario to obtain an ENED signal requires consecutive absorption of one photon of each color and measurement of the contribution of the real spherical harmonic $Y_{3,-2}(\hat{\boldsymbol{p}}) \sim p_x p_y p_z$ to the PAD. This can be achieved either through

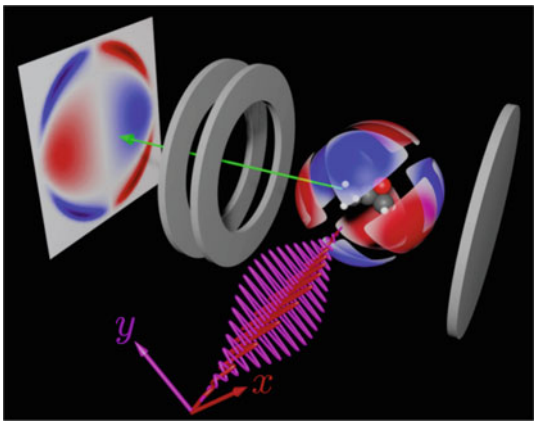

Fig. 2 The contribution from the real spherical harmonic $Y_{3,-2}(\hat{\boldsymbol{p}}) \sim p_x p_y p_z$ to the photoelectron angular distributions has opposite signs for opposite enantiomers but is independent of the relative phase between the ω and 2ω fields. It can be measured via direct 3D detection in a COLTRIMS setup or in a VMI setup with the geometry shown here

direct 3D detection in a COLTRIMS setup [21] or with a velocity map imaging setup with the geometry shown in Fig. 2 (previous works have used a different geometry for which the ENED signal is averaged out). We derived analytical expressions for this case [19] and performed computations in methyloxirane that reveal an ENED signal corresponding to 1% of the total cross section, a value within reach of current experimental capabilities [21].

This contribution is organized as follows: in Sect. 2.1 we review the fundamentals of recent developments concerning the PADs of chiral molecules subject to the bichromatic field (1). In Sect. 2.2 we provide general symmetry conditions regarding the dichroism and enantio-sensitivity of the PAD. In Sect. 3 we discuss how to generate the ENED signal and explain the approximations leading to our estimation of its value. Finally, Sect. 4 summarizes our conclusions.

2 Enantio-Sensitivity and Dichroism in Photoelectron Angular distributions

2.1 Previous Developments

We will consider the photoionization of gas phase randomly oriented chiral molecules and in particular the probability $W(\theta, \phi)$ that a photoelectron is emitted in the direction $\hat{\boldsymbol{p}}$ as specified by (θ, ϕ) in spherical coordinates in the laboratory frame. This probability distribution is real and it is thus natural to expand it in terms of *real* spherical harmonics as

$$W(\theta, \phi) = \sum_{l,m} b_{l,m} Y_{l,m}(\theta, \phi). \tag{2}$$

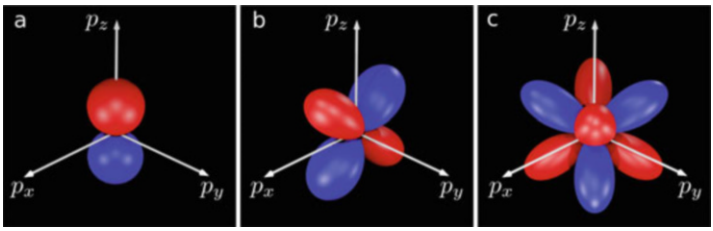

Fig. 3 Structure of the real spherical harmonics (**a**) $Y_{1,0}(\hat{\boldsymbol{p}})$, (**b**) $Y_{2,1}(\hat{\boldsymbol{p}})$, and (**c**) $Y_{3,-2}(\hat{\boldsymbol{p}})$

This expansion is equivalent to encapsulating all the information encoded in the photoelectron angular distribution $W(\theta, \phi)$ into the expansion coefficients $b_{l,m}$. Using the symmetry of the electromagnetic interaction (at the level of the electric dipole approximation) we can figure out which coefficients are non-zero and how they behave with respect to a change of molecular handedness or with respect to a change of polarization (see [19] for general symmetry analysis and [22] for multiphoton rules). For example, for one-photon ionization with circularly polarized light, the photoelectron angular distribution $W(\theta, \phi)$ is fully described by the coefficients $b_{0,0}$, $b_{1,0}$, and $b_{2,0}$. All the other coefficients being zero. A symmetry analysis reveals that while $b_{0,0}$ and b_{20} are neither sensitive to the molecular handedness nor to the polarization of the light, $b_{1,0}$ changes sign when we change either the molecular handedness or the polarization of the light. Thus the dipolar asymmetry $b_{1,0}Y_{1,0}(\theta, \phi) \sim b_{1,0}\cos\theta \sim b_{1,0}p_z$ associated with this contribution (see Fig. 3a), which describes more electrons going 'forward' than 'backward' or vice versa, is both enantio-sensitive and dichroic. This phenomenon is known as "photoelectron circular dichroism" or short PECD [23–25] and has been the driver of the electric-dipole revolution in chiro-optical spectroscopy that has taken place over the last decade [26].

Let us now focus on the bichromatic field described by Eq. (1). Depending on the relative phase δ between the x and y components we can have any of the Lissajous figures shown in Fig. 1. An interesting feature of this field is that it rotates clockwise during half of the cycle and counter-clockwise during the other half. This makes the question of its interaction with chiral molecules a very interesting one. References [6, 18] were the first ones to consider this problem. They found that for such fields the photoelectron angular distribution has a contribution from the real spherical harmonic $Y_{2,1}(\hat{\boldsymbol{p}}) \sim p_x p_z$ and that the associated coefficient $b_{2,1}$ is enantio-sensitive and dichroic. What do we mean by dichroic here? We mean that the $b_{l,m}$ coefficient changes sign when we change the phase of the y component by π, which is the same thing we do for circularly polarized light when we want to reverse its polarization. For example, if the field (1) with $\delta = 0$ yields a positive $b_{2,1}$(for a given molecule, photoelectron energy, and ionization regime), then setting $\delta = \pi$ yields a negative $b_{2,1}$ (for the same molecule, photoelectron energy, and ionization regime). So, while in the monochromatic case with circularly polarized light we had enantio-sensitivity and dichroism encoded in a dipolar pattern, namely $Y_{1,0}(\hat{\boldsymbol{p}}) \sim p_z$, in this

bichromatic case enantio-sensitivity and dichroism are encoded in a quadrupolar pattern, namely in $Y_{2,1}(\hat{\boldsymbol{p}}) \sim p_x p_z$ (see Fig. 3b). Inspired by these works [6, 18] we decided to explore how the other $b_{l,m}$ coefficients behave in terms of enantio-sensitivity and dichroism.

2.2 Disentangling Dichroism from Enantio-Sensitivity

Our symmetry analysis (valid for any ionization regime) revealed the conditions that a $b_{l,m}$ coefficient must satisfy in order to be non-zero, or enantio-sensitive, or dichroic. These are summarized in Table 1. Note that these conditions depend on the specific orientation of the electric field. For example, in Ref. [19] we considered a different orientation of the electric field in the laboratory frame (ω along z and 2ω along z) and thus we arrived to different conditions. Therefore, what we want to remark here is not so much the particular conditions but rather that as a result of those conditions the $b_{l,m}$ coefficients will be distributed into three partially overlapping sets like shown in Fig. 4b, independently of the orientation of the field.

To put this into perspective, we compare it with the usual situation encountered with monochromatic circularly polarized light (see Fig. 4a). In that case one can show that the set of dichroic coefficients and the set of enantio-sensitive coefficients are identical. That is, for circularly polarized light, enantio-sensitivity and dichroism always come together. But in the bichromatic case these two sets are not identical. So instead of having only two categories of non-zero coefficients, the bichromatic case yields four. As Fig. 4 shows, category I contains the non-zero coefficients that are neither enantio-sensitive nor dichroic. Category II contains the non-zero coefficients that are both enantio-sensitive and dichroic. Categories I and II are the standard categories we are familiar with in the circularly polarized case. But now we also have a category III containing the non-zero coefficients that are dichroic but not enantio-sensitive. This means that these coefficients change sign when we change the relative phase δ by π, but not when we change the molecular handedness. This is interesting but not totally unheard of. These coefficients basically reflect the asymmetry of the Lissajous figures in Fig. 1 along y. And finally, category IV is also new and it contains the coefficients which are enantio-sensitive but not dichroic, which we have termed ENED in the introduction. The existence of this category is interesting because it is unexpected to have a signal which records the molecular chirality but is insensitive to the exact polarization state of the light.

Table 1 Conditions on l and m for non-zero, enantio-sensitive, and dichroic $b_{l,m}$ coefficients in a photoelectron angular distribution [see Eq. (2)] resulting from ionization with the bichromatic field in Eq. (1)

Non-zero	[(odd l) and ($m < 0$)] or [(even l) and $m \geq 0$]
Enantio-sensitive	odd $l - m$
Dichroic	(odd $l - m$ and $m \geq 0$) or (even $l - m$ and $m < 0$)

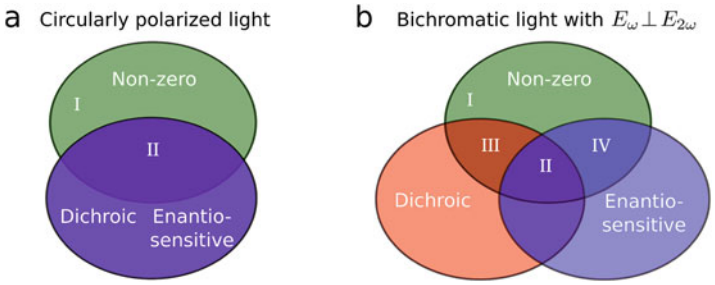

Fig. 4 Diagram of the sets of non-zero, enantio-sensitive, and dichroic $b_{l,m}$ coefficients describing the photoelectron angular distribution [see Eq. (2)] in the case of ionization using either (**a**) a circularly polarized field or (**b**) a bichromatic field with frequencies ω and 2ω linearly polarized perpendicular to each other [see Eq. (1)]. For circularly polarized light the subset of non-zero dichroic coefficients is identical to the subset of non-zero enantio-sensitive coefficients, leading to only two categories of non-zero coefficients. This identity is broken in the bichromatic case, leading to four categories of non-zero coefficients

Table 2 Explicit classification of $b_{l,m}$ coefficients with l up to 4 according to Table 1. Categories assigned according to Fig. 4

Non-zero	$b_{0,0}$	$b_{1,-1}$	$b_{2,0}$	$b_{2,1}$	$b_{2,2}$	$b_{3,-3}$	$b_{3,-2}$	$b_{3,-1}$	$b_{4,0}$	$b_{4,1}$	$b_{4,2}$	$b_{4,3}$	$b_{4,4}$
Enantio-sensitive	No	No	No	Yes	No	No	Yes	No	No	Yes	No	Yes	No
Dichroic	No	Yes	No	Yes	No	Yes	No	Yes	No	Yes	No	Yes	No
Category	I	III	I	II	I	III	IV	III	I	II	I	II	I

Consider now how these categories are populated. Table 2 explicitly shows how the $b_{l,m}$ coefficients with $l \leq 4$ and $-l \leq m \leq l$ are distributed among the different categories. We can see that we have several terms of each category, except for category IV, where we only find one occurrence. That is, at least for low values of l, category IV is, as one would expect, exotic.

3 The ENED Signal

Let us now focus on the enantio-sensitive but not dichroic coefficient $b_{3,-2}$. This coefficient is associated with the real spherical harmonic $Y_{3,-2}(\hat{\boldsymbol{p}}) \sim p_x p_y p_z$ which describes an octupolar pattern (see Fig. 3c). This octupole can emerge e.g. as a result of the two-photon resonantly enhanced ionization process $|0\rangle \xrightarrow{\omega} |j\rangle \xrightarrow{2\omega} |\boldsymbol{p}\rangle$, where $|0\rangle$ denotes the ground state, $|j\rangle$ denotes a bound excited state, and $|\boldsymbol{p}\rangle$ denotes a scattering state with photoelectron momentum $\boldsymbol{p}$.

As a first estimation of the contribution of this octupole to the total cross section $b_{0,0}$, we have calculated the ratio $b_{3,-2}/b_{0,0}$ in methyloxirane using the HOMO and HOMO+1 orbitals as an approximation to the ground state $|0\rangle$ and excited state $|j\rangle$. We have set $\omega = 7.28\,\text{eV}$ at exact resonance with the HOMO $\rightarrow$

HOMO+1 transition and we have neglected the (non-resonant) contribution of all other orbitals to the signal at photoelectron energy $E_k = \omega + 2\omega - I_p = 10\,\text{eV}$, where $I_p = 11.8\,\text{eV}$ is the binding energy of the HOMO orbital. Under these approximations, the value of $b_{3,-2}/b_{0,0}$ calculated at second-order perturbation theory is independent of field parameters and depends only on the transition dipoles. The latter have been calculated with state-of-the-art methods [27, 28] and yield $b_{3,-2}/b_{0,0} = 0.008$. That is, the ENED signal is of the order of 1% of the total cross section and thus its measurement in the laboratory is within reach of current experimental capabilities [21]. It can be measured either through direct 3D angularly resolved photoelectron detection in a COLTRIMS setup, or through 2D velocity map imaging in the geometry shown in Fig. 2.

4 Conclusions

We have studied general aspects of the photoelectron angular distributions (PADs) resulting from the ionization of randomly oriented chiral molecules with bichromatic fields with frequencies ω and 2ω linearly polarized perpendicular to each other. Our symmetry analysis of this process reveals fundamental differences with respect to the monochromatic circularly polarized case, in terms of how enantio-sensitivity and dichroism are reflected in the PAD.

Most interestingly, we find that there can be contributions to the PAD that are enantio-sensitive (i.e. have opposite signs for opposite enantiomers) but are nevertheless insensitive to the exact polarization state as determined by the relative phase between the two perpendicular components, and thus insensitive to the instantaneous ellipticity of the field. The robustness of this type of signals is protected by the symmetry of the interaction and is in this sense reminiscent of the symmetry-protected Haldane phase in 2D systems.

We show that this enantio-sensitive but non-elliptically dichroic signal can emerge in two-photon resonantly enhanced ionization and estimate it to be of the order of 1% of the total cross section in a common chiral molecule (methyloxirane), i.e. within current experimental capabilities in COLTRIMS and VMI setups.

Acknowledgments We acknowledge stimulating discussions with O. Smirnova. A.O. acknowledges funding from the European Union's Horizon 2020 research and innovation programme under the Marie Sklodowska-Curie grant agreement No 101029393 and support provided to his host group (Maciej Lewenstein's Quantum Optics Theory) at ICFO by: ERC AdG NOQIA; Ministerio de Ciencia e Inovación, Agencia Estatal de Investigaciones (PGC2018-097027-B-I00/10.13039/501100011033, CEX2019-000910-S/10.13039/501100011033, Plan Nacional FIDEUA PID2019-106901GB-I00, FPI, QUANTERA MAQS PCI2019-111828-2, QUANTERA DYNAMITE PCI2022-132919, Proyectos de I+D+I "Retos Colaboración" QUSPIN RTC2019-007196-7); European Union NextGenerationEU (PRTR); Fundació Cellex; Fundació Mir-Puig; Generalitat de Catalunya (European Social Fund FEDER and CERCA program, AGAUR Grant No. 2017 SGR 134, QuantumCAT U16-011424, co-funded by ERDF Operational Program of Catalonia 2014-2020); Barcelona Supercomputing Center MareNostrum (FI-2022-1-0042); EU Horizon 2020 FET-OPEN OPTOlogic (Grant No 899794); National Science

Centre, Poland (Symfonia Grant No. 2016/20/W/ST4/00314); European Union's Horizon 2020 research and innovation programme under the Marie-Sklodowska-Curie grant agreement No 847648 ("La Caixa" Junior Leaders fellowships ID100010434: LCF/BQ/PI19/11690013, LCF/BQ/PI20/11760031, LCF /BQ/PR20/11770012, LCF/BQ/PR21/11840013).

References

1. Lux, C., Wollenhaupt, M., Bolze, T., Liang, Q., Köhler, J., Sarpe, C., Baumert, T.: Angew. Chem., Int. Ed. **51**(20), 5001 (2012). https://doi.org/10.1002/anie.201109035. https://onlinelibrary.wiley.com/doi/abs/10.1002/anie.201109035
2. Lehmann, C.S., Ram, R.B., Powis, I., Jansenn, M.H.M.: J. Chem. Phys. **139**(23), 234307 (2013). https://doi.org/10.1063/1.4844295. http://aip.scitation.org/doi/10.1063/1.4844295
3. Beaulieu, S., Ferré, A., Géneaux, R., Canonge, R., Descamps, D., Fabre, B., Fedorov, N., Légaré, F., Petit, S., Ruchon, T., Blanchet, V., Mairesse, Y., Pons, B.: New J. Phys. **18**(10), 102002 (2016). https://doi.org/10.1088/1367-2630/18/10/102002. http://stacks.iop.org/1367-2630/18/i=10/a=102002
4. Dreissigacker, I., Lein, M.: Phys. Rev. A **89**(5), 053406 (2014). https://doi.org/10.1103/PhysRevA.89.053406. http://link.aps.org/doi/10.1103/PhysRevA.89.053406
5. Harada, Y., Haraguchi, E., Kaneshima, K., Sekikawa, T.: Phys. Rev. A **98**(2), 021401 (2018). https://doi.org/10.1103/PhysRevA.98.021401. https://link.aps.org/doi/10.1103/PhysRevA.98.021401
6. Rozen, S., Comby, A., Bloch, E., Beauvarlet, S., Descamps, D., Fabre, B., Petit, S., Blanchet, V., Pons, B., Dudovich, N., Mairesse, Y.: Phys. Rev. X **9**(3), 031004 (2019). https://doi.org/10.1103/PhysRevX.9.031004. https://link.aps.org/doi/10.1103/PhysRevX.9.031004
7. Goetz, R.E., Koch, C.P., Greenman, L.: Phys. Rev. Lett. **122**(1), 013204 (2019). https://doi.org/10.1103/PhysRevLett.122.013204. https://link.aps.org/doi/10.1103/PhysRevLett.122.013204
8. Ayuso, D., Neufeld, O., Ordonez, A.F., Decleva, P., Lerner, G., Cohen, O., Ivanov, M., Smirnova, O.: Nat. Photonics **13**, 866 (2019). https://doi.org/10.1038/s41566-019-0531-2. https://www.nature.com/articles/s41566-019-0531-2
9. Yachmenev, A., Onvlee, J., Zak, E., Owens, A., Küpper, J.: Phys. Rev. Lett. **123**(24), 243202 (2019). https://doi.org/10.1103/PhysRevLett.123.243202. https://link.aps.org/doi/10.1103/PhysRevLett.123.243202
10. Milner, A.A., Fordyce, J.A., MacPhail-Bartley, I., Wasserman, W., Milner, V., Tutunnikov, I., Averbukh, I.S.: Phys. Rev. Lett. **122**(22), 223201 (2019). https://doi.org/10.1103/PhysRevLett.122.223201. https://link.aps.org/doi/10.1103/PhysRevLett.122.223201
11. Baykusheva, D., Zindel, D., Svoboda, V., Bommeli, E., Ochsner, M., Tehlar, A., Wörner, H.J.: Proc. Natl. Acad. Sci. **116**(48), 23923 (2019). https://doi.org/10.1073/pnas.1907189116. https://www.pnas.org/content/116/48/23923
12. Planas, X.B., Ordóñez, A., Lewenstein, M., Maxwell, A.S.: arXiv:2202.07289 [physics] (2022). https://arxiv.org/abs/2202.07289
13. Fehre, K., Eckart, S., Kunitski, M., Janke, C., Trabert, D., Hofmann, M., Rist, J., Weller, M., Hartung, A., Schmidt, L., Jahnke, T., Braun, H., Baumert, T., Stohner, J., Demekhin, P., Schöffler, M., Dörner, R.: Phys. Rev. Lett. **126**(8), 083201 (2021). https://doi.org/10.1103/PhysRevLett.126.083201. https://link.aps.org/doi/10.1103/PhysRevLett.126.083201
14. Faccialà, D., Devetta, M., Beauvarlet, S., Besley, N., Calegari, F., Callegari, C., Catone, D., Cinquanta, E., Ciriolo, A.G., Colaizzi, L., Coreno, M., Crippa, G., De Ninno, G., Di Fraia, M., Galli, M., Garcia, G.A., Mairesse, Y., Negro, M., Plekan, O., Geetha, P.P., Prince, K.C., Pusala, A., Stagira, S., Turchini, S., Ueda, K., You, D., Zema, N., Blanchet, V., Nahon, L., Powis, I., Vozzi, C.: Phys. Rev. X **13**(1), 011044 (2023). https://doi.org/10.1103/PhysRevX.13.011044.

15. Fanood, M.M.R., Ram, N.B., Lehmann, C.S., Powis, I., Janssen, M.H.M.: Nat. Commun. **6**, 7511 (2015). https://doi.org/10.1038/ncomms8511. https://www.nature.com/articles/ncomms8511
16. Alexander, K., Christian, L., Tom, R., Stefanie, Z., Cristian, S., Arne, S., Thomas, B.: ChemPhysChem **17**(8), 1119 (2016). https://doi.org/10.1002/cphc.201501067. https://onlinelibrary.wiley.com/doi/10.1002/cphc.201501067
17. Comby, A., Bond, C.M., Bloch, E., Descamps, D., Fabre, B., Petit, S., Mairesse, Y., Greenwood, J.B., Blanchet, V.: Chirality **32**(10), 1225 (2020). https://doi.org/10.1002/chir.23267. http://onlinelibrary.wiley.com/doi/abs/10.1002/chir.23267
18. Demekhin, P.V., Artemyev, A.N., Kastner, A., Baumert, T.: Phys. Rev. Lett. **121**(25), 253201 (2018). https://doi.org/10.1103/PhysRevLett.121.253201. https://link.aps.org/doi/10.1103/PhysRevLett.121.253201
19. Ordonez, A.F., Smirnova, O.: Phys. Chem. Chem. Phys. **24**, 7264 (2022). https://doi.org/10.1039/D1CP05833A. https://pubs.rsc.org/en/content/articlelanding/2022/cp/d1cp05833a
20. Gu, Z.C., Wen, X.G.: Phys. Rev. B **80**(15), 155131 (2009). https://doi.org/10.1103/PhysRevB.80.155131. https://link.aps.org/doi/10.1103/PhysRevB.80.155131
21. Beauvarlet, S.: Dynamiques électroniques chirales résolues aux échelles attoseconde et femtoseconde sondées par des schémas de polarisation variés. Ph.D. thesis, Université de Bordeaux (2022). https://tel.archives-ouvertes.fr/tel-03663259
22. Ordonez, A.F., Smirnova, O.: Phys. Chem. Chem. Phys. **24**, 13605 (2022). https://doi.org/10.1039/D1CP05645J. https://pubs.rsc.org/en/content/articlelanding/2022/cp/d1cp05645j
23. Ritchie, B.: Phys. Rev. A **13**(4), 1411 (1976). http://journals.aps.org/pra/abstract/10.1103/PhysRevA.13.1411
24. Powis, I.: J. Chem. Phys. **112**(1), 301 (2000). https://doi.org/10.1063/1.480581. http://scitation.aip.org/content/aip/journal/jcp/112/1/10.1063/1.480581
25. Böwering, N., Lischke, T., Schmidtke, B., Müller, N., Khalil, T., Heinzmann, U.: Phys. Rev. Lett. **86**(7), 1187 (2001). https://doi.org/10.1103/PhysRevLett.86.1187. http://link.aps.org/doi/10.1103/PhysRevLett.86.1187
26. Ayuso, D., Ordonez, A.F., Smirnova, O.: arXiv:2203.00580 [physics] (2022). http://arxiv.org/abs/2203.00580
27. Toffoli, D., Stener, M., Fronzoni, G., Decleva, P.: Chem. Phys. **276**(1), 25 (2002). https://doi.org/10.1016/S0301-0104(01)00549-3. https://www.sciencedirect.com/science/article/pii/S0301010401005493
28. Stranges, S., Turchini, S., Alagia, M., Alberti, G., Contini, G., Decleva, P., Fronzoni, G., Stener, M., Zema, N., Prosperi, T.: J. Chem. Phys. **122**(24), 244303 (2005). https://doi.org/10.1063/1.1940632. https://aip.scitation.org/doi/abs/10.1063/1.1940632

Experimental Investigation of Topological Property of Degenerate Singularities in Rescattering Processes

Tomoya Mizuno, Tianqi Yang, Takayuki Kurihara, Nobuhisa Ishii, Teruto Kanai, Oleg I. Tolstikhin, Toru Morishita, and Jiro Itatani

Abstract We measure rescattering photoelectron momentum distributions (PEMDs) of randomly oriented CO_2 molecules by a carrier-envelope phase (CEP)-stable few-cycle pulse. A cutoff structure of measured PEMDs agrees quantitatively with the Airy function-like universal distribution calculated by the adiabatic theory. This behavior is guaranteed by the singularity theory, and originates from the topological property of a caustic, which is singularity of action described by the Hamiltonian formulation. We experimentally reveal the topological properties underlying the caustic in the rescattering processes.

Keywords Strong-field rescattering · Caustic · Degenerate singularity

1 Introduction

Photoionization of an atom and molecule in an intense field is one of the most fundamental processes in strong field physics. Recently, several experimental and theoretical works revealed that the cutoff structures of high order harmonic generation (HHG) [1] and rescattering photoelectron momentum distribution (PEMD) [2–4] show the universal distribution that is described by the Airy function. This is attributed to a caustic, which is the singularity of the action described in the Hamiltonian formulation [5–10]. The limited number of the equivalence class of the singularity are stable by small perturbations of the Hamiltonian and the initial

T. Mizuno (✉) · T. Yang · T. Kurihara · N. Ishii · T. Kanai · J. Itatani
The Institute for Solid State Physics, The University of Tokyo, Kashiwa, Chiba, Japan
e-mail: mizuno.tomoya@issp.u-tokyo.ac.jp

O. I. Tolstikhin
Moscow Institute of Physics and Technology, Dolgoprudny, Russia

T. Morishita
Institute for Advanced Science, The University of Electro-communications, Chofu-shi, Tokyo, Japan

L. Argenti et al. (eds.), *Proceedings of the 8th International Conference on Attosecond Science and Technology*, Springer Proceedings in Physics 300,
https://doi.org/10.1007/978-3-031-47938-0_13

state [8–10]. In the stable equivalence class, the characteristic distribution and the stability of the caustic are topological properties. On the other hand, any unstable singularities can transform to other class of singularities by small perturbations, resulting in no-universal distribution. The universal behaviors among different strong-field phenomena, such as HHG and PEMD [1–4, 11–14] can be explained by the topological property of the stable singularities [8–10].

In this work, we measure PEMDs for CO_2 molecules near half-cycle cutoffs associated with the rescattering caustic by a carrier-envelope phase (CEP)-stable few-cycle field. The CEP-stable few-cycle pulses enable us to resolve contribution of only one caustic to a PEMD. We experimentally investigate and confirm backward rescattering cutoff structures associated with the A_2 class of the caustic in the PEMDs generated by the ionization of randomly oriented CO_2 with linearly polarized few-cycle infrared pulses. We confirm universality associated with the singularity of action.

2 Degenerate Singularities in the Hamiltonian System

In this section, we briefly introduce the concepts of degenerate singularity [8–10]. A singularity of action $S(t; \mathbf{k})$ as a function of time t in the Hamiltonian formulation is given below

$$\partial S(t_0; \mathbf{k})/\partial t = 0, \tag{1}$$

where $\mathbf{k}$ represents parameters, such as photoelectron momentum or frequency of HHG. This equation defines a singular point t_0 of the action $S(t; \mathbf{k})$. The singular point t_0 of action is usually called a saddle point or a critical point in physics. Therefore, Eq. (1) is so-called the saddle point equation. When the equation has a degenerate root, it is called a degenerate singular point. The degenerate singular condition is then given by

$$\partial S(t_0; \mathbf{k_0})/\partial t = \partial^2 S(t_0; \mathbf{k_0})/\partial t^2 = 0, \tag{2}$$

where $\mathbf{k_0}$ is so-called caustic corresponding to the degenerate singularity. At the caustic, two or more semiclassical trajectories coalesce in phase space. Thus, this is a generalized concept of a focal point in optics [5, 8–10].

The degenerate singular point of $S(t; \mathbf{k})$ can be classified by the following equation

$$\partial S(t_0)/\partial t = \partial^2 S(t_0)/\partial t^2 = \cdots = \partial^n S(t_0)/\partial t^n = 0, \text{ and } \partial^{n+1} S(t_0)/\partial t^{n+1} \neq 0. \tag{3}$$

This equation is equivalent that the saddle point equation of action $S(t;\mathbf{k})$ has n-degenerate roots. This singularity is so called the A_n singularity, and the degeneracy n completely characterizes the singularities of action among the A_n class [8–10]. The class of singularity is topological invariant. The normal form associated with the A_n singularity [10] is given as $S_n(t;\mathbf{k}) = t^{n+1} + k_{n-1}t^{n-1} + k_{n-2}t^{n-2}\cdots + k_1 t$, where parameter $\mathbf{k}$ is a $(n-1)$-dimensional vector $(k_1, k_2, \cdots, k_{n-1})$ and the origins of both $\mathbf{k}$ and t correspond to the caustic and the degenerate singular point, respectively. Any actions with the A_n singularity always can be transformed into the normal form $S_n(t;\mathbf{k})$ by diffeomorphic mapping. Therefore, it is sufficient to consider only the normal form $S_n(t;\mathbf{k})$ in the same equivalence class of a caustic.

In the quantum scattering theory [7], a scattering amplitude $f(\mathbf{k})$ is approximately given in the oscillatory integral as follows

$$f(\mathbf{k}) = \int_{-\infty}^{\infty} g(t)\exp\left[iS_n(t;\mathbf{k})\right]dt, \tag{4}$$

where $g(t)$ represents a smooth function describing the amplitude. Based on the steepest descent method, the asymptotic form of the oscillatory integral around the caustic $\mathbf{k_0}$ expressed by the normal form $S_n(t;\mathbf{k})$ is given in

$$f(\mathbf{k}) \approx g(0)\int_{-\infty}^{\infty}\exp\left[iS_n(t;\mathbf{k})\right]dt = g(0)\Phi_n(\mathbf{k}), \tag{5}$$

and

$$\Phi_n(\mathbf{k}) = \int_{-\infty}^{\infty}\exp\left[i(t^{n+1} + k_{n-1}t^{n-1} + k_{n-2}t^{n-2} + \cdots + k_1 t)\right]dt, \tag{6}$$

where $\Phi_n(\mathbf{k})$ represents the universal distributions around the caustics associated with the A_n class. Therefore, the oscillatory integral around the A_n class always shows the universal distribution expressed by $\Phi_n(\mathbf{k})$, because the distributions in the normal form always can be transformed into any action in the same equivalence class by diffeomorphic mapping [5, 8–10]. For the $A_{1,2,3}$ classes, $\Phi_{1,2,3}(\mathbf{k})$ are related to the Gaussian integral, Airy and Pearcey functions, respectively. Especially, in case of the A_1 class, the asymptotic form of the oscillatory integral of a scattering amplitude based on the saddle point method is useful to evaluate a scattering amplitude in strong-field phenomena [15, 16]. This formulation considers only contributions of semiclassical trajectories to a scattering amplitude, and falls at a caustic. In this work, we focus on the rescattering caustic associated with the A_2 class.

3 Adiabatic Theory for Rescattering Processes

We present the rescattering amplitude based on the Adiabatic theory [17], and is given in Ref. [3]. The amplitude from a given half-cycle in the vicinity of the corresponding caustics is given by

$$I(k_z) = \int_{-\infty}^{\infty} \frac{A_0(F(t_i))\, f(|u_f|, \pi)}{|(t - t_i)^3 F(t_i)|^{1/2}} \exp\left[i(S_r(t; k_z)\right] dt, \tag{7}$$

where $S_r(t; k_z)$ is the action based on the three-step model, which is defined in Ref. [3], $f(|u_f|, \pi)$ denotes the scattering amplitude for electron-ion elastic scattering with incident momentum $|u_f|$ in the backward direction, and A_0 represents transverse momentum distribution of outgoing electrons in the asymptotic part of the Siegert eigenfunction. The times of t_i and t_r represent the moment of tunneling ionization and rescattering, respectively, associated with the caustic. The k_z denotes photoelectron momentum along the polarization axis. The function $F(t)$ represents an electric field. The details are presented in Ref. [3]. The action $S_r(t; k_z)$ describing the rescattering process has the caustic k_q associated with the A_2 singularity at the half-cycle cutoff. Based on the singularity theory [8–10] and the adiabatic theory [3], the asymptotic form of the rescattering amplitude around the caustic associated with A_2 class is given by

$$I(k_z) \simeq \mathrm{Ai}(C\left[k_z - k_q\right]) \left(\frac{2}{S_r'''}\right)^{1/3} \frac{2\pi A_0(F(t_i))\, f(|u_f|, \pi)}{|(t_r - t_i)^3 F(t_i)|^{1/2}} \exp\left[i(S_r(\tilde{t_r}, k_z)\right], \tag{8}$$

where $\mathrm{Ai}(z)$ represents the Airy function, and $\tilde{t_r}$ is the point where the second derivative of the action $S_r(t; k_z)$ in t vanishes. The coefficient C is given by

$$C = \left(\frac{2}{S_r'''}\right)^{1/3} |u_f|. \tag{9}$$

The PEMD $P_c(k_z)$ around a caustic can be obtained by $P_c(k_z) = |I(k_z)|^2$. The dependence of $P_c(k_z)$ on k_z is described by the Airy function; all the other factors in $P_c(k_z)$ do not depend on k_z, merely influences the absolute yield. Indeed, the Airy function represents the universal distribution for various phenomena belonging to the A_2 singularity class [1–7, 13]. The argument of the Airy function turns to zero at the quantum caustic $k_z = k_q$, hence, $P_c(k_z)$ rapidly decays beyond this point. The relative k_z-dependence of the PEMD around the caustic of A_2 class is characterized by two parameters of k_q and C. We can calculate these parameters using the adiabatic theory [3]. Strictly speaking, this universality appears only for

cutoff structure of PEMDs of atoms and oriented molecules. For randomly oriented molecules, generally the universality is not guaranteed. Nevertheless, under the condition that Stark shift is negligibly small, relative PEMDs for randomly oriented molecules are also expected to show the universal distribution. It is because two parameters of k_q and C, which characterize the relative distribution of PEMD around the caustic, are mostly independent of the molecular orientation in that case. Our laser parameters and target of a nonpolar molecule of CO_2 satisfy this condition, thus PEMDs for CO_2 is expected to show universal behavior even in randomly oriented molecules.

4 Experiment

We measure PEMDs for randomly oriented CO_2 molecules near half-cycle cutoffs associated with the rescattering caustic by a carrier-envelope phase (CEP)-stable few-cycle field. We use linearly-polarized intense infrared fields at 1600 nm with a pulse duration of 14 fs from an OPCPA system [18]. The PEMD in the parallel direction to the polarization is measured by a time-of-flight photoelectron spectrometer as a function of the CEP [4, 19].

5 Results

Figure 1 show measured PEMDs $P(k_z)$ for randomly oriented CO_2 at CEPs of 0, 0.8 and 1.6 $\times\pi$ at an estimated effective intensity of 6.61×10^{13} W/cm^2, and a pulse duration of 14.05 fs. Around the half-cycle cutoff (HCO) associated with the A_2 class caustic, measured PEMDs are reproduced by the Airy function-like distribution based on the adiabatic theory. This universal behavior is independent of the target species and any other parameters, and is characterized only by the class of the singularity. We experimentally verify the universal distribution of the oscillatory integrals around the caustic. This behavior always appears around a caustic, independent of target species and phenomena, and is characterized only by the class of the caustic, because this is the topological property of the caustic, corresponding to the degenerate singularity.

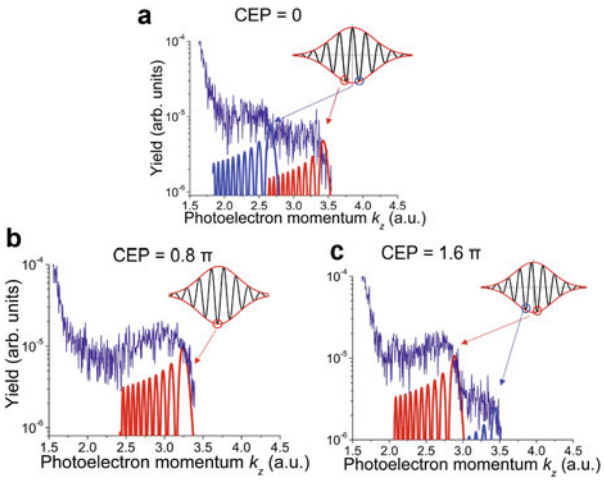

Fig. 1 Measured PEMDs $P(k_z)$ for randomly oriented CO_2 (thin black curves) at selected CEPs ϕ of (**a**) 0, (**b**) 0.8 π, and (**c**) 1.6 π at an estimated effective intensity of 6.61 $\times$ 10^{13} W/cm^2, and a pulse duration of 14.05 fs. The red, blue and green thick curves show calculated PEMDs $P_c(k_z)$ corresponding to a half cycle of the electric field, as depicted in the top figures

Acknowledgments This research was in part supported by Grant-in-Aid for Scientific Research (S) Grant number 18H05250 and Scientific Research (C) Grant number 20K05358 of the Japan Society for the Promotion of Science.

References

1. Frolov, M.V., et al.: Analytic formulae for high harmonic generation. J. Phys. B **42**, 035601 (2009)
2. Frolov, M.V., et al.: Analytic formulas for above-threshold ionization or detachment plateau spectra. Phys. Rev. A **79**, 033406 (2009)
3. Morishita, T., et al.: Adiabatic theory of strong-field photoelectron momentum distribution near a backward rescattering caustic. Phys. Rev. A **96**, 053416 (2017)
4. Mizuno, T., et al.: Observation of the quantum shift of a backward rescattering caustic by carrier-envelope phase mapping. Phys. Rev. A **103**, 043121 (2021)
5. Berry, M.V., Upstill, C.: Catastrophe optics; morphologies of caustic and their diffraction patterns. Prog. Optics **18**, 257 (1980)
6. Kirkby, W., et al.: Quantum caustics and the hierarchy of light cones in quenched spin chains. Phys. Rev. Res. **1**, 033135 (2019)
7. Connor, J.: Catastrophes and molecular collisions. Mol. Phys. **31**, 33 (1976)
8. Arnold, V., et al.: Singularities of Differential Maps, vols. 1 and 2. Birkhäuser, Boston (1980)
9. Arnold, V.: Singularity of Caustics and Waves. Springer, Dordrecht (1990)
10. Arnold, V.: Normal forms of functions in neighborhoods of degenerate critical points. Russ. Math. Surv. **29**, 10 (1974)
11. Raz, O., et al.: Spectral caustics in attosecond science. Nat. Photonics **6**, 170 (2012)

12. Faccialà, D., et al.: Probe of multielectron dynamics in xenon by caustics in high-order harmonic generation. Phys. Rev. Lett. **117**, 093902 (2016)
13. Morimoto, Y., Hommelhof, P.: Intracycle interference in the interaction of laser and electron beams. Phys. Rev. Res. **2**, 043089 (2020)
14. Uzan, A.J., et al.: Attosecond spectral singularities in solid-state high-harmonic generation. Nat. Photonics **14**, 183–187 (2020)
15. Nayak, A., et al.: Saddle point approaches in strong field physics and generation of attosecond pulses. Phys. Rep. **833**, 1 (2019)
16. Jaŝarevicć, A., et al.: Application of the saddle-point method to strong-laser-field ionization. J. Phys. A: Math. Theor. **53**, 125201 (2020)
17. Tolstikhin, O.I., Morishita, T.: Adiabatic theory of ionization by intense laser pulses: finite-range potentials. Phys. Rev. A **86**, 043417 (2012)
18. Ishii, N., et al.: Sub-two-cycle, carrier-envelope phase-stable, intense optical pulses at 1.6 μm from a BiB_3O_6 optical parametric chirped-pulse amplifier. Opt. Lett. **37**, 4182 (2012)
19. Geiseler, H., et al.: Carrier-envelope phase mapping in laser-induced electron diffraction. Phys. Rev. A **94**, 033417 (2016)

Simulating Strong Field Tunnel Ionization of Molecules

L. Ortmann, A. AlShafey, A. Staudte, and A. S. Landsman

Abstract Recently we introduced a method to quantify the relative contribution of upfield versus downfield ionization when a diatomic molecule is exposed to intense infrared light [1]. Applying this to previously measured electron momenta distributions following strong field ionization of N2, we found approximately a 2 : 1 ratio of electrons ionized from a downfield atom, relative to upfield. This suggests that the bound state wave function largely adapts adiabatically to the changing laser field, although the nonadiabatic process of ionization enhancement still contributes significantly even in neutral molecules. Here, we discuss the Quantum Trajectory Monte Carlo (QTMC) used to simulate electron trajectories, and explore possible modifications of the model [1].

Keywords Strong field ionization · Diatomic molecules · Attosecond electron dynamics · Semiclassical simulations

1 Introduction

When a diatomic molecule is exposed to intense light, the valence electron may tunnel from a higher potential (corresponding to an upfield atom) due to the suppressed internuclear barrier. This process is known as ionization enhancement and is a key mechanism in strong field ionization of molecules. Alternatively, the bound electron wave function can evolve adiabatically in the laser field, resulting in ionization from the downfield atom. We recently introduced a method for quantitatively retrieving the ratio of ionization events at the upfield and downfield

L. Ortmann · A. AlShafey · A. S. Landsman (✉)
Department of Physics, The Ohio State University, Columbus, OH, USA
e-mail: landsman.7@osu.edu

A. Staudte
Joint Attosecond Science Lab of the National Research Council and the University of Ottawa, Ottawa, ON, Canada

L. Argenti et al. (eds.), *Proceedings of the 8th International Conference on Attosecond Science and Technology*, Springer Proceedings in Physics 300,
https://doi.org/10.1007/978-3-031-47938-0_14

atomic site in a diatomic molecule by comparing experimental data with quantum trajectory Monte Carlo simulations (QTMC) [1]. Our technique is based on the electron's deflection in the asymmetric Coulomb potential of the molecule that is tilted against the laser polarization direction. This introduces an asymmetry in the final photoelectron momentum distribution, which depends on the ratio of electrons born at the upfield or downfield atom. We then applied this method to available experimental data from strong field ionization of a neutral N_2 molecule with infrared laser light [2]. We found that although adiabatic evolution of the bound electron wave function (leading to increased downfield ionization) dominates for neutral molecules, nonadiabatic enhanced ionization still makes a significant contribution under typical experimental conditions, corresponding to the intermediate value $\gamma \approx 1$, where γ is the Keldysh parameter.

The results described above rely on comparison of experimental data with semiclassical simulations. Below we detail Quantum Trajectory Monte Carlo simulations for modeling strong field ionization of diatomic molecules. Such simulations are valuable in interpreting strong field ionization experiments, where the Time Dependent Schrodinger Equation (TDSE) simulations become formidable even for a much simpler case of a helium atom [3]. The computational costs of TDSE scale unfavorably with wavelength, making semiclassical simulations, such as the ones presented in this paper, especially valuable for more complicated systems (such as molecules) or lower-frequency mid-infrared fields.

2 General Approach

Below we present the methods behind Quantum Trajectory Monte Carlo (QTMC) simulation of molecules. These simulations arose from Classical Trajectory Monte Carlo (CTMC) simulations, with essential difference being that a phase is attached to each trajectory, accounting for quantum interference [4]. This becomes especially valuable for simulations of molecules, where trajectories coming from different parts of the molecule can interfere with each other (see Fig. 1).

2.1 Details of QTMC Simulations

To understand the asymmetry observed in the experimental data, Quantum Trajectory Monte Carlo (QTMC) simulations were performed [5], where the corrections proposed in [6] and the phase depending on the atomic positions with respect to the polarization direction introduced in [7] were included. The peak intensity was set to $I = 1.3 \times 10^{14}\ W/cm^2$ and the wavelength is 800 nm, just as in the experiment [2]. As we want to compare our results directly to experimental results, assuming a constant intensity is not sufficient but we have to take into account that there is a spatial variation of the intensity in the focal volume. This intensity profile is

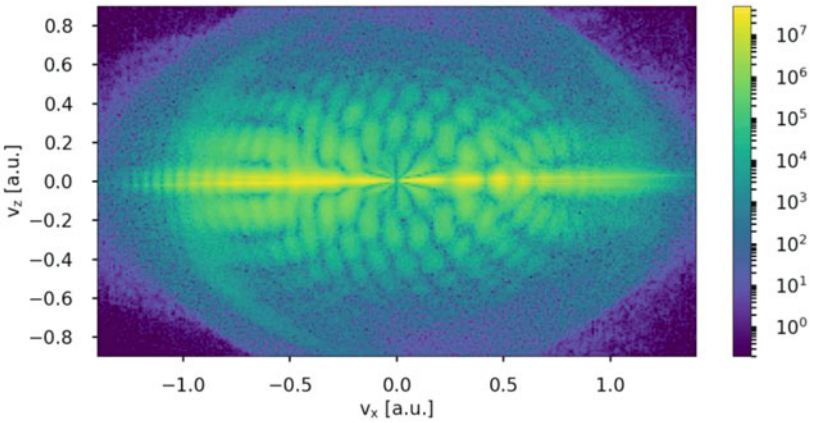

Fig. 1 Results of Quantum Trajectory Monte Carlo Simulations (QTMC) after strong field ionization of an N2 molecule. The peak laser intensity is 1.3×10^{14} W/cm^2 and wavelength is 800 nm, same as in [2]

commonly described by a Lorentzian along the laser beam axis, which for the sake of consistency with the nomenclature of cylindrical coordinates we will set to z for the following derivation, and by a Gaussian profile in ρ, the distance perpendicular to the beam axis [8].

Furthermore, in order to take into account that the shape of the molecular orbital changes the probability distribution of the initial transverse momentum, we modified the probability distribution by a pre-factor obtained in a partial Fourier transform [9], analogously to the way described in [10]. The molecular orbital that is needed for this method was computed in the STO-6G Gaussian basis with the restricted Hartree-Fock (RHF) method using the quantum chemistry package GAMESS [11]. In the basis set name, STO stands for 'Slater Type Orbitals' and 6G signifies that each atomic Slater-type orbital is represented by six Gaussian basis functions. The accuracy of the RHF/STO-6G calculation is supported by the fact that the ionization potential, computed according to Koopmans' theorem [12] as minus the energy of the highest occupied molecular orbital, is 0.57 a.u. = 15.5 eV. This value is very close to the experimentally observed ionization potential of 15.6 eV.

The laser is polarized along the x-axis and is six cycles long under a cosine-squared-envelope. The ionization potential is chosen to be Ip = 15.6 eV [13]. Since we are in the intermediate nonadiabatic regime ($\gamma = 0.9994$), the nonadiabatic ionization theory of Li et al. [14] was used to describe the initial conditions at the tunnel exit. The Coulomb potential used during propagation is the same as the one described in the supplementary of [2] and in [7], where the positive charge that the molecule has after ionization is distributed equally between the two atomic centers.

One of the main challenges is that the tunneling barrier is not only modified by the laser field but also by the Coulomb potential from the other nucleus. Since the mutual distortion of the Coulomb wells is so weak at the tunnel exit that it is a

good approximation to employ the atomic theory of Ref. [14] with the unshifted ionization potential of Ip = 15.6 eV to calculate the initial spatial conditions. Subsequently, as this theory assumes an atom placed at the origin, we merely shift this result by the central position of the respective atom the electron is born at.

Thus, we calculate the tunnel exits. In contrast, the tunnel width that mainly determines the tunneling probability is strongly affected by the internuclear Coulomb distortion and we cannot simply employ an atomic ionization theory that does not properly account for this effect when calculating the rates. Since solving this problem of the ratio of ionization from the up and downfield well is the aim of this work, we scan through different ionization ratios. This will lead to different degrees of asymmetry, which can then be compared to the asymmetry obtained from the experiment. To this end, we defined the ratio q of ionization from the two different sites as $q = \frac{\#up - \#down}{\#up + \#down}$, where #*up* and #*down* are the number of electrons born upfield and downfield, respectively. The limits of $q = -1$ and $q = +1$ therefore correspond to the electrons being born exclusively downfield or upfield, respectively. Note that the two different atoms change being the up- and downfield atom several times during the pulse as the sign of the electric field changes.

A sample momentum distribution obtained in the described QTMC simulation is shown above.

2.2 Results

Sweeping over the ionization ratio in QTMC simulations, one can obtain a unique map of the ionization site ratio onto the asymmetry parameter. Locating the experimental asymmetry parameter on this theoretical map (see green dot in Fig. 2 below) allows to estimate the ratio at which the electrons were released from the up- and downfield well from the experimental data. The result indicates that ionization from the downfield well is favored in the studied system. Asymmetries like the one described here can be expected in any system that exhibits a notable asymmetry in the molecular potential with respect to the axis of polarization direction and thus to have a wide range of applications. The method presented in [1] stands out in that it tracks the ionization site for single ionization of neutral molecules, where the technique of analyzing Coulomb explosion, that has so far been used to track ionization sites in diatomic molecules, is not applicable.

As the asymmetry in the momentum distribution is due to the asymmetry in the Coulomb potential, this work also stands in line with those recent publications that highlight the importance of including the Coulomb effect as accurately as possible when theoretically describing holographic effects [15–19]. In particular, this study is a case in point for the strength of QTMC simulations over using SFA theories. As highest accuracy is required in terms of the Coulomb potential here, it is not sufficient to include the Coulomb potential perturbatively as it is, for example, done in Coulomb-corrected SFA theories [20, 21].

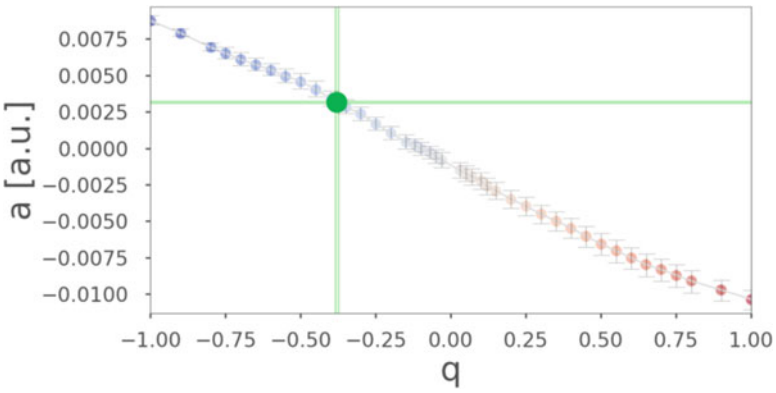

Fig. 2 Asymmetry in the electron momentum distribution (given by parameter "a" on the y-axis) as a function of the ratio of upfield vs. downfield ionization, given by "q" on the x-axis. The experimental asymmetry parameter (green dot) is extracted from the measurements published in [2]. In [1], the ratio q is extracted by comparing experimental data to QTMC simulations (points plotted with error bars). The experimental $q = -0.379$ obtained from this figure (see intersection of the vertical green line with the x-axis) corresponds to roughly two downfield electrons appearing for every upfield electron. The error bars account for the uncertainly in orientation of plus/minus 5 degrees

3 Conclusion and Outlook

Improvement of the theory presented here could be achieved by higher accuracy in the theoretical description of the diatomic model. For example, it is not clear whether it is a good approximation to distribute the ionic charge evenly to the two atomic centers after ionization. Even though the model of even charge distribution has been successfully applied in the theoretical interpretation of the very experimental data that are again used here, in the TDSE simulations [2] and the QTMC simulations in [7], a deeper study along these lines seems warranted, in particular if the theory is applied to other molecular systems.

Speaking of other systems, it seems important to emphasize that the theory presented can be applied to other molecules and laser parameters as well.

A larger bond length of the molecule would be expected to lead to a more pronounced asymmetry in the photoelectron momentum distribution, as long as the underlying assumptions of our model are satisfied. However, one should keep in mind that a larger bond length might change the whole underlying process, for example, of how the remaining positive charge is distributed to the ionic cores. Varying the bond length would be interesting in particular in that one might observe the transition from the electron being primarily born at the downfield atom to the electron being localized at the upfield well. Whereas dominant ionization from the downfield atom is expected in small molecules in which adiabatic adaption of the electron position plays a dominant role, as it was found to be the case for the N2 molecule presented in this chapter, the electron can be localized at the upfield well

in larger molecules due to nonadiabatic effects that are crucial in the phenomenon of ionization enhancement (CREI).

Acknowledgments We acknowledge support from the U.S. Department of Energy, Office of Basic Energy Sciences, Atomic, Molecular and Optical Sciences Program under Award No. DE-SC0022093.

References

1. Ortmann, L., AlShafey, A., Staudte, A., Landsman, A.S.: Tracking the Ionization Site in Neutral Molecules. Phys. Rev. Lett. **127**, 213201 (2021)
2. Meckel, M., Staudte, A., Patchkovskii, S., Villeneuve, D., Corkum, P., Doerner, R., Spanner, M.: Signatures oft he continuum electron phase in molecular strong-field photoelectron holography. Nat. Phys. **10**, 594–600 (2014)
3. Majety, V.P., Zielinski, A., Scrinzi, A.: Photoionization of a few electron systems: a hybrid coupled channel approach. New J. Phys. **17**, 063002 (2015)
4. Peng, L.Y., Jiang, W.C., Geng, J.W., Xiong, W.H., Gong, Q.: Tracing and controlling electronic dynamics in atoms and molecules by attosecond pulses. Phys. Rep. **575**, 1–71 (2015)
5. Li, M., Geng, J.W., Liu, H., Deng, Y., Wu, C., Peng, L.Y., Gong, Q., Liu, Y.: Classical-quantum correspondence for above-threshold ionization. Phys. Rev. Lett. **112**, 113002 (2014)
6. Shvetsov-Shilovski, N.I., Lein, M., Madsen, L., Rasanen, E., Lemell, C., Burgdoerfer, J., Arbo, D.G., Tokesi.: Semiclassical two-step model for strong-field ionization. Phys. Rev. A. **94**, 013415 (2016)
7. Liu, M., Li, M., Wu, C., Gong, Q., Staudte, A., Liu, Y.: Phase structure of strong-field tunneling wave packets from molecules. Phys. Rev. Lett. **116**, 163004 (2016)
8. Hansch, P., Walker, M., Van Woerkom, L.: Spatially dependent multiphoton multiple ionization. Phys. Rev. A. **54**, R2559–R2562 (1996)
9. Murray, R., Liu, W., Ivanov, M.Y.: Partial fourier-transform approach to tunneling ionization: Atomic systems. Phys. Rev. A. **81**, 023413 (2010)
10. Walt, S.G., Ram, N.B., Atala, M., Shvetsov-Shilovski, N.I., Von Conta, A., Baykusheva, D., Lein, M., Woerner, H.J.: Dynamics of valence-shell electrons and nuclei probed by strong-field holography and rescattering. Nat. Commun. **8**, 15651 (2017)
11. Schmidt, M.W., Baldridge, K.K., Boatz, J.A., Elbert, S.T., Gordon, M.S., Jensen, J.H., Koseki, S., Matsunaga, N., Nguyen, K.A., Su, S., Windus, T.L., et al.: General atomic and molecular electronic structure system. J. Comput. Chem. **14**, 1347–1363 (1993)
12. Ramachandran, D., G., & Namboori.: Computational Chemistry and Molecular Modeling: Principles and Applications. Springer (2008)
13. Huber, P.: Molecular Spectra and Molecular Structure: IV. Constants of Diatomic Molecules. Springer (2013)
14. Li, M., Geng, J.W., Han, M., Liu, M.M., Peng, L.Y., Gong, Q., Liu, Y.: Subcycle nonadiabatic strong-field tunneling ionization. Phys. Rev. A. **93**, 013402 (2016)
15. Song, X., Lin, C., Sheng, Z., Liu, P., Chen, Z., Yang, W., Hu, S., Lin, C.D., Chen, J.: Unraveling nonadiabatic ionization and coulomb potential effect in strong-field photoelectron holography. Sci. Rep. **6**, 28392 (2016)
16. Shi, G., Xu, J., Zhang, H., Lin, C., Song, X., Chen, J., Yang, W.: Coulomb potential effects in strong-field photoelectron holography with midinfrared laser. J. Phys. Conf. Ser. **869**, 012003 (2017)
17. Maxwell, A., Morisson de faria, C.: Coulomb-free and coulomb-distorted recolliding quantum orbits in photoelectron holography. J. Phys. B. **51**, 124001 (2018)

18. Danek, J.: Coulomb Effects in the Dipole and Nondipole Regimes of Strong-Field Ionization. PhD thesis. Ruprecht-karls-universitat Heidelberg (2018)
19. Lopez, S.D., Arbo, D.G.: Holographic interferences in photoelectron spectra: different approaches. Eur. Phys. J. D. **73**, 2 (2019)
20. Ciappina, M., Perez-Hernandez, J.A., Landsman, A.S., Zimmermann, T., Lewenstein, M., Roso, L., krausz, ferenc.: Carrier-wave Rabi-flopping signatures in high-order harmonic generation for alkali atoms. Phys. Rev. Lett. **114**, 143902 (2015)
21. Popruhzenko, S., Bauer, D.: Strong field approximation for systems with coulomb interaction. J. Mod. Opt. **55**, 2573–2589 (2008)

Control of Photoelectron-Ion Entanglement in Attosecond Laser-Induced Photoionization of H_2

Lisa-Marie Koll, Tobias Witting, and Marc J. J. Vrakking

Abstract We report experiments where vibrational wave packets are produced in H_2^+ by the ionization of neutral H_2 by a sequence of two phase-locked attosecond pulse trains (APTs) with a variable time delay. Changes in the degree of vibrational coherence in the H_2^+ cation with the XUV-XUV time delay can be explained in terms of the dependence of the degree of ion+photoelectron entanglement on the two-pulse delay.

Keywords Attosecond pump-probe spectroscopy · Ion+photoelectron entanglement · Vibrational coherence · Electronic coherence · Ultrafast processes · Schmidt decomposition

1 Introduction

In the last two decades, attosecond science has developed into a vibrant research field, where ultrafast dynamics involving electronic motion is investigated using pump-probe experiments that either use attosecond pulse trains (APTs) or isolated attosecond pulses (IAPs) formed through the process of High-Harmonic Generation (HHG) [1, 2]. Given that attosecond pulses produced by HHG have wavelengths in the extreme ultra-violet (XUV) or even soft X-ray part of the spectrum, attosecond pulses are ionizing radiation for any sample (solid, liquid or gaseous) that is placed in their path. This creates the possibility for the emergence of entanglement in attosecond experiments.

Entanglement refers to a situation in quantum mechanics where the wave function of a quantum system consisting of multiple parts cannot be written as a direct product of wave functions of the individual parts [3]. In the case of photoionization, entanglement occurs when the ion+photoelectron wave function

L.-M. Koll (✉) · T. Witting · M. J. J. Vrakking (✉)
Max-Born Institute (MBI), Berlin, Germany
e-mail: lisa.koll@mbi-berlin.de; marc.vrakking@mbi-berlin.de

L. Argenti et al. (eds.), *Proceedings of the 8th International Conference on Attosecond Science and Technology*, Springer Proceedings in Physics 300,
https://doi.org/10.1007/978-3-031-47938-0_15

cannot be written as the direct product of an ionic wavefunction and a photoelectron wavefunction, i.e.

$$\Psi \neq \psi_{\text{ion}} \otimes \psi_{\text{photoelectron}} \tag{1}$$

but instead can only be written as a sum of direct products, i.e.

$$\Psi \sim \sum\nolimits_{\alpha,\beta} \psi_{\text{ion},\alpha} \otimes \psi_{\text{photoelectron},\beta} \tag{2}$$

where α and β are quantum numbers that characterize the properties of the ion and the photoelectron, respectively.

Entanglement can have measurable consequences in attosecond experiments, in particular when, as is commonly the case, the experiment only includes observations within one of the two-subsystems. A prominent example are charge migration experiments [4–6], where the objective is the observation of electronic motion (i.e. electronic coherence) in the cation that is left behind by the photoionization process. These experiments typically do not include measurements of the properties of the accompanying photoelectron. However, if the ion+photoelectron quantum system is entangled, i.e. if selected states of the cation are accompanied by photoelectrons with different properties, then entanglement will prevent the observation of the electronic coherence and the charge migration process.

A simple example of this is presented by the H_2 molecule, which upon photoionization at sufficiently high photon energies (a few tens of eV) can produce the cation in the $1s\sigma_g$ or $2p\sigma_u$ electronic state. It is well established that the formation of a coherent superposition of these two electronic states leads to measureable consequences, namely a preferred laboratory-frame localization of the remaining bound electron on one of the two protons in the molecule [7]. This localization is a direct consequence of the fact that in a coherent superposition of the $1s\sigma_g$ and $2p\sigma_u$ states, the parity is no longer well-defined. However, due to ion+photoelectron entanglement, photoionization of H_2 by an attosecond pulse does not produce a laboratory-frame electron localization: given that dipole selection rules dictate that the symmetry of the ion+photoelectron wave function formed upon photoionization must be ungerade, the formation of the $1s\sigma_g$ electronic state is accompanied by the formation of photoelectrons with odd orbital angular momentum, whereas formation of the $2p\sigma_u$ electronic state is accompanied by photoelectrons with even angular momentum. In other words, the state that is formed upon photoionization strongly resembles a Bell state [3], and electron localization can and will only be observed in an attosecond pump-probe experiment as a result of further interaction of the probe laser with either the cation or the photoelectron that are formed, removing/reducing the entanglement of the quantum state that is initially formed by the XUV photoionization process [8].

Recently, we have started investigating the role of entanglement in attosecond experiments in our laboratory, by focusing on the vibrational dynamics (i.e. vibrational coherence) that can be induced in H_2^+ cations upon ionization by an

IAP or APT. As will be described below, we have performed experiments where H_2 was ionized by a sequence of two APTs with a variable time delay between them [9], and have observed that the degree of vibrational coherence in the H_2^+ cation depends on the XUV-XUV time delay in a manner that is fully consistent with predictions based on an assessment of the dependence of the expected degree of ion+photoelectron entanglement on the two-pulse delay. In this paper, we will summarize both our experimental [9] and theoretical [10] work on this problem, and provide an outlook towards future work on the role of entanglement within attosecond science.

2 Experiment

The experimental setup, shown in Fig. 1a, was described in detail in [9, 11], and therefore only a brief description will be given here. In the experiment, 2 mJ, 28 fs near-infrared (NIR) laser pulses from a 1 kHz Ti:Sapphire laser system were compressed using a 1 m long, 340 μm inner diameter, differentially pumped, Neon-filled (2 bar) hollow core fiber. After compensating for second and third-order dispersion, the pulses had a 1.4 mJ pulse energy and a pulse duration of 5 fs. Most of the pulse energy (80%) was used for HHG, whereas the remaining part (20%) was used as the probe pulse in the XUV + NIR pump-probe experiment.

The part of the NIR pulse used for HHG was sent into an ultra-stable, dispersion-balanced Mach-Zehnder interferometer, where the pulse was split into two phase-locked replicas with a relative delay controlled by a motorized delay stage. The interferometer was passively and actively stabilized. Passive stabilization was implemented by building the interferometer on a vibrationally decoupled bread-board, and by mounting the retro-reflectors on a stainless steel plate to shift the resonance frequencies away from dominant noise sources in the lab. The active stabilization was realized by co-propagating a 473.36 nm cw laser through the interferometer, and inducing interference fringes upon recombination of the two beams on a camera. Path length variations were measured by Fast Fourier transform processing using the Takeda algorithm [12]. The derived error signal was fed to a proportional-integral-derivative (PID) controller driving the delay stage. With this setup the delay between the two NIR pulses could be varied over a range of 400 fs with a < 10 as residual jitter. The accuracy and the stability of the Mach-Zehnder interferometer were validated using an experiment where excited state energies of Helium were determined (see Fig. 1b) [11].

To generate APTs by HHG, the collinear NIR pulse pair was focused into an Ar gas cell by a spherical mirror ($f = 750$ mm). The generated XUV beam and the NIR probe beam were recombined and imaged into a velocity map imaging (VMI) spectrometer [13], where they crossed a pulsed H_2 gas jet supplied by a nozzle integrated in the repeller electrode [14]. The polarization of the XUV and NIR beams was in the plane of the microchannel plate (MCP) detector. After the VMI chamber, XUV spectra were recorded using an XUV spectrometer [15]. In

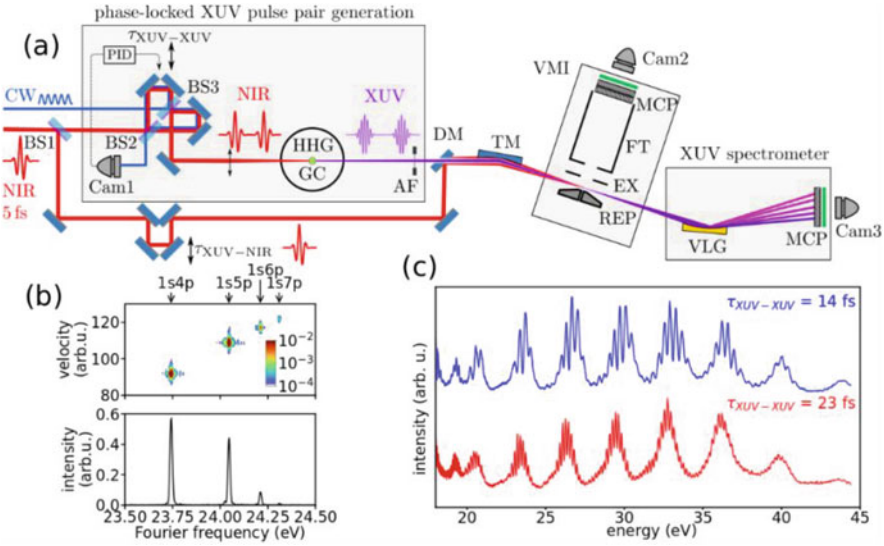

Fig. 1 (**a**) Experimental setup for the generation of phase-locked XUV pulses. (Adapted from [11]). A 5 fs NIR pulse is split into two parts, one of which is used for XUV generation and the other as the NIR probe pulse in the pump-probe experiment. The HHG driving pulse is sent through a passively and actively stabilized Mach-Zehnder Interferometer, in order to generate a phase-locked NIR pulse pair. The two phase-locked XUV pulses resulting from HHG are recombined with the NIR probe pulse and focused into the velocity map imaging (VMI) spectrometer by a toroidal mirror (TM). Abbreviations: *DM* drilled mirror, *BS* beam splitter, *CAM* camera, *AF* aluminum filter, *EX* Extractor electrode, *REP* Repeller, *MCP* microchannel plate, *VLG* variable line-spacing grating, *PID* proportional-integral-derivative feedback. (**b**) Experimental validation of the accuracy and stability of the Mach-Zehnder interferometer. (Adapted from [11]). Helium Rydberg states were excited using the phase-locked XUV pulses and ionized after a 1 ps delay using a narrowband NIR pulse. The Fourier transform power spectrum (FTPS) of the photoelectron yield as a function of the photoelectron momentum and $\tau_{XUV-XUV}$ is shown. Four peaks corresponding to the Rydberg states 1s4p–1s7p are visible with a linewidth of 0.022 eV. (**c**) measured XUV spectra for $\tau_{XUV-XUV}$=14 and 23 fs

Fig. 1c, XUV spectra for two time delays $\tau_{XUV-XUV}$ are shown. In the frequency domain, the spectra exhibit a modulation with a period inversely proportional to the delay, $\Delta\omega = \frac{2\pi}{\tau_{XUV-XUV}}$ a.u.

In the experiment, the two phase-locked XUV pulses were used to ionize H_2, forming a coherent superposition of vibrational levels in the $1s\sigma_g$ state of the H_2^+ cation. This vibrational wave packet oscillates back and forth between the inner and outer turning points of the $1s\sigma_g$ potential curve. At a variable time delay $\tau_{XUV-NIR}$, the NIR probe pulse projected the vibrational wave packet onto the repulsive $2p\sigma_u$ state, leading to dissociation. H^+ ions were then measured using the VMI spectrometer. Images were recorded as a function of $\tau_{XUV-XUV}$ (from 11 fs to 102 fs in 3 fs steps) and $\tau_{XUV-NIR}$ (from −50 fs to 800 fs in 4 fs steps). The lower limit of $\tau_{XUV-XUV}$ was chosen to avoid the regime where the two NIR driving pulses interfere with each other during the HHG process.

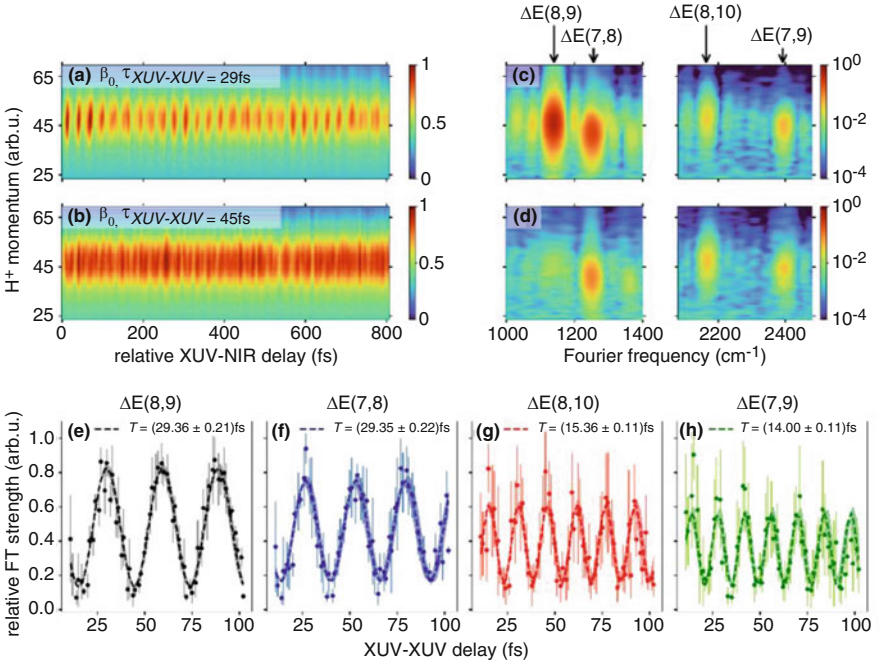

Fig. 2 (**a**) and (**b**) H^+ yield as a function of the H^+ momentum (in arbitrary units) and $\tau_{XUV-NIR}$ for two different $\tau_{XUV-XUV}$. (**c**) and (**d**) Fourier transform power spectra of the data shown in the left column. Pronounced quantum beats at frequencies $\Delta E_{v,v'}$ are visible, due to interfering dissociative ionization pathways involving vibrational states v and v'. (**e**) to (**h**) strength of the selected two-level quantum beats as a function of $\tau_{XUV-XUV}$ with the oscillation period given by the inset. The error bars represent the weighted average of multiple pump-probe scans. The experimental data points (given as dots) are fitted to sinusoidal curves (dashed lines) along with the corresponding standard deviation of the fit (shaded area). (Figure adapted from [9]))

Three-dimensional H^+ momentum distributions were retrieved by an inverse Abel transform [16]. Given that the H^+ ions are produced by means of a two-photon (XUV + NIR process), the angular distributions were expressed in terms of a superposition of Legendre polynomials up to fourth order [17].

In Fig. 2a, b the angle-integrated H^+ yield $\beta_0\left(v_{H^+}, \tau_{XUV-XUV}, \tau_{XUV-NIR}\right)$ is shown for $\tau_{XUV-XUV}$= 29 fs and 45 fs as a function of the H^+ momentum (in arbitrary units) and $\tau_{XUV-NIR}$. Vibrational motion of the wave packet with a period of ~30 fs, and the dephasing and rephasing of the wave packet can clearly be recognized. In Fig. 2c, d the corresponding Fourier transform power spectra (FTPS) are shown. Pronounced features in the FTPS result from nearest-neighbor and next-nearest-neighbor quantum beats. Interestingly, the strength of the nearest-neighbor quantum beats are much weaker for $\tau_{XUV-XUV}$ = 45 fs than for $\tau_{XUV-XUV}$= 29 fs, in contrast with the next-nearest-neighbor quantum beats, which have a comparable strength at both delays.

In Fig. 2e to h the intensity of the dominant nearest-neighbor and next-nearest neighbor quantum beats are plotted as a function of $\tau_{\mathrm{XUV-XUV}}$. Clearly, the intensity of the peaks in the FTPS oscillates as a function of $\tau_{\mathrm{XUV-XUV}}$, with a period inversely proportional to the frequency of the quantum beat. The vibrational quantum beats are observed when $\tau_{\mathrm{XUV-XUV}} = \frac{2n\pi}{\Delta E_{v,v'}}$, with n an integer and $\Delta E_{v,v'}$ the energy difference between two vibrational states. However, they are absent when $\tau_{\mathrm{XUV-XUV}} = \frac{(2n+1)\pi}{\Delta E_{v,v'}}$.

The ability to observe the vibrational quantum beats depends on the coherence properties of the vibrational states. As we will show below, for certain $\tau_{\mathrm{XUV-XUV}}$ entanglement between the H_2^+ ion and the photoelectron accompanying its formation can limit the vibrational coherence and therefore the ability to observe specific quantum beats.

3 Calculations

In order to support the interpretation of the experiments, the pump-probe experiment was replicated in calculations, where an H_2 molecule aligned along the pump/probe polarization axis was ionized by a sequence of two IAPs with a variable delay, forming a vibrational wavepacket in the H_2^+ cation that was probed at a variable time delay using a short UV (rather than a short NIR) probe pulse. Just like in the experiment, the pump-probe sequence led to the formation of H^+ fragments, and momentum-resolved H^+ fragment distributions were calculated as a function of the pump-probe delay $\tau_{\mathrm{XUV-UV}}$, the delay between the two IAPs $\tau_{\mathrm{XUV-XUV}}$ and the accompanying photoelectron momentum [10].

Technically, the calculations were performed by propagating the time-dependent Schrödinger equation (TDSE) in two dimensions, with one dimension reserved for the internuclear motion and one for the motion of the photoelectron. Nuclear (k) and photoelectron (p) momentum-resolved H^+ fragment yields were obtained by applying the time-dependent surface flux (TSURFF) method [18, 19]. Details on the computational method can be found in [20].

The XUV pulse pair consisted of a pair of 10-cycle, ω_{XUV}=0.8 a.u. laser pulses with a peak field strength of 0.001 a.u., whereas the UV probe was a 5-cycle, ω_{UV}=0.114 a.u. (400 nm) laser pulse with a peak field strength of 0.004 a.u. The calculations satisfactorily reproduced the experimentally observed behavior, namely the oscillation of the intensity of selected two-level quantum beats as a function of $\tau_{\mathrm{XUV-XUV}}$, with a maximum occurring for $\tau_{\mathrm{XUV-XUV}} = \frac{2n\pi}{\Delta E_{v,v'}}$, and a minimum for $\tau_{\mathrm{XUV-XUV}} = \frac{(2n+1)\pi}{\Delta E_{v,v'}}$ (see [10]). There are several ways in which the calculations allow to conclude that this behavior is due to ion+photoelectron entanglement.

Firstly, it is straightforward to consider the influence of $\tau_{\mathrm{XUV-XUV}}$ on the photoelectron kinetic energy distributions that accompany the formation of two vibrational states v and v'. The interference between the two IAPs creates a

modulation in the XUV spectrum, with successive maxima separated by $\Delta\omega = \frac{2\pi}{\tau_{\mathrm{XUV-XUV}}}$ a.u. (see Fig. 1c). When $\Delta\omega$ is an integer divisor of $\Delta E_{v,\,v'}$, then the photoelectron spectra accompanying the formation of vibrational states v and v' line up with each other (see Fig. 3 of [10]), except in the wings of the spectrum, where it is recognizable that the two spectra are in fact offset by $\Delta E_{v,\,v'}$. In this case a measurement of the photoelectron momentum or kinetic energy does not contain significant information on the quantum state (v or v') of the accompanying cation, and hence the vibrational coherence between v and v' can be clearly observed in the FTPS. Conversely, when $\Delta\omega$ is a half-integer divisor of $\Delta E_{v,\,v'}$, then the photoelectron spectra accompanying the formation of v and v' are offset from each other over the entire photoelectron kinetic energy range, indicating that a possible measurement of the photoelectron kinetic energy would allow a determination, with a high probability of success, of the quantum state of the accompanying cation. Hence, in this case the ion+photoelectron quantum system is entangled and the vibrational coherence between v and v' is not observed.

Secondly, the availability of the 2D ion+photoelectron wave function within the TDSE calculation allows the evaluation of several measures that quantify the degree of entanglement between the ion and the photoelectron. The first of these, the so-called "purity", is obtained by using the 2D ion+photoelectron wave function to determine the reduced ionic density matrix, which in the basis of cationic vibrational states can be written as

$$\rho_{vv'} = \int dx \psi_{vx} {\psi_{v'x}}^{*} \tag{3}$$

In this expression ψ_{vx} describes a contribution to the total ion+photoelectron wave function, where the cation occupies vibrational state v and the photoelectron coordinate is x. Figure 3a, b show the reduced ionic density matrix for two delays between the two XUV IAPs, namely $\tau_{\mathrm{XUV-XUV}}$ is 7.2 and 15.7 fs [10]. At a delay of 15.7 fs, corresponding to a maximum in the intensity of the two-level quantum beats in the FTPS, both diagonal and off-diagonal reduced density matrix elements are non-zero, the latter being a measure of the existence of vibrational coherence. At a delay of 7.2 fs, the diagonal reduced density matrix elements retain the same values, but the off-diagonal reduced density matrix elements involving adjacent vibrational states ($|v - v'| = 1$) are zero, indicating that there is no coherence between these states. The reason is, as before, ion+photoelectron entanglement, i.e. the fact that the photoelectrons accompanying the formation of cationic states v and v' contain "which-way" information that allows a determination (in principle) of the quantum state of the cation.

Thirdly, the reduced density matrices shown in Fig. 3a, b can be used to perform a Schmidt-decomposition [3]. The Schmidt rank quantifies the number of direct products (see Eq. (2)) that are needed for an accurate representation of the wavefunction, and thus quantifies if the ion+photoelectron wave function is separable (Schmidt rank of 1) or entangled (Schmidt rank of 2 or higher). In the present case, singular value decomposition (SVD) of the reduced ionic density

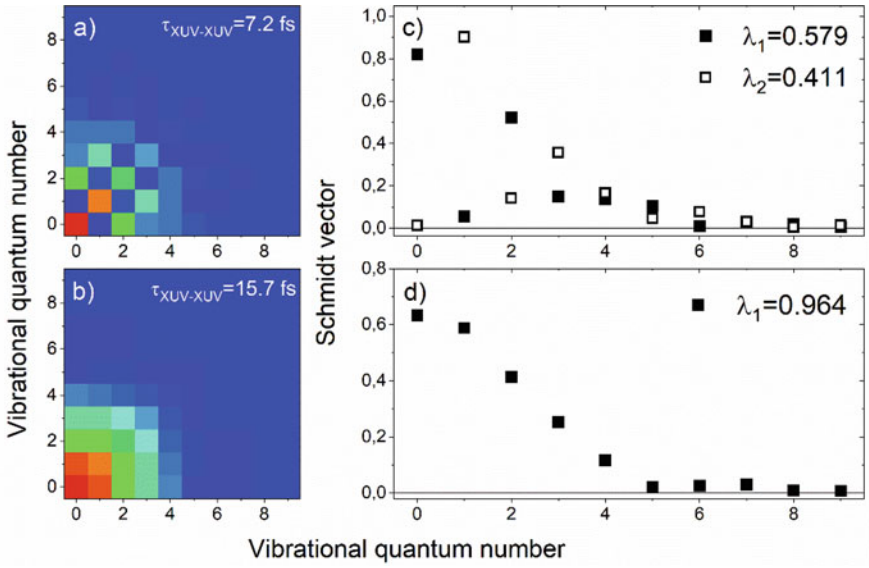

Fig. 3 (**a**) and (**b**) reduced ionic density matrices ρ_{ion} describing the vibrational coherence following ionization of H_2 by a sequence of two attosecond laser pulses with relative delay $\tau_{XUV-XUV}$= 7.2 and 15.7 fs. The diagonal density matrix elements, indicating the populations of the vibrational states, do not depend on $\tau_{XUV-XUV}$. However, as a result of ion+photoelectron entanglement, the vibrational coherence (described by the off-diagonal density matrix elements) is markedly different; (**c**) and (**d**) Schmidt decomposition of the reduced ionic density matrices ρ_{ion} shown in (**a**) and (**b**). In the former case, the photoelectron+ion quantum system is in a mixed state, with Schmidt rank 2, with the two Schmidt vectors corresponding to superpositions of predominantly even-v, respectively, odd-v vibrational states. In the latter case, the Schmidt rank is 1, and all vibrational states form a coherent superposition

matrices at $\tau_{XUV-XUV}$= 7.2 fs and 15.7 fs reveals that for $\tau_{XUV-XUV}$= 7.2 fs the system is described by a mixed quantum state with Schmidt rank 2 (with Schmidt coefficients 0.579 and 0.411), with the two Schmidt vectors corresponding to superpositions of predominantly even-v, respectively, odd-v vibrational states (see Fig. 3c). Conversely, for $\tau_{XUV-XUV}$= 15.7 fs, the system is well-described by a pure state with Schmidt rank 1 (Schmidt coefficient 0.964) that contains both even and odd vibrational states (see Fig. 3d).

4 Conclusions and Outlook

In this paper we have shown that the degree of vibrational coherence in H_2^+ cations that result from the ionization of neutral H_2 by a pair of phase-locked APTs is controlled by the degree of ion+photoelectron entanglement that is created in the ionization process. We have observed that a high degree of ion+photoelectron

entanglement occurs whenever the delay between the two phase-locked XUV pulses $\tau_{\mathrm{XUV-XUV}} = \frac{(2n+1)\pi}{\Delta E_{v,v'}}$, whereas a high degree of vibrational coherence is observed whenever $\tau_{\mathrm{XUV-XUV}} = \frac{2n\pi}{\Delta E_{v,v'}}$. Hence in these experiments the two-pulse time delay $\tau_{\mathrm{XUV-XUV}}$ acts as a control parameter that allows to tune the degree of ion+photoelectron entanglement, or, conversely, the degree of vibrational coherence.

While the use of a pair of phase-locked XUV pulses (with a variable delay) is thus far not common within attosecond science, and has to our knowledge not previously been used in attosecond pump-probe experiments, we argue that the role of ion+photoelectron entanglement, as observed in our experiment, is likely to be quite common, in particular in attosecond experiments where the interpretation of the experiment depends on the detailed quantum properties (including symmetry) of the system under investigation. As an example of this, we have discussed in the introduction of this paper the well-studied problem of electron localization in the course of dissociative ionization of H_2 [7, 8]. The observation of electron localization in an attosecond XUV + NIR pump-probe experiment requires that the initial ion+photoelectron entanglement that results from the XUV photoionization process (which prevents the observation of electron localization) is converted into electronic coherence, i.e. the existence of a coherent superposition of the $1s\sigma_g$ and $2p\sigma_u$ states. This suggests that the observable degree of electronic coherence and electron localization sensitively depend on the properties of the accompanying photoelectron (i.e. its velocity, as well as its laboratory frame and/or molecular frame angular distribution), and suggests the importance of kinematically complete coincidence experiments as a tool towards the investigation of the role of entanglement in attosecond experiments. In addition, building on the results that we have presented in this paper for the case of vibrational coherence, we expect that the degree of electronic coherence and electron localization can be controlled by a phase-locked sequence of two IAPs with a variable delay. Efforts to observe this behavior are currently ongoing in our laboratory.

Besides the entanglement between the photoelectron kinetic energy and the vibrational or electronic dynamics in the cation that we have discussed in this paper, there are other forms of entanglement that one may encounter in attosecond experiments. As two examples, we mention the entanglement between electronic and nuclear motion in the photoexcitation of molecules that was recently analyzed by Blavier et al. [21], and the entanglement between radial and angular properties of the photoelectrons resulting from atomic photoionization, recently reported by Busto et al. [22].

We conclude that in the foreseeable future studies of the role of entanglement are likely to be a prominent topic within attosecond science. Among other reasons, these studies are important in order to gain a better understanding of the role that entanglement may play as a limiting factor towards the observation of phenomena of high interest, such as attosecond charge migration [23].

Acknowledgments The authors acknowledge Lorenz Drescher and Laura Maikowski for their role in the development of the Mach-Zehnder interferometer used to generate the phase-locked XUV pulse pair.

References

1. Agostini, P., DiMauro, L.F.: The physics of attosecond light pulses. Rep. Prog. Phys. **67**, 813–855 (2004)
2. Krausz, F., Ivanov, M.: Attosecond physics. Rev. Mod. Phys. **81**, 163–234 (2009)
3. Nielsen, M.A., Chuang, I.L.: Quantum Computation and Quantum Information: 10th Anniversary Edition. Cambridge University Press, Cambridge (2010)
4. Breidbach, J., Cederbaum, L.S.: Migration of holes: Formalism, mechanisms, and illustrative applications. J. Chem. Phys. **118**, 3983–3996 (2003). https://doi.org/10.1063/1.1540618
5. Remacle, F., Levine, R.D.: An electronic time scale in chemistry. Proc. Natl. Acad. Sci. U. S. A. **103**, 6793–6798 (2006)
6. Calegari, F., et al.: Ultrafast electron dynamics in phenylalanine initiated by attosecond pulses. Science. **346**, 336–339 (2014). https://doi.org/10.1126/science.1254061
7. Kling, M.F., et al.: Control of electron localization in molecular dissociation. Science. **312**, 246–248 (2006)
8. Sansone, G., et al.: Electron localization following attosecond molecular photoionization. Nature. **465**, 763–U763 (2010). https://doi.org/10.1038/Nature09084
9. Koll, L.-M., Maikowski, L., Drescher, L., Witting, T., Vrakking, M.J.J.: Experimental control of quantum-mechanical entanglement in an attosecond pump-probe experiment. Phys. Rev. Lett. **128**, 043201 (2022). https://doi.org/10.1103/PhysRevLett.128.043201
10. Vrakking, M.J.J.: Control of attosecond entanglement and coherence. Phys. Rev. Lett. **126**, 113203 (2021). https://doi.org/10.1103/PhysRevLett.126.113203
11. Koll, L.-M., Maikowski, L., Drescher, L., Vrakking, M.J.J., Witting, T.: Phase-locking of time-delayed attosecond XUV pulse pairs. Opt. Express. **30**, 7082–7095 (2022). https://doi.org/10.1364/OE.452018
12. Takeda, M., Ina, H., Kobayashi, S.: Fourier-transform method of fringe-pattern analysis for computer-based topography and interferometry. J. Opt. Soc. Am. **72**, 156–160 (1982). https://doi.org/10.1364/JOSA.72.000156
13. Eppink, A.T.J.B., Parker, D.H.: Velocity map imaging of ions and electrons using electrostatic lenses: Application in photoelectron and photofragment ion imaging of molecular oxygen. Rev. Sci. Instrum. **68**, 3477–3484 (1997). https://doi.org/10.1063/1.1148310
14. Ghafur, O., et al.: A velocity map imaging detector with an integrated gas injection system. Rev. Sci. Instrum. **80**, 033110 (2009). https://doi.org/10.1063/1.3085799
15. Kita, T., Harada, T., Nakano, N., Kuroda, H.: Mechanically ruled aberration-corrected concave gratings for a flat-field grazing-incidence spectrograph. Appl. Opt. **22**, 512–513 (1983)
16. Whitaker, B.J.: Imaging in Molecular Dynamics, Technology and Applications. Cambridge University Press, Cambridge (2003)
17. Reid, K.L.: Photoelectron angular distributions. Annu. Rev. Phys. Chem. **54**, 397–424 (2003)
18. Scrinzi, A.: T-SURFF: fully differential two-electron photo-emission spectra. New J. Phys. **14** (2012). https://doi.org/10.1088/1367-2630/14/8/085008
19. Yue, L., Madsen, L.B.: Dissociation and dissociative ionization of H2+ using the time-dependent surface flux method. Phys. Rev. A. **88**, 063420 (2013). https://doi.org/10.1103/PhysRevA.88.063420
20. Vrakking, M.J.J.: Ion-photoelectron entanglement in photoionization with chirped laser pulses. J. Phys. B Atomic Mol. Phys. **55**, 134001 (2022). https://doi.org/10.1088/1361-6455/ac6e17

21. Blavier, M., Levine, R.D., Remacle, F.: Time evolution of entanglement of electrons and nuclei and partial traces in ultrafast photochemistry. Phys. Chem. Chem. Phys. **24**, 17516–17525 (2022). https://doi.org/10.1039/D2CP01440H
22. Busto, D., et al.: Probing electronic decoherence with high-resolution attosecond photoelectron interferometry. Eur Phys J D. **76**(7), 112 (2022). https://doi.org/10.48550/ARXIV.2111.12037
23. Ruberti, M.: Onset of ionic coherence and ultrafast charge dynamics in attosecond molecular ionisation. Phys. Chem. Chem. Phys. **21**, 17584–17604 (2019). https://doi.org/10.1039/C9CP03074C

Part III
Attosecond Spectroscopy of Condensed Matter

Ultrafast Second-Harmonic XUV Spectroscopy: A Novel Probe for Symmetry

Michael Zuerch

Abstract Extreme-ultraviolet second-harmonic generation spectroscopy (XUV-SHG) is a novel spectroscopy that enables probing element-selective symmetry-broken states. This renders XUV-SHG especially useful to study surfaces, interfaces, and symmetry-broken bulk states in otherwise complex chemical environments. In a string of recent works, XUV-SHG was successfully applied to study the role of lithium in various compounds. One of the most striking recent results studied the role of Li symmetry-breaking displacement causing the emergence of polarity in the polar metal $LiOsO_3$. Furthermore, the directional dependence of the SHG process allows geometry specific measurements. Given the femtosecond nature of the probe pulses, one can readily envision this method to be applied to study interfacial carrier dynamics in complex in-operando environments that are difficult to probe with conventional ultrafast methods.

Keywords Nonlinear x-ray spectroscopy · Symmetry breaking · Polar metal

1 Introduction

Understanding interfacial chemistry, electronic structure as well as symmetry properties at a molecular level is of great importance for investigating the structure-function relationship of matter. A key challenge lies in isolating relevant observables to one or very few atomic layers forming an interface. For decades, surface-sensitive photoemission techniques as well as nonlinear optical and infrared spectroscopy have been successfully applied to study surface chemistry and physical phenomena. Despite the significant progress in understanding surfaces, most of the techniques

M. Zuerch (✉)
Department of Chemistry, University of California at Berkeley, Berkeley, CA, USA

Lawrence Berkeley National Laboratory, Materials Sciences Division, Berkeley, CA, USA
e-mail: mwz@berkeley.edu

L. Argenti et al. (eds.), *Proceedings of the 8th International Conference on Attosecond Science and Technology*, Springer Proceedings in Physics 300,
https://doi.org/10.1007/978-3-031-47938-0_16

at hand do not provide the required sensitivities, e.g., at a buried layer or when the interface of interest is emersed in a complex chemical environment. For example, photocatalytic systems typically consist of multi-layered structures consisting of a photoabsorber and catalyst which are immersed in a bath of liquid or gas. In such systems, especially within *in operando* conditions, elucidating interfacial properties and dynamics is difficult. A similar situation applies to symmetry-broken materials where emerging properties often stem from the lack of symmetry. In complex quantum materials more than one part of the material can contribute to these properties. Disentangling different contributions to symmetry is of great importance to better understand the emergence of novel properties to inform material design and discovery.

There is a lack of methods that allow measuring interfaces and symmetry properties with the sensitivity required to obtain the electronic and molecular structure. Given their high penetration depths, X-rays in general appear suitable due to their sensitivity to core-electrons hence providing element specificity. In standard X-ray absorption spectroscopy (XAS), spectra collected by traversing through a material contain information associated with either side of an interface, i.e., mostly bulk. An emerging method to overcome this limitation is extreme-ultraviolet / soft X-ray second harmonic generation spectroscopy (XUV-SHG) [1]. In this type of spectroscopy, two XUV photons of frequency ω are resonantly absorbed by a core-electron and the resulting SHG photon at frequency 2ω is detected. This process satisfies the relationship $I_{2\omega} \sim \chi^{(2)}(\omega)\, I_{\omega}{}^2$, where $\chi^{(2)}(\omega)$ is the second-order nonlinear susceptibility containing material properties pertaining to broken symmetry. The generally low magnitude of the second-order nonlinear response compared to the linear dielectric response of a material requires tens or hundreds of GW peak power, largely requiring free-electron laser (FEL) sources. The second-order nonlinear susceptibility $\chi^{(2)}$ is a tensor of rank 3. The different tensor components encode information of the nonlinear dielectric response in different planes of the crystal. When a material is inversion-symmetric, all tensor elements are zero making SHG a sensitive probe to broken inversion symmetry. This property allows using SHG to study symmetry within bulk or at any interface. In SHG experiments determining $\chi^{(2)}(\omega)$ becomes the central task which can be achieved by fitting a measured $I_{2\omega}$–I_{ω} dependence.

The first observation of second harmonic generation in the hard X-ray regime by Shwartz et al. used 7.3 keV photon energy on a diamond crystal [2]. This first observation showed the feasibility of SHG experiments with FELs but found that the response observed appeared not to be sensitive to symmetry-breaking. This was explained by that excited electrons at such high photon energies can be treated as free particles causing the dominant nonlinearity to stem from plasma-like properties. In contrary, Lam et al. demonstrated on graphite films of varying thickness at the carbon K edge [1] in the soft X-ray that indeed at such more moderate photon energies one obtains sensitivity to symmetry. Elemental specificity in XUV-SHG was first demonstrated in $GaFeO_3$, which has a symmetry-broken bulk state, at

the iron M edge [3]. The second harmonic spectra exhibited strong resonances indicative of the large asymmetry of iron within the unit cell of $GaFeO_3$. A central advantage of XUV-SHG is the capability to measure buried interfaces. This was first demonstrated by Schwartz et al. who studied a perylene-boron junction [4]. Supported by numerical simulations they were able to show that that spectral shifts observed at the boron K edge were dependent on the interfacial bond length. This can be rationalized by the interfacial charge transfer shifting the valence state energies. A series of recent works that specifically studied symmetry-breaking by lithium in different materials will be more closely discussed in the following section.

2 Lithium-Specific Measurement in Symmetry-Broken Solids

Following the initial works in XUV-SHG that showed that the soft X-ray and extreme ultraviolet are suitable regimes for studying elemental resolved symmetry-breaking, a series of works focused on the role of lithium. These works address the inherent difficulty to measure lithium within solids with conventional scattering techniques, such as electron or X-ray scattering. This is due to the low atomic number of lithium having a low scattering cross-section which often results in strong dominance of signals contributed by other heavier elements in presence.

A first study of the role of lithium in quantum materials targeted an interesting physical phenomenon where ferroelectricity and metallicity coexist in a single material which was first theoretically proposed by Anderson and Blount in 1965 [5]. These properties normally contradict each other as free electrons from a metallic state would be expected to shield local dipoles preventing long-range order. However, as predicted in this theoretical work, such polar metals can exist for certain crystals undergoing a second-order phase transition where free electrons cannot entirely shield electric dipoles. It took almost 50 years when Shi et al. successfully synthesized $LiOsO_3$ and demonstrated its polar metal properties [6]. Since this first discovery large interest has been put forward for such materials as possible building blocks in highly integrated circuitry where polar metals combine metallic conduction with the capability to store information in the long-range dipole order. In the recent years, more materials have been found to belong to this material class [7].

Despite these first discoveries many questions pertaining to the emergence of these properties remained. Especially the exact role of the lithium atoms in $LiOsO_3$ is difficult to study with conventional scattering techniques. To contribute to the study of this novel material, Berger et al. studied the symmetry-breaking in the polar phase of $LiOsO_3$ using XUV-SHG specific to lithium (Fig. 1) [8]. In this material, the polar metal phase emerges at temperatures below 140 K where $LiOsO_3$ undergoes a second-order phase transition with lithium atoms being displaced along a polar axis causing ferroelectricity while free electrons stemming from Os 5d states sustain conductivity of the material rendering it a polar metal. XUV-SHG

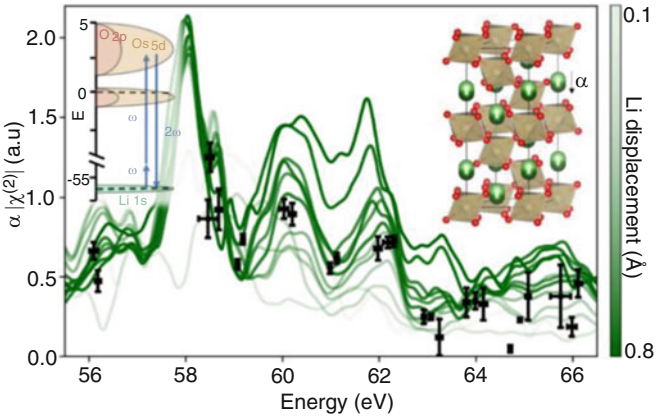

Fig. 1 XUV-SHG spectra and simulation depending on Li displacement in $LiOsO_3$ at 60 K. Lines with different shades of green represent different amount of Li displace α along the polar axis from centrosymmetry. The black squares represent measured data. The inset shows pictographically the energy diagram for the experiment conducted in two-photon resonance with the Li 1 s state

spectra were measured around the Li K-edge (56–66 eV) by focusing an intense free-electron laser beam onto the material with photon energies in the range of 28–33 eV. It was possible to estimate the displacement of Li from centrosymmetry of about 0.5 Å which is consistent with first neutron diffraction measurements on that material [6]. The experiments in concert with advancements of numerical simulation using time-dependent DFT methods have provided deeper insights into how the XUV-SHG spectrum encodes information about the dielectric environment of a single atomic species in its symmetry-broken state. Further, in this work the importance of considering the directional dependence of the $\chi^{(2)}$ tensor was studied in [8], which is discussed in detail in Sect. 3.

Following this first work, the role to symmetry-breaking of the Li atom was further studied in $LiNbO_3$ where in addition to the second harmonic spectrum for the first time the polarization of the XUV-SHG signal itself was studied [9]. For this, the researchers inserted a polarizer consisting of a multilayer mirror selecting the XUV-SHG signal under 45° angle of incidence [10]. The resulting XUV-SHG polarimetry signal was related to expected symmetries from the crystal structure. Also, this work was the first showing several absorption features of different elements, Li and Nb at the K and N edges respectively, that are spectrally separate but measured in the same experiment indicating contributions to symmetry-breaking by both elements within the unit cell.

3 Interpretation of Second-Order Susceptibility Tensor Components

A crucial aspect for all XUV-SHG measurements is the correct treatment of the experimental geometry and directional dependence of the rank 3 second-order susceptibility tensor. Typically, for given polarizations and crystal orientation one obtains a projection of the weighted tensor components $\chi^{(2)}_{ijk}$ onto an effective $\chi^{(2)}_{eff}$. Figure 2a–d show the calculated independent tensor components for $LiOsO_3$ at the Li K edge, where the point group results in four independent tensor components. Inspecting the projected charge density (Fig. 2, projection into the z-x-plane) allows to qualitatively interpret the tensor components. For example, $\chi^{(2)}_{zzz}$ (Fig. 2a) represents a condition where two driving field components and the second-order polarization point into the z direction which is along the polar bond. In this case, one observes a strong dependence of the second-order response at the Li edge which can be rationalized by the strong symmetry-breaking afforded by Li in this direction. In contrary, inspecting $\chi^{(2)}_{xxy}$ (Fig. 2c) one finds only a comparatively small response since all involved fields and polarization point perpendicular to the polar axis. Taking such geometric effects into account enables one to not only measure element-specific symmetry-breaking but also amplify the response w.r.t. to a specific symmetry-direction of the crystal if that is desired.

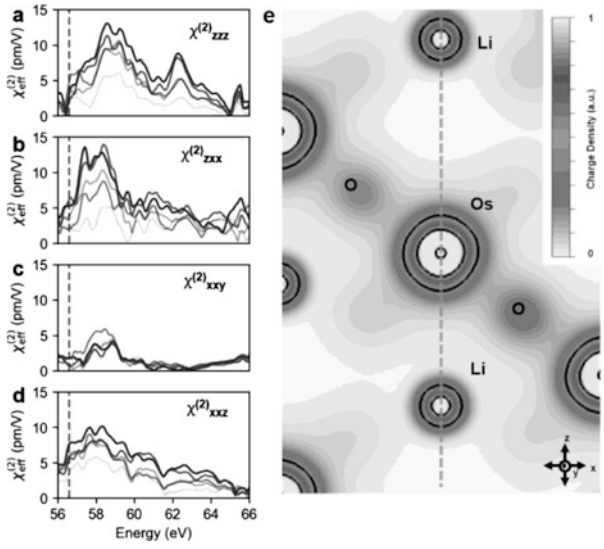

Fig. 2 Interpretation of tensor components of $LiOsO_3$. (**a**)–(**d**), four numerically calculated independent tensor components for varying Li atom displacement. (**e**) Projection of the charge density into the z-x plane with Li atom displaced along the polar axis (dashed gray line). (Panels taken from Ref. 8 with permission from the authors)

4 Outlook

All the works mentioned in Sects. 1, 2, and 3 made use of the high pulse intensities afforded by FEL sources. Using table-top sources, for example driven by high harmonic generation (HHG), can be a route to improve access to XUV-SHG in the coming years. HHG sources generally exhibit pulses in the femtosecond regime with high coherence which renders them in general suitable sources to obtain high peak intensities. Limiting factors are the comparatively low energy per pulse in the pJ to nJ range with only few examples of pulses above 10 nJ energy per pulse. Scaling such sources to higher pulse energy could open routes to table-top XUV-SHG [11]. A first proof-of-principle experiment for table-top XUV-SHG has been performed by Helk et al. who used a post-amplified HHG source that reached ~111 nJ pulse energy and a tight focusing geometry using an off-axis ellipsoidal mirror [12]. In addition, other recent advancements in achieving attosecond FEL pulses [13] provide interesting new opportunities in materials sciences using XUV-SHG spectroscopy in combination with methods that were recently developed to study materials with transient XUV spectroscopies [14–27]. An open topic to study in more detail in the context of strongly driven materials is the interplay between different material responses such as self-induced transparency and two-photon absorption [28] in relation to second-harmonic generation. Despite its novelty XUV-SHG has already shown its importance in studying surfaces, buried interfaces and symmetry properties of relevant materials with emerging properties.

Acknowledgments M.Z. acknowledges funding by the W. M. Keck Foundation, funding from the UC Office of the President within the Multicampus Research Programs and Initiatives (M21PL3263), and funding from Laboratory Directed Research and Development Program at Berkeley Lab (107573).

References

1. Lam, R.K., et al.: Soft X-ray second harmonic generation as an interfacial probe. Phys. Rev. Lett. **120**, 023901 (2018)
2. Shwartz, S., et al.: X-ray second harmonic generation. Phys. Rev. Lett. **112**, 163901 (2014)
3. Yamamoto, S., et al.: Element selectivity in second-harmonic generation of $GaFeO_3$ by a soft-X-ray free-electron laser. Phys. Rev. Lett. **120**, 223902 (2018)
4. Schwartz, C.P., et al.: Angstrom-resolved interfacial structure in buried organic-inorganic junctions. Phys. Rev. Lett. **127**, 096801 (2021)
5. Anderson, P.W., Blount, E.I.: Symmetry considerations on martensitic transformations: 'ferro-electric' metals? Phys. Rev. Lett. **14**, 532–532 (1965)
6. Shi, Y., et al.: A ferroelectric-like structural transition in a metal. Nat. Mater. **12**, 1024–1027 (2013)

7. Du, D., et al.: High electrical conductivity in the epitaxial polar metals LaAuGe and LaPtSb. APL Mater. **7**, 121107 (2019)
8. Berger, E., et al.: Extreme ultraviolet second harmonic generation spectroscopy in a polar metal. Nano Lett. **21**, 6095–6101 (2021)
9. Uzundal, C.B., et al.: Polarization-resolved extreme-ultraviolet second-harmonic generation from $LiNbO_3$. Phys. Rev. Lett. **127**, 237402 (2021)
10. Sumi, T., et al.: Separating non-linear optical signals of a sample from high harmonic radiation in a soft X-ray free electron laser. E-J. Surf. Sci. Nanotechnol. **20**, 31–35 (2022)
11. Helk, T., Zürch, M., Spielmann, C.: Perspective: towards single shot time-resolved microscopy using short wavelength table-top light sources. Struct. Dyn. **6**, 010902 (2019)
12. Helk, T., et al.: Table-top extreme ultraviolet second harmonic generation. Sci. Adv. **7**, eabe2265 (2021)
13. Duris, J., et al.: Tunable isolated attosecond X-ray pulses with gigawatt peak power from a free-electron laser. Nat. Photonics. **14**, 30–36 (2020)
14. Zürch, M., et al.: Direct and simultaneous observation of ultrafast electron and hole dynamics in germanium. Nat. Commun. **8**, 15734 (2017)
15. Cushing, S.K., et al.: Differentiating Photoexcited carrier and phonon dynamics in the Δ, L, and Γ valleys of Si(100) with transient extreme ultraviolet spectroscopy. J. Phys. Chem. C. **123**, 3343–3352 (2019)
16. Cushing, S.K., et al.: Hot phonon and carrier relaxation in Si(100) determined by transient extreme ultraviolet spectroscopy. Struct. Dyn. **5**, 054302 (2018)
17. Zürch, M., et al.: Ultrafast carrier thermalization and trapping in silicon-germanium alloy probed by extreme ultraviolet transient absorption spectroscopy. Struct. Dyn. **4**, 044029 (2017)
18. Geneaux, R., Marroux, H.J.B., Guggenmos, A., Neumark, D.M., Leone, S.R.: Transient absorption spectroscopy using high harmonic generation: a review of ultrafast X-ray dynamics in molecules and solids. Philos. Trans. R. Soc. Math. Phys. Eng. Sci. **377**, 20170463 (2019)
19. Kaplan, C.J., et al.: Femtosecond tracking of carrier relaxation in germanium with extreme ultraviolet transient reflectivity. Phys. Rev. B. **97**, 205202 (2018)
20. Géneaux, R., et al.: Attosecond time-domain measurement of core-level-exciton decay in magnesium oxide. Phys. Rev. Lett. **124**, 207401 (2020)
21. Buades, B., et al.: Attosecond state-resolved carrier motion in quantum materials probed by soft x-ray XANES. Appl. Phys. Rev. **8**, 011408 (2021)
22. Gaynor, J.D., et al.: Solid state core-exciton dynamics in NaCl observed by tabletop attosecond four-wave mixing spectroscopy. Phys. Rev. B. **103**, 245140 (2021)
23. Sidiropoulos, T.P.H., et al.: Probing the energy conversion pathways between light, carriers, and lattice in real time with attosecond core-level spectroscopy. Phys. Rev. X. **11**, 041060 (2021)
24. Lucchini, M., et al.: Attosecond dynamical Franz-Keldysh effect in polycrystalline diamond. Science. **353**, 916–919 (2016)
25. Niedermayr, A., et al.: Few-femtosecond dynamics of free-free opacity in optically heated metals. Phys. Rev. X. **12**, 021045 (2022)
26. Schlaepfer, F., et al.: Attosecond optical-field-enhanced carrier injection into the GaAs conduction band. Nat. Phys. **14**, 560–564 (2018)
27. Volkov, M., et al.: Attosecond screening dynamics mediated by electron localization in transition metals. Nat. Phys. **15**, 1145–1149 (2019)
28. Hoffmann, L., et al.: Saturable absorption of free-electron laser radiation by graphite near the carbon K-edge. J. Phys. Chem. Lett. **13**(39), 8963–8970 (2021)

From Ultrafast Light-Induced Currents to Spatially-Resolved Field Sampling

Johannes Blöchl, Johannes Schötz, Boris Bergues, and Matthias F. Kling

Abstract The sampling of petahertz light fields opens up a new regime for field-resolved spectroscopy of ultrafast light-matter interactions. We derived a theoretical model tested against systematic experimental studies on the emergence of macroscopic currents in photoconductive field sampling. The model overcomes previous heuristic interpretations and can aid in the design of more sensitive and more efficient photoconductive devices. Furthermore, we implemented a near-field method for the spatio-temporal sampling of near-petahertz fields, enabling full vectorial field characterization of light beams with orbital angular momentum.

Keywords Ultrafast physics · Carrier-envelope-phase · Field-sampling · Petahertz electronics · Nanophotonics

1 Introduction

The possibility to generate and steer electric charges with the electric field of near-infrared to visible light with frequencies reaching the petahertz (PHz) range may boost the speed of modern electronics. Light-field driven currents do not only promise to revolutionize the field of attosecond physics, but are inherent to the development of petahertz electronics. Intense few-cycle laser pulses can

J. Blöchl · J. Schötz · B. Bergues
Physics Department, Ludwig-Maximilians-Universität Munich, Garching, Germany

Max Planck Institute of Quantum Optics, Garching, Germany

M. F. Kling (✉)
Physics Department, Ludwig-Maximilians-Universität Munich, Garching, Germany

Max Planck Institute of Quantum Optics, Garching, Germany

SLAC National Accelerator Laboratory, Menlo Park, CA, USA

Applied Physics Department, Stanford University, Stanford, CA, USA
e-mail: kling@stanford.edu

L. Argenti et al. (eds.), *Proceedings of the 8th International Conference on Attosecond Science and Technology*, Springer Proceedings in Physics 300,
https://doi.org/10.1007/978-3-031-47938-0_17

induce conductivity within a fraction of an optical cycle, enabling the ultrafast manipulation of electric currents. As an example, the related light-induced currents in a gas medium, in nanostructures or solids may be controlled by the carrier-envelope-phase (CEP) of a short laser pulse [1–7]. The phase dependence of the currents can be exploited for a new generation of more compact and easy-to-use devices, which enable the probing of the CEP [8], even in single-shot mode [6]. Moreover, when employing a sufficiently short laser pulse, the sub-cycle current burst can act as a temporal gate which can be utilized for sampling the electric field of light [9–19]. In contrast to the current gold standard for the measurement of petahertz electric fields, attosecond streaking [20, 21], employing light-induced current sampling avoids the use of complex ultrahigh-vacuum setups, making it much more widely accessible. Similar arguments can be made for a current sampling device of the CEP of a short laser pulse [6] that may replace the stereo-above-threshold-ionization phasemeter [22]. Despite the growing importance of ultrafast photoconductive measurements, a rigorous model for connecting the microscopic electron dynamics to the macroscopic external signal was lacking. We have developed a theoretical framework tested against systematic experimental studies on the signal formation in gas-phase photoconductive sampling [7]. The quantitative model overcomes previous heuristic interpretations and can aid in the design of more sensitive and more efficient photoconductive devices.

We furthermore implemented a new technique to probe petahertz light fields at arbitrary points in space [19]. It relies on the tunneling ionization with a perturbation for the time-domain observation of an electric field (TIPTOE) [9] locally sampled with a single metallic nanometric needle tip. Not only do we demonstrate that this approach, termed nanoTIPTOE [19], is equally reliable as TIPTOE, but we also show that it enables the measurement of the time-dependent field evolution in the entire focal plane. By directly recording electric currents from the needle tip, we avoid the use of complex high-vacuum equipment and time-of-flight spectroscopy.

2 Light-Induced Currents in the Gas Phase

Light-field induced currents generated in a gaseous medium between two electrodes have become increasingly important in the ultrafast scientific community. The CEP dependence of currents in ambient air were exploited in a novel single-shot phasemeter device [6]. Additionally, the sampling of the electric field of light has been demonstrated with simple air-gap devices [9, 13, 15].

The growing significance of these devices has been the main motivation for further investigations by Schötz et al. [7] on the relation between the microscopic charge dynamics resulting from the laser-matter interaction and the macroscopic currents that are detected. Those systematic studies have revealed that the process responsible for the formation of the current in related experiments is more complex than described in earlier purely heuristic models. These models usually separated the current into three contributions: (a) photoemission from direct electrode illumina-

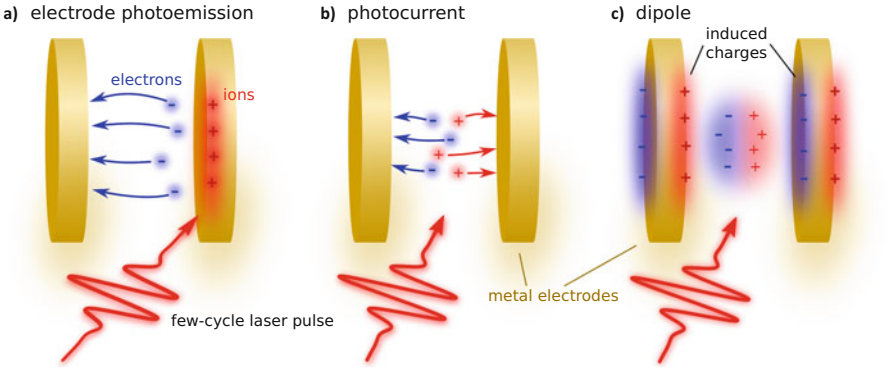

Fig. 1 Mechanisms for photocurrent generation—(**a**) Direct Photoemission from electrode illumination (**b**) Photocurrent by real charge propagation to the electrode(s) (**c**) Induced current from dipole formation. Figure adapted from Ref. [7], licensed under a Creative Commons Attribution 4.0 International License (CC BY 4.0), see https://creativecommons.org/licenses/by/4.0/

tion, (b) photocurrent by real charge propagation to the electrode(s), and (c) induced dipole contributions, see Fig. 1. While typically, the direct electrode illumination can be avoided experimentally and neglected, a rigorous treatment including the other two current generation mechanisms in one model was lacking. Furthermore, microscopic details were missing, including charge generation, scattering, and Coulomb interaction between the charged particles.

Schötz et al. [7] have addressed this longstanding issue for currents in gas phase media. The simulations combine microscopic modeling of the laser induced ionization, and charge propagation through extensive particle-in-cell (PIC) simulations. These simulations take both the Coulomb interaction and electron-atom scattering into account. The currents are obtained by employing the Shockley-Ramo theorem [23–26]. The simulations were compared to systematic experimental studies as a function of gas type, gas pressure, electrode distance, laser intensity, and carrier-envelope phase.

Experimentally, the manipulation of the microscopic electron dynamics is challenging due to the inherent inter dependencies: The electron mean-free path depends on quantities such as gas pressure, kinetic energy of the electrons, and the gas type. The incident intensity influences the number of generated charges (and therefore their interaction) and the electron energy spectra. All these quantities have an influence on the detected current signals. Consequently, the vetting of the developed rigorous model with experimental data required multi-dimensional experimental parameter scans.

One of the most insightful comparisons between theory and experiment is the pressure dependence, see Fig. 2. At very low pressures, the light-induced current signal is suppressed due to the low particle density, limiting the creation of charges, see Fig. 2a. This regime is followed by a linear increase in signal with pressure. For pressures approaching ambient conditions, which have been prevalent

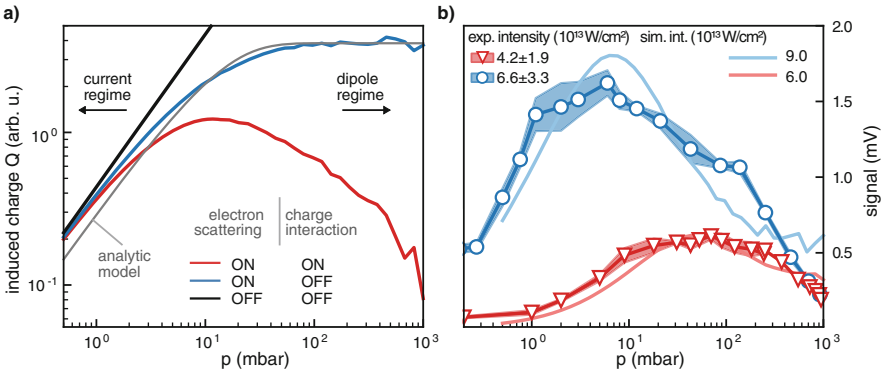

Fig. 2 Role of electron dynamics in light induced currents—(**a**) Signal scaling with pressure for different simulated microscopic processes in nitrogen at an intensity of 0.7×10^{14} W/cm^2. (**b**) Experimental and theoretical phase dependent signal for different intensities in argon. Figure adapted from Ref. [7], licensed under a Creative Commons Attribution 4.0 International License (CC BY 4.0), see https://creativecommons.org/licenses/by/4.0/

in previous experimental work [6, 9, 13, 15], the signal strength decreases again. The simulations show good agreement with this overall behavior. Moreover, the contributions of different mechanisms in the simulation, such as charge-interaction or scattering, can be switched on and off to identify their contribution to the pressure scaling. If there was no scattering or charge-interaction, the signal would be proportional to the pressure (black line in Fig. 2a). With scattering enabled but without charge interaction, we see better agreement for the low pressure regime. The signal would reach a plateau for higher pressures (blue line in Fig. 2a). This can be explained as follows: on the one hand, the electron mean free path scales as $1/p$ and on the other hand, the number of generated electrons scales linearly with pressure. Both effects combined result in the plateau at higher pressures. Neglecting charge interaction, the dependence of the induced charge Q on the electrode as a function of pressure can be described by an analytical expression given by eq. (1) in [7]:

$$Q \propto \frac{qpl_{\mathrm{mfp}}}{D}\left(1 - e^{-0.5D/l_{\mathrm{mfp}}}\right) \tag{1}$$

There, q is the electron charge, p is the pressure, D is the electrode distance and l_{mfp} is the mean-free path of the electron. This analytic expression (gray line in Fig. 2a) agrees well with the simulations and approximates the experimental results well for low pressures.

Now, experimentally, we observed a decrease of the signal after a certain threshold pressure. This decrease is—as the simulations confirm (red line in Fig. 2a)—a result of charge interactions, which limit the separation of positive and negative charges and thus the dipole that is formed. The full simulations may be compared to expectations from the former heuristic models. The heuristic interpretations are valid in the two extremes: the low pressure regime can be identified with the

photocurrent regime, see Fig. 1b, whereas the high pressure regime can be identified with the dipole regime, see Fig. 1c. We note that the Shockley-Ramo approach permits to describe the entire pressure range within one simulation model, and even allows to obtain relative contributions from photocurrents versus dipole currents in an intermediate regime.

The findings described in Ref. [7] suggest that the light-induced signal-strength maximizes, depending on the gas type and intensity, at a pressure of a few to a few tens of millibars, see Fig. 2b. The pressure where the maximum occurs does not only depend on the gas type but shifts with incident intensity [7], cf. Fig. 2b. The difference at this maximum to the signal at ambient pressure may exceed one order of magnitude. This signal increase can be taken advantage of in a future generation of more efficient gap devices for petahertz electronics applications.

3 Spatially-Resolved Field Measurements with Nanometric Needle Tips

Light-induced currents can be employed in the sampling of optical fields [9, 13–16, 18, 19], demonstrating advantages in speed, simplicity and reliability of these novel optoelectronic techniques. These methods rely on an ultrashort pump pulse that generates a current burst during its strongest optical half cycle by driving a nonlinear strong-field ionization process. Due to that nonlinearity, for a few-cycle pulse the process acts as a sub-cycle temporal gate.

In TIPTOE [9]-type techniques, this sub-cycle current is linearly perturbed by a second laser field interfering with the pump, which results in a modulation of the current proportional to the perturbing field during the gate. A time-delay scan between the two pulses then reveals the electric field of the perturbing pulse, which itself is too weak to ionize the sample on its own. These processes can be driven in the gas [9], on camera sensors [18], using on-chip nanostructure assemblies [16], or even in nanometric needle tips [19]. For the latter case, the working principle of the field sampling process is illustrated in Fig. 3. There, the current burst (red area) induced by the pump beam (solid blue) is perturbed by a probe beam (dashed), resulting in a modulation of the emitted charge, ΔQ, which follows the perturbing field during the gate. The change in emitted charge is being detected as a change of the ionization current. The requirement of having a single ionization burst translates to a broad spectral response in TIPTOE-type methods. For pump pulses much longer than the transform-limit or narrowband pulses, however, the method may become inaccurate [10] as the spectral response narrows with an increasing number of ionizing half-cycles [10, 16, 19]. Thus, very short pulses are a requirement for accurate TIPTOE measurements.

So far, a cos-shape pump pulse was implicitly assumed, meaning that the temporal gate is at time zero. It has been shown in the literature that the CEP of the pump pulse maps to the CEP of the detected waveform and that the CEP of the pump might also change the width of the spectral response, see Refs. [10, 16, 17, 19].

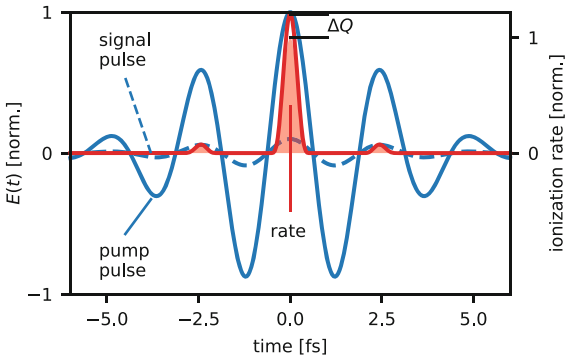

Fig. 3 The TIPTOE mechanism at metallic surfaces [16, 19]—A few-cycle pump beam (solid blue) ionizes the sample resulting in the ionization rate as shown as red area. Note that ionization in every second half-cycle is suppressed by the presence of the surface [27]. A second laser pulse (dashed) perturbs the ionization (red line) leading to a change in emitted charge ΔQ, which follows the perturbing field during the gate

In practical applications, as demonstrated in Ref. [19], this change of the width of the spectral response is often negligible, allowing to sample the electric field of the probe beam up to a constant phase offset, which is the pump beam CEP, without controlling the latter.

Although TIPTOE has become a well established time-domain field characterization methodology, its application to spatially resolved measurements were hitherto limited, either in frequency or in spatial resolution [11, 18]. Recently, the application of the TIPTOE-principle to nanometric needle tips overcame these limitations and enabled the probing of structured laser beams in space and time [19]. In the field sampling technique termed nanoTIPTOE, the spatial resolution stems from localization of the field enhancement at the tip apex, see inset in Fig. 4a. Within a small volume at the end of the tip, the field is enhanced compared to the incident field. When the incident intensity is tuned correctly, the ionization can be limited to the apex only, resulting in a confined probing volume. Consequently, the field sampling process occurs only near the apex of the nanometric needle tip, giving rise to the high spatial resolution which can be achieved with nanoTIPTOE.

Experimentally, the setup consists of a metallic tip which is electronically connected to a transimpedance amplifier for the detection of the currents induced by two laser pulses, see Fig. 4a. The validity of this approach is manifested in a reference measurement taken with TIPTOE in air, with which Blöchl et al. [19] demonstrated that the response of the nanometric needle tip is sufficiently flat such that the near-field practically follows the incident field up to a constant enhancement factor, see Fig. 4b. The depicted measurement scheme allowed measurements as fast as a few minutes even over several hundreds of femtoseconds delay.

Having demonstrated that the nanoTIPTOE signal indeed follows the electric field of the incident light, the nanometric needle tip could then be spatially scanned through the focal plane which yielded a spatiotemporal movie of the field amplitudes

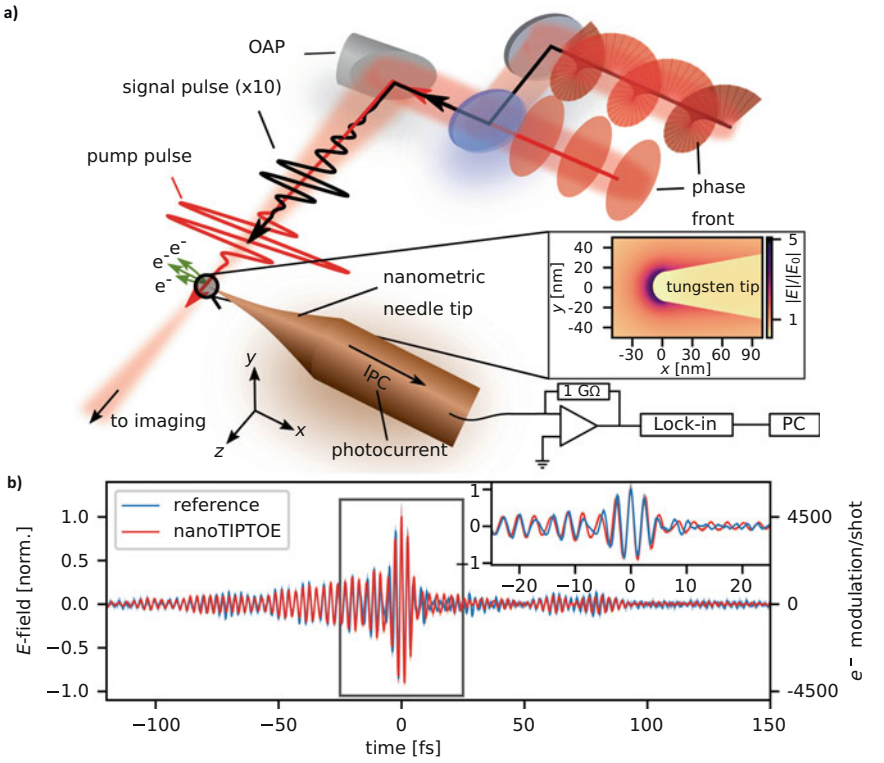

Fig. 4 Spatially-resolved field-sampling with a nanometric needle tip—(**a**) Two laser beams were focused onto a tungsten nanometric needle tip. The ionization current was transimpedance amplified and lock-in detected. The pump pulse was a few-cycle Gaussian pulse, whereas the signal pulse could be modified to carry orbital angular momentum, manifested in the helical phase shape. (**b**) The time-delay scan indicates the high precision that can be achieved with a nanometric tip compared to a reference taken with usual TIPTOE in the gas. Figure adapted from Ref. [19]

of the signal beam. If the latter is modified such that is possesses an internal structure, like a beam carrying orbital angular momentum (OAM), see Fig. 4a, the nanoTIPTOE approach can be employed for sampling the time resolved field evolution in the focal plane (see Fig. 5a). There, the optical vortex rotating around the propagation axis of light is shown. A comparison of the data to the theoretical expectations, Fig. 5b–e, identified the main features of the mode shape and phase front of the OAM beam measured in Ref. [19]. The ring-like mode exhibits a minimum in the center, whereas the phase shows the expected helical scaling as it increases by 2π for one revolution within the focal plane.

In summary, the nanoTIPTOE technique represents a precise method for field sampling which exploits the near-field localization for spatially resolved measurements while profiting from all advantages that come with a current detection scheme. It's first utilization for the probing of OAM beams provides field-resolved access to spatially structured light and opens the door to future applications.

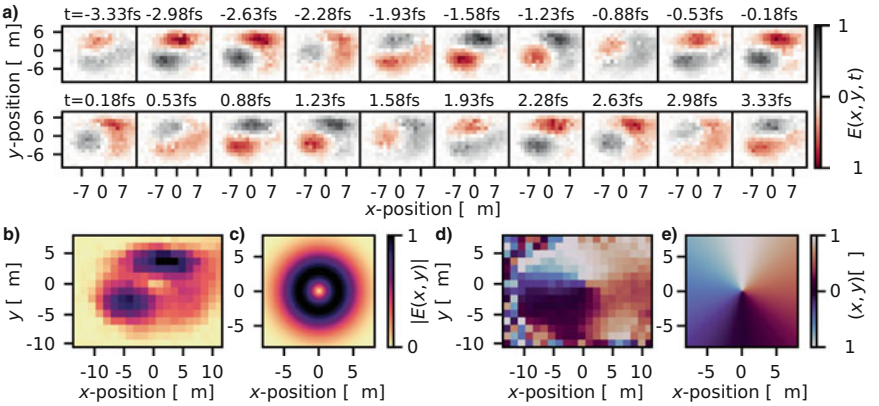

Fig. 5 Spatially resolved OAM beam measurements—(**a**) Focal amplitudes of the OAM beam for different points in time. (**b, c**) The extracted amplitudes (**b**) and the theoretical expectation for a Laguerre-Gaussian mode (**c**). (**d, e**) Spatial phase $\varphi(x, y)$ extracted from the data (**d**) and theory (**e**). Figure adapted from Ref. [19]

4 Conclusion

We have reported on recent work on light-induced currents and their applications. A quantitative modelling of the macroscopic current formation based on the Shockley-Ramo theorem was introduced, which included charge generation, particle scattering and charge interactions [7]. The model agrees quantitatively with experimental observations and permits predictive simulations for building more effective field sampling devices. Additionally, the spatially resolved field sampling method nanoTIPTOE [19] was described, which permits sampling electric fields in space and time. It constitutes a new optoelectronic tool for probing spatially structured near-petahertz light. Possible applications are reaching from ultrafast light-field detection to spatially resolved time-domain spectroscopy.

Acknowledgments J.B. and J.S. acknowledge support by the Max Planck Society via the Max Planck School of Photonics, and the IMPRS for Advanced Photon Science. M.F.K. acknowledges support by the Max Planck Society via the Max Planck Fellow program. M.F.K.'s work at SLAC is supported by the U.S. Department of Energy, Office of Science, Basic Energy Sciences, Scientific User Facilities Division.

References

1. Schiffrin, A., Paasch-Colberg, T., Karpowicz, N., Apalkov, V., Gerster, D., Mühlbrandt, S., Korbman, M., Reichert, J., Schultze, M., Holzner, S., Barth, J.V., Kienberger, R., Ernstorfer, R., Yakovlev, V.S., Stockman, M.I., Krausz, F.: Optical-field-induced current in dielectrics. Nature **493**(7430), 70–74 (2013). https://doi.org/10.1038/nature11567

2. Rybka, T., Ludwig, M., Schmalz, M.F., Knittel, V., Brida, D., Leitenstorfer, A.: Sub-cycle optical phase control of nanotunnelling in the single-electron regime. Nat. Photonics **10**(10), 667–670 (2016). https://doi.org/10.1038/nphoton.2016.174
3. Putnam, W.P., Hobbs, R.G., Keathley, P.D., Berggren, K.K., Kärtner, F.X.: Optical-field-controlled photoemission from plasmonic nanoparticles. Nat. Phys. **13**(4), 335–339 (2017). https://doi.org/10.1038/nphys3978
4. Ludwig, M., Kazansky, A.K., Aguirregabiria, G., Marinica, D.C., Falk, M., Leitenstorfer, A., Brida, D., Aizpurua, J., Borisov, A.G.: Active control of ultrafast electron dynamics in plasmonic gaps using an applied bias. Phys. Rev. B **101**(24), 241412 (2020). https://link.aps.org/doi/10.1103/PhysRevB.101.241412
5. Ludwig, M., Aguirregabiria, G., Ritzkowsky, F., Rybka, T., Marinica, D.C., Aizpurua, J., Borisov, A.G., Leitenstorfer, A., Brida, D.: Sub-femtosecond electron transport in a nanoscale gap. Nat. Phys. **16**(3), 341–345 (2020). https://doi.org/10.1038/s41567-019-0745-8
6. Kubullek, M., Wang, Z., von der Brelje, K., Zimin, D., Rosenberger, P., Schötz, J., Neuhaus, M., Sederberg, S., Staudte, A., Karpowicz, N., Kling, M.F., Bergues, B.: Single-shot carrier–envelope-phase measurement in ambient air. Optica **7**(1), 35–39 (2020). https://doi.org/10.1364/OPTICA.7.000035. http://www.osapublishing.org/optica/abstract.cfm?URI=optica-7-1-35
7. Schötz, J., Maliakkal, A., Blöchl, J., Zimin, D., Wang, Z., Rosenberger, P., Alharbi, M., Azzeer, A.M., Weidman, M., Yakovlev, V.S., Bergues, B., Kling, M.F.: The emergence of macroscopic currents in photoconductive sampling of optical fields. Nat. Commun. **13**(1), 962 (2022). https://doi.org/10.1038/s41467-022-28412-7
8. Yang, Y., Turchetti, M., Vasireddy, P., Putnam, W.P., Karnbach, O., Nardi, A., Kärtner, F.X., Berggren, K.K., Keathley, P.D.: Light phase detection with on-chip petahertz electronic networks. Nat. Commun. **11**(1), 3407 (2020). https://doi.org/10.1038/s41467-020-17250-0
9. Park, S.B., Kim, K., Cho, W., Hwang, S.I., Ivanov, I., Nam, C.H., Kim, K.T.: Direct sampling of a light wave in air. Optica **5**(4), 402–408 (2018). https://doi.org/10.1364/OPTICA.5.000402. http://www.osapublishing.org/optica/abstract.cfm?URI=optica-5-4-402
10. Cho, W., Hwang, S.I., Nam, C.H., Bionta, M.R., Lassonde, P., Schmidt, B.E., Ibrahim, H., Légaré, F., Kim, K.T.: Temporal characterization of femtosecond laser pulses using tunneling ionization in the UV, visible, and mid-IR ranges. Sci. Rep. **9**(1), 16067 (2019). https://doi.org/10.1038/s41598-019-52237-y
11. Saito, N., Ishii, N., Kanai, T., Itatani, J.: All-optical characterization of the two-dimensional waveform and the Gouy phase of an infrared pulse based on plasma fluorescence of gas. Opt. Express **26**(19), 24591–24601 (2018). https://doi.org/10.1364/OE.26.024591. http://www.opticsexpress.org/abstract.cfm?URI=oe-26-19-24591
12. Hwang, S.I., Park, S.B., Mun, J., Cho, W., Nam, C.H., Kim, K.T.: Generation of a single-cycle pulse using a two-stage compressor and its temporal characterization using a tunnelling ionization method. Sci. Rep. **9**(1), 1613 (2019). https://doi.org/10.1038/s41598-018-38220-z
13. Korobenko, A., Johnston, K., Kubullek, M., Arissian, L., Dube, Z., Wang, T., Kübel, M., Naumov, A.Y., Villeneuve, D.M., Kling, M.F., Corkum, P.B., Staudte, A., Bergues, B.: Femtosecond streaking in ambient air. Optica **7**(10), 1372–1376 (2020). https://doi.org/10.1364/OPTICA.398846. http://www.osapublishing.org/optica/abstract.cfm?URI=optica-7-10-1372
14. Sederberg, S., Zimin, D., Keiber, S., Siegrist, F., Wismer, M.S., Yakovlev, V.S., Floss, I., Lemell, C., Burgdörfer, J., Schultze, M., Krausz, F., Karpowicz, N.: Attosecond optoelectronic field measurement in solids. Nat. Commun. **11**(1), 430 (2020). https://doi.org/10.1038/s41467-019-14268-x
15. Zimin, D., Weidman, M., Schötz, J., Kling, M.F., Yakovlev, V.S., Krausz, F., Karpowicz, N.: Petahertz-scale nonlinear photoconductive sampling in air. Optica **8**(5), 586–590 (2021). https://doi.org/10.1364/OPTICA.411434. http://www.osapublishing.org/optica/abstract.cfm?URI=optica-8-5-586
16. Bionta, M.R., Ritzkowsky, F., Turchetti, M., Yang, Y., Cattozzo Mor, D., Putnam, W.P., Kärtner, F.X., Berggren, K.K., Keathley, P.D.: On-chip sampling of optical fields with attosecond resolution. Nat. Photonics **15**(6), 456–460 (2021). https://doi.org/10.1038/s41566-021-00792-0

17. Liu, Y., Gholam-Mirzaei, S., Beetar, J.E., Nesper, J., Yousif, A., Nrisimhamurty, M., Chini, M.: All-optical sampling of few-cycle infrared pulses using tunneling in a solid. Photon. Res. **9**(6), 929–936 (2021). https://doi.org/10.1364/PRJ.420916. http://www.osapublishing.org/prj/abstract.cfm?URI=prj-9-6-929
18. Liu, Y., Beetar, J.E., Nesper, J., Gholam-Mirzaei, S., Chini, M.: Single-shot measurement of few-cycle optical waveforms on a chip. Nat. Photonics **16**(2), 109–112 (2022). https://doi.org/10.1038/s41566-021-00924-6
19. Blöchl, J., Schötz, J., Maliakkal, A., Šreibere, N., Wang, Z., Rosenberger, P., Hommelhoff, P., Staudte, A., Corkum, P.B., Bergues, B., Kling, M.F.: Spatiotemporal sampling of near-petahertz vortex fields. Optica **9**(7), 755–761 (2022). https://doi.org/10.1364/OPTICA.459612. http://opg.optica.org/optica/abstract.cfm?URI=optica-9-7-755
20. Itatani, J., Quéré, F., Yudin, G.L., Ivanov, M.Y., Krausz, F., Corkum, P.B.: Attosecond streak camera. Phys. Rev. Lett. **88**(17), 173903 (2002). https://link.aps.org/doi/10.1103/PhysRevLett.88.173903
21. Kienberger, R., Goulielmakis, E., Uiberacker, M., Baltuska, A., Yakovlev, V., Bammer, F., Scrinzi, A., Westerwalbesloh, T., Kleineberg, U., Heinzmann, U., Drescher, M., Krausz, F.: Atomic transient recorder. Nature **427**(6977), 817–821 (2004). https://doi.org/10.1038/nature02277
22. Wittmann, T., Horvath, B., Helml, W., Schätzel, M.G., Gu, X., Cavalieri, A.L., Paulus, G.G., Kienberger, R.: Single-shot carrier–envelope phase measurement of few-cycle laser pulses. Nat. Phys. **5**(5), 357–362 (2009). https://doi.org/10.1038/nphys1250
23. Shockley, W.: Currents to conductors induced by a moving point charge. J. Appl. Phys. **9**(10), 635–636 (1938). https://doi.org/10.1063/1.1710367
24. Ramo, S.: Currents induced by electron motion. Proc. IRE **27**(9), 584–585 (1939). https://doi.org/10.1109/JRPROC.1939.228757
25. He, Z.: Review of the Shockley–Ramo theorem and its application in semiconductor gamma-ray detectors. Nucl. Instrum. Methods Phys. Res. Sect. A: Accel. Spectrom. Detect. Assoc. Equip. **463**(1), 250–267 (2001). https://doi.org/10.1016/S0168-9002(01)00223-6. https://www.sciencedirect.com/science/article/pii/S0168900201002236
26. Riegler, W.: An application of extensions of the Ramo–Shockley theorem to signals in silicon sensors. Nucl. Instrum. Methods Phys. Res. Sect. A: Accel. Spectrom. Detect. Assoc. Equip. **940**, 453–461 (2019). https://doi.org/10.1016/j.nima.2019.06.056. https://www.sciencedirect.com/science/article/pii/S0168900219309015
27. Yalunin, S.V., Gulde, M., Ropers, C.: Strong-field photoemission from surfaces: theoretical approaches. Phys. Rev. B **84**(19), 195426 (2011). https://link.aps.org/doi/10.1103/PhysRevB.84.195426

Attosecond Core-Exciton Dynamics in Wide-Gap Insulators

Giacomo Inzani, Shunsuke A. Sato, Giacinto D. Lucarelli, Bruno Moio, Rocío Borrego-Varillas, Fabio Frassetto, Luca Poletto, Hannes Hübener, Umberto De Giovannini, Angel Rubio, Mauro Nisoli, and Matteo Lucchini

Abstract An option to overcome the limits of electronics are excitons, quasi-particles generated by the electron-hole Coulomb interaction. A fundamental prerequisite is the possibility to control their properties with optical fields. We adopted attosecond reflection spectroscopy to investigate the interplay between core excitons and ultrashort infrared pulses in MgF_2. Their ultrafast response is divided into two contributions, unfolding on different time scales, related to the exciton dual nature. Namely, we discern the atomic-like behaviour, dominating the few-femtosecond response, from the excitonic solid-like characteristics, with sub-femtosecond timing. Theoretical models highlight the role of the exciton binding energy in dictating their optical response.

G. Inzani · B. Moio
Department of Physics, Politecnico di Milano, Milano, Italy

S. A. Sato
Center for Computational Science, University of Tsukuba, Tsukuba, Japan

Max Planck Institute for the Structure and Dynamics of Matter, Hamburg, Germany

G. D. Lucarelli · M. Nisoli · M. Lucchini (✉)
Department of Physics, Politecnico di Milano, Milano, Italy

Institute for Photonics and Nanotechnologies, IFN-CNR, Milano, Italy
e-mail: matteo.lucchini@polimi.it

R. Borrego-Varillas
Institute for Photonics and Nanotechnologies, IFN-CNR, Milano, Italy

F. Frassetto · L. Poletto
Institute for Photonics and Nanotechnologies, IFN-CNR, Padova, Italy

H. Hübener
Max Planck Institute for the Structure and Dynamics of Matter, Hamburg, Germany

U. De Giovannini · A. Rubio
Max Planck Institute for the Structure and Dynamics of Matter, Hamburg, Germany

Nano-Bio Spectroscopy Group, Universidad del País Vasco, San Sebastian, Spain

L. Argenti et al. (eds.), *Proceedings of the 8th International Conference on Attosecond Science and Technology*, Springer Proceedings in Physics 300,
https://doi.org/10.1007/978-3-031-47938-0_18

Keywords Attosecond · Excitons · Attosecond reflection spectroscopy

1 Introduction

Limitations of current electronic devices have become evident during the last decade [1]. Several options, like valleytronics [2], spintronics [3], and excitonics [4] were explored to overcome them. In all these cases, it is essential to control the optical properties of a material. Understanding the related light-induced physical phenomena is, therefore, fundamental. At the same time, attosecond spectroscopy unveiled novel phenomena in condensed matter physics on the few- and sub-femtosecond (fs) time scales [5]. Moreover, the importance of virtual carriers [6] and intra-band motion [7] in determining the electron dynamics in solids has been demonstrated. In previous studies, however, light-induced sub-cycle features related to core excitons in dielectrics were never observed [8, 9].

In this work, core-exciton dynamics at the Mg $L_{2,3}$ edge (∼56 eV) of monocrystalline MgF_2 are investigated by attosecond reflection spectroscopy (ARS). The exciton formation, induced by the absorption of extreme ultraviolet (XUV) photons, and the subsequent decay are dressed by delayed few-fs infrared (IR) pulses. A direct comparison between the experimental and theoretical results attributes the observed dynamics to two distinct physical mechanisms, revealing the dual atomic-solid nature of core excitons. In particular, the excitonic atomic response unfolds over few femtoseconds, while the solid-like behaviour appears as sub-femtosecond oscillations. Basing on a Wannier-Mott model, our interpretation of the ultrafast exciton-crystal interaction extends also to valence excitons, which are more promising from a technological perspective. Thus, it allows us to propose the exciton binding energy as a knob to control these quasi-particles in future applications.

2 Experimental Setup

A commercial Ti:Al_2O_3 laser system cascaded with an hollow-core fiber compressor [10] delivers CEP-stabilized 1-mJ, 5-fs pulses at the entrance of the attosecond transient reflectivity beamline [11]. The pulses are centered around 800 nm and have a repetition rate of 10 kHz. 70% of the pulse energy is focused onto an Ar gas target to drive the high-order harmonic generation (HHG) process. Isolated attosecond pulses are generated by using the ionization gating technique [12]. The cutoff energy of the XUV spectrum extends above 56 eV, covering the $L_{2,3}$ absorption edge of Mg. The remaining fraction of the IR radiation is delayed and collinearly recombined to the XUV radiation, forming the pump beam. The XUV and IR radiation is focused by a gold-plated toroidal mirror in the first target of the beamline, where a neon gas jet is placed. Here, a two-color photoemission experiment is performed, collecting photoelectron spectra with a time-of-flight spectrometer. This experiment,

performed simultaneously to the actual measurement on the solid-state sample, is used to characterize the IR and XUV radiation and to calibrate the absolute XUV-IR delay. After the TOF chamber, the diverging radiation is refocused, by a second toroidal mirror, into the endstation for attosecond reflectivity experiments. Both XUV and IR impinge on an MgF_2 (001) single-crystal sample at an angle of 73.5°. The XUV radiation reflected by the sample is steered into an XUV spectrometer by a gold mirror. The relative XUV-IR time delay is actively stabilized with a residual standard deviation of 24 as, ensuring the required attosecond temporal resolution [13]. The propagation between the first and the second focus induces an additional (propagation) delay between XUV and IR pulses [14]. Its value, fundamental for an absolute calibration of the experimental delay axis, has been characterized by independent measurements and amounts to 240 ± 13 as [11].

3 Results

The static (unpumped) experimental reflectivity $R_0(E)$ of MgF_2, the theoretical calculation and the reflectivity computed from data reported in literature [15] are presented in Fig. 1a. XUV-induced transitions probe the Mg $L_{2,3}$ absorption edge (∼56 eV), involving the Mg^{2+} 2p states and the conduction band. A bright excitonic feature (A), replicated by spin-orbit splitting (∼0.44 eV, feature A'), is observed. The IR dressing of these excitons is studied by attosecond reflection spectroscopy. The measured quantity, reported in Fig. 1b, is the transient differential reflectivity, $\Delta R/R(E,\tau) = [R(E,\tau) - R_0(E)]/R_0(E)$, where R and R_0 are the reflectivity

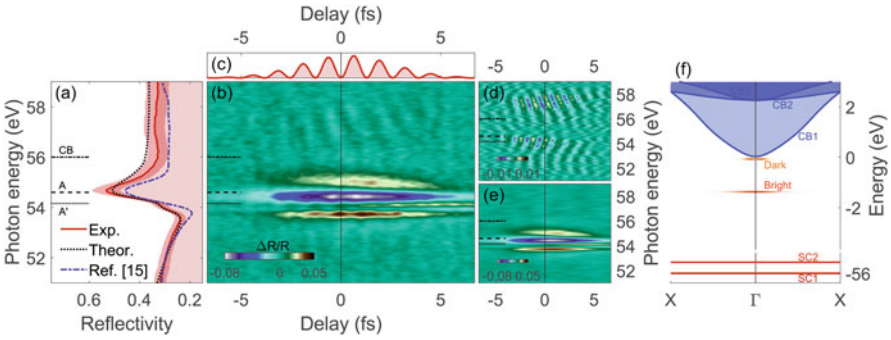

Fig. 1 (**a**) Unpumped experimental (red) and calculated (black) reflectivity of MgF_2 at 73.5°, compared to data reported in literature (blue dashed) [15]. The onset of the conduction band (dash-dotted) and the Mg^{2+} semi-core states (A dashed, A' dotted) are marked by the black horizontal lines. The dark shaded region extends over twice the standard deviation of the measurement. (**b**) Differential transient reflectivity of MgF_2. (**c**) Squared modulus of the simultaneously measured IR vector potential. (**d**) Sub-fs and (**e**) few-fs components of the differential transient reflectivity trace. (**f**) Conduction band structure (CB1, CB2, CB3), dark and bright excitonic states, semi-core (SC1, SC2) Mg^{2+} states

of the sample with and without the IR field, τ is the XUV-IR delay and E the XUV photon energy (for positive delays, the XUV pulse comes first). The squared modulus of the experimentally measured IR vector potential, $|A_{IR}(t)|^2$, is reported in Fig. 1c.

The transient differential reflectivity trace can be decomposed in two main contributions: sub-fs oscillations in the reflectivity (Fig. 1d) at twice the frequency of the IR radiation, and a few-fs signal (Fig. 1e). Analyzing the band structure [16] (Fig. 1f), we can consider that an XUV pulse is inducing transitions involving the Mg $2p$ semi-core states (SC1 and SC2) and states above the Fermi level. The Coulomb electron-hole interaction forms a core-exciton (A and A'), but only s-symmetric states (bright) will be populated by dipole-allowed transitions, while the ones with p character are optically dark. For positive delays, the bright and dark states and the conduction band are coupled by the IR pulse, giving IR-induced variations of the reflectivity. For large negative delays, instead, the IR pulse precedes the XUV one, and the exciton is not formed yet. A nonlinear fit of the experimental trace gives a core exciton decay time constant of 2.35 ± 0.3 fs, similar to those already reported in literature for other dielectrics [8, 9]. However, to obtain an accurate estimate of the parameters of the excitonic dipole, more refined ptychographic techniques should be adopted [17].

The experimental results (also reported in Fig. 2a) are compared with three different theoretical approaches: a single-particle single-hole Wannier-Mott model (Fig. 2b) describing both the exciton and crystal properties; a pure-exciton model (Fig. 2c), describing the exciton as a three-level atom; and a pure-crystal model (Fig. 2d) [18]. In the full and exciton-only calculations, we used an exciton binding energy of 1.4 eV, matching the experimental value. Only the full and exciton-only calculations reproduce the few-fs dynamics, thus proving that they have an atomic-

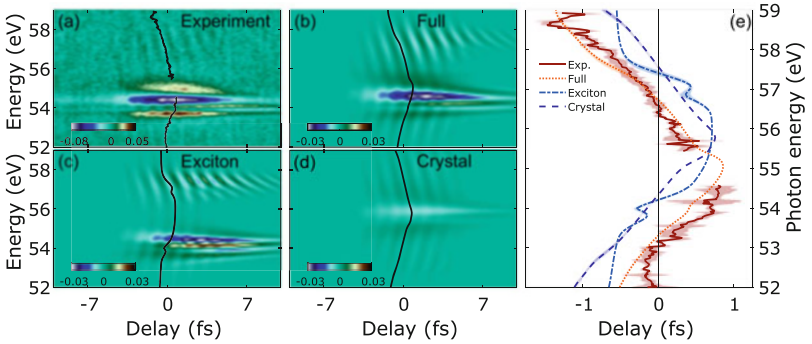

Fig. 2 (**a**) Experimental transient reflectivity trace compared to the simulated ones with (**b**) the full model, (**c**) the exciton-only model, and (**d**) the crystal-only model. The black lines mark the phase delay of the $2\omega_{IR}$ oscillations. We used the same color scale to represent the full, exciton-only and crystal-only calculations. (**e**) Phase delay of the oscillations for the experimental (brown), full model (orange), exciton only (light-blue) and crystal only (blue) traces. A $\pm\sigma$ interval is represented by shaded regions

like origin, i.e. the IR-induced Stark-shift between the dark and bright exciton states. Considering instead the sub-fs dynamics, a precise characterization the phase delay between the oscillations and $|A_{IR}(t)|^2$ (Fig. 2e) is possible. The exciton-only model fails in reproducing the data even qualitatively, although fast oscillations are still present due to the optical Stark effect [19]. In this picture, the Stark effect changes the exciton binding energy $E_b = -\hbar^2/(2\mu a_0^2)$, where $\mu = 0.24 m_e$ is the reduced mass of the electron-hole system. This modulation of the binding energy affects the excitonic Bohr radius (1.65 Å at equilibrium), as expected from the IR-induced acceleration of the electron and hole in opposite directions. However, the timing of these oscillations is inconsistent with the experimental one. Instead, a quantitative agreement is present only with the full model, while the crystal-only model reproduces a similar feature shifted to larger photon energies. This allows us to attribute those fast features to a pure bulk phenomena, namely intra-band motion [7]. Eventually, the full model shows both few-fs and sub-fs features within the same order of magnitude of the experimental measurement. Deviations from the experimental values might originate from underestimating the pump intensity, unavoidable experimental imperfections, and approximations in theoretical models. Nevertheless, these discrepancies should not affect the results we will discuss. Therefore, only the full Wannier-Mott model is thus able to show both the atomic- and solid-like nature of core excitons. Therefore, the effect of the IR dressing is to induce a motion of virtual charges (dynamical Franz-Keldysh effect) [6] in the conduction band, altering the exciton properties. This gives IR-induced oscillations in the reflectivity whose phase relation is close to the one of the crystal. In this picture the exciton motion in real space can be related to the experimental sub-fs features.

To gain further insight on the exciton dynamics, we used the full Wannier-Mott model to study the dependence on the exciton binding energy. Increasing the binding energy, the radius of the exciton decreases and its properties are less influenced by those of the crystal, significantly changing the few-fs features (Fig. 3a–f). The energy-dependent shape of the timing of the oscillations, instead, is almost preserved, but shifted to lower energies, and the phase delay increases. Smaller binding energies, in turn, decrease the exciton localization: the exciton will thus react almost in phase with the external field, decreasing the phase delay (Fig. 3g). The exciton binding energy, that can be changed by dielectric screening or inducing a strain in the crystal, can thus be used as a tuning knob to control the interaction with the surrounding crystal [20–22] for Wannier-Mott excitons in general, including valence excitons.

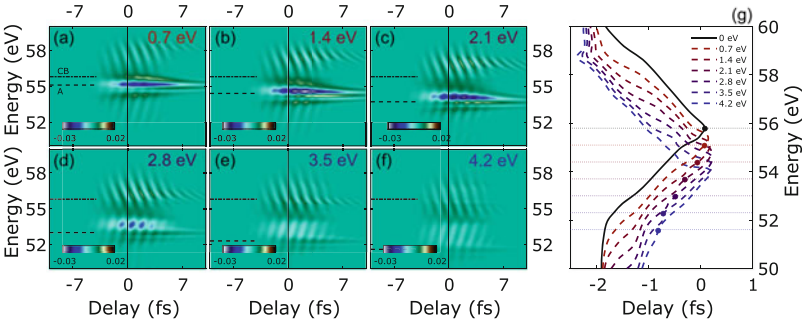

Fig. 3 (**a**–**f**) Simulated transient reflectivity traces for different exciton binding energies (0.7, 1.4, 2.1, 2.8, 3.5 and 4.2 eV). Horizontal lines mark the onset of the conduction band (dash-dotted) and of the A exciton transition (dashed). (**g**) Phase delay of the oscillations in simulations for different exciton binding energies, compared to the crystal-only case (black). The onset of the A exciton transition (in colors) and the onset of the conduction band (black) are marked. Circles show the phase delay corresponding to the A exciton transition

4 Conclusions

We studied the interaction between conduction states and core excitons in MgF_2 on the attosecond time scale. The uniqueness of our experimental setup allowed for a precise comparison with three different theoretical models. The optical Stark effect is found to be mainly dictating the atomic-like few-fs optical response, while sub-fs dynamics are interpreted in terms of interaction of the IR-dressed conduction band with the exciton state. The dependence of the sub-fs optical response on the exciton binding energy is proposed to be exploited to control excitonic properties on ultrafast time scales.

Acknowledgments This project received funding from the European Research Council (ERC) under the European Union's Horizon 2020 research and innovation programme (Grant Agreement No. 848411 title AuDACE). M.L., G.I. and L.P. further acknowledge funding from MIUR PRIN aSTAR, Grant No. 2017RKWTMY. S.S., H.H., U.D.G. and A.R. were supported by the European Research Council (ERC-2015-AdG-694097) and Grupos Consolidados UPV/EHU (IT1249-19).

References

1. Markov, I.L.: Limits on fundamental limits to computation. Nature **512**, 147–154 (2014)
2. Vitale, S.A., Nezich, D., Varghese, J.O., Kim, P., Gedik, N., Jarillo-Herrero, P., Xiao, D., Rothschild, M.: Valleytronic: opportunities, challenges, and paths forward. Small **14**, 1801483 (2018)
3. Žutić, I., Fabian, J., Das Sarma, S.: Spintronics: fundamentals and applications. Rev. Mod. Phys. **76**, 323 (2004)

4. Koch, S.W., Kira, M., Khitrova, G., Gibbs, H.M.: Semiconductor excitons in new light. Nat. Mater. **5**, 523–531 (2006)
5. Borrego-Varillas, R., Lucchini, M., Nisoli, M.: Attosecond spectroscopy for the investigation of ultrafast dynamics in atomic, molecular and solid-state physics. Rep. Prog. Phys. **85**, 066401 (2022)
6. Lucchini, M., Sato, S.A., Ludwig, A., Herrmann, J., Volkov, M., Kasmi, L., Shinohara, Y., Yabana, K., Gallmann, L., Keller, U.: Attosecond dynamical Franz-Keldysh effect in polycrystalline diamond. Science **353**, 916–919 (2016)
7. Schlaepfer, F., Lucchini, M., Sato, S.A., Volkov, M., Kasmi, L., Hartmann, N., Rubio, A., Gallmann, L., Keller, U.: Attosecond optical-field-enhanced carrier injection into the GaAs conduction band. Nat. Phys. **14**, 560–564 (2018)
8. Moulet, A., Bertrand, J.B., Klostermann, T., Guggenmos, A., Karpowicz, N., Goulielmakis, E.: Soft X-ray excitonics. Science **357**, 1134–1138 (2017)
9. Géneaux, R., Kaplan, C.J., Yue, L., Ross, A.D., Bækhøj, J.E., Kraus, P.M., Chang, H.-T., Guggenmos, A., Huang, M.-Y., Zürch, M., Schafer, K.J., Neumark, D.M., Gaarde, M.B., Leone, S.R.: Attosecond time-domain measurement of core-level-exciton decay in magnesium oxide. Phys. Rev. Lett. **124**, 207401 (2020)
10. Nisoli, M., De Silvestri, S., Svelto, O.: Generation of high energy 10 fs pulses by a new pulse compression technique. Appl. Phys. Lett. **68**, 2793 (1996)
11. Lucarelli, G.D., Moio, B., Inzani, G., Fabris, N., Moscardi, L., Frassetto, F., Poletto, L., Nisoli, M., Lucchini, M.: Novel beamline for attosecond transient reflection spectroscopy in a sequential two-foci geometry. Rev. Sci. Instrum. **91**, 053002 (2020)
12. Ferrari, F., Calegari, F., Lucchini, M., Vozzi, C., Stagira, S., Sansone, G., Nisoli, M.: High-energy isolated attosecond pulses generated by above-saturation few-cycle fields. Nat. Photon. **4**, 875–879 (2010)
13. Huppert, M., Jordan, I., Wörner, H.J.: Attosecond beamline with actively stabilized and spatially separated beam paths. Rev. Sci. Instrum. **86**, 123106 (2015)
14. Schlaepfer, F., Ludwig, A., Lucchini, M., Kasmi, L., Volkov, M., Gallmann, L., Keller, U.: Gouy phase shift for annular beam profiles in attosecond experiments. Opt. Express **25**, 3646–3655 (2017)
15. Hanson, W.F., Arakawa, E.T., Williams, M.W.: Optical properties of MgO and MgF2 in the extreme ultraviolet region. J. Appl. Phys. **43**, 1661–1665 (1972)
16. Jouanin, C., Albert, J.P., Gout, C.: Band structure and optical properties of magnesium fluoride. J. Phys. - Paris **37**, 595–602 (1976)
17. Dolso, G.L., Moio, B., Inzani, G., Di Palo, N., Sato, S.A., Borrego-Varillas, R., Nisoli, M., Lucchini, M.: Reconstruction of ultrafast exciton dynamics with a phase-retrieval algorithm. Opt. Express **30**, 12248–12267 (2022)
18. Lucchini, M., Sato, S.A., Lucarelli, G.D., Moio, B., Inzani, G., Borrego-Varillas, R., Frassetto, F., Poletto, L., Hübener, H., De Giovannini, U., Rubio, A., Nisoli, M.: Unravelling the intertwined atomic and bulk nature of localised excitons by attosecond spectroscopy. Nat. Commun. **12**, 1021 (2021)
19. Bakos, J.S.: AC stark effect and multiphoton processes in atoms. Phys. Rep. **31**, 209–235 (1977)
20. Chernikov, A., van der Zande, A.M., Hill, H.M., Rigosi, A.F., Velauthapillai, A., Hone, J., Heinz, T.: Electrical tuning of exciton binding energies in monolayer WS2. Phys. Rev. Lett. **115**, 126802 (2015)
21. Ju, L., Wang, L., Cao, T., Taniguchi, T., Watanabe, K., Louie, S., Rana, F., Park, J., Hone, J., Wang, F., McEuen, P.: Tunable excitons in bilayer graphene. Science **358**, 907–910 (2017)
22. Aslan, O.B., Deng, M., Heinz, T.F.: Strain tuning of excitons in monolayer WSe2. Phys. Rev. B **98**, 115308 (2018)

Polarization-Shaped Strong Field Control Over Valley Polarization with Mid-IR Light

Igor Tyulnev, Julita Poborska, Álvaro Jiménez-Galán, Lenard Vamos, Olga Smirnova, Mikhail Ivanov, and Jens Biegert

Abstract We induce valley-control in MoS_2 with a polarization-shaped mid-infrared light field. The trefoil-shaped pump field is characterized by high harmonic spectroscopy and valley polarization is read our by a probe field via second harmonic generation.

Keywords Valleytronics · TMDC · Two-dimensional · High-harmonic generation · High-harmonic spectroscopy · Strong-field · Sub-cycle · Lightwave electronics · Optical control

I. Tyulnev · J. Poborska · L. Vamos
ICFO – Institut de Ciencies Fotoniques, The Barcelona Institute of Science and Technology, Barcelona, Spain

Á. Jiménez-Galán
Max-Born-Institut, Berlin, Germany

O. Smirnova
Max-Born-Institut, Berlin, Germany

Technische Universität Berlin, Berlin, Germany

M. Ivanov
Max-Born-Institut, Berlin, Germany

Institute für Physik, Humboldt-Universität zu Berlin, Berlin, Germany

Department of Physics, Imperial College London, London, UK

J. Biegert (✉)
ICFO – Institut de Ciencies Fotoniques, The Barcelona Institute of Science and Technology, Barcelona, Spain

ICREA, Barcelona, Spain
e-mail: jens.biegert@icfo.eu

L. Argenti et al. (eds.), *Proceedings of the 8th International Conference on Attosecond Science and Technology*, Springer Proceedings in Physics 300,
https://doi.org/10.1007/978-3-031-47938-0_19

1 Introduction

Polarization shaping of the temporal evolution of an optical light field provides additional degrees of freedom to interrogate matter and control its properties. The emergent complex electrical currents are controlled on the sub-cycle scale of the optical field and provide enticing new ways to process information or to switch the properties of a material on ultrafast timescales. The non-linear motion of field-driven electrons in a material radiate at optical frequencies; thus, detecting high-order harmonic radiation provides insight into the dynamic evolution of carriers. This potential was first recognized in Ref. [1] with the detection of high harmonics (HH) of the mid-IR driver in bulk ZnO and led to numerous investigations of the electron-hole dynamics [2, 3], of many-body effects in correlated systems [4], the interplay of different bands [5], and recently the detection of quantum phases in superconductors [6]. Confining the dynamics to two-dimensional layers, e.g., in graphene-like materials or transition-metal-dichalcogenides (TMDCs), allows for the study of HH dynamics below and above the bandgap without complicating the interpretation due to propagation effects [7]. The broken inversion symmetry of a monolayer led to observation of Berry curvature dependent effects [8]. Rotation of the light's polarization vector determines the recombination times of electron-hole trajectories from K and K′ symmetry points [7]. In contrast, circular polarization carries spin angular momentum that lifts the valley degeneracy through optical selection rules [9, 10].

Here, we extend the control over the valley degree of freedom into the strong-field regime by matching the driving field polarization to the crystal symmetry of 2H-MoS2. To this end, we shape the polarization of the optical electric field into a three-fold symmetric "trefoil" shape. To achieve such three-fold symmetry, we combine pulses of two colors while manipulating the handedness of their circular polarization. The so-tailored field is characterized by symmetry-resolved chiral spectroscopy, where selection rules result in circularly polarized harmonics of odd and even orders from the inversion symmetric material. With the off-resonant strong-field trefoil acting as a pump, a modulation in the bandgap at high symmetry points K and K′ is observed in a non-collinear geometry pump-probe experiment.

The measurement of the second harmonic of the probe field is a clear sign of the valley polarization induced by the trefoil pump field.

2 Valley Polarization in MoS_2

The light carries spin angular momentum and can, thus, induce asymmetry of carriers between valleys in reciprocal space during resonant excitation of the bandgap in the K/K′ points. The degree of circular polarization is linked to the valley contrasting magnetic moment "m," which defines the coupling strength $|P|^2$. For the quantum number "m" to be non-zero, the spatial inversion symmetry of

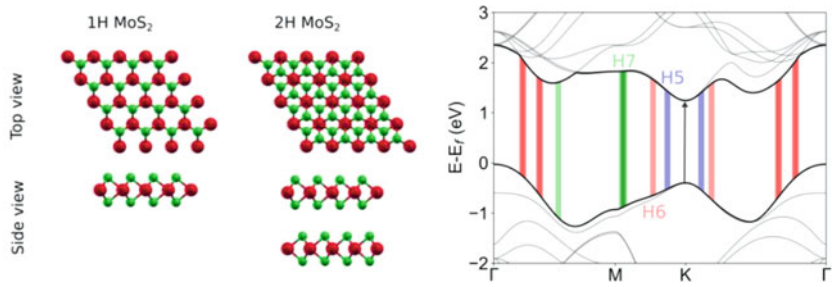

Fig. 1 Left: Top and side view of the trigonal prismatic crystal structure of 1H- and 2H-MoS_2. Right: 2H-MoS_2 band structure; Blue, red, and green represent gaps that fit H5, H6, and H7 emission energies and the bandwidth of the 3.2 μm driving field

the crystal must be broken. Such inversion symmetry breaking occurs naturally for monolayer TMDCs. The material becomes valley polarized, and the electron motion depends on the sign of the valley index and the Berry curvature at the respective high symmetry point [11].

In contrast, a bi-layer system in the 2H phase is symmetric under spatial inversion due to the rotated second layer (Fig. 1), and valley asymmetry cannot be induced with circularly polarized light. However, symmetry breaking can be re-introduced through the structuring of light when the system is excited off-resonantly by a trefoil-shaped strong field. In the following, we leverage this prospect for inducing valley polarization.

3 Polarization Shaping and Trefoil Generation

We use our home-built mid-infrared OPCPA system [12] at 3.2 μm for the experiment. For the polarization shaping, a 97 fs pulse is split within a Mach-Zehnder interferometer into two components in which one is frequency doubled. The polarization states and intensity ratio between fundamental and second harmonic are carefully controlled by waveplates. Both beams are recombined and then focused onto the sample. We use a vacuum electric field amplitude of 0.05 V/Å in the mid-IR and derive the probe beam at 800 nm from the same OPCPA with full optical synchronization. The pump-probe experiment is performed in non-collinear geometry to ensure the distinguishability of components from the trefoil pump and 800-nm probe.

4 Polarization Resolved Chiral Spectroscopy

First, we perform chiral spectroscopy to confirm the trefoil shape of the pump beam. Analog to Ref [13], we generate HHs in GaSe with varying polarization shapes of the driving field.

Figure 2 shows the results for the measurement of harmonic orders 5–7 (H5-H7). The figure shows how the harmonic signals vary with crystal rotation. Lineouts of H5 are also shown on a polar plot with the polarization type illustrated. The left column is the HH spectrum for a linearly polarized 3.2 μm driving field. The harmonic response from the hexagonal crystal yields six peaks during a full rotation scan. The harmonic intensity is maximized when the laser polarization aligns with the crystal axis which occurs every 60° and completely disappears with the polarization rotated 30° further. Changing the driving field to circular polarization minimizes the H6 signal due to optical selection rules [14], while the other harmonics do not show any clear angle dependence due to the isotropic polarization. Finally, the two-color trefoil field shows three-fold symmetry in the H5 and H7 responses, which show maxima 120° apart. This behavior is understood when considering the crystal as a combination of Ga and Se sublattices, which are addressed by the trefoil three times each in a full rotation. Having confirmed the generation of a trefoil field, we now turn to the TMDC.

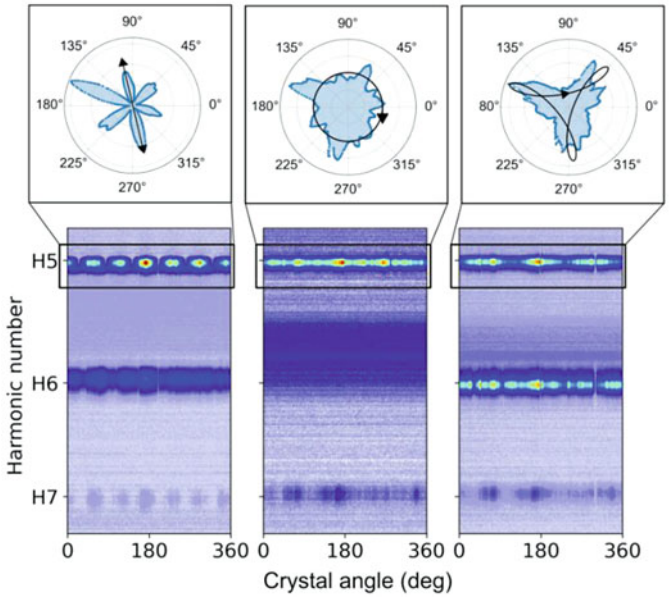

Fig. 2 Polarization scans for linear, circular, and trefoil driving fields. Harmonic spectra from GaSe are recorded as a function of the crystal rotation angle

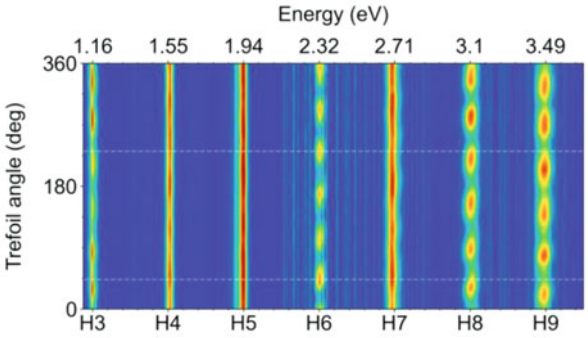

Fig. 3 The trefoil field drives high harmonic spectrum in 2H-MoS_2 as a function of the polarization rotation

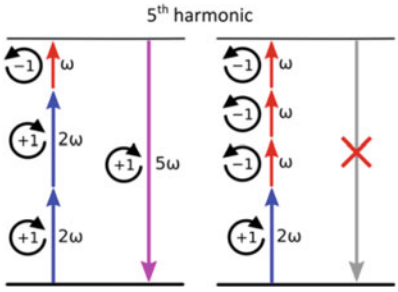

Fig. 4 Trefoil selection rules from two-color photon mixing with opposite spin-angular momentum

To investigate strong field-induced valley polarization, we used a 10-μm thin crystal of 2H-MoS_2. The material is mounted without substrate, thus avoiding contamination and background.

Figure 3 shows the recorded spectra for 360° of polarization rotation of the trefoil field only. Due to the six-fold symmetry of the material's 2H phase, we find that each harmonic modulates with 60° periodicity. This is in accord with scans in which the linear polarization aligns with the crystal axis. Note that 2H-MoS2's lowest band gap of 1.66 eV is at the K point, while the gaps at Γ and M are at 2.43 eV and 2.76 eV, respectively. From the transitions illustrated in Fig. 1, H5 is the first inter-band harmonic since it gets emitted closest to the K point.

As previously explained, although the sample is inversion symmetric, the bi-circular pump generates even harmonics. We also find that the strengths of H3 and H6 reduce by several orders of magnitude. This is explained by the selection rules (3 N + 1) and (3 N + 2) due to the conservation of spin-angular momentum during the frequency mixing of the two colors (see Fig. 4). Note that according to theory, harmonic orders (3 N) are forbidden. We attribute the observable small signal to slight imperfections of the pump, i.e., slight ellipticity of the pump polarization [15]. However, the strong and clear modulation of the signal with similar peak amplitudes over the 360° rotation proves the existence of a symmetric trefoil shape.

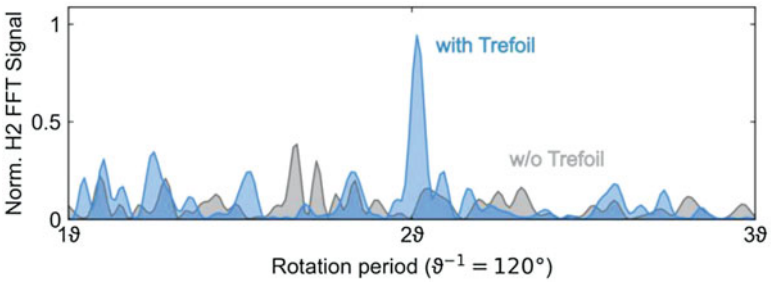

Fig. 5 Shown is the probe (H2) signal's dependency on the pump trefoil rotation. A clear modulation with 60° periodicity appears during strong field excitation, matching the six-fold symmetry of the 2H-MoS_2 sample

5 Strong Field-Induced Valley Control

Figure 5 shows the modulation of the second harmonic (SH) signal generated by the probe beam. A Fast Fourier Transform (FFT) of two different measurements, one with the trefoil as a pump and one without a trefoil, clearly shows that the trefoil field indeed induces non-resonant valley polarization.

When applying the trefoil field and rotating its polarization angle, the probe exhibits modulation every 60° of the pump's rotation; this shows in the FFT as a peak at 2 theta. As discussed in [16], strong-field interaction between the trefoil field and 2D materials like 1H-MoS2 reduces the band gap at the K or K′ points, depending on the orientation of the trefoil. Note that this process is not limited to the monolayer due to the off-resonant excitation and is, thus, universal.

6 Summary

We show experimental results from polarization-shaped trefoil fields that non-resonantly induce valley polarization in a TMDC material. Generating and measuring the effects of valley polarization are all-optical, thus providing control over material properties at the sub-cycle scale of PHz optical fields. High harmonic spectroscopy is employed to characterize and measure the efficacy of valley polarization.

Acknowledgments J.B. and group acknowledge financial support from the European Research Council for ERC Advanced Grant "TRANSFORMER" (788218), ERC Proof of Concept Grant "miniX" (840010), FET-OPEN "PETACom" (829153), FET-OPEN "OPTOlogic" (899794), FET-OPEN "TwistedNano" (101046424), Laserlab-Europe (871124), Marie Skłodowska-Curie ITN "smart-X" (860553), MINECO for Plan Nacional PID2020–112664 GB-I00; AGAUR for 2017 SGR 1639, MINECO for "Severo Ochoa" (CEX2019-000910-S), Fundació Cellex Barcelona, the

CERCA Programme/Generalitat de Catalunya, and the Alexander von Humboldt Foundation for the Friedrich Wilhelm Bessel Prize.

References

1. Ghimire, S., DiChiara, A., Sistrunk, E., et al.: Observation of high-order harmonic generation in bulk crystal. Nat. Phys. **7**, 138–141 (2011)
2. Parks, A.M., Ernotte, G., Thorpe, A., McDonald, C.R., Corkum, P.B., Taucer, M., Brabec, T.: Wannier quasi-classical approach to high harmonic generation in semiconductors. Optica. **7**, 1764–1772 (2020)
3. Vampa, G., Hammond, T., Thiré, N., et al.: Linking high harmonics from gases and solids. Nature. **522**, 462–464 (2015)
4. Silva, R., Blinov, I., Rubtsov, A., Smirnova, O., Ivanov, M.: High harmonic imaging of ultrafast many-body dynamics in strongly correlated systems. Nat. Photo. **12**, 266 (2018)
5. Tancogne-Dejean, N., Mücke, O., Kärtner, F., Rubio, A.: Ellipticity dependence of high-harmonic generation in solids originating from coupled intraband and interband dynamics. Nat. Commun. **8**, 745 (2017)
6. Elu, U., et al.: High harmonic spectroscopy of quantum phase transitions in high-T_c superconductor. Proc. Natl. Acad. Sci. **119**(40), e2207766119 (2022)
7. Yoshikawa, N., Nagai, K., Uchida, K., et al.: Interband resonant high-harmonic generation by valley polarized electron–hole pairs. Nat. Commun. **10**, 3709 (2019)
8. Liu, H., Li, Y., You, Y., et al.: High-harmonic generation from an atomically thin semiconductor. Nat. Phys. **13**, 262–265 (2017)
9. Zeng, H., Dai, J., Yao, W., et al.: Valley polarization in MoS_2 monolayers by optical pumping. Nat. Nanotech. **7**, 490–493 (2012)
10. Liu, Y., Gao, Y., Zhang, S., et al.: Valleytronics in transition metal dichalcogenides materials. Nano Res. **12**, 2695–2711 (2019)
11. Xiao, D., Yao, W., Niu, Q.: Valley-contrasting physics in graphene: magnetic moment and topological transport. Phys. Rev. Lett. **99**, 23 (2007)
12. Elu, U., Maidment, L., Vamos, L., Biegert, J., et al.: Seven-octave high-brightness and carrier-envelope-phase-stable light source. Nat. Photonics. **15**, 277–280 (2021)
13. Heinrich, T., Taucer, M., Kfir, O., et al.: Chiral high-harmonic generation and spectroscopy on solid surfaces using polarization-tailored strong fields. Nat. Commun. **12**, 3723 (2021)
14. Nariyuki, S., Peiyu, X., Faming, L., Teruto, K., Jiro, I., Nobuhisa, I.: Observation of selection rules for circularly polarized fields in high-harmonic generation from a crystalline solid. Optica. **4**, 1333–1336 (2017)
15. Jiménez-Galán, Á., Zhavoronkov, N., Schloz, M., Morales, F., Ivanov, M.: Time-resolved high harmonic spectroscopy of dynamical symmetry breaking in bi-circular laser fields: the role of Rydberg states. Opt. Express. **25**, 22880–22896 (2017)
16. Jiménez-Galán, Á., Silva, R., Smirnova, O., et al.: Lightwave control of topological properties in 2D materials for sub-cycle and non-resonant valley manipulation. Nat. Photonics. **14**, 728–732 (2020)

Part IV
Panel Discussion

The Future of Attosecond Science

Nirit Dudovich, Li Fang, Mette Gaarde, Ursula Keller, Alexandra Landsman, Maria Richter, Nina Rohringer, and Linda Young

Abstract Conferences are incredible opportunities to strengthen the inclusive outlook of our scientific community. The participation of female scientists, postdocs, and graduate students in the ATTO VIII conference was remarkable, with more than 40% of female invited speakers. The Local Organizing Committee seized this oppor-

N. Dudovich
Department of Complex Systems, Weizmann Institute of Science, Rehovot, Israel
e-mail: nirit.dudovich@weizmann.ac.il

L. Fang (✉)
Department of Physics, University of Central Florida, Orlando, FL, USA
e-mail: li.fang@ucf.edu

M. Gaarde
Department of Physics and Astronomy, Louisiana State University, Baton Rouge, LA, USA
e-mail: mgaarde1@lsu.edu

U. Keller
Department of Physics, ETH Zürich, Zürich, Switzerland
e-mail: kursula@ethz.ch

A. Landsman
Department of Physics, The Ohio State University, Columbus, OH, USA
e-mail: landsman.7@osu.edu

M. Richter
Max Born Institute, Berlin, Germany
e-mail: maria.richter@mbi-berlin.de

N. Rohringer
Center for Free-Electron Laser Science CFEL, Deutsches Elektronen-Synchrotron DESY, Hamburg, Germany
e-mail: nina.rohringer@physik.uni-hamburg.de

L. Young
Chemical Sciences and Engineering Division, Argonne National Laboratory, Lemont, IL, USA

The James Franck Institute and Department of Physics, The University of Chicago, Chicago, IL, USA
e-mail: lindayoung@uchicago.edu

L. Argenti et al. (eds.), *Proceedings of the 8th International Conference on Attosecond Science and Technology*, Springer Proceedings in Physics 300,
https://doi.org/10.1007/978-3-031-47938-0_20

tunity to promote an atmosphere that welcomes all. An entirely female evening panel, with experience across the attosecond science spectrum, was convened to explore the Future of Attosecond Science in the evening session of Wednesday, July 13. Furthermore, a booklet entitled Perspectives in Attosecond Science was compiled by Dr. Shima Gholam-Mirzaei of the University of Ottawa and ATTO co-chairs Luca Argenti and Michael Chini, in collaboration with members of the Local Organizing Committee and others, which included interviews with female scientists at all career levels and which was included in the conference materials. The text has been minimally edited to improve clarity and readability.

Keywords Attosecond science · Plasma-based accelerators · Free electron lasers · Research collaborations · Physics professional societies · Physics education · Multidimensional spectroscopy · Advanced detectors · Ultrafast laser industry · History of Ultrafast Technology

1 Panel Discussion

Li Fang: Good evening everyone. My name is Li Fang. I am an assistant professor at UCF and a member of the ATTO Local Organizing Committee. I will be chairing this session. In this session, we are going to have a broad discussion of what is on the horizon of attosecond science. This session's name, as you can see in the abstract book, is "The Future of Attosecond Science". It is very important that all of you provide active contributions to this discussion. We would like to hear from all of you. Before we open the discussion to the audience, we will touch on a few broad topics with help from a small group of representatives of the whole spectrum of attosecond science. We decided to take the opportunity of ATTO to offer the podium to an all-female panel so that the youngest members of the community can appreciate the essential role that women have played in this field, in this community, and appreciate the role they themselves can play in the future Let me introduce the panelists. I will call the names in alphabetical order. When I call your name, please come to the stage. Dr. Nirit Dudovich from Weizmann Institute of Science in Israel (applause), Dr. Mette Gaarde from Louisiana State University (applause), Dr. Ursula Keller from ETH in Zurich Switzerland (applause), Dr. Alexandra Landsman from The Ohio State University (applause), Dr. Maria Richter from the Max-Born Institute in Berlin Germany (applause), Dr. Nina Rohringer from University of Hamburg Germany (applause), Dr. Linda Young from Argonne National Laboratory and University of Chicago (Fig. 1) (applause). We will have two rounds, and we will keep each round within about 20 minutes so that we have time for contributions from the audience. The first question is: What are the most promising directions in light generation and spectroscopic techniques? What pulse parameters can we achieve in the next 10–20 years, and what breakthroughs are required to do that? Is there a volunteer to answer that first question? (laughter).

Fig. 1 Panel on the future of attosecond science. Left to right: Linda Young, Nina Rohringer, Maria Richter, Alexandra Landsman, Ursula Keller, Mette Gaarde, and Nirit Dudovich. The panel was chaired by Li Fang (right, standing)

Ursula Keller: OK, I think I will volunteer for this impossible question. First, I would like to, in the name of all of us, thank the organizers to give this visibility to the women. I mean, you know, I'm a little bit at the end of my career and I want to just say that this is very special, and I am very honored to be surrounded by these excellent women here around me, and to make them visible, I very much appreciate that (applause). With regards to sources, I can tell you that I cannot predict the future. This is one thing I have learned in my career. Over the time of thirty years, because that's from the start of my professor position to where I am pretty much now, thirty years, I never would have predicted we are where we are today. Totally not. We overachieved any of my predictions. Because we are thinking linear, and never thinking nonlinear, and there is always some unexpected breakthrough and suddenly we make a quantum jump and all our predictions go basically beyond. But I actually honestly think that, when we are pushing now the measurement techniques, I think a lot of the stuff that I can predict, which is this linear progression, is that we need to keep working on signal-to-noise on our measurement, and for the next generation of people, they need to understand noise. One of the ways I was successful: I learned during my PhD about noise. This is now in my book, so read the book (laughter) – and you're going to hear that statement many many many times. My own students learn that and actually it helps them – because you need to know about noise to make something visible when you want to measure it, OK? One development that I see from people who are now installing beamlines – many of the running beamlines all have the same parameters – when you actually look at all the publications, we're all at the same kind of parameters in terms of our measurement, between destroying the sample and just getting signals. Some are a little bit better, but we're all in the same order of magnitude. We all have clear the vision – I mean the vision of core-level spectroscopy; the physics is clearly lined out, what we could do – but right now we're limited by signal-to-noise

ratio. One of the new technologies that I can see for people who now build up a new beamline is dual comb seeding of amplifier systems. That's because, traditionally, we do pump-probe with mechanical delay lines, but now with this dual comb seed laser, we have the possibility to do that much faster. And if we make a measurement much faster, then we only take the high-frequency noise. So, the faster you measure, you always have a 1/f noise, more or less, and then you only integrate the noise from the measurement time on and higher up. The faster you measure, the lower the noise. So, set up a beamline. There are trade-offs of course. Nothing comes for free. I don't have the perfect answer, you have to think it through for your application, but think dual comb, and read my book (laughter and applause).

Nina Rohringer: I would like to comment. I was really impressed to see this huge progress in attosecond transient absorption, the way solid samples are characterized now, and I think the advance in this field was greatly driven by the availability of sources at many different universities. Many groups could achieve progress and work in parallel towards this progress. I think for free-electron lasers, the beamtime is still scarce. A group may have one source available at a time, two beamtimes in a year. You can employ three-four sources in parallel, but it's still not comparable with what one can do with a series of experiments and a dedicated program. So, progress is limited by the access people have to these sources. Therefore, I think that if we can somehow shrink these accelerators to plasma-based accelerators or other schemes that are currently discussed and approached, it would make a big leap forward in that direction because the accessibility is just going to be widened up. I think that's also the reason why a lot of national laboratories around the world are now investing really big in this laser-plasma development. In the future, this is a game-changing technological step that's really necessary to change the way we can do science.

Linda Young: I just wanted to come back to this idea that you can't predict the future, because it's quite interesting. I think you can't predict the future so well in laser-based things, because they are very spontaneous in one lab, but I have to say I am so impressed with how free-electron lasers came into being. Right? This was actually a vision of Claudio Pellegrini in 1992, and then it got realized in 2009. And maybe this wasn't actually predicting the future, but he was certainly envisioning what you could do, and that really set the course. I heard last night, or the night before at dinner, that Persis Drell's husband, who is an accelerator physicist at SLAC and was the director of SLAC at that time, never believed it was going to work. And then it worked, like within 30 minutes or something. It is quite amazing, and I'd have to say "hats off" to these accelerator physicists. They are really good. And so, maybe, these plasma things that Claudio [Emma] talked about can actually shrink it. Seriously, as Nina mentioned, you can't make much progress if you don't have access.

Nirit Dudovich: I think another really interesting direction, we'll hear about this tomorrow perhaps, is to take this field of attosecond science that was really based on classical light sources, into quantum optics. And I think, for me, there's so many open questions that are still not clear. There have been some breakthrough experiments and some beautiful theories that have been presented, but I think

we're really doing our first steps in this direction. For example, can we enhance the efficiency of this mechanism once the source itself becomes quantum? Can we resolve some correlation or quantum phenomena that we cannot resolve with classical light? UK: I would like to add to all of what has been said. Currently, the cost for running an attosecond beamline, for a single professor, is coming to the edge even in Switzerland, which means that a lot of other places find it much tougher to finance it. And the reality is, if you want to go with these cutting-edge lasers, they tend to break down, so your PhD students who actually would like to do the attosecond science and not really necessarily the laser physics science, are kind of pulled into the laser technician side one way or the other. So, I really think we need to revisit how we organize this science at the university level, and that is something I tried to do at ETH. At this point, I've failed, but [for the science to be sustainable] we need to learn to share beamlines on a university level. That requires some respect for the space, for the different professors, for the research area, not that one overly-ambitious professor is stealing the ideas from everybody else, which of course doesn't work. And it requires that you have maybe some working beamlines with paid technicians that help you to keep running these beamlines, that you switch it on in the morning and it actually works within an hour, which would be really wonderful, and you could do your experiment. And you could roll in different target chambers. And then, at the same time, do some beamline development, because I really think we need to do a combination. Normally, if you develop some beamline, you don't want to touch it when it works. At the same time, you want to improve your beamlines, and for this you need to do good laser physics at the side. And no professor can do both anymore. Look at Zewail – he did femtosecond laser spectroscopy, femtochemistry, and he did femtosecond laser development. You cannot do that in the attosecond anymore with the funding that you can normally get. So join up as teams, learn to respect each other's research space and properly credit each other's ideas. And then, I think you can also move ahead and make a lot more progress (applause).

Mette Gaarde: I wanted to speak, not so much to specific sources, but more to big ideas. I have been doing attosecond science for now twenty years in the US, where ultrafast AMO is a much smaller field than it is in Europe and we are often dwarfed by the cold atoms and quantum information communities. The idea of the attosecond x-ray laser and in general the x-ray, even the femtosecond laser and the XFELs, really has been a gathering point for ultrafast science in the US. The department of energy has constructed and paid for the LCLS, of course, but I think the grand idea of what you can do, not what can the individual do but what can the field do overall, with these types of light sources, really is a gathering point as well. The development of attosecond x-ray pulses then will also overall help the development of tabletop XUV sources because there is an overall interest in the grand ideas.

LF: Thanks. I think the audience may share these same thoughts. There is often a dream system you want to test and ideas you want to realize in an experiment. I'd like to frame the question differently, so that theorists can have more input. Did you ever think, at any point, "Why can my experimental collaborators not do this?

I've already done the simulations, it's a beautiful result, and they just don't have the tools or the parameters to realize it?"

Maria Richter: At the moment I am extremely intrigued by and excited about the possibilities we have, and especially by the idea that the generation of light is a two-way street: we can shape matter with light, but matter can also shape light. This is a really interesting field. We now have access to excellent light waveforms that are sculpted with sub-cycle precision, and I think there's lots of room to use them for applications. One practical example is the coupled nonadiabatic electronic-nuclear dynamics, an essential problem in our field, which is inherently happening on the atto- and femtosecond timescale, so there's huge potential to use these mid-IR light waveforms that are sculpted on the sub-cycle timescale. There are also many other examples in which we create and use new states of matter, and these new states of matter allow us to create completely new light and new methods of generating light.

LF: We are seeing more of that.

Alexandra Landsman: To answer your question of whether theorists can imagine an experimental situation and then ask experimentalists "why can you guys not do it yet?", I think that this has actually been the condition of our field for some decades, when Keldysh's strong-field approximation theory, as it was developed back in the 60's, could not be experimentally confirmed until decades later. Perhaps we lack imagination today because we seem to be working in a regime that is experimentally accessible. Thinking just a few years in advance, I would dream about attosecond pump-attosecond probe experiments which now I think are quite achievable with attosecond XFELs like LCLS.

LF: It is achievable, it's just highly expensive. Let's move on to the next question: At its inception, attosecond science was just a sub-branch of atomic, molecular, and optical physics. Over the years, however, the field has expanded to condensed matter systems. The question is: Will attosecond science become more relevant to other areas as well?

MG: I would like to answer a slightly different question (laughter). I happen to be chair of the Division of AMO Physics, part of the American Physical Society, this coming year, which means that I will be chair of the DAMOP meeting in 2023 (applause). My point is that ultrafast science and ultrafast processes in condensed matter very much, in my opinion, have a home within DAMOP as well. Coming back to attosecond science, I think it is important to realize that ultrafast science is a relatively small part of AMO science in America, and yet it is extremely important that ultrafast science survives in America, that the US keeps making contributions to the field. So, I would like to encourage everyone in the audience, especially the young people, to join the American Physical Society if you are not already a member. It is very cheap for students, and it is also relatively cheap for early career members. There are dedicated annual APS meetings: the DAMOP meeting, as well as the Division of Laser Science meeting, which is another divisional meeting – I know that Mike Chini is involved in this – which is another place where ultrafast science happens. These are meetings where, if you submit a contributed abstract, you can give a talk. So, it is not just invited talks; there are talks by lots of young people as well. The DAMOP meeting is always full for the ultrafast part of the

program, so it is a vibrant part of our program. Attending DAMOP is something worth considering, of course mostly for the American community. Next year the meeting will be on the west coast, in Spokane WA, and I hope to see many of you there. Please consider submitting suggestions for invited talks, there's a thesis prize that is given out every year, so – I'm sorry, this is kind of a shameless plug for DAMOP, but you gave me a microphone – I think that DAMOP and ultrafast go very well together.

UK: OK, now, I fully support this. Now let me now go back to the question (laughter). Spreading out, and I really think we are at the time where we can spread out. I think, we see it already at this conference. I don't know how you feel, but, you know, it goes from something I don't know or understand to something else I don't know or understand. I mean, we only share one thing, and that's kind of pump-probe in one form or the other, right? But the underlying investigation becomes so complex that, in the details, it's so diverse. Either I'm a physical chemist, or I'm a condensed matter physicist, or I'm a laser physicist, or a cutting-edge measurement technique developing person. I think this field is now evolving into the level where it doesn't become a live focus, it's just one tool out of many on the quest in your science question. And for this we also need to broaden our education at the university, the way we usually teach quantum mechanics in physics. When you look at all the physics textbooks, we leave time behind us extremely well. Do you remember how you learned quantum mechanics in physics? So they tell you, "oh, there is this time-dependent Schrodinger equation" and then we go to the time-independent, and the rest is all about time-independent. Now I actually try to put time back into quantum mechanics in undergraduate education. You know: with waves and wave packets and so on, which of course is always challenging because waves are challenging for students, but then how can you understand the harmonic oscillator without the wave packet, right? When you bring time in, you can tell every time, in every single quantum mechanical question, bring in time, and we don't have an answer. We don't even agree on tunneling time. We agree on tunneling rate, but not on time. As soon as you bring into all the quantum mechanical questions time, you get a heated discussion. Some theoreticians tell you that you are not allowed to ask this question, which I already heard when I was a student, and I'm still hearing it today. So we need to more broadly educate at the university, and that's why I'm saying you need to have a shared technology platform in ultrafast science like people have a cleanroom facility that they share, where we also bring in the education of letting students do pump-probe experiments at an early age so they even start thinking about time resolution in biology, in condensed matter, in physical chemistry, everywhere, right? I think we then can bring in these people to actually think about time in quantum mechanics and wherever it is. But we need to also put a stronger focus on the education.

AL: We already have a lot of important efforts in plasma physics and I feel that's only going to increase, especially as we go to higher intensities. So, using plasmas both as a source for higher-intensity pulses and as accelerators for electron beams. But, why don't we go broader? While it is impossible to predict the future, we could expand into biology and medicine, and there is already some concrete, promising

evidence that that's possible. For example, Ferenc Krausz was talking about using light for cancer detection.

ND: I would like to add on a very different aspect of attosecond spectroscopy. I think over the years it's quite amazing what a jump this field made. The sources become more and more advanced, and the systems that we can look at become more and more complex, together with true advances in theory. But I think what we are still lacking, and I think this is my own frustration, is the proper spectroscopic method. I think we're not there yet. And whenever we perform an experiment, I feel that we're still limited in terms of the interpretation we can make. We always have more than one explanation to what we observe, but we do not have the proper tool to separate different channels, to fully understand what is going on there. So, I believe that the spectroscopic methods are not there yet. One promising direction, which was also mentioned in Misha [Ivanov]'s talk, is to go to multidimensional spectroscopy. I think eventually we have to go there. The dynamics itself are so complicated that we have to go to multidimensional spectroscopy and think about additional experimental observables that would allow us to have a better understanding. So, if you were asking in your question, what kind of system can you look at beyond solid? I would say let's take one step backward and try to understand what we have already. I don't think we are there yet.

LF: Thanks for going back to my first question (laughter).

NR: I would like to second what you were saying. I think we are having real problems. As a theorist, you are always running behind what experimentalists and spectroscopic measurements are measuring for complex systems, such as these big molecules or solid state systems. I think the bottleneck is really electronic structure calculations and combined electron-nuclear calculations for these systems, and from the experimental side it would be great to find a method that combines imaging at the electronic length scale and spectroscopy at the same time, and at some point, not to measure only static effects, but to do it in pump-probe settings. This is a possible future direction that might be really game-changing. It's very hard but you can try to work on that.

LY: I'd like to follow up. There's a lot of emphasis on pump-probe, but in fact that's not really what a lot of people are interested in. They're actually interested in making movies, and you'd just like to follow in time all the coordinates of your nuclei and your electrons, and you can maybe do this if you have fast enough detectors. And this is something really limiting when you go to high rep-rate XFELs or lasers, since you can't get a fast two-dimensional detector yet. I mean, we are using 2D detectors operating at - I don't know - hundreds of hertz or something like this. It would be really great if you could have an energy-resolving 2D detector that operated at a megahertz, instead. Then you could actually pull out some of this information that you want, and you can't do it now! Right? Developing high-repetition detectors is something that it is not only interesting for this community, but also for the astronomical community. They're making lots of x-ray detectors that are energy-resolving and maybe pixelated and maybe read out at a rapid rate, and this would be also really cool.

LF: I feel like I should have asked this question first. Dr. Richter mentioned the connection between physical chemistry, and how people would like to see not just the electronic dynamics but also the nuclear dynamics together. Do you think that attosecond science, or attosecond sources, will become just a tool – as ultrafast lasers or femtosecond lasers have – for all other fields, or that it will stand as having its own identity? Stand as an individual science, say 20 years from now?

UK: I can answer that question. Of course it has to become a tool, like any femtosecond laser, and when you look at them even today, femtosecond lasers are still a scientific topic. I started thirty years ago on laser development, mode locking and so on, and when I started in attosecond science in 2010, I thought I will roll down my efforts on the laser development. But I couldn't roll down, because there was always something new popping up on really interesting laser physics, and I could never roll down half of my research group because we just had new ideas on it. So I really think of attosecond pulse generation as a laser physics point of view will stay a topic for a long time, and then of course we're going to move to zeptoseconds, right? I mean there's no limit in time. And then on the other side it will become a tool, like femtosecond lasers today are a tool that people can just simply buy and they don't want to know how these femtoseconds really came along.

LF: I expect the cost for an attosecond beamline will drop over time to a level that is within reach for any research group. Right now, as you said, it's just really high and not affordable for a starting group.

UK: That's just a question of time.

MG: In some sense, I think you could turn the argument around and say that until it becomes a tool that most users don't think about how to use, the field does not move beyond being a very high level "boutique". That's not a very nice word, but I mean in some sense isn't harmonic generation and having a femtosecond harmonic generation source now something – I'm sorry to all the experimentalists – that you can more or less buy off the shelf?

UK: Not yet.

MG: But it's close, yes?

UK: Yeah, but that's the thing that limits us to small little damage and seeing signal, yes? We are... there.

MG: Yes, but you cannot do that with an attosecond light source, right? And I think that if you really want to go broad, if you really want to have an impact, then you need it to be much more accessible.

UK: Sure, definitely. It's starting. In Europe, even a really hard-core condensed matter physicist is now getting an attosecond beamline financed. But there are so many parameters with these lasers. And all of these parameters is your investment, and you're stuck in it, right? And that's why I think it makes sense, when you look at the groups that do extremely well, for example Lund, to learn to share some lasers and invest in some technicians. I think that's the way to go. That depends not only on your university but also on the professors in the local places, which should make a conscious decision to share and make an effort. And just collect, very selectively, the good scientists who are willing to follow the share concept. To a certain extent, you need to get a running horse, because we're still doing really one-of-a-kind type of

experiments, but then you need to also do some beamline development at the side. And you cannot do development on the same equipment you use for production, right? That doesn't work. If there is some funding agencies here, because I bumped into somebody from AFOSR, from the US, I hear a lot from the US colleagues that they have hardly any chance to get money for laser development. And if you need anybody who gives a little bit of a talk to your funding agencies, I'm happy to do that. Because that is definitely not good. In comparison to the time when I came to the US, the US was a clear leader. We wouldn't call the US a clear leader anymore, right? And it had a lot to do with the funding agencies not funding laser technology. OK? It's not good.

LF: I probably can quote what you said in my proposal.

NR: I want to encourage this community. The community is growing and the expertise is growing, we have many people who are trying to develop novel techniques or make use of new sources. At the x-ray free electron lasers, sometimes you feel like in a small circus. You meet the same people at different experimental stations over and over again. The community that does experiments at these sources is actually pretty small in AMO science. You could also think about innovative experiments you could do there. You have heard today about the opportunities that there are. You take a week of group vacation (laughter), a group outing not to go hiking in the mountains but to go to an FEL and do experiments and propose experiments. The real value of the method will grow by many people bringing new ideas and new impact in that area.

AL: To answer the question, I will have to go back to the issue of funds, because we already have a vibrant distinct community. I think it will survive as long as it is well-funded. It's not completely possible to predict how funding will go, but, with the progress and the advances in the field, it looks good to me. So, I can certainly see it as a very vibrant and active community 20 years from now.

MG: It is our responsibility to keep it funded, in the end. This is how the funding comes, because there are ideas and there are applications and because the field spreads beyond doing just a few things to doing many things. And this is what we're doing, right? People keep innovating in experiment and theory and this is how you keep the funding going.

MR: Yes, and we keep the funding going especially when we have the abilities to focus on practical applications, and I think already this week we saw the broad possibilities we step into, like new engineering, new material sciences , optoelectronics, spintronics, there are of course the dreams also by using attosecond science of sustainable energies in terms of solar cells, photovoltaics, even the dream of remediating nuclear waste. To follow up with what Nina said a few minutes ago, I also see that we are strongly pushed back by the, nowadays, limitations on easily accessible, accurate quantum chemistry structure calculations. What doesn't seem to be touched here at the conference, but what might be interesting especially in this question, is the advances in machine learning. In general, I'm skeptical regarding the hype of artificial intelligence, and for some reason we've already lived through several so-called artificial intelligence winters, but I think machine learning for the purpose of structure calculations in quantum chemistry might be a path to pursue.

LF: We have 20 minutes left. Thank you for all the great answers and input (applause). Now we are open to interventions and questions from the audience. Aud: I just wanted to follow up on a comment that Linda made. I feel like historically our community has not been that involved in the development of new detectors, we've relied on other communities for detectors, and I feel like we're coming up at a time where the detectors that we have are not really the detectors that we need, and so I was just wondering if you could give any perspective. We are also seeing now that the attosecond science community is becoming a part of and interacting more with the accelerator community. Do you have any perspective or ideas on how we can work on the development of new detectors for our needs.

LY: Yeah, I think there is a lot of synergy. If you look to the synchrotron filed, they got most of their detectors from high-energy physics collaborations, mostly in PSI. Now there's a very well-known company called Dectris that sells almost all of the pixelated detectors that are used both at synchrotrons and even at XFELS. But there's a lot more that can be done. Right now they're typically photon counting or analog mode, but you would really like to have something like energy-resolving pixelated detectors, and that's something that no one is working on so much except for the astronomy community. You guys are right here next to NASA. So I think it's something that we can really contribute a lot to. It would help our own research, and I think there's some connections to be made there.

UK: And great start-up company opportunities for the younger generation working on detectors.

Aud (Subhendu Kahaly): I would like to know your opinion on two things. One is there are four fundamental states of matter, but there is a fifth which is vacuum. In attosecond science domain, we mostly look at the low intensity side. There is a huge community, however, which is looking at the higher intensity part. Do you think it is a good idea that we extend and open the doors to the community which are looking for and are breaking the vacuum, or to the extreme laser plasma side, but still connected with the ultrafast dynamics studies?

UK: I think it's already happening with ELI, which is pushing exactly that. They are building, and these are basically when you are then talking that kind of intensity, that's definitely beyond your laser facility type of endeavor, and that's why in Europe we have this ELI concept and we have experts here. You should, stand up and say something, another really really excellent woman there.

Aud (Katalin Varju): Well thank you very much, actually Subhendu is from ELI as well (laughter). And also when you said that we need to share, it really hit a chord in me that at ELI this is what we are trying to do. We want to share our systems, so user proposals are welcome.

Aud (Kahaly): This is a question that always emerges when I'm having informal discussion with experts in the field. Do you think it's a good idea in future conferences to keep a separate small pocket which would be dedicated to applications of attoscience. What is application depends on individual perception or perspective, but I mean more applied attoscience.

MG: Actually, I think it might be interesting to have, as part of future ATTO conferences, something on how to start up your own company. Thinking about

applications, something directed at the young people that was more career focused, inviting some people who have started their own companies. Maybe in a parallel session. At the big APS meetings we often do something like this. There are career sessions and they are very popular, lots of young people, because it provides a way to see what is the non-academic track but where I could still use my training. And I think that attosecond science is ripe for this as well.

NR: I think we have to reach out to other communities. I was reviewing a big battery research project, a European one, and I'm asking the question if they're interested in time-dependent processes. Sure, their time dependent processes are hundreds of loading cycles of a battery, but I mean the short timescales, they're not even on their radar if there could be something interesting. At the moment we are reaching out to solid-state physicists, to figure out what their problems are, what solutions and techniques we can provide, and at a later point in time we have to reach out to these other communities and see if time dependent problems are of relevance in that area. Another thing is bridging different scales. Even in solid state physics you still have the problem of a superconducting gap, and the techniques that we use, with resonant elastic x-ray scattering, using 10 keV photons, or to look into these kind of tiny energy ranges. So maybe another good idea would be to think for time-domain spectroscopies, along with x-ray imaging methods, that would resolve these very tiny energy scales where you cannot just work as a purely spectroscopic measurer anymore. We need to reach out to some of these communities and try to get them to collaborate. I think that's the way we should walk on.

Aud: When I studied physics some decades ago, femtosecond physics was known as the shortest timescale of physics and the cutting-edge technology in both theory and experiments. Now it's attosecond physics. If we look two decades in the future, do you anticipate that that there will be a decade of yoctosecond physics in theory or research, or can we say that there is a limit that at such short timescales there will be no interesting physics anymore and the practical limits to make experiments are too hard?

UK: Is there a limit on time? You know, in terms of the shortest time, there is always a prediction in the end – this is the shortest time event that can be measured. Actually, Paul Corkum was talking about the shortest time event that can be measured, just recently. Howard Reiss was recently visiting us and giving us a lecture. He thought that at one point the atomic unit of time is the shortest time to be measured, and I must ask "Why, why why?". When you think about how time is defined, it's counting periodic cycles. There is no limit when you look at the electromagnetic spectrum, where it stops cycling, right? It goes up to higher and higher frequency as long as we measure, as long as we manage to count the cycles, time becomes more accurate. People already talk about nuclear photonics, to do the whole spectroscopy of the nucleon. And that is for sure untouched physics, and for this you need to get a good training in nuclear physics to begin with, and learn about what time measurement means, which should belong in the education we're giving to young people, and then they put things together. One project at ELI, for example, is going along those lines, into nuclear photonics. That's for sure a hot topic to go into. Also challenging, but there is no limit. I'm really convinced.

AL: I actually really liked the name attosecond because it's the natural timescale of electron motion inside matter. I think we'll probably be able to have zeptosecond pulses, but we can still call it attosecond science because we will still be studying how electrons evolve inside matter.

Aud: I guess this might be a little bit provocative, but I wonder what's your perspective on the connection between experimentalists and theorists. We see a great connection at this conference. I cannot speak for other experimentalists, but as an experimentalist myself, sometimes I am under the impression that theory is a black box. Sometimes it matches greatly with the results and we have to take the leap of faith to believe that is correct. I don't know whether other people feel similar things, so what's your perspective? Maybe educating experimentalists like me to better appreciate the accuracy and the machinery of a theory framework.

NR: You are a solid-state physicist and you are interest in, also highly correlated electronic systems. I mean, it's the holy grail of theory to describe these systems, and the theory we have at hand is not in the state to be quantitatively predictive without any tuning parameters. That's another limitation at the moment. And that applies to chemical reaction dynamics, electron and nuclear dynamics coupled in molecules, and even the ground state electronic structure in solids. It's pretty difficult!

Aud: Since we are looking at the future, the future is also how we promote our field to the general audience and also to the physics students. Condensed matter physics and high-energy physicists sell very well their own field. We AMO physicists, however, sell terribly badly our field. We need to change. While nowadays attosecond physics is merging with condensed matter physics, so that our field is not confined to AMO anymore, I still think that as a community we need to do a better job to reach out to physics students and also to the general audience. The perception of the general audience is important because that's where the money is coming. At the end of the day it's tax payers who are paying our salaries, and we need to advertise better the importance of our field. What do you have to say about this?

MG: Amen! (applause)

UK: I agree. When you look also at the Nobel prize winner in ultrafast science in physics, it's pretty much a sad story. There was a femtochemistry Nobel prize winner, but all the physics that went into getting these short pulses to begin with, they never got the Nobel Prize. I can name a couple of them, Chuck Shank, (Erich) Ippen, a lot of the people who've done the first femtosecond spectroscopy in the physics community never got the Nobel Prize. And that has been a tradition because they fought each other like hell. You know when I watch the quantum optics community, then this year they define the area so small that they find these three people that win the Nobel Prize, and when you win the Nobel Prize that's a boost for the field, for everybody, for us. And then they define the field a little bit differently, and then they get the next Nobel Prize. And the ultrafast laser physicists, they were fighting each other. I mean I watched it as a young student, it was very competitive. They could never agree. There was [Professor] Kaiser in Germany, then there were the people in France, the people in the US, and they could never agree on the three, instead of kind of dividing up the pie so that they can find the three this year and

the other three the next year and the other three the other next year. You know, we need to learn to live and let live. Live and let live. That also means on the science reviews. Accept the review, and be generous to your colleagues, right? (applause)

LF: That's good advice.

UK: Live and let live! Be happy if your colleagues have a success, and don't be a competitive spoilsport. (applause)

MG: I think that some of it comes back to what is the big idea? What is the thing that you can tell to the kindergartener and to the person who would otherwise be interested in cosmology or be interested in quantum computation? Because those are things that people think they can hold onto. How many first-year physics students want to do cosmology, and then figure out they don't actually want to do it? But they think they want to do cosmology, right? What is it that we can bring? Is it the idea of the time evolution? The making of the movie? But what are you going to use the movie for? Why does it matter that you can time-resolve something? I think I'm very much in agreement with you that, until we have a concise answer to that, we are not doing a good enough job of selling ourselves.

NR: Yeah, I could start with my daughter as a kind of guinea pig for this. When she was four, and changing kita in the kindergarten, she came home and at some point she was really upset at the dinner table, and she said "Couldn't you make something useful in your life? Be a medical doctor or something?" Because I think she couldn't defend my state in front of her friends over there. Yeah, I mean it's difficult to sell our job to the society. It's challenging.

LF: But it's important to bring the attention to the public.

Aud: First I had a common question. I thought it was interesting that you mentioned that we don't sell our community that well, because, when we look at the talks given every second reference that we put up there is a Science or a Nature. So to the scientific community, we are really hyping ourselves up. Everyone's always going for that highest journal. Yet now we're talking about, well we need to be more cooperative. We don't really even have a journal that is specialized in attosecond science where we can write nice long technical papers, where we can explain to each other what we're actually doing. The papers we write are four pages, from which no one knows what anyone did, none of the technical details, no one can actually reproduce each other's results. Until we get over the Science and Nature phase, I don't think we'll be able to be that cooperative. So I think that also comes, we have to take a hit there.

UK: OK, that is now going way beyond the attosecond science. That is of course a broad discussion, and I agree. I'm a professor who never had a Science or Nature publication before I became a professor. Because it never was a measure of success during my time, to actually have a Nature or Science paper. And I agree with you, it's not healthy that suddenly the journals would matter, right? But that's a broad discussion and that's unfortunately a development in science which I also don't like. I don't know the way out of it.

Aud: But a specialized journal might be something that our community could start.

Aud: Thank you for these nice discussions. I think Nirit mentioned that the next frontier for attosecond science could be bringing quantum optics ideas into attosecond science. This is something that I'm personally interested in, I'm developing some ideas with limited resources. Can you share some more thoughts on what we can do to get the community more excited and maybe funding agencies interested in bringing quantum optics ideas to attosecond science, and maybe develop attosecond quantum optics?

ND: First, tomorrow there will be, I think, an excellent session on that topic. To me, it's still an open question how we link quantum optics with attosecond science. What are the advantages it brings? I think it just opens up new questions which are not answered yet. And can we use it to see phenomena which are not observable with classical light? But I must admit, I don't have clear answers. Maybe other people in this audience who gave more thought into this topic can answer that better.

LF: OK I think we can have more discussions after the session is closed. I think it's time, and before we close this session, I just wonder if the panel, if you have something you want to say to the students in the audience. This is the next generation workforce: bring some excitement to the field.

UK: Now we're on the spot. Honestly in my whole career this is the first time on a panel with only women, so I'm still really excited about this I have to say. And my message to anybody is: You can do it! I mean, look at all these people! And I really would like to encourage also the next generation – do it better than us in terms of equal opportunity. Think about dual career. I actually think this is a great opportunity in your life. You can manage risk with different careers. It is not a problem, it is an opportunity. And make sure that your partner can expand in their careers fully. My husband and I, we did it. The rest of the world wasn't ready when we did it, but we did it anyway and I have no regrets. OK? We just did it. Just do it and marry the right partner. (laughter)

MG: Oh, I agree with that one. (laughter)

UK: Just do it, guys!

MG: I would add exactly to that. I would say don't say "no" because you don't think you can do it. Say "yes" more than you say "no". I mean, not to the marriage part. (laughter) That was the science part.

LF: OK, let's thank the panelists for the great discussion (applause) and also thank the audience for the great questions. If you have other questions you want to ask, you can talk to the panelists after the session is closed.

Correction to: Attosecond Physics and Quantum Information Science

M. Lewenstein, N. Baldelli, U. Bhattacharya, J. Biegert, M. F. Ciappina, T. Grass, P. T. Grochowski, A. S. Johnson, Th. Lamprou, A. S. Maxwell, A. Ordóñez, E. Pisanty, J. Rivera-Dean, P. Stammer, and P. Tzallas

Correction to:
Chapter 4 in: L. Argenti et al. (eds.), *Proceedings of the 8th International Conference on Attosecond Science and Technology*, Springer Proceedings in Physics,
https://doi.org/10.1007/978-3-031-47938-0_4

The original version of the chapter "Attosecond Physics and Quantum Information Science" was published with few XML errors, and as a result, two affiliations of the coauthor Tobia Grass were missing. The changes have been updated in this version.

The updated version of this chapter can be found at
https://doi.org/10.1007/978-3-031-47938-0_4

L. Argenti et al. (eds.), *Proceedings of the 8th International Conference on Attosecond Science and Technology*, Springer Proceedings in Physics 300,
https://doi.org/10.1007/978-3-031-47938-0_21